On the Processing of Doppler Signals in Ultrasonic Blood Velocity Measurements

by

Kjell Kristoffersen

Div. of Engineering Cybernetics
The Norwegian Institute of Technology
Trondheim 1985

On the Processing of Doppler Signals in Ultrasonic Blood Velocity Measurements

by

Kjell Kristoffersen

Div. of Engineering Cybernetics
The Norwegian Institute of Technology
Trondheim 1985

NTH-Trykk
1986

LIST OF CONTENTS: PAGE

LIST OF CONTENTS, continued PAGE

PREFACE

The bulk of this work was carried out at the Norwegian Institute of Technology, div. of Engineering Cybernetics, and SINTEF, div. of Automatic Control, in the period 1981-1983. I left Trondheim for a new assignment the late fall of 1983, so that a large portion of the material has been "sleeping" for two years prior to publication. This is unfortunate in view of the rapid development of digital technology that has taken place in the meantime; a different approach to some of the hardware related issues (spectrum analysis using BBDs, e.g.) would certainly have been taken today. A positive aspect of the delay is that during the time passed, some of the results and techniques derived in this thesis have been incorporated into commercial equipment. This has allowed for the presentation of some practical results in the summary of this thesis, which would not have been available two years ago.

LIST OF PAPERS

This thesis is based on five papers and one report:

I. K. Kristoffersen, "Optimum Receiver Filtering in Pulsed Doppler Ultrasound Blood Velocity Measurements", **IEEE Transactions on Ultrasonics, Ferroelectrics, and Frequency Control**, vol. UFFC-33, pp. 51-58, Jan. 1986.

II. B. Angelsen and K. Kristoffersen, "Discrete Time Estimation of the Mean Doppler Frequency in Ultrasonic Blood Velocity Measurements," **IEEE Trans. Biomed. Eng.**, vol. BME-30, pp. 207-214, Apr. 1983.

III. K. Kristoffersen and B. Angelsen, "A Comparison between Mean Frequency Estimators for Multigated Doppler Systems with Serial Signal Processing," **IEEE Trans. Biomed. Eng.**, vol. BME-32, pp. 645-657, Sept. 1985.

IV. K. Kristoffersen, "Time Domain Estimation of the Center Frequency and Spread of Doppler Spectra in Diagnostic Ultrasound," preprint; accepted for publication in **IEEE Transactions on Ultrasonics, Ferroelectrics, and Frequency Control.**

V. K. Kristoffersen, "Real Time Spectrum Analysis in Doppler Ultrasound Blood Velocity measurements," SINTEF report # STF48 F84030, Nov. 1984.

VI. K. Kristoffersen and B. Angelsen, "A time shared ultrasound Doppler measurement and 2D imaging system," submitted for publication in **IEEE Trans. Biomed. Eng.**

In the text, the papers are referred to by their Roman numerals.

1. INTRODUCTION.

During the past two decades, ultrasound-based techniques have become indispensable tools in several areas of noninvasive diagnostics. **Echo amplitude imaging**, the 'medical sonar', came into common clinical practice already in the early 1970's, primarily in obstetrics and cardiology. It is now used routinely in a variety of fields. There has also been a growing interest in the clinical application of **Doppler ultrasound** for the measurement of blood velocity in humans. The underlying principle is the Doppler effect, i.e., the change in frequency that occurs when a soundwave is scattered by the red cells of flowing blood. By measuring this frequency shift, the velocity of blood in most of the larger vessels and in the heart can be measured noninvasively. A number of diseases in the circulatory system can be detected and assessed using Doppler ultrasound. A typical example of its usefulness is in the diagnosis of obstructions to blood flow, which can be detected from a local increase in the blood velocity.

The subjects of this dissertation are the design, analysis and evaluation of methods for signal processing in Doppler ultrasound blood velocity meters, with some emphasis on applications in cardiology. A number of different topics is covered; optimal filtering of the received Doppler echos, processing of the Doppler signal for extraction of its information contents (frequency estimation, spectrum analysis), and, finally, a method for the real time combination of Doppler measurements and echo imaging. The thesis is divided into several self contained parts, which are summarized in detail in Section 3. However, to provide necessary background for the reader who is not familiar with Doppler techniques, a brief review of the basics of diagnostic ultrasound will first be given.

2. BASICS OF DIAGNOSTIC ULTRASOUND

2.1 Doppler measurements

The use of continuous wave (CW) Doppler for the measurement of blood velocity was reported by Satomura as early as 1957 [1]. The CW Doppler instrument is simple, but it gives no range resolution in the measurement. This deficiency was overcome by the pulsed wave (PW) Doppler instrument, first reported by Baker in 1967 [2]. The sampled nature of the pulsed Doppler introduces a limit on the maximum frequency or, correspondingly, the maximum blood velocity that can be measured. Later on, effort has been put into the development of different types of instruments that give range resolution with maintained ability to measure high velocities (the correlation Doppler principle [3], PRBN codes [4]). However, in spite of considerable effort, no clinically useful device based on any of these concepts has been presented, and they have, therefore, been omitted from this review.

2.1.1 Continuous wave Doppler

Fig. 1 shows a block diagram of a simple CW Doppler instrument [5]. A soundwave with frequency f_o (in the range 1-20 MHz) is emitted continuously towards a vessel containing blood flowing with velocity $\vec{v}$ (time steady plug flow assumed). The back-scattered ultrasound then has the center frequency $f_o + f_d$, where the Doppler frequency f_d is given as [6]

$$f_d = - \frac{f_o}{c_b} (\vec{n}_t + \vec{n}_r) \cdot \vec{v} \qquad (1)$$

where $\vec{n}_t$, $\vec{n}_r$ are the axes of the transmitting and receiving transducers, respectively (see Fig. 1), and c_b is the speed of sound in blood (1560 m/s). When $\vec{n}_t$ and $\vec{n}_r$ are colinear with the angle α to the blood velocity, the magnitude of the Doppler shift becomes

$$|f_d| = \frac{f_o}{c_b} |\vec{v}| \cos \alpha \qquad (2)$$

Thus, the Doppler shift is proportional to the axial velocity component $|\vec{v}|\cos \alpha$, that is, the component of the velocity that is parallel with the soundbeam direction. The angle α, therefore, needs to be known to determine the velocity from the measured Doppler shift. By convention, blood moving towards the transducer has a positive axial velocity, since it gives a positive Doppler shift.

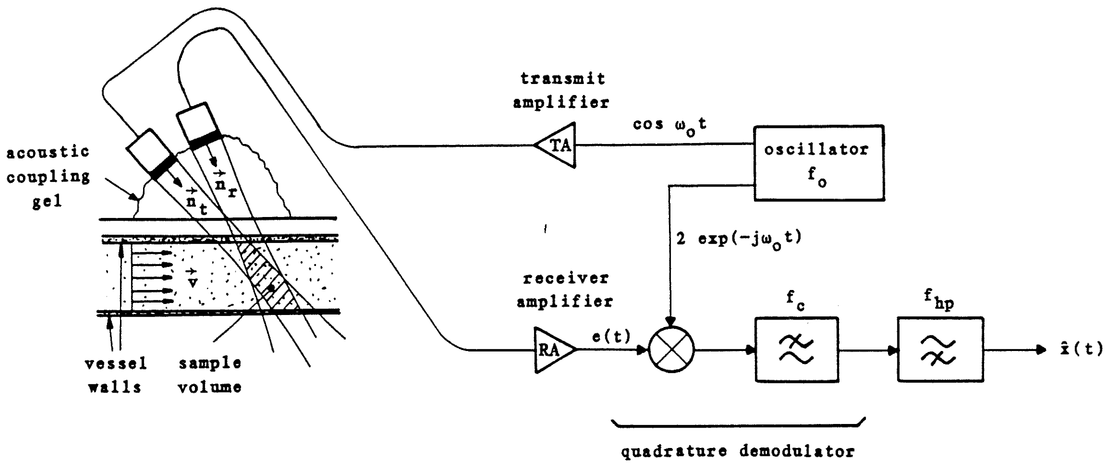

Fig. 1 Measurement of blood velocity using CW Doppler ultrasound.

The received Doppler echos may be written on the form [6]

$$
\begin{aligned}
e(t) &= \mathrm{Re}\{\hat{x}(t)e^{j\omega_0 t}\} \\
&= \frac{1}{2}\,(\hat{x}(t)e^{j\omega_0 t} + \hat{x}^*(t)e^{-j\omega_0 t})
\end{aligned}
\qquad (3)
$$

where $*$ denotes complex conjugate and $\omega_0 = 2\pi f_0$ is the angular ultrasound frequency. The scattering of ultrasound from blood is incoherent, and it can be shown that the echo from blood is a Gaussian stochastic process [8]. The process is narrowband, since the blood velocity is much smaller than the speed of sound. The complex variable $\hat{x}(t)$ in (3) is referred to as the complex envelope of $e(t)$, or simply **the complex Doppler signal.** The complex exponentials in (3) are known entities, determined by the reference oscillator. Hence, all information about the blood velocity in the received signal is contained in its complex envelope.

It is convenient to perform the signal analysis on the complex envelope $\hat{x}(t)$ (baseband processing), rather than using the received RF signal $e(t)$. The complex Doppler signal can be extracted from the received echo using **complex** (or **quadrature**) demodulation: The RF echo is multiplied by $2\exp(-j\omega_0 t)$, yielding the product terms $\hat{x}(t) + \hat{x}^*(t)\exp(-j2\omega_0 t)$. The second term is narrowband, centered around $-2\omega_0$, and it can be removed by lowpass filtering the product at a cutoff frequency $f_c \ll 2\omega_0$ (see Fig. 1). The cutoff frequency determines the noise bandwidth of the CW instrument, which must be higher than the maximum Doppler shift that is to be measured. Since $v/c_b \ll 1$, it is easy to implement CW Doppler systems with sufficient bandwidth to measure velocities up to 6-7 m/s. This is the upper limit of blood velocities that may occur in the human body.

A high-pass filter with cutoff frequency f_{hp} is inserted into the signal path in Fig. 1. It is required because the Doppler signal from blood is obscured in the received signal by high-intensity echos from tissue and vessel walls. Tissue structures move more slowly than the blood (possible exceptions are valve motions in the heart), and these clutter signals can, therefore, be removed by high-pass filtering. Nevertheless they represent problems, as they may be as much as 80-100 dB stronger than the desired signal from the blood, thereby causing dynamic range problems. The cutoff frequency of the high-pass filter is normally chosen in the range 100 Hz - 1.5 kHz, depending on the ultrasound frequency and the application. The fractional scattering crossection of blood increases as f_o^4 [8], whereas the intensity of the echos from tissue (specular reflections) stay largely unchanged with frequency. Therefore, the requirements to dynamic range of the receiver and efficient highpass filtering reduce rapidly with increasing ultrasound frequency. - An unfortunate side-effect of the high-pass filtering is the removal of low frequency Doppler shifts from blood. This may cause systematic errors in measurements of blood flow on the basis of the mean Doppler frequency [6].

In the plug flow situation shown in Fig. 1, each red blood cell that travels through the intercept region of the transmitting and receiving beam (the **sample volume**) generates a Doppler burst of finite time duration or, correspondingly, nonzero bandwidth. This is referred to as the **transit time effect** [7]. At any time instant, the backscattered echo signal is formed as the sum of individual contributions from a large number of randomly located blood cells within the sample volume. The **power spectrum** of $\hat{x}(t)$, therefore, becomes a narrow frequency distribution centered around $f_o + f_d$, rather than a single Doppler line.

Velocity gradients in the blood vessel cause the power spectrum to become broader than in the plug flow case. If the transit time effect is neglected and the sample volume is insonified uniformly, the power spectrum of the complex Doppler signal corresponds directly to the velocity distribution in the sample volume [7][8]. The constant of proportionality between velocity and frequency is given by the Doppler equation. **Spectrum analysis,** therefore, has become the common processing method for the extraction of velocity information from the Doppler signal. Alternately, **single frequency estimators** may be employed for this purpose. These are simpler processing devices, implemented in the time domain, which extract a single parameter from the power spectrum of the Doppler signal (or equivalently, the velocity distribution). Parameters which relate to the center frequency of the spectrum are mean [9][10] and root mean square Doppler shift [5][11][12]. Other parameters of interest are the maximum Doppler shift [13], or the mean square bandwidth of the spectrum [55].

The Doppler shift from blood is in the audible range for the ultrasound frequencies that are used in diagnostic ultrasound. Thus, by listening to $\mathbf{Re}\{\hat{x}(t)\}$ or $\mathbf{Im}\{\hat{x}(t)\}$ (or both, in stereo), the operator can detect the presence of a Doppler signal and evaluate its characteristics qualitatively (e.g., center frequency (pitch), narrowband vs. broadband signal). The presence of an audio signal greatly reduces the problem with the angular dependency of (2): In clinical practice, the transducer may be angulated until the maximum frequency shift is heard; most often a small angle to the vessel has then been obtained. Errors due to a small angle offset may then be neglected, since $\cos\alpha \approx 1 - ½\alpha^2 \approx 1$ when α is small.

The ultrasound carrier frequency in CW Doppler is normally chosen such that the signal-to-noise ratio is maximized. The logarithmic attenuation of ultrasound per unit length of tissue increases linearly with f_o [14], whereas the scattering of ultrasound from blood increases as f_o^4. This has led to the use of relatively low-frequency ultrasound (1-3.5 MHz) for measurements on vessels deeper than 4-5 cm, and higher frequencies (up to 20 MHz) for use on the more shallow peripheral vessels and peroperative applications.

The blood velocity in arteries has pulsatile time variations, with period given by the heart rate. If the instantaneous blood velocity is to be measured, scarce time is available for analysis; the blood velocity may change significantly over a 10 ms time interval. The finite analyzing time inevitably leaves errors (bias, variance) in the velocity estimate. It is, therefore, important to derive methods that extract a maximum of information contents from the signal.

2.1.2 Pulsed Doppler

A block diagram of a pulsed wave (PW) Doppler instrument is shown in Fig. 2, together with some associated timing signals [16]. In pulsed measurements, bursts of ultrasound with center frequency f_o and duration T_p, are emitted at a constant pulse repetition frequency (PRF) $f_s = 1/T_s$. The bursts are phase coherent with respect to the internal reference oscillator. A common transducer is employed for both transmission and reception. The tquadrature demodulator serves the same purpose as in CW Doppler. The demodulated echo from each burst is filtered through a low-pass receiver filter prior to range-gating (sampling) an elapsed time T_d after the pulse emission. If finite bandwidth effects are nelected, this signal sample originates from a localized sample volume, extending longitudinally from $c_tT_d/2$ to $c_t(T_d-T_p)/2$ from the transducer's face, where c_t denotes the speed of sound in tissue (≈ 1540 m/s). Thus, the PW Doppler gives **range resolution**. As in CW Doppler, the lateral dimensions of the sample volume are determined by the width of the soundbeam.

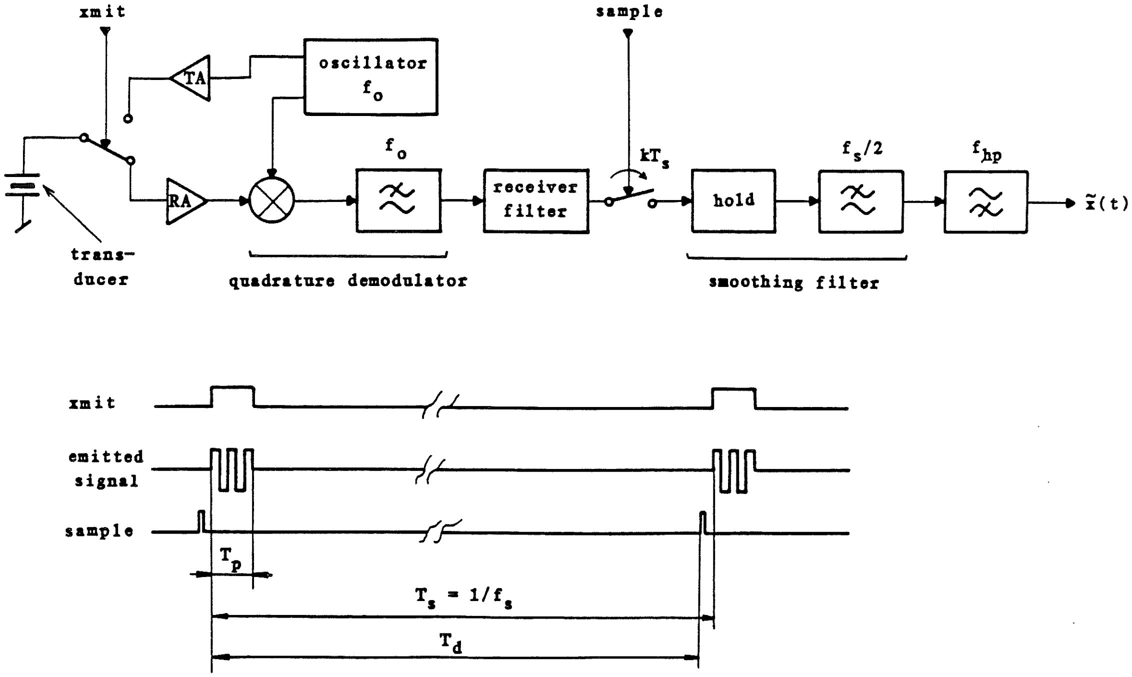

Fig. 2 Block diagram of a pulsed Doppler instrument.

The emitted soundbursts are phase coherent. The signal sequence $\{\hat{x}(kT_s)\}$ can, therefore, be regarded as samples of the continuous Doppler signal $\hat{x}(t)$ that would have been measured if the selected sample volume were insonified by a CW Doppler with no interference from the surrounding environment [8]. It follows from complex sampling theory that $\hat{x}(t)$ can be reconstructed without errors by lowpass filtering (smoothing) of the sampled sequence, provided that the total bandwidth of $\hat{x}(t)$ is smaller than the pulse repetition frequency f_s [18]. The smoothing filter is normally an analog low-pass filter with a symmetric frequency response that rolls off at the Nyquist frequency (Fig. 3(a)). Correct reconstruction is obtained when the magnitude of the maximum Doppler shift in the CW Doppler signal, f_{max}, is less than the Nyquist frequency, i.e.,

$$|f_{max}| < \tfrac{1}{2} f_s \tag{4}$$

The high-pass filter in Fig. 2 serves the same purpose as in CW Doppler.

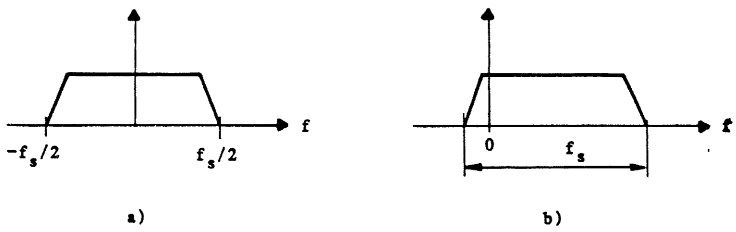

Fig. 3 Frequency responses of smoothing low-pass filters for a pulsed Doppler instrument.
a) Symmetric frequency response.
b) Asymmetric frequency response.

A pulsed Doppler system is always associated with some degree of **range ambiguity.** The echo sampled at the elapsed time T_d from a pulse emission may contain components from several sample volumes, located at the ranges $c_t(T_d + nT_s)/2$, where $n = 0,1,...$ It was initially assumed that the predominant component originated from the first (closest) range cell, $n = 0$. This holds if the signal from the $n = 1,2,..$ ranges are so attenuated that they become obscured by the signal from the closest range cell. This may, however, not always be the case; this situation will be described later.

A necessary condition to avoid spurious sample volumes between the transducer and the range of interest is that the echo from one burst has arrived before a new one is emitted. If the sample volume of interest is located at a range **d**, this is equivalent to requiring

$$f_s \leq \frac{c_t}{2d} \tag{5}$$

Equality is attained if the emission of a soundburst follows immediately after the sampling of the echo of the previous one ('optimal PRF'). Combining (2), (4), and (5) now yields the well-known formula for the maximum unambiguous range-velocity product of a pulsed Doppler instrument [6],

$$d|\vec{v}|\cos\alpha \leq \frac{c_t c_b}{8f_o} \tag{6}$$

This equation is plotted in Fig. 4 for various ultrasound frequencies [18]. In cardiology, velocities up to 7 m/s may be encountered in ranges down to 12-15 cm. As would be expected from the figure, violation of the range-velocity product frequently occurs, even when the very low carrier frequency 1 MHz is employed. When (6) is violated, the smoothed signal $\tilde{x}(t)$ in Fig. 2 becomes an **aliased** version of the continuous time Doppler signal $\hat{x}(t)$ from the selected range cell; its power spectrum no longer corresponds to the velocity distribution in the sample volume. This effect may lead to a severe underestimation of the velocity, or even an apparent reversal of its direction; it has caused extensive confusion and misinterpretations in the clinical literature in the past [18].

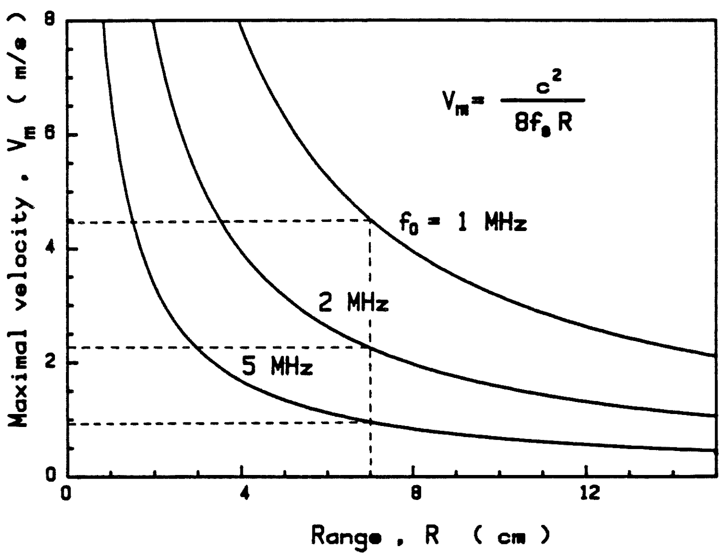

Fig. 4 Maximum unambiguous axial velocity component (corresponding to the Nyquist limit) versus range in pulsed Doppler. Reprinted from [18].

The resolution of a PW instrument can be taylored to suit different needs by the manipulation of variables such as carrier frequency, transducer focusing and bandwidth, burstlength, and the bandwidth of the receiver. Resolution and sensitivity are, however, conflicting requirements in pulsed Doppler [17]. In situations with sensitivity problems (which are common in cardiology), it is an advantage to use a relatively large sample volume. A large sample volume may also help to keep some fraction of the sample volume within the area of interest (e.g., a small jet) throughout the entire cardiac cycle. This may be impossible if a small sample volume is employed, due to dislocations when the heart contracts [18].

The velocity limit of a pulsed Doppler instrument can be increased in several ways:

i) An obvious method is to lower the carrier frequency f_0 as much as possible (see (6)). However, this reduces the fractional scattering crossection from blood, so that a reduction cannot be extended indefinitely without severely degrading the signal-to-noise ratio of the measurement. A low ultrasound frequency also gives dynamic range problems, because of the relative increase of clutter echos from tissue. The lowest useful ultrasound frequency for cardiac Doppler seems to be on the order of 1 MHz.

ii) A different principle can be used when the axial velocity component of the blood is of mainly one direction: A smoothing filter with an asymmetric frequency response can then be employed, Fig. 3(b). If the axial velocity in the sample volume is of one sign only, this approach increases the range velocity product (6) with a factor of two. This particular approach has not been used in practice, but equivalent techniques have been applied in spectrum analysis (see Fig. 3.8 in the report "Real Time Spectral Analysis .." reprinted in chapter V of this thesis).

iii) A third possibility is to increase the PRF above the limit (5) and run the pulsed Doppler with deliberate range ambiguity, i.e., with one or more spurious sample volumes located between the transducer and the sample volume of interest. If the increased velocity is confined to a small region in space (as is the case in valvular stenoses or insufficiencies), the ambiguity can most often be resolved using independent information: Using pulsed Doppler with a normal, nonambiguous PRF, the range(s) where (4) is violated can be determined, but the magnitude of the Doppler shift cannot be quantified. By switching to a higher, ambiguous, PRF, the high Doppler shifts can be measured without frequency aliasing. In the latter case, the associated ambiguous sample volume(s) must be checked out one by one, using a normal PRF, to exclude the possibility that the high velocity recorded originated from any of them. This method was first reported by Hatle et al. [18, pp. 171], and it is now commonly referred to as 'High-PRF' technique.

The velocity information can be extracted from the smoothed signal $\tilde{x}(t)$ in Fig. 2 using the same methods as in CW Doppler. If the dimensions of the sample volume are small compared to the vessel, the velocity gradients within it become small, and the use of single frequency estimators for signal analysis may be acceptable (the Doppler spectrum is narrow-band in this situation).

Note from Fig. 2 that it is possible to sample the echo from each soundburst at several different ranges, and process the Doppler signals from the different range cells in parallel. In this way, the entire axial velocity field along the soundbeam may be examined. This type of instrument is referred to as a Multi-Gated Doppler with parallel signal processing. It has not come into widespread use, because of the relatively large amount of hardware that is required.

A digital approach to multigated Doppler has been developed by Brandestini [19]-[21]. He substituted the analog highpass filter and the smoothing lowpass filter in Fig. 2 with a discrete time high-pass filter, and employed discrete time single frequency estimation to extract the velocity information. The combination of discrete time signal processing and high-speed hardware allowed the processing units of his instrument to be timeshared (multiplexed) between the Doppler signals from a large number of range gates. This type of instrument is referred to as a multi-gated Doppler with serial signal processing. In concept, it is similar to the Moving Target Indicator used in Radar [22]. It has the attractive property that the amount of hardware becomes largely independent of the number of range gates. The digital approach to multi-gated Doppler has later been refined by Hoeks [23].

In cardiac ultrasound, a relatively low carrier frequency is required to obtain deep penetration and a high range-velocity product. As previously pointed out, the power ratio between tissue clutter and Doppler signal from blood may then become extremely unfavorable. While an analog high-pass filter with 100-120 dB stopband attenuation is relatively simple to design, a comparable performance of a digital multigated instrument with **N** gates requires 16-20 bits A/D convertion **2N** times (complex signal) per T_s time units. Typically, T_s is in the range 25-200 µs, depending on the depth of the vessel. This kind of A/D converter performance is not yet easy to obtain, which is probably the reason why the majority of the digital Doppler instruments so far reported have employed high ultrasound frequencies, intended for measurements on peripheral vessels.

2.1.3 Flow imaging

A two dimensional still-image of blood flow (arteriography, flow map, 2D Doppler image) may be formed by scanning the sample volume of a PW Doppler over a crossection of a vessel and map the corresponding two-dimensional distribrution of the velocity [24][25]. The technique is illustrated in Fig. 5, where a multigated Doppler instrument is employed in order to speed up the data acquisition. The parameters mapped may several, e.g., the the mean Doppler frequency, the bandwidth of the Doppler spectrum, or simply the power of the Doppler signal in each pixel of the image. The magnitude of the parameter(s) is displayed in color or grayscale coding.

The data acquisition time for a 2D flow image may be reduced strongly by the combined use of an electronically swept beam and a multigated Doppler. Using this approach, Pourcelot reported real-time flow imaging of the carotid arteries already in 1979, mapping the mean Doppler shift in 10 x 10 spatial pixels at a rate of 15 imgs/s [27]. His system employed 10 transducers in a linear array configuration and a 10 channel multi-gated instrument with parallel signal processing. A similar approach, employing CW Doppler, has been reported by Arenson et al. [41].

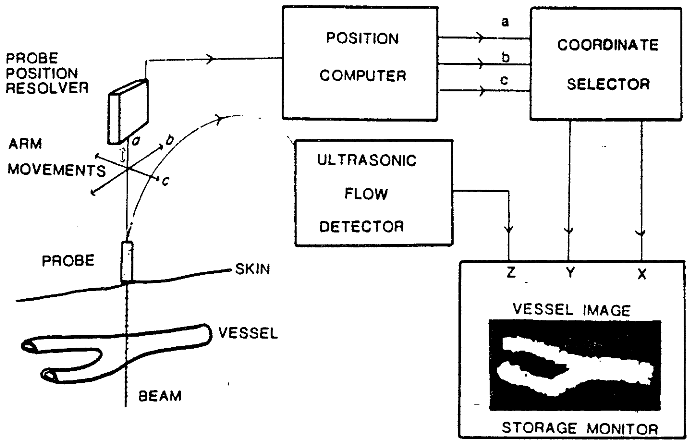

Fig. 5 Block diagram of 2D flow imaging based on a multigated Doppler instrument. Reprinted, with permission, from [26].

The real-time combination of 2D echo imaging and flow imaging of the heart was accomplished more recently by two different groups; Namekawa, Omoto et. al [53]-[55], and Bommer [56]. Both systems employ the combination of phased array sector scanning and a multi-gated Doppler with serial signal processing. The approach of the Japanese group is especially interesting, as both magnitude and bandwidth of the Doppler shift are mapped simultaneously. The mapping of bandwidth is motivated by the fact that in regions with disturbed flow, there are large velocity gradients in the sample volume and correspondingly, a large bandwidth of the Doppler spectrum. The combined mapping of mean frequency and bandwidth reduces problems due to aliasing, which are inherent in any PW Doppler system, under conditions of disturbed flow. The japanese flow imaging system maps a positive mean Doppler shift to red, a negative shift to blue, whereas the mean square bandwidth of the signal controls the amount of green in each pixel of the image. The intensity of a color is proportional to the magnitude of its associated spectral parameter. The color-flow image is presented as an overlay to the B&W echo image.

2.2 Clinical applications of Doppler ultrasound

Doppler methods are currently used in a variety of clinical applications. Some of the most important are listed below;

- detection and assessment of valvular stenoses, regurgitations, shunts, and similar defects that give disturbed flow patterns in the heart;
- detection and assessment of peripheral vascular disease;
- measurement of blood flow;
- real time flow mapping of the heart.

One of the most successful applications of Doppler ultrasound has been in cardiology, where the pressure drop across an obstruction to flow, Δp, can be estimated noninvasively from measurement of the spatial maximum velocity, v_{max}, of the blood. This maximum velocity occurs in the center of the orifice of the obstruction. If the pressure drop is high enough to have clinical significance, it can be estimated from the Bernoulli equation in the very simple form [30]

$$\Delta p = 4\, v_{max}^2 \quad [\text{mm Hg}/(\text{m/s})^2] \tag{7}$$

Both mean and peak pressure drop may be estimated from the time course of the spatial maximum velocity over the cardiac cycle. Thus, a measure for the additional load on the heart caused by e.g. a valvular stenosis can be obtained by noninvasive means. The maximum blood velocity in the sample volume can be extracted from the Doppler signal using spectrum analysis [30], or by simpler analog tracking filter techniques [13].

Localized stenoses in peripheral arteries can be detected from a local increase in blood velocity [26]. Smaller plaques give disturbed flow near the vessel walls, which causes broadening of the velocity distribution or, correspondingly, 'spectral broadening' compared to normals [29].

Volume flow measurements using Doppler ultrasound may be performed in several ways; the simplest is to use a wide sample volume that covers the entire vessel crossection. If the vessel is insonified uniformly, it can be shown that the mean Doppler frequency $\bar{f}$ then becomes proportional to the spatial average velocity over the vessel crossection [7]. The constant of proportionality is given by the Doppler equation (2), regardless of the velocity profile. If the angle α and the area A of the vessel can be measured by some independent technique (e.g., echo imaging), the volume flow can be calculated from the simple relation

$$Q = \frac{c_b}{2 f_o \cos \alpha} A \bar{f}_d \qquad (8)$$

Alternately, volume flow can be calculated by measuring the entire spatial velocity field and integrate it over a vessel crossection [6]. The use of the latter method is limited to relatively large vessels, since the measurement of the velocity field becomes inaccurate if any of the linear dimensions of the sample volume becomes comparable to the vessel diameter.

Examples on other successful applications of Doppler ultrasound are the measurement of blood flow in the human fetus [32], intraoperative guidance for surgeons during brain- or open heart surgery [33][34], and post surgical monitoring of cardiac output using implantable transducers [50]. Also, PW Doppler has been employed as a measurement device in a pneumatic servo system for the noninvasive measurement of human arterial pressure waveforms [35].

Real-time color-flow mapping is a new technique, and its final role in the clinical practice has not yet been established. However, the method has already proven to be very useful in the detection of multiple lesions of the heart [54]. Also, it is currently the only noninvasive method that can actually visualize jet flow. This gives invaluable information about the angle between a high-velocity jet and the soundbeam, information that can be used to improve the accuracy of a subsequent quantitative CW or High-PRF PW examination. When the sensitivity of the flow-map systems approaches that of conventional Doppler systems, it seems likely that the time required for the examination of a patient with a suspected flow anomaly will be reduced.

2.3 Echo amplitude imaging

Ultrasound echo imaging is based on the emission of short pulses of ultrasound (2-10 MHz) into the body. When the pulse encounters a tissue boundary, a change of acoustical impedance occurs.

A fraction of the pulse energy is then reflected. These reflections can be picked up as echos on the surface of the body. By measuring the time-of-flight from pulse emission to echo return, the depth of the tissue inhomogeneity can be determined. Various imaging modalities are used in diagnostics. The simplest is the **A-mode** (Amplitude), which is simply an oscilloscope display of the echo amplitude vs. time.

Echos from a beating heart change position during the heart cycle. These movements can be visualized using **M-mode** (Motion), a display format where time runs along the horizontal axis and tissue depth (i.e., elapsed time from pulse emission to the echo return) along the negative vertical axis. The display is intensity modulated with the amplitude of the received echos, giving the type of display shown in the right part of Fig. 6. M-scan provides excellent time resolution of, e.g., valve motions, because of its high line update rate (PRF ≈ 1000 Hz).

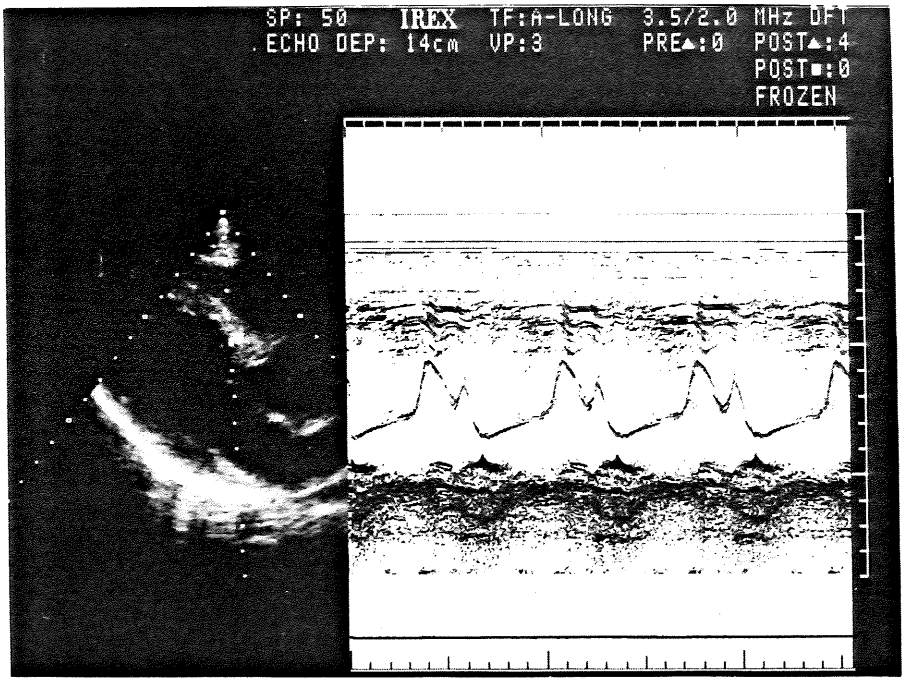

Fig. 6 Combined B-scan (left) and M-mode (right) of the heart. The B-scan shows the left atrium, mitral valve, left ventricle and the aorta. The M-shaped echo in the M-mode is the movement of the mitral leaflet. The M-mode is recorded along the dotted line near the middle of the sector.

However, the by far most useful imaging modality is two dimensional real-time imaging, or **B-scan** (Brightness). A 2D image with an update rate on the order of 30 images per second can be formed by repeated scanning of the soundbeam across the area imaged. The echos intensity modulate the display in the same way as in M-mode. In obstetrics and abdominal imaging it is common to use a set of transducers configured as a linear array. Each transducer may be selected for transmit and receive by means of electronic multiplexing. This approach yields an image with a rectangular format. For cardiac applications, the best acoustical window available is the small space between two adjacent ribs in the thorax. In this situation, a sector scan (shown in Fig. 6) is a better choice, as the faceplate of a sector transducer can be made much smaller than that of a linear array with the same field of view at larger depths. A sectorial scan can be obtained by either mechanically sweeping a transducer across the sector (using an electrical motor), or by electronically steering the soundbeam from a multielement transducer (the phased array method). Both methods are used in practice. A more complete review of imaging techniques can be found in numerous textbooks, e.g. Wells [28].

2.4 Some limiting factors in ultrasonic imaging systems

From a clinical perspective, the ultimate cardiac diagnostic ultrasound instrument would provide high resolution, three-dimensional real time images (at least 15 imgs/s) of both tissue structures and the blood flow in the heart. One may think that such a device can be implemented simply by scanning the soundbeam sufficiently rapid over the area to be imaged. However, there are physical limitations to this. The speed-of-sound and the maximum depth range of such an instrument limit the PRF along each direction in space to the value given by (5), i.e., approximately 5 kHz for a 15 cm depth range. With an image update rate of 15 per second, this allows for the acquisition of echos from 330 bursts per image. For comparison, a high-quality 2D echo image alone consists of data from 120 bursts, typically.

The acquisition of echo amplitude information for imaging must be considered as a relatively efficient process, since only one ultrasound pulse is needed to collect the data for an image vector. For cardiac imaging, this time is on the order of 200 μs. The beam, in contrast, must remain stationary for a much longer time period if the blood velocity along the beam axis is to be estimated with any reasonable degree of accuracy (multi-gated Doppler processing assumed). A 2 ms Doppler signal segment may be analyzed with ≈ 500 Hz frequency resolution, which corresponds to 20 cm/s velocity resolution with 2 MHz ultrasound. If 2 ms of data is acquired per beam, the data acquisition process for flow imaging becomes 10 times slower than that for regular 2D imaging.

The data acquisition rate may be increased by transmitting bursts into several directions of the field of view at the same time, but the number is strongly limited in practice: For one, it is hard to avoid interference between the different beams. Another problem is the maximum spatial peak temporal average (SPTA) ultrasound intensity at the transducer's face, which is limited to 100 mW/cm2 for safety reasons [36]. If several beams enter the body through a common surface, as would be the case in cardiac imaging, the acoustic intensity for each beam must be reduced accordingly. Consequently, the signal-to-noise ratio degrades in direct proportion with the number of beams employed.

Alternately, it is tempting to claim that the data acquisition of a combined echo/Doppler system may be speeded up by running independent echo and Doppler equipment simultaneously in a frequency multiplexed system. This approach has in fact been patented [49]. However, in practice, the large bandwidth and dynamic range required make it very difficult to obtain the necessary degree of isolation between the two systems. During Doppler measurements, therefore, the echo scanning must seize; otherwise phase-shifted echos from the sweeping soundbeam interfere with the highly sensitive Doppler measurement [57]. All clinically useful schemes for the combination of Doppler and 2D imaging yet presented have either been based upon some kind of timesharing between the imaging and Doppler data acquisition, or simply extracted both amplitude and phase (Doppler) information from the echo of the same soundburst.

Regardless of timesharing problems, pulsed Doppler systems have intrinsic limitations of their own. One limitation is that only the axial blood velocity component is measured. This may be solved by insonifying each sample volume from different directions and measure different projections of the velocity. However, the limited number of acoustical windows in the thorax again makes this approach difficult in measurements on the heart. The uncertainty of the angle between the soundbeam and the flow reduces anyway when a two- or three-dimentional flow map is present, since the direction of the velocity vector often can be assessed from it (see Fig. 5). Other potential problems are violation of the range-velocity product, and inadequate signal-to-noise ratio. The latter problem may be reduced by trading off resolution for sensitivity.

The above discussion indicates that real time measurement of three-dimensional velocity fields in the heart is a very difficult task. The real time combination of 2D echo imaging with a low velocity-resolution flow image of the type presented by Namekawa et al. [53][55] extracts about as much information as can be obtained with a single-beam system. Although the velocity resolution of their system is limited, it has nevertheless added value and insight in cardiology, because of its unique ability to visualize the presence, direction, extension and the dynamics of flow jets caused by obstructions or leakages in the heart [54].

3. SUMMARY AND CONCLUSIONS

At the time this work was started, its main objective was to prepare grounds for the design of a multi-gated Doppler instrument to be used in real-time flow mapping. As is apparent from the preceding sections, cardiac flow mapping became a reality more than two years before this thesis was submitted. However, it is to be hoped that some of the results obtained may contribute to the design of systems with improved performance in the future.

The work was concentrated in two main areas;

i) improvement on signal processing in Doppler systems in general, with especial emphasis on discrete time methods that can be applied in pulsed multi-gated instruments with serial signal processing;

ii) improve timesharing methods for the real time combination of conventional PW/CW systems with 2D echo imaging.

The multi-gated Doppler system is the single most critical subsystem in a real-time flow imaging system. The method employing serial signal processing is a cost effective way of implementing such a system, although the performance of an all-digital implementation is still limited by the speed/accuracy product and cost of current A/D converters. Also, the concept of serial signal processing superimposes severe restrictions on the complexity of the arithmetic operations that can be performed. The reason is the very large amount of data that must be processed. For example, a multi-gated Doppler instrument with 1 mm resolution and 15 cm depth-of-field generates some 1.5 megawords, each of at least 12 bit width, that must be filtered and analyzed every second. The demand for simplicity of the signal processing algorithms is, thus, very strong.

Within the general framework above, the dissertation consists of six self contained parts:

I. K. Kristoffersen, "Optimum Receiver Filtering in Pulsed Doppler Ultrasound Blood Velocity Measurements", IEEE Transactions on Ultrasonics, Ferroelectrics, and Frequency Control, vol. UFFC-33, pp. 51-58, Jan. 1986.

II. "Discrete Time Estimation of the Mean Doppler Frequency in Ultrasonic Blood Velocity Measurements," **IEEE Trans. Biomed. Eng.**, vol. BME-30, pp. 207-214, Apr. 1983.

III. "A Comparison between Mean Frequency Estimators for Multi-gated Doppler Systems with Serial Signal Processing," **IEEE Trans. Biomed. Eng.**, vol. BME-32, pp. 645-657, Sept. 1985.

IV. "Time Domain Estimation of the Center Frequency and Spread of Doppler Spectra in Diagnostic Ultrasound," accepted for publication in **IEEE Transactions on Ultrasonics, Ferro-electrics, and Frequency Control.**

V. "Real Time Spectrum Analysis in Doppler Ultrasound Blood Velocity measurements," SINTEF report # STF48 F84030, Nov. 1984.

VI. "A time shared ultrasound Doppler measurement and 2D imaging system," submitted for publication in **IEEE Trans. Biomed. Eng.**

Individual summaries of these publications are given below.

3.1 Paper I: Optimal receiver filtering in pulsed Doppler

The importance of efficient receiver filtering in a pulsed Doppler system has been recognized by a number of investigators. There has been a general consensus in that the best tradeoff between axial resolution and signal-to-noise ratio is obtained when the bandwidth of the receiver filter is of the same order as that of the transmitted soundburst [6][7][23][37]. However, this conclusion seems to have been reached in a rather intuitive manner. Based upon Angelsen's model of the scattering process from blood [8], Paper I derives the impulse response of the optimal receiver filter; i.e., the impulse response that gives the best signal-to-noise ratio for a given length of the sample volume. The time duration of this impulse response is denoted the **range-gating interval** in the following. The optimal impulse response becomes an eigenfunction of a covariance kernel, associated with its largest eigenvalue, over the range-gating interval. The covariance kernel is proportional to the envelope of the echo received from a point scatterer convolved with itself.

In current medium-to-low resolution Doppler systems, the envelope of the echo from a point scatterer is approximately rectangular. In this case, it turns out that the impulse response of the optimal receiver filter becomes nearly rectangular also, with time duration equal to that of the transmitted burst. This result is appealing, since a filter with a rectangular impulse response is simple to implement in hardware; it requires only an integration of the quadrature components of the received echos over the range-gating interval. Moreover, the bandwidth of such a filter may be varied simply by varying the length of the integration period. This type of input filter has previously been proposed by Peronneau et al. [37].

It is well known that the optimal receiver filter in Radar and Sonar reception is the matched filter [38]. The reason why the solution is different in diagnostic Doppler is that the envelope of the echo from blood is not known: The scattering of ultrasound from blood is incoherent, caused by random fluctuations in its density and compressibility, whereas specular reflection from a (plane) distinct target (as is a common case in Radar) yields an echo with the same envelope as that of the emitted pulse.

It is also shown in Paper I that when the bandwidths of the transmitted burst and the receiver filter are significantly different, the attainable signal-to-noise ratio is solely determined by the larger bandwidth. This result means that methods for combined echo/Doppler that are based upon the extraction of image (envelope) and Doppler information from the echo of the same soundburst easily become compromized: If a short soundburst (i.e., large bandwidth) is employed to get a good axial resolution in the image, it is impossible to obtain the same signal-to-noise in the Doppler measurement as if a longer burst of the same energy was used.

3.2 Papers II-IV: Discrete time estimation of spectral parameters

This part of the dissertation contains an evaluation of time domain methods for estimating parameters of the Doppler spectrum (mean frequency, bandwidth). The advantage of using time-domain metods for this purpose is their computational efficiency: The spectral parameters are estimated directly, without need for an intermediate spectrum analysis. The basis for the first two papers (II,III) was methods previously established in the continuous time domain [6][7][9][10], and the discrete time frequency estimators presented by Brandestini [19][20]. Brandestini's frequency detection scheme averaged a discrete time approximation to the **instantaneous frequency** of the Doppler signal over the estimation interval. This estimator, however, suffers from a severe deficiency: it exhibits aliasing phenomena for signals with maximum frequencies well below the Nyquist frequency [39]. This deficiency was more recently overcome by Hoeks [23], who employed an adaptive interpretation of the instantaneous frequency to correct for aliasing.

In Paper II, a discrete time estimator of the mean Doppler frequency was derived and evaluated (computer simulations and experiments). It has a simple structure, and it is well suited for a recursive implementation in a multigated instrument with serial data processing. The mean frequency estimate is formed as a weighted sum over samples of the complex Doppler signal's autocorrelation function at different lags. With 8 lags, the estimator can be made practically unbiased for frequency shifts in the range **(-0.45 PRF+w, 0.45 PRF+w)**, where the interval offset **w** can be chosen arbitrarily. Thus, in a case where the axial velocity field is of one sign only, velocities up to 90 percent of the PRF may be analyzed.

In the next paper (III), eight different implementations of the same estimator were studied in terms of bias and variance (numerical calculations only). The purpose of that work was to quantify the tradeoffs involved when estimator simplifications are done. Simplifications are important to minimize the amount of hardware in a high-speed realization of the estimator. The paper investigated both the effect of structural simplifications, taking advantage of some symmetry relations in the correlation function of a complex Gaussian process, as well as hard limiting of one of the signal components prior to the correlation (sign-multiplication). The estimator proposed in Paper II had the simplest structure possible, and it also employed hard limiting. Paper III revealed that this implementation is not a very good one, as the combination of hard limiting and a simple structure yields a poor performance (high variance) when the signal-to-noise ratio is low. Hard limiting can, however, be advised if more complex estimator structures are employed. This still gives substantial savings in hardware compared to the case when ordinary multiplication is employed, at the cost of increasing the standard deviation of the estimate with about 12 percent.

The last paper in this group, Paper IV, was written in response to two papers that were published just recently: Barber et. al presented a new 'instantaneous frequency' estimator which, they claimed, had properties superior to those of the true mean frequency estimator in the case of adverse signal-to-noise ratios and high Doppler shifts. In the subsequent parts of this thesis, this estimator is referred to as the **correlation-angle** estimator, since its output is proportional to the phase angle of the autocorrelation function of the complex Doppler signal at unity sample lag. Although not spelled out very explicitly, this estimator appears to have been used earlier by Namekawa, Kasai et al. [53][54]. In a recent work, they presented a cardiac color-flow map system made on the basis of estimating the correlation angle and an approximation to the mean square (MS) bandwidth of the spectrum [55]. The latter estimator is referred to as the **correlation-decay** approximation to the MS bandwidth.

Neither the work of Barber et. al nor that of Kasai et. al made any attempt to investigate the statistical properties of their estimators. This analysis is carried out in Paper IV, which compares the new estimators to the true mean frequency frequency estimator derived in II and III, the instantaneous frequency estimator of Hoeks, and an alternate estimator of MS bandwidth derived in the paper. It turns out that for estimation of the center frequency of the Doppler spectrum, the 'true' mean frequency estimator yields by far the lowest variance for wideband signals or/and low signal-to-noise ratios. This result is not entirely in conflict with the conclusion of Barber et al., because they reported problems at small Doppler shifts, where the signal-to-noise ratio of their system was the lowest. The reason why they got better results with the correlation-angle estimator for higher Doppler shifts could have been that their mean frequency estimator was different from the one investigated in Paper IV.

For estimation of MS bandwidth, however, the simple correlation-decay estimator turns out to give good results. This estimator is simpler to implement than the alternate estimator derived in the paper, and it yields a low variance estimate that is essentially unbiased for bandwidths less that 50 percent of the sampling frequency.

3.3 Report V: Spectrum analysis

As previously mentioned, the maximum blood velocity across obstructions to blood flow is an important parameter in the diagnosis of various heart diseases [18]. In a large fraction of these situations, the sample volume of a pulsed or CW Doppler cannot be made small enough to be put into a region of flow without velocity gradients, meaning that the mean Doppler shift bears little relation to the maximum velocity. Spectrum analysis is then a better approach to velocity estimation, from which information about the entire velocity distribution in the sample volume can be deduced. Spectrum analysis allows for the use of a relatively large sample volume in these situations; this simplifies the aiming problems and gives an increased signal-to-noise ratio [18].

Report V covers a number of topics related to real-time spectral analysis of the complex Doppler signal. It concentrates on the averaged modified periodogram spectrum estimator developed by Welch [40], which was chosen because of its ease of implementation. Its statistical properties (bias, variance) was originally derived by Welch for real Gaussian signal inputs. Report V derives expressions for bias and variance of the spectrum estimate in the case of complex Gaussian signals. It turns out that the difference between the real and the complex case is rather small. Other subjects analyzed in the report are the averaging of individually compressed periodograms to reduce the dynamic range requirements to a hardwired spectrum averager, and the use of thresholding ('reject') to suppress white noise in the spectrum estimate. It is shown that thresholding is an efficient method to remove the white noise spectrum component only when the variance of the spectrum estimate is relatively low, such as when a small number of relatively uncorrelated spectrum estimates have been averaged.

The use of complex spectrum analysis to resolve aliases in PW Doppler systems is also discussed in the report. Practical measurements resolving Doppler shifts up to nearly two times the PRF (i.e., four times the Nyquist limit) is demonstrated, using a conventional pulsed Doppler instrument with analog smoothing filters. Smoothing filters with optimal frequency responses for pulsed Doppler instruments are also derived in the report.

The report gives a recommended system architecture for a hard-wired 64-sample spectrum analyzer with a computation time on the order of 128 μs. The design employs analog Bucket Brigade Devices in a Chirp Z Transform configuration, which allows for a very compact hardware design. Time compression is used to take full advantage of the processing capacity of the BBD devices. The high speed of the spectrum analyzer makes it well suited for use in flow mapping applications (calculation of 32 different power spectra can be done in only 4.1 ms).

A spectrum analyzer has later been designed on the basis of the report[1]. This analyzer computes a moving average of eight compressed power spectra, calculated from segments of up to 64 samples of the complex Doppler signal. The output spectrum is updated every millisecond. Examples of the analyzer's output are shown in Fig. 7 and Fig. 8. The panels show spectral displays of signals from the human aorta, measured with 3 MHz PW Doppler on a healthy person in steady-state physiological conditions. The acoustical power output of the instrument was deliberately reduced in the measurements, so that the signal-to-noise ratio of the measurement was poor. In the lower panel, the spectrum was passed through a threshold device prior to display, to reduce the background noise. Note the difference in quality between Fig. 7 and Fig. 8. The latter figure shows analysis using non-overlapping signal segments and no averaging. As is obvious from the figure, the thresholding removes both the signal and the noise in this case. These results were predicted in the report.

[1]Integrated part of the "SD-100" and "PCD-4" diagnostic Doppler products, VINGMED a/s, Horten, Norway. Spectrum analyzer hardware designed by Hans Torp, SINTEF, div. of autom. control.

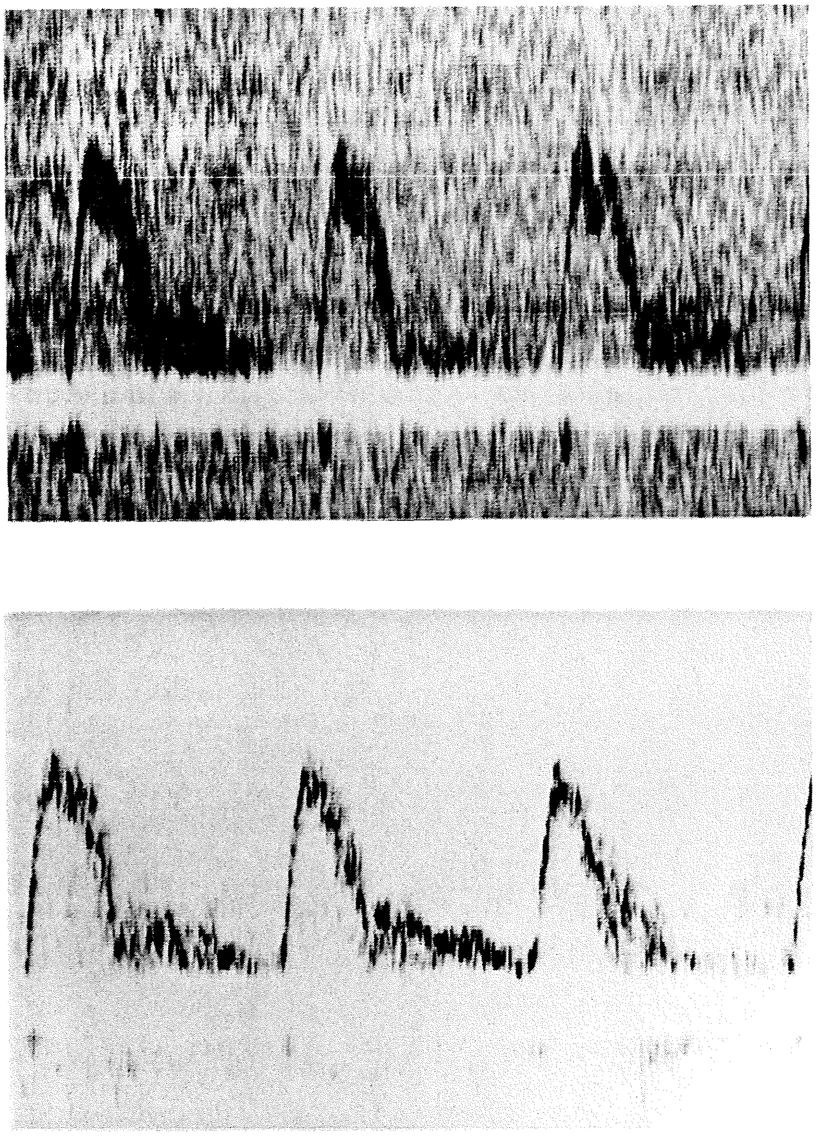

Fig. 7 Performance examples of the spectrum analyzer designed on the basis of the report. The vertical span of the figures is equal to the sampling rate, f_s = 8 kHz. Each spectral line is the average of eight individually compressed, 64-sample modified periodograms, calculated on the basis of 64-sample consecutive signal segments spaced 1 ms apart (87 percent overlap). The 64-sample spectrum estimate was interpolated linearly to 128 samples prior to display.

Upper panel: Direct display of the spectrum.

Lower panel: Thresholding is employed to remove the background noise.

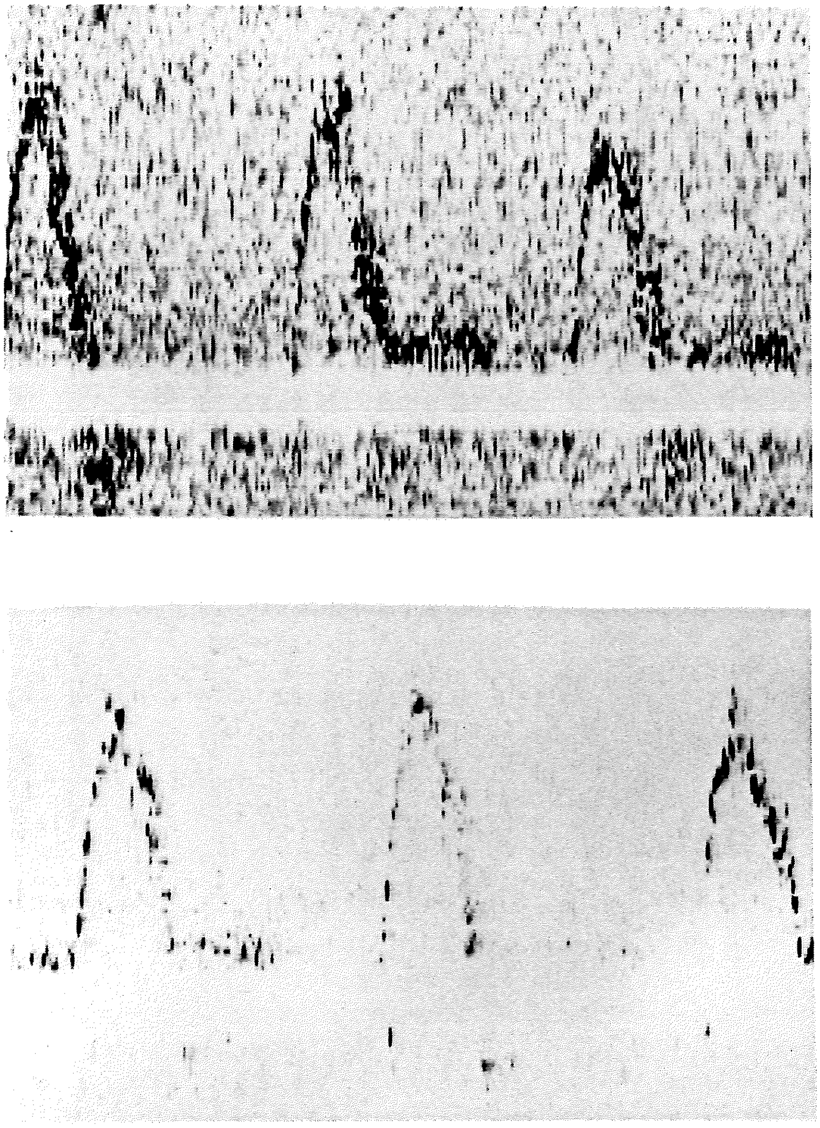

Fig. 8 The signal is similar as in Fig. 7, but no averaging and no overlap is employed in the analysis.
Upper panel: Direct display of the spectrum.
Lower panel: Thresholding is employed to remove the background noise.

3.4 Paper V: Echo/Doppler combination

In cardiology, it is essential to have image guided location of the Doppler sample volume, preferably in real time. Precise location of the sample volume within the complex geometry of the heart is, nevertheless, possible without echo guidance, as the characteristic click-like Doppler signals from the valves can be used as aural landmarks [18]. Near-zero angle to flow can most often be obtained by angulating the soundbeam until the highest Doppler shift (pitch) is heard. However, this 'blind' technique is time consuming to use and not too easy to learn. Also, it is solely based upon the skill of the operator, so that after the examination, no hard evidence exists in the patient file to prove that the operator actually was measuring what he/she claimed to do.

The early combinations of echo and Doppler technology all suffered from deficiencies. The first approach was the **M/Q-mode**, where Doppler and M mode information was extracted from the echos of the same soundburst [42]. One drawback with this method is that the Doppler and M-mode have different design requirements: While resolution is important in M-mode, resolution and sensitivity are conflicting requirements in Doppler. Secondly, useful M-mode and Doppler recordings can rarely be obtained from the same acoustical windows. Far better in this respect is the **Duplex-principle** [43][44], where every other soundburst is used alternately for full 2D imaging and Doppler measurement. The deterioration of image quality that results from the Duplex operation can be tolerated, since the image only serves as a guide for location of the Doppler sample volume. More severe problems follow from the reduction of the Doppler PRF by a factor of 2, since aliasing is a problem even with a full PRF. By 'freezing' a B-scan image recorded immediatetely prior to the Doppler examination, full quality Doppler registrations with still-image guidance can be obtained. This is, however, not entirely satisfactory, since the distance between the heart and the transducer changes with both heart contraction and breathing.

It was felt that the above principles did not represent the best approach to image guided Doppler measurements, and a successful combination between a phased array sector B-scanner and a single range PW/CW Doppler on the basis of a fast-alternating timesharing scheme has previously been reported by Angelsen and Kristoffersen [45]. Using this method, the B-scanner first performs a full image scan ($\approx$ 20 ms), followed by a somewhat longer period of time where it is turned off, and Doppler information is acquired. The timesharing cycle is repeated 15 times per second typically, corresponding to 15 Hz image guidance. Using this scheme, the image quality becomes similar as in the Duplex situation, whereas the reduction of PRF for the Doppler device does not occur; it may, in fact, be run even in CW mode. Instead, dropouts occur in the measurement of the temporal velocity waveform, but this can be tolerated if the imaging period is short. The main problem with the scheme is that the periodical interrupts of the Doppler signal cause a so strong modulation of the audio output from the instrument that most of its value as an operator's aid in aiming is lost. Even if the presence of a real-time 2D echo/Doppler combination in itself simplifies aiming, an audible Doppler signal is still necessary; the angle between the soundbeam and the flow direction cannot always be assessed from the image.

To remove the signal dropouts, an estimate of the missing Doppler signal can be filled in during the imaging interrupt. In the original paper [45], a rather crude method for signal filling was employed: The signal segment that preceded an interrupt was repeated during the interrupt, and windowing was used to remove discontinuities in the transitions between the measured and the replayed signal segments. An improved method for performing signal filling of the Doppler signal in timeshare operation is developed and evaluated experimentally in Paper VI. The basic principle is to synthesize an artificial Doppler signal with properties that approximate those of the signal segment gated out. The synthesis is done by FIR filtering of white noise; a windowed version of the last 10 ms of Doppler signal prior to an interrupt is used to form the complex coefficients of the filter. This yields an artificial Gaussian signal with power spectrum proportional to the magnitude squared frequency response of the coefficients, i.e., the periodogram of the coefficients. The method gives a 'filled' signal with an audible sound that is a better approximation to the real Doppler signal than that resulting from the repetition scheme.

A hardwired implementation of this method has been implemented in a commercial phased array sector scanner[2]. An example of its performance is given in Fig. 9, which shows a pulsed 2 MHz real-time image guided measurement on the aortic outflow tract, apical view. The rightmost part of the velocity panel coincides in time with the image shown to the left.

[2]"Meridian," Johnson & Johnson Ultrasound, Ramsey, N.J., USA.

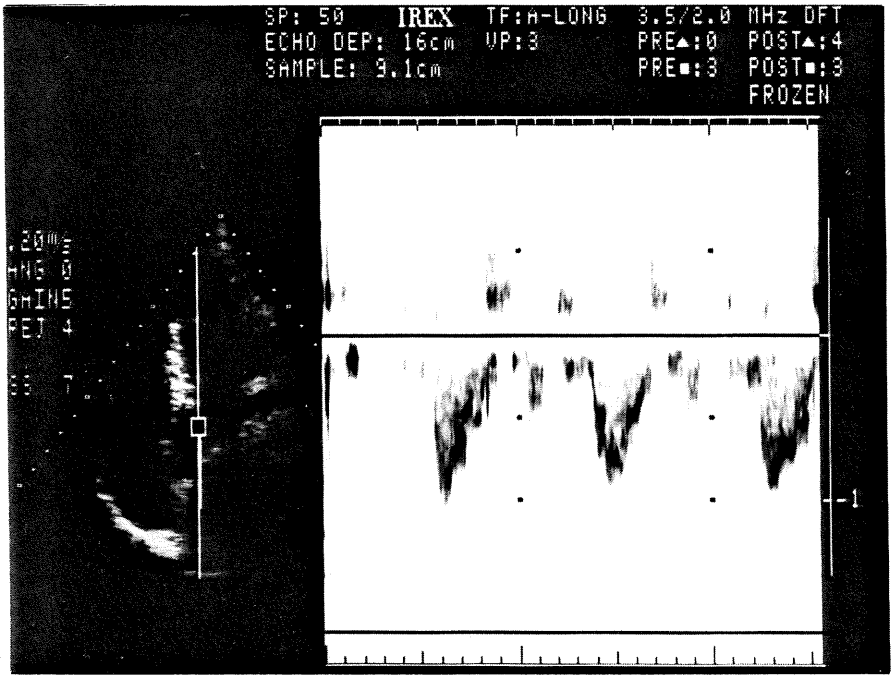

Fig. 9 Examples of real-time image guided PW Doppler measurement in commercial equipment using the method from Paper VI. The position of the Doppler sample volume is indicated by the square box. The image updating rate was 15 Hz.

4. ACKNOWLEDGEMENTS

I wish to express my sincere thanks to:

My friend and coworker Professor Bjørn Angelsen, div. of Biomedical Engineering at the University of Trondheim, who introduced me to the field of Doppler ultrasound and encouraged me to begin with this work. His never-failing optimism and support have been of invaluable inspiration in my studies;

Associate professor Hans Torp, div. of Biomedical Engineering at the University of Trondheim, for years of cooperation and stimulating discussions; he also carried out the experiments necessary to make Figs. 7 and 8 in Section 2 of this thesis;

Knut Grimnes, head of the Div. of Automatic Control, SINTEF, Trondheim, for giving me excellent working conditions during my assignment at his department;

Professor Jens Glad Balchen, Div. of Engineering Cybernetics at the Norwegian Institute of Technology, Trondheim, for his kind support while working at his department;

Chairman Arne Wøien, Vingmed A/S, Horten, for allowing me time to complete this work;

Kjell Arne Ingebrigtsen, President of Vingmed A/S, Horten, for his friendly advise, support and reading of the manuscript;

Liv Hatle, M.D., Dept. of Medicine at the University of Trondheim, for giving me insight into clinical applications of Doppler ultrasound in cardiology;

Terje Skjærpe, M.D., for years of clinical advice and assistance in making Figs. 6 and 9 in Section 2 of this thesis;

Professor Lars Walløe, div. of Informatics at the University of Oslo, for giving me access to the computer system at his laboratory during the completion phase of this study (and for never missing any chance to put pressure on me to finalize the thesis);

B. Sc. Robert H. Livermore, VINGMED, INC, for revising the English of some of the manuscripts;

Mrs. Eli Kvithyll, SINTEF div. of. autom. control, for typing parts of the manuscript;

Mr. Ståle Amland for helping to prepare the figures;

The staff at the laboratory of Biomedical Engineering at SINTEF div. of automatic control, for years of good cooperation and friendly attitude to my studies.

This study was supported by grants from the Norwegian Institute of Technology, Trondheim.

5. REFERENCES

[1] S. Satomura: "Ultrasonic Doppler method for the inspection of cardiac functions," **J. Acoust. Soc. Am.**, vol. 29, pp. 1181-1185, 1957.

[2] D.W. Baker and D.W. Watkins: "A phase coherent pulse Doppler system for cardiovascular measurements", **Proc. 20th Ann. Conf. on Eng. in Med. and Biol.**, vol. 27 (1967).

[3] V.L. Newhouse and Ph. J. Bendick: "Analysis of random signal blood flow measurement", **IEEE Ultrasonics Symp.**, pp. 94-97, Nov. 1973.

[4] D.J. Cathignol, C. Fourcade, J.Y. Chapelon: "Transcutaneous blood flow measurements using pseudorandom noise Doppler system", **IEEE Trans. Biom. Eng.**, Vol. BME-27, No. 1, pp. 30-36, Jan. 1980.

[5] S.W. Flax, J.G. Webster, S.J. Updike: "Statistical evaluation of the Doppler ultrasonic blood flowmeter", **ISA Transactions**, Vol. 10, No. 1, pp.1-20, 1971.

[6] B.A.J. Angelsen: "Transcutaneous Measurement of Blood Velocity and Flow in the Thorax by Ultrasound and the Doppler Effect". Report 75-78-W, Inst. of. eng. cyb., Norwegian Institute of Technology, Trondheim 1974

[7] W.R. Brody: "Theoretical analysis of the Ultrasonic Blood Flowmeter", Ph.D. thesis and technical report, Stanford Electronics Laboratories, Stanford University, California (1971). Report no. 4958-1.

[8] B.A.J. Angelsen: "A theoretical study of the scattering of ultrasound from blood", **IEEE Trans. Biomed. Eng.**, vol BME-27, pp. 61-67, Feb. 1980.

[9] B.A.J. Angelsen: "Instantaneous frequency, mean frequency and variance of mean frequency estimators for ultrasonic blood velocity Doppler signals", **IEEE Trans. on BME**, vol. BME-28, No. 11, 1981.

[10] L. Gerzberg and J.D. Meindl: "Power-spectrum centroid detection for Doppler systems applications", **Ultrasonic Img.**, vol. 2, pp. 232-261, 1980.

[11] R. S. Reneman, H. E. Clarke, N. Simmons, and M. P. Spencer, "**In vivo** comparison of electromagnetic and Doppler flowmeters: With special attention to the processing of the analog Doppler signal," **Card. Res.**, vol. VII, pp. 557-556, 1973.

[12] A. Papoulis, "**Probability, random variables, and stochastic processes**". New York: McGraw-Hill, 1965, p. 487.

[13] B.A.J. Angelsen: "Analog estimation of the maximum frequency of Doppler spectra in ultrasonic blood velocity measurements", rep. no. 76-21-W, SINTEF div. of autom control, Trondheim, Jan. 1976.

[14] B. A. Coughlan, M.G. Taylor, D.H. King, "On-line display of Doppler-shift spectra by a new time-compression analyser", in R.S. Reneman (ed.): "**Cardiovascular applications of Ultrasound**", pp. 85-107, Amsterdam: North-Holland 1973.

[16] D.W. Baker: "Pulsed ultrasonic Doppler blood flow sensing", **IEEE Trans. S. ans US.**, vol. SU-17, No. 3, pp. 170-185, July 1970.

[17] D.W. Baker, S.L. Johnson and D.E. Strandness: "Prospects for quantitation of transcutaneous pulsed Doppler techniques in cardiology and peripheral vascular disease". In "**Cardiovascular applications of Ultrasound**" (Ed. R.S. Reneman), pp. 108-124. Amsterdam: North Holland/American Elsevier, 1974

[18] L. Hatle, B. Angelsen: "**Doppler ultrasound in cardiology - physical principles and clinical applications**", New York, USA: Lea and Fabiger 1982.

[19] M. Brandestini: "Signalverarbeitung in perkutanem Ultraschall Doppler Blutfluss Messgeraten", Eidgenossischen Technischen Hochschule, Ph.D. dissertation, ETH5711, Zurich, Zwitzerland 1976.

[20] M. Brandestini: "Topoflow - A full range Doppler velocity meter". **IEEE Trans. on S and Us**, SU-25, pp. 287-293, 1978.

[21] M.A. Brandestini, M.K. Eyer and J.G. Stephenson: "M/Q-mode echo cardiography - The synthesis of conventional echo with digital multigate Doppler". In: **Proceedings 3rd Symposium on Echocardiology**, Amsterdam, The Netherlands: Martinus Nijhoff, 1979, pp.441-446

[22] M.I. Skolnik: "**Introduction to Radar systems**", New York: McGraw-Hill Book Co. 1962.

[23] A.P.G. Hoeks: "On the development of a Multi-gate pulsed Doppler system with serial data-processing", University of Maastricht, Ph.D. dissertation, Maastricht, the Netherlands, 1982.

[24] D.E. Hokanson, D. Mozersky, D.S. Sumner, D.E. Strandness jr.: "Ultrasonic arteriography: a new approach to arterial

visualization", **Biomed. Eng.**, No. 6, p. 420, 1971.

[25] P. J. Fish, "Multichannel direction resolving Doppler angiography," in **Proc. 2nd European Congr. on Ultrason. in Medicine,**" pp. 153-159. Amsterdam: Exerpta Medica 1975.

[26] P. Atkinson, J.P. Woodcock: **"Doppler Ultrasound and its use in clinical measurements"**. London: Academic press 1982.

[27] L.G. Pourcelot: "Real-time blood flow imaging", in C.T. Lancee (ed.): **"Echocardiology"**, pp. 421-429, The Hague: Martinus Nijhoff 1979.

[28] P. N. T. Wells: "Physics and instrumentations," in B.B Goldberg and P.N.T. Wells (eds.), **"Ultrasound in clinical diagnosis,"** pp. 1-30. N.Y.: Churchill Livingstone 1983.

[29] R.L. Powis: "Doppler spectral broadening in normal blood flow and disease", **Am. Rev. Diagnostics**, vol. 1, pp. 3-8, March-April 1983.

[30] J. Holen, R. Aaslid., K. Landmark, S. Simonsen: "Determination of pressure gradient in mitral stenosis with a non-invasive ultrasound Doppler technique," **Acta Med. Scand.**, vol. 199, pp 455-460, 1976

[32] S.H. Eik-Nes, K. Marsal, A.O. Brubakk, K. Kristoffersen, M. Ulstein: "Ultrasonic measurement of human fetal blood flow", **J. Biom. Engng.**, vol. 4, pp. 28-36, Jan. 1982.

[33] H. Nornes, A. Grip, P. Wikeby, "Intraoperative evaluation of cerebral hemodynamics using directional Doppler technique. Part I: Arteriovenous malformations," **J. Neurosurg**, vol. 50, pp. 145-151, Feb. 1979.

[34] P. Moulder, M.J. Teague, V.J. Manuele, "Intraoperative Doppler coronary artery finder," **Ann. Thorac. Surg.**, vol. 24, pp. 430-432, 1977.

[35] R. Aaslid, A.O. Brubakk: "Accuracy of an ultrasound Doppler servo method for noninvasive determination of instantaneous and mean arterial blood pressure", **Circulation**, vol. 64, pp. 753-759, 1981.

[36] Report from The Comittee on Bioeffects of the American Institute of Ultrasound in Medicine, "Biological effects of ultrasonic energy on living mammals," **Ultrasound Med. Biol.**, vol. 2, no. 4, p. 351, 1976.

[37] P.A. Peronneau, J.-P. Bournat, A. Bugnon, A. Barbet and M. Xhaard: "Theoretical and practical aspects of pulsed Doppler flowmetry: real-time application to the measure of instan-

taneous velocity profiles **in vitro** and **in vivo**". In **"Cardiovascular applications of Ultrasound"** (Ed. R.S. Reneman), pp. 66-84. Amsterdam: North Holland/American Elsevier, 1974

[38] D.O. North: "Analysis of the Factors which Determine Signal/Noise Discrimination in Radar". **Proc. IEEE**, vol. 51, July 1963

[39] B.A.J. Angelsen, K. Kristoffersen: "On ultrasonic MTI measurements of velocity profiles in blood flow", **IEEE Trans. on BME**, vol. BME-26, No. 12, pp. 665-671, 1979.

[40] P.D. Welch: "The use of fast Fourier transform for the estimation of power spectra: A method based on time averaging over short, modified periodograms", **IEEE Trans. Audio Electroacoust.**, vol. AU-15, pp. 70-73, June 1967.

[41] J. W. Arenson, R. S. C. Cobbold, K. Wayne Johnston, "Real-time two-dimensional blood-flow imaging using a Doppler ultrasound array", in E. A. Ask and C. R. Hill (eds.): **Acoustical Imaging**, vol. 12. Plenum Press, 1982.

[42] D.W. Baker, S. Rubenstein and G.S. Lorch: "Pulsed Doppler echo- cardiography: Principles and applications". **Am. J. of Med.**,vol. 63, pp. 69,80, july 1977.

[43] D.J. Phillips, J.E. Powers, M.K. Eyer, W.M. Blackshear jr., K.C. Boidly, D.E. Strandness jr., D.W. Baker: 'Detection of peripheral vascular desease using the Duplex Scanner III'. **Ultrasound in Med. and Biol.**, Vol. 6, No. 3, pp. 205-218, 1980.

[44] A. Kitabatake et. al.: "Non-invasive visualization of intra-cardiac flow by multigate Doppler technique". In: W. Bleifeldt, D. Harder, H.-K. Leetz, N. Schaldac (eds): **Proceedings world congress on medical physics and biomedical engineering**, sept. 5-11, Hamburg 1982. Published by NPBE-1982 e.W, Hamburg 1982

[45] B.A.J. Angelsen, K. Kristoffersen: 'Combination of 2D-Echo Amplitude Imaging and Doppler Measurements. In: M.P. Spencer (ed.): **Cardiac Doppler Diagnosis.** Boston: Martinus Nijhoff 1984.

[49] P. S. Green, L. F. Schafer, J. C. Taenzer, J. F. Holzemer, S. D. Ramsey Jr., J. R. Suarez, "Real-time Ultrasonic Imaging and Doppler Profile Display System and Method," U.S. pat. no. 4141 347, Feb. 1979.

[50] K. Matre, L. Segadal, H. Engedal, "Continuous measurement of aortic blood velocity, after cardiac surgery, by means of an

extractable Doppler ultrasound probe," **J. Biomed. Eng.**, vol. 7, pp. 84-88, Apr. 1985.

[52] W. D. Barber, J. W. Eberhard, S. G. Carr, "A new time domain technique for velocity measurements using Doppler ultrasound," **IEEE Trans. Biomed. Eng.**, vol. BME-32, pp. 213-229, March 1985.

[53] K. Namekawa, C. Kasai, M. Tsukamoto, and A. Koyano, "Real-time bloodflow imaging system utilizing auto-correlation techniques," in **Proc. Ultrasound '82**, R. A. Lerski, P. Morley (eds.). Pergamon Press, 1982, pp. 203-208.

[54] R. Omoto, ed., **Color atlas of real-time two-dimentional Doppler echocardiography**, Tokyo: Shindan-To-Chiryo Co., Ltd, 1984, p. 11.

[55] C. Kasai, K. Namekawa, A. Koyano, R. Omoto, "Real-Time Two-Dimensional Blood Flow Imaging Using an Autocorrelation Technique," **IEEE Trans. Sonics Ultras.**, vol. SU-32, pp. 458-464, May 1985.

[56] W. Bommer, L. Miller, "Real-time Two Dimensional color-flow Doppler: Enhanced Doppler Flow-imaging in the Diagnosis of Cardiovascular Disease", (Abstract) **Am. J. Cardiology**, vol. 49, p. 943, 1982.

[57] Kazuhiro Iinuma, Kinya Takamizawa: "Ultrasonic Doppler Apparatus". US patent # 4,318,413, Mar. 9, 1982.

Optimal Receiver Filtering in Pulsed Doppler Ultrasound Blood Velocity Measurements

KJELL KRISTOFFERSEN

***Abstract*—In pulsed Doppler blood velocity measurements, coherent bursts of ultrasound are emitted at a fixed repetition rate. The complex envelope of the received echos is extracted by complex demodulation, passed through a receiver filter for noise reduction, and finally range-gated to yield samples of the Doppler signal from a localized depth. This paper shows that during a time interval of length equal to the duration of a transmitted ultrasound burst, the envelope of the echo from blood may be regarded as a sample function from a stationary stochastic process. The power of the process is proportional to the energy of the emitted soundburst, and the shape of its covariance function is equal to the envelope of the echo from a point scatterer convolved with itself. Optimum signal-to-noise ratio in the range gated Doppler signal is obtained when the impulse response of the receiver filter is chosen as an eigenfunction of this covariance function, corresponding to its maximum eigenvalue over the range-gating interval. When the signal envelope is a rectangular pulse, it turns out that the optimal impulse response of the receiver filter also becomes nearly rectangular. A receiver filter with a perfectly rectangular impulse response yields, for all practical purposes, performance equivalent to that of the optimal filter in this case. It is also shown that when the bandwidths of the emitted soundburst and the receiver filter are significantly different, the signal-to-noise ratio is solely determined by the largest of the two.**

I. Introduction

The RECEIVED signal in pulsed Doppler blood velocity measurements is formed by incoherent scattering of ultrasound from a large number of randomly located blood cells [1]. The shape of the returned echo is therefore not known. This is different from radar applications with distinct targets, where the echo is a scaled and delayed replica of the emitted signal, possibly with some distortion from the propagating medium. It is well known that the matched filter maximizes the signal-to-noise ratio (SNR) in radar reception [2]. In general, this does not hold in the incoherent scattering situation one faces in blood velocity measurements.

The receiver filter in a pulsed Doppler instrument affects both its axial resolution and the noise bandwidth of the system. Although a number of investigators have pointed out its importance, their reasonings seem to have been done on a rather qualitative basis. Perroneau [3] suggested a receiver filter that averaged (integrated) the output from the Doppler signal quadrature demodulator over a time period equal to the duration of the emitted soundburst. This view has later been adopted by Atkinson and Woodcock [4]. Brody [5] and Angelsen [6] both pointed out that the filter should have a bandwidth comparable to that of the emitted pulse. Hoeks stated that 'the effective duration of the impulse response of this combined filter (transducer, receiver, and filter) should be equal to the duration of the emission to achieve the best axial resolution with the highest signal-to-noise ratio' [7].

Although all of the above statements agree qualitatively, it is the objective of this paper to give a more analytical treatment of the subject. To do so, a review of the scattering theory from Angelsen [1] is given in the next section. On this basis, the receiver filter that maximizes the signal-to-noise ratio for a given duration of its impulse response is derived.

Manuscript received February 6, 1984; March 20, 1985. This work was supported by the Norwegian Institute of Technology.

The author is with the Division of Engineering Cybernetics, The Norwegian Institute of Technology, N 7034 Trondheim, Norway.

IEEE log number 8405988.

II. Transducer Output in Pulsed Doppler Measurements

A. Review of a Scattering Model

Angelsen modeled the blood as a continuum, with random fluctuations in compressibility $\kappa(\vec{r}, t)$ and mass density $\rho(\vec{r}, t)$ [1]. The ultrasound scattering is caused by interaction between the incident soundwave and these fluctuations. In this model, the time-varying spatial cell concentration $n_c(\vec{r}, t)$ in blood was written as

$$n_c(\vec{r}, t) = n_0(\vec{r}, t) + n(\vec{r}, t) \tag{1}$$

where $n_0 = \langle n_c \rangle$ is the local ensemble average, and n is the fluctuation of n_c around its mean. Angelsen also argued for the validity of a delta correlation for the fluctuations,

$$\langle n(\vec{r}, t)n(\vec{r} + \vec{\xi}, t + \tau)\rangle = \langle n^2(\vec{r}, t)\rangle \cdot \delta(\vec{\xi} - \vec{\zeta}(\vec{r}, t, \tau)) \tag{2}$$

where $\vec{r} + \vec{\zeta}$ is the position of the fluid element at time $t + \tau$ which at time t had the position $\vec{r}$. The assumption of delta correlations is valid when the correlation lengths of the fluctuations are much smaller than the dimensions of the resolution cell through which they are observed; i.e. the Doppler sample volume.

In this paper the ultrasound transducer is assumed to be large compared to the wavelength, so the plane wave approximation to the sound field can be applied. It is assumed that bursts of ultrasound with angular carrier frequency ω_0 and pulse repetition frequency (PRF) f_s =

$1/T_s$, are emitted and received by the same transducer. Let z be the distance between the transducer and the sample volume along the beam axis $\vec{n}_t$; i.e. $z = |\vec{z}| = ct/2$, where t is the elapsed time between pulse emission and reception, and c is the speed of sound. The complex envelope of the received Doppler signal (the complex Doppler signal) from burst k can then be written as

$$\tilde{x}_k(z) = q \int d^3\xi\, R(\vec{\xi})\tilde{s}(|\vec{\xi} - \vec{z}|) \cdot \exp\left[-j\frac{2\omega_0}{c}\vec{n}_t \cdot \vec{\xi}\right] n\left(\vec{\xi}, \frac{z}{c} + kT_s\right). \quad (3)$$

The integration extends over the entire region of a nonzero integrand. The quantity q is a complex constant of proportionality, and $R(\cdot)$ is related to the acoustic field of the transducer and the scattering properties of blood

$$R(\vec{\xi}) = \frac{\omega_0^2}{c^2}|A(\vec{\xi})|^2\{\gamma_\kappa - \gamma_\rho\} \quad (4)$$

where $|A|^2$ is the combined transmit/receive spatial sensitivity of the transducer. The constants γ_κ and γ_ρ relate to the scattering from fluctuations in compressibility and mass density, respectively.

In (3), $\tilde{s}(|\vec{\xi} - \vec{z}|)$ is the normalized envelope of the received echo from a point scatterer, with the argument scaled in length units. Its shape is determined by both the excitation waveform and the bandwidth of the transducer. In the following, the notation becomes simpler if the temporal pulse shape $s(t)$ (the signal signature) is introduced,

$$s(t) = \tilde{s}(ct/2) \qquad t > 0 \quad (5)$$

Unless otherwise stated, it shall be assumed that $s(t)$ is nonzero only on the finite time interval $(0, T_p)$, with energy normalized to E, i.e.

$$\int_0^{T_p} dt\, |s(t)|^2 = \frac{1}{2\pi}\int_{-\infty}^{\infty} d\omega\, |S(\omega)|^2 = E \quad (6)$$

where $S(\omega) = F\{s(t)\}$ is the Fourier transform of $s(t)$. When the PRF is constant, E is proportional to the average emitted acoustic power density. In clinical measurements the emitted acoustic power density should be limited (< 100 mW/cm^2 SPTA) for patient safety considerations [8].

B. Autocorrelation Function of the Received Signal

The autocorrelation function of the backscattered signal must be known to perform an analysis on the effect of receiver filtering. The autocorrelation function, or the covariance function, of the signal from the range $z = ct_1/2$ is defined as

$$K(\tau, \sigma) = \langle \tilde{x}_k^*(t_1 - \tau)\tilde{x}_k(t_1 - \sigma)\rangle. \quad (7)$$

This may be expressed in terms of the signal signature $s(t)$. Based on the assumption given in (2), Angelsen was able to calculate the correlation $\langle \tilde{x}_k^*(z_1)\tilde{x}_m(z_2)\rangle$ [1, (29)]. Setting $k = m$, $z_1 = c(t_1 - \tau)/2$ and $z_2 = c(t_1 - \sigma)/2$ in his expression yields

$$K(\tau, \sigma) = |q|^2 \int d^3\xi\, R(\vec{\xi})\tilde{s}\left(\left|\vec{\xi} - \frac{c}{2}(t_1 - \tau)\vec{n}_t\right|\right) \cdot R(\vec{\zeta})\tilde{s}\left(\left|\vec{\zeta} - \frac{c}{2}(t_1 - \sigma)\vec{n}_t\right|\right) \cdot \exp\left[-j\frac{\omega_0}{c}\vec{v}(\vec{\xi}) \cdot \vec{n}_t(\tau - \sigma)\right]\langle n^2(\vec{\xi})\rangle \quad (8)$$

where

$$\vec{\zeta} = \vec{\xi} + \tfrac{1}{2}\vec{v}(\vec{\xi})(\tau - \sigma).$$

The complex exponential in this formula represents the Doppler effect, while the remaining terms determine the bandwidth of the back-scattered echo. In blood velocity measurements, the Doppler shifts are considerably smaller than $1/T_p$ (underspread targets). Moreover, the transmit duty cycle is small ($T_p << T_s$), and the velocities of the scatterers are much smaller than the speed of sound. In combination, this allows for simplifications of (8). The following approximations can be made.

1) It is valid to set $\vec{\xi} = \vec{\zeta}$.

Proof: As a consequence of $v << c$, the two terms that contain $\tilde{s}(\cdot)$ will overlap only if $|\tau - \sigma| < T_p$; otherwise the integrand becomes zero. Within the region of a nonzero integrand one then has the bound

$$|\vec{v}(\vec{\xi})(\tau - \sigma)| < v_{\max}T_p \quad (9)$$

where $v_{\max}$ is the maximum velocity in the sample volume. The axial length of the sample volume (as viewed from the output of the receiver transducer) is $cT_p/2$, with T_p typically corresponding to 5-20 oscillations of the ultrasound frequency. Now $v_{\max}$ is on the order of 1 m/s, whereas $c = 1560$ m/s. The quantity (9) therefore spans only a tiny fraction of one wavelength, and the approximation is fully justified.

2) The complex exponential in the integrand may be approximated with unity.

Proof: The magnitude of its argument is bounded by

$$\left|\frac{\omega_0}{c}\vec{v}(\vec{\xi}) \cdot \vec{n}_t(\tau - \sigma)\right| \le 2\pi\frac{f_{\max}}{2}T_p = 2\pi\frac{f_{\max}}{2f_s}\frac{T_p}{T_s}, \qquad |\tau - \sigma| < T_p \quad (10)$$

where

$$f_{\max} = 2\frac{v_{\max}}{c}f_0\cos\alpha \quad (11)$$

is the maximal Doppler shift in the backscattered signal, and α is the angle between $v_{\max}$ and the beam axis. In meaningful situations $f_{\max}/f_s < 1$ (no frequency aliasing), and the ratio T_p/T_s is very small, typically 0.005–0.05. One obtains the worst case bound

$$2\pi\frac{1}{2}\frac{f_{\max}}{f_s}\frac{T_p}{T_s} \le 0.05\pi. \quad (12)$$

The approximation is therefore valid in the actual velocity range.

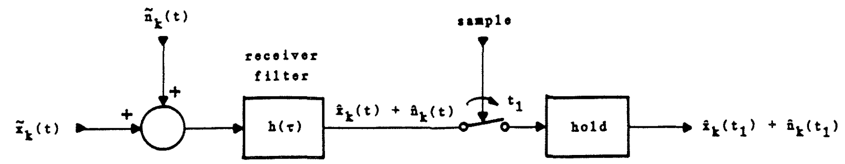

Fig. 1. Model for receiver filtering and range gating in pulsed Doppler ultrasound measurements.

3) The attenuation of the soundbeam over the axial length of the sample volume is neglected, i.e.

$$R\left(\vec{\xi} - \frac{c}{2}(t_1 - \tau)\vec{n}_t\right) \approx R\left(\vec{\xi} - \frac{c}{2}t_1\vec{n}_t\right), \quad |t_1 - \tau| < T_p. \qquad (13)$$

4) The entire sample volume is located in blood with uniform scattering properties. Then $\langle n^2(\vec{\xi})\rangle = \langle n^2\rangle$ can be put outside the integral sign in (8).

Finally, assume that the coordinate system is oriented such that the beam axis is parallel with the ξ_3-axis. Using the above approximations then yield the simplified autocorrelation function

$$K(\tau, \sigma) = k_s(t_1)\int_{-\infty}^{\infty} dt_1\, s(t_1 - \tau)\, s(t_1 - \sigma) \qquad (14)$$

where

$$k_s(t) = \frac{c}{2}\,|q|^2\,\langle n^2\rangle \int d\xi_1 \int d\xi_2\, R^2(\vec{\xi}_1 + \vec{\xi}_2 + \tfrac{1}{2}ct\vec{n}_t). \qquad (15)$$

Equation (6) has been used to substitute the spatial pulse $\tilde{s}(z)$ with the temporal pulse $s(t)$. The scaling factor $k_s(t)$ is a slowly varying function of t, incorporating both the effects of attenuation and diffraction of the soundwave in tissue. For simplicity, $k_s(t_1)$ is set to unity in the rest of the paper.

Several observations can now be made.

- When observed for a short period of time (on the order of T_p), the back-scattered signal approximates a sample function from a covariance stationary stochastic process. This follows because k_s varies slowly with t_1; for a short timeframe the autocorrelation function then varies essentially with $|\tau - \sigma|$ only. In this approximation, the echo from a soundburst may be regarded as the output from a linear filter with impulse response $s(t)$, excited by complex valued white noise. This model yields the same autocorrelation function as (14).
- If the pulse length is finite, (14) shows that $K(\tau, \sigma) \equiv 0$ for $|\tau - \sigma| > T_p$. The backscattered signal is then a moving average (MA) stochastic process.
- The autocorrelation function is real. Consequently, the real and the imaginary parts of the complex envelope are uncorrelated.
- The autocorrelation function of the echo from one soundburst is independent of the blood velocity.
- When k_s is unity, the following relation holds

$$K(\tau, \tau) = E \qquad (16)$$

stating that the power of the back-scattered echo from blood depends only on the energy of the signal signature; it does not vary with neither shape nor duration of the signature.

It should be emphasized that the above statements are valid only for the conditions under which eq. (14) was derived.

III. Receiver Filtering in Doppler Blood Velocity Measurements

A. The Optimal Receiver Filter

A model for the range gating in a pulsed Doppler instrument is shown in Fig. 1. The output from the demodulator is modeled as a sum of the signal from blood $\tilde{x}_k(t)$ and complex valued white noise $\tilde{n}_k(t)$. The output from the receiver filter is sampled at time t_1, yielding a sample of the Doppler signal originating from the range $\sim ct_1/2$.

The noise sources in the Doppler reception are of different types. Clutter echos from tissue and spurious echos caused by reverberations yield strong, undesirable signals with low Doppler shifts. This type of noise has a high sample-to-sample correlation, and may therefore be removed by subsequent highpass filtering of the range-gated Doppler signal. A second type is thermal noise from the preamplifier and the receiver transducer. Its contribution is strongly affected by the characteristics of the receiver filter. Thus, provided the receiver/demodulator/highpass filter chain is not saturated by low-frequency clutter, only the thermal noise is of importance in the evaluation of the receiver filter. Viewed in this context, the white noise model seems reasonable. The correlation function of the noise is then

$$\langle \tilde{n}_k^*(t)\tilde{n}_m(\tau)\rangle = N_0\delta(t - \tau)\delta_{km}. \qquad (17)$$

The axial amplitude weighting of the sample volume of a pulsed Doppler instrument is determined by the shape of the received echo from a point scatterer, as observed on the output of the receiver filter in Fig. 1, i.e.

$$w(t) = \int_{-\infty}^{\infty} d\tau\, h(\tau)s(t - \tau) \qquad (18)$$

The length of this echo is $T_p + T_r$, where T_r is the duration of the receiver filter impulse response $h(\tau)$. The corresponding axial length of the sample volume becomes $c(T_p + T_r)/2$. The axial resolution of the instrument therefore degrades linearly with T_r. In the derivation of the impulse response of the optimal receiver filter, it shall be assumed that T_r is finite (FIR filtering). Note that the term *sample volume* has different meanings if the echo is sampled prior to or after the receiver filter. This occurs because the receiver filter smears out the backscattered echos.

When the sample gate closes at time t_1, the signal and noise components of the receiver filter output are

$$\hat{x}_k(t_1) = \int_0^{T_r} d\tau\, h(\tau)\tilde{x}_k(t_1 - \tau) \tag{19}$$

$$\hat{n}_k(t_1) = \int_0^{T_r} d\tau\, h(\tau)\tilde{n}_k(t_1 - \tau) \tag{20}$$

The resulting sample is a weighted average of the input signal to the receiver filter during the time $(t_1 - T_r, t_1)$. In the rest of this work this is referred to as the range gating interval. It is straightforward to show that the signal and noise powers become

$$P_s = \langle|\hat{x}_k(t_1)|^2\rangle = \int_0^{T_r} d\sigma \int_0^{T_r} d\tau\, h^*(\tau)\, K(\tau, \sigma)\, h(\sigma) \tag{21}$$

$$P_n = \langle|\hat{n}_k(t_1)|^2\rangle = N_0 \int_0^{T_r} d\tau\, |h(\tau)|^2 \tag{22}$$

where the covariance kernel $K(\tau, \sigma)$ has been defined in (7). Note that from the definition, the kernel is Hermitian, i.e. $K(\tau, \sigma) = K^*(\sigma, \tau)$. Using operator notation, maximizing the signal-to-noise ratio is equivalent to maximization of the functional

$$\mathrm{SNR} = \frac{P_s}{P_n} = \frac{1}{N_0}\frac{(Kh, h)}{\|h\|^2} \tag{23}$$

where the inner product and the norm are defined as

$$(g, h) = \int_0^{T_r} dt\, g(t)\, h^*(t) \tag{24}$$

$$\|h\| = \sqrt{(h, h)}. \tag{25}$$

From the theory of functional analysis it then follows by definition that

$$\max_h \frac{(Kh, h)}{\|h\|^2} = \|K\| \tag{26}$$

stating that the maximum attainable signal-to-noise ratio is proportional to the norm of the kernel K. Because it is nonnegative (being a covariance kernel) and Hermitian, its eigenvalues are real and nonnegative [9]. It can be shown that the norm of a Hermitian kernel is equal to its maximum eigenvalue λ_1, and that it is attained when $h(\tau)$ is the corresponding eigenfunction [9]. Therefore, the optimum impulse response $h_0(\tau)$ is the solution of the integral equation

$$\int_0^{T_r} d\sigma\, K(\tau, \sigma)\, h_0(\sigma) = \lambda_1 h_0(\tau), \qquad 0 \le \tau \le T_r \tag{27}$$

that corresponds to the maximum eigenvalue λ_1.

An expression for the covariance kernel has already been derived in (14), showing that $K(\tau, \sigma)$ is real. Moreover, Hermitian kernels always have real eigenvalues, and it follows that the impulse response of the optimal receiver filter is real. In the previous section it was shown that the blood velocity does not enter into the expression for the covariance kernel, and, consequently, the optimal receiver filter also becomes independent of the blood velocity.

The optimal receiver filter can now be calculated for an arbitrary signature by solving the eigenvalue problem (27) with the kernel (14). Unfortunately, this is not always an easy task, but the calculations are carried out in Section IV for the special case when the signature is rectangular. At this stage, further general observations regarding SNR and receiver filtering shall be made.

B. SNR Versus Axial Resolution

It is of interest to investigate the effect of a change in axial resolution, while keeping the emitted acoustic energy constant. The lengths of the soundburst and the impulse response of the receiver filter should then be changed proportionally, i.e. $T_p' = \beta T_p$, and $T_r' = \beta T_r$. The burst energy is kept constant by the scaling $s'(t) = s(t/\beta)/\sqrt{\beta}$. Combining with (14) and (27) yield the relations

$$K'(\tau, \sigma) = K(\tau/\beta, \sigma/\beta) \tag{28}$$

$$h_0'(t) = h_0(t/\beta) \tag{29}$$

$$\lambda_1' = \beta\lambda_1 \tag{30}$$

stating that signal-to-noise ratio increases proportionally with the axial length of the sample volume when the acoustic energy is kept constant. The result holds for any type of receiver filter (shown by setting $h'(t) = h(t/\beta)$ in (21) and (22), combine with (28) and substitute into (23)). Sensitivity and resolution are therefore conflicting requirements in pulsed Doppler measurements, a point which has been recognized by a number of investigators [10, p. 111] [11, pp. 229]. The underlying mechanism is that the power of the back-scattered signal is constant when the pulse energy is kept constant, whereas the noise bandwidth of the receiver decreases with increasing range-gating interval. The improvement in signal-to-noise ratio stops when the resolution is decreased to a point where the entire sample volume no longer is fully embodied in blood or no longer covers the region of interest, e.g. a stenotic jet in heart measurements.

A bound can be established for the attainable signal to noise ratio vs. axial resolution. The kernel $K(\tau, \sigma)$ is Hermitian, and it follows from Mercer's theorem that [2]

$$\int_0^{T_r} d\tau\, K(\tau, \tau) = T_r E = \sum_{i=1}^{\infty} \lambda_i \tag{31}$$

where $\lambda_1 > \lambda_2 > \cdots \geq 0$. Therefore, for any type of receiver filter the signal-to-noise ratio is bounded by

$$\mathrm{SNR} \leq \frac{1}{N_0}\lambda_1 \leq \frac{E}{N_0}T_r. \tag{32}$$

The left equality applies if the optimum filter is used, while the right applies if the kernel possesses only one nonzero eigenvalue. The bound increases linearly with the product of the range gating interval and the pulse energy. Moreover, it can be shown that the largest eigenvalue is a nondecreasing function of T_r for any covariance kernel of the convolution type; i.e. $K(\tau, \sigma) = K(\tau - \sigma)$ [2].

Section III-C will show that the signal-to-noise ratio is entirely symmetrical with respect to $s(t)$ and $h(t)$; if they are interchanged, the SNR does not alter. Equation (32) then implies that

$$\mathrm{SNR} \leq \frac{1}{N_0}\lambda_1 \leq \frac{E}{N_0}\min\{T_r, T_p\} \tag{33}$$

i.e. the SNR is bounded by the smallest of T_r and T_p, whereas the axial length of the sample volume is determined by their sum. Viewed on this background, Hoeks' statement on receiver filtering (cited initially) seems reasonable.

Equations (31) and (33) indicate that when $T_r + T_p$ is fixed, there exists an optimal signal signature/receiver filter design combination which maximizes the ratio $\lambda_1/\Sigma_{i=1}^{\infty}\lambda_i$. It is not clear what this design actually is, but in Section 4 it is shown that the rectangular pulse/optimum filter combination approaches the bound (33) fairly closely for all combinations of T_p and T_r.

C. A Frequency Domain Formulation for SNR

The time domain approach used in the previous sections does not give much insight when $s(t)$ or $h(t)$ is of the IIR class, e.g. exponentially decaying. A frequency domain formulation is better suited in this case. Equation (21) and (22) may be Fourier-transformed and substituted into (23) to yield

$$\mathrm{SNR} = \frac{1}{N_0}\frac{\int_{-\infty}^{\infty} d\omega\, |S(\omega)|^2\, |H(\omega)|^2}{\int_{-\infty}^{\infty} d\omega\, |H(\omega)|^2}$$

$$= 2\pi\frac{E}{N_0}\frac{\int_{-\infty}^{\infty} d\omega\, |S(\omega)|^2\, |H(\omega)|^2}{\int_{-\infty}^{\infty} d\omega\, |H(\omega)|^2 \int_{-\infty}^{\infty} d\omega\, |S(\omega)|^2} \tag{34}$$

where $H(\omega) = F\{h(t)\}$. The transition between the two versions follows by multiplying the numerator and the denominator by E, and then substitute (6) for E in the denominator. Note that the signal signature and the receiver filter impulse response enter into the expression in exactly the same way; the SNR does not alter if they are interchanged. Even time reversed versions of these waveforms may be employed, because

$$|F\{s(-t)\}|^2 = |S^*(\omega)|^2 = |S(\omega)|^2 \tag{35}$$

However, such a time reversal would in general change the axial weighting of the sample volume.

Both $S(\omega)$ and $H(\omega)$ are normally well behaved lowpass functions. They may then be described in terms of their equivalent noise bandwidths (ENBW), defined as

$$B_s = \frac{1}{2\pi\,|S(0)|^2}\int_{-\infty}^{\infty} d\omega\, |S(\omega)|^2 \tag{36}$$

$$B_h = \frac{1}{2\pi\,|H(0)|^2}\int_{-\infty}^{\infty} d\omega\, |H(\omega)|^2 \tag{37}$$

If B_s and B_h are significantly different, the one with the larger bandwidth may be assumed to be constant, equal to its dc value, over the entire bandwidth of the other. By substituting the above expression for $S(0)$ or $H(0)$, whichever belongs to the greater bandwidth function, into (34), one obtains the relation

$$\mathrm{SNR} \simeq \frac{E}{N_0 \max\{B_s, B_h\}}, \qquad B_s \ll B_h \text{ or } B_s \gg B_h \tag{38}$$

stating that the signal-to-noise ratio then is solely determined by the largest of the receiver and the signature ENBW's.

For a given signature, it has already been shown how to derive the optimal receiver filter. A different, suboptimal, approach may instead be taken: Based upon (38) it seems reasonable to select a receiver filter that satisfies $B_h = B_s$. The best resolution is then obtained if the filter with the shortest impulse response is selected among all filters with the same ENBW. This filter is the pure averager; it has a purely rectangular impulse response of duration $T_r = 1/B_s$. The latter statement can be proved by rewriting (37), using Parseval's theorem, to

$$B_h = \frac{\int_0^{T_r} dt\, h^2(t)}{\left|\int_0^{T_r} dt\, h(t)\right|^2} \geq \frac{\int_0^{T_r} dt\, h^2(t)}{\int_0^{T_r} dt \int_0^{T_r} dt\, h^2(t)} = \frac{1}{T_r} \tag{39}$$

where the Schwarz inequality has been employed on the denominator. Apparently, equality is obtained if $h(t)$ is rectangular. This proves that no other impulse response of duration T_r has an ENBW that is smaller than $1/T_r$; i.e. that of the pure averager. Note that when (38) is valid, (39) implies that the combination of a rectangular signature and the averager receiver filter attains the bound (33).

D. The Matched Filter in Blood Velocity Measurements

In most radar and sonar applications the shape of the returned echos equals that of the transmitted signal, with a delay determined by the range of the target. With an underspread target at the range $ct_1/2$, the covariance kernel (7) then takes the form

$$K(\tau, \sigma) = E\left[\frac{1}{\sqrt{E}} s(t_1 - \tau)\right]\left[\frac{1}{\sqrt{E}} s(t_1 - \sigma)\right] \quad (40)$$

This kernel is separable. Its only eigenvalue is $\lambda_1 = E$, with the associated eigenfunction (normalized)

$$h_m(\tau) = \frac{1}{\sqrt{E}} s(t_1 - \tau). \quad (41)$$

This impulse response is referred to as the matched filter for the real valued pulse $s(t)$. It was first derived by North [12]. The fundamental difference from the incoherent case is that the kernel $K(\tau, \sigma)$ has one single eigenvalue, meaning that λ_1 is independent both of the duration and the shape of the pulse. In the frequency domain, (41) translates to

$$H_m(\omega) = \frac{1}{\sqrt{E}} S^*(\omega) \exp(-j\omega t_1). \quad (42)$$

It is of interest to evaluate the matched filter in incoherent scattering reception. Setting $t_1 = 0$ in (41), substituting into (23) and combining with (14) yield

$$\begin{aligned} \text{SNR} &= \frac{1}{N_0 E} \int_0^{T_p} d\tau \int_0^{T_p} d\sigma \\ &\quad \cdot \int_{-\infty}^{\infty} dt\, s(-\tau)s(t - \tau)s(t - \sigma)s(-\sigma) \\ &= \frac{1}{N_0 E} \int_{-\infty}^{\infty} dt\, K^2(t, 0) \end{aligned} \quad (43)$$

The signal-to-noise ratio thus is proportional to the "energy" of the correlation function, whereas in the coherent case it is solely determined by the energy of the signature (compare with (7)).

The frequency domain equivalent to (43) follows from (34) and (42)

$$\text{SNR} = \frac{E}{N_0 B_{ss}} \quad (44)$$

where

$$B_{ss} = \frac{1}{2\pi} \frac{\left(\int_{-\infty}^{\infty} d\omega\, |S(\omega)|^2\right)^2}{\int_{-\infty}^{\infty} d\omega\, |S(\omega)|^4} \quad (45)$$

The quantity B_{ss} also arises in the context of spectral analysis, where it has been referred to as the "statistical bandwidth" of the time "window" $s(t)$ [14]. For the class of windows used there (e.g. Hanning), its size is typically 45 percent greater than the 3-dB bandwidth.

There may be situations where the matched filter receiver is preferable, although it does not guarantee optimal signal to noise ratio for a given T_r. One such case is when very high axial resolution is needed. This can be obtained by using a short rectangular pulse with a high energy. However, this approach may not always be tolerable from a patient safety point of view. An alternative solution is to use pulse compression by emitting coded pulses or chirps, and increase resolution by matched filtering. The signal-to-noise performance of such a concept can be found from (43) and (44). Note that these equations are valid only under the assumptions that led to (14). If, for example, long codes (duration on the order of T_s) are employed, both the matched filter and the covariance kernel become functions of the velocity.

It is worth noting that matched filtering in blood velocity measurements in principle maximizes the unwanted clutter echos from tissue. This occurs because specular reflectors give echos that are replica of the signal signature. The matched filter thus enhances the unwanted signals from tissue, rather than the desired signal from blood. However, the next section shows that the difference between the matched and the optimal receiver filter is very small in the common situation, where rectangular-like bursts satisfying $T_p << T_s$ are employed.

IV. The Rectangular Pulse Signature

The signal signature is now assumed to be rectangular with duration T_p and energy E. This is a good approximation to the situation in medium-to-low resolution pulsed Doppler systems ($T_p \sim$ 10–20 cycles of the ultrasound carrier frequency). The signature is given by

$$s(t) = \begin{cases} \sqrt{E/T_p}, & 0 < t < T_p \\ 0, & \text{elsewhere} \end{cases} \quad (46)$$

with the associated covariance kernel

$$K(\tau, \sigma) = \max\left\{0, E\left(1 - \frac{|\tau - \sigma|}{T_p}\right)\right\}. \quad (47)$$

The solution of the eigenvalue problem (27) with the above kernel has been given by Kailath when $E = T_p = 1$ and $T_r \leq 1$ [13]. He showed that the set of eigenvalues $\{\lambda_i'\}$ of the normalized kernel were solutions of the trancendental equation

$$\tan \frac{T_r}{\sqrt{2\lambda_i'}} = \sqrt{\frac{2\lambda_i'}{(2 - T_r)^2}} \quad (48)$$

with associated eigenfunctions (not normalized)

$$h_i'(t; T_r) = \cos \sqrt{\frac{2}{\lambda_i'}}\, t \pm \sqrt{\frac{2\lambda_i'}{(2 - T_r)^2}} \sin \sqrt{\frac{2}{\lambda_i'}}\, t. \quad (49)$$

For the largest eigenvalue ($i = 1$), the positive sign applies. From (29) and (30) one then has for general E, T_p and $T_r < T_p$:

$$h_0(t; T_r) = h_1'(t/T_p; T_r/T_p) \qquad 0 < t < T_r \quad (50)$$

$$\text{SNR}_{\max} = \frac{\lambda_1}{N_0} = \frac{ET_p\lambda_1'}{N_0} \quad (51)$$

Equation (48) is easy to solve by iteration. The resulting optimal impulse responses $h_0(t)$, normalized to $\|h_0\| = 1$,

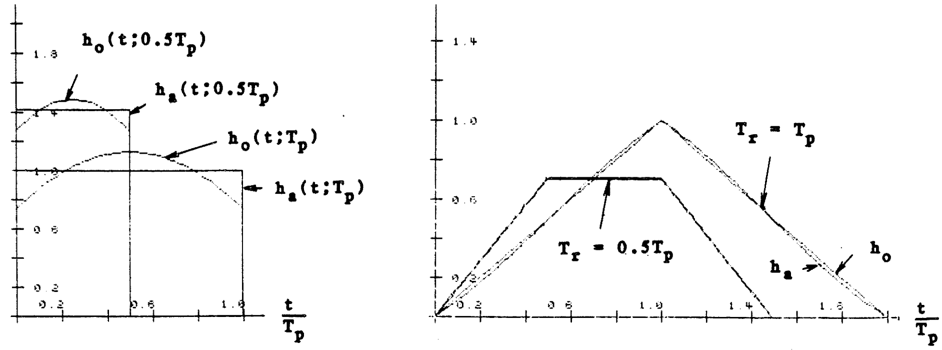

(a) (b)

Fig. 2. (a) Impulse responses of the optimal and the pure averaging receiver filters for $T_r/T_p = 0.5$ and $T_r/T_p = 1$. (b) Corresponding axial amplitude weighting of the sample volume.

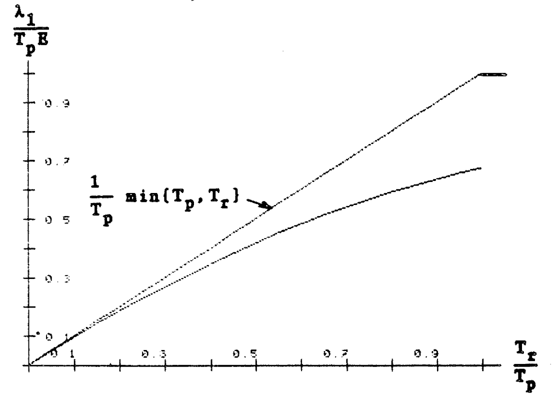

Fig. 3. Maximum eigenvalue of the covariance kernel for the rectangular pulse vs. duration of the range gating interval.

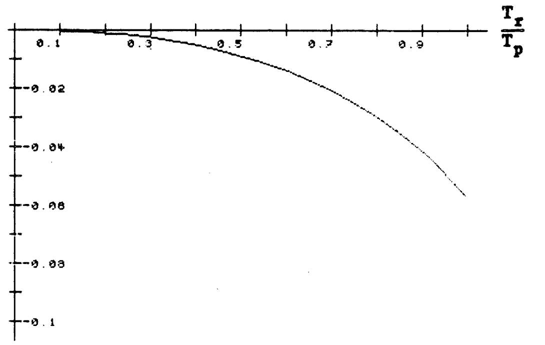

Fig. 4. Loss in signal to noise ratio (in dB units) using the averager receiver filter, with reference to an optimal receiver filter with an impulse response of the same duration.

are plotted in Fig. 2(a) for the cases $T_r/T_p = 0.5$ and $T_r/T_p = 1$. They differ little from rectangular pulses; for comparison these are also shown in the figure. Fig. 2(b) shows the envelope of the output from the receiver filters in Fig. 2(a) when the input is the echo from a single scatterer.

The maximum attainable signal-to-noise ratio using the rectangular pulse signature is proportional to the maximum eigenvalue λ_1. This is plotted vs. T_r/T_p in Fig. 3, together with the bound $\lambda_1 = E \min\{T_r, T_p\}$. As expected from (33), the figure reveals that an increased range gating interval gives little incremental improvement in signal to noise ratio when T_r/T_p approaches unity. In the limit, the following result holds for covariance stationary processes [2]

$$\begin{aligned}\lim_{T_r \to \infty} \lambda_1 &= \max_{\omega} \int_{-\infty}^{\infty} dt\, K(t, t_1) e^{-j\omega t} \\ &= \max_{\omega} \{|S(\omega)|\}^2 \\ &= \max_{\omega} \left\{ ET_p \left[\frac{\sin(\omega T_p/2)}{(\omega T_p/2)}\right]^2 \right\} = ET_p. \qquad (52)\end{aligned}$$

Therefore, increasing T_r/T_p significantly above unity degrades resolution, while the improvement in signal to noise ratio is very small (λ_1 increases from 0.68 ET_p to ET_p, i.e. 1.7 dB). The limiting mechanism is that both signal and noise add incoherently in the receiver filter when $T_r/T_p \gg 1$.

For comparison, the pure averaging filter has also been studied. Its impulse response is

$$h_a(t; T_r) = \begin{cases} 1/\sqrt{T_r}, & 0 < t < T_r \\ 0, & \text{elsewhere.} \end{cases} \qquad (53)$$

Substituting (37) and (43) into (14) yields

$$\mathrm{SNR}_a = \frac{ET_r}{N_0}\left(1 - \frac{T_r}{3T_p}\right), \quad 0 \le T_r \le T_p. \qquad (54)$$

When $T_r = T_p$, this becomes the matched filter for the rectangular pulse; the SNR could then have been derived more easily from (43). The ratio between the signal-to-noise ratios (51) and (54) is plotted in Fig. 4 when T_r/T_p varies. The signal-to-noise ratio deteriorates very little from the case when the optimum filter is used. For T_r/T_p

= 1, the averager performs only 0.06 dB worse than the optimal filter.

V. Conclusion

When the rectangular pulse model is valid (medium-to-low resolution systems), the performance of the averager filter is nearly indiscernible from that of the optimal. From a hardware design point of view this is very appealing. The averager is simple to implement, requiring only an integration of the demodulator output over the range-gating interval. The choice of integration time becomes a resolution vs. signal-to-noise ratio tradeoff. The suggestion of Peronneau ($T_p = T_r$) seems to be a good compromise. Selecting $T_r \neq T_p$ gives loss in sensitivity for a given axial resolution, but provides a more even axial weighting of the sample volume, see Fig. 2(b). This may be desirable in blood-flow measurements based on estimation of the mean Doppler shift over a vessel cross section [5].

When $T_r = T_p$, no combination of signal signature and receiver filter can exceed the bound ET_p/N_0. A rectangular signature and a pure averager filter then exhibits only 1.7-dB loss in sensitivity compared to the bound. This means that the simple combination of a rectangular pulse and integration of the output from the demodulator has near optimum resolution vs. sensitivity properties. It seems unlikely that the bound ET_p can be fully attained for any combination of a real signal envelope and receiver filter with $T_r = T_p$. This would require the existence of a real covariance kernel of the convolution type with only one nonzero eigenvalue.

For high resolution Doppler systems, the rectangular pulse model is no longer valid. Less conclusive results have then been obtained. However, it has been indicated that the ENBW of the receiver filter should be matched to that of the pulse, and that the averager filter seems to be a good choice even in this case.

A general observation has been that high resolution and good signal-to-noise ratio are conflicting requirements in pulsed Doppler blood velocity measurements. The conflict between resolution and SNR is of special importance in combined M-mode/Doppler systems. Short bursts are then required to obtain good M-mode recordings. Compared to medium resolution Doppler systems, this gives a loss in the signal to noise ratio attainable. The loss cannot be recovered by any type of receiver filtering (follows from (38)).

When the sample volume is fully embodied in blood, the SNR increases in direct proportion with the pulse energy. A Doppler system employing constant acoustic power output and a variable PRF requires the functional relationship $E \sim 1/f_s$. Assuming that the sample volume is left unchanged, this means that the signal-to-noise ratio and the PRF become inversely related. Most pulsed Doppler systems extract velocity information by spectral analysis of the range gated Doppler signal. When the PRF is increased, the bandwidth of the noise in this signal increases correspondingly. The signal bandwidth, however, is unchanged. The ratio between the signal and the noise spectral densities (the spectral signal-to-noise ratio) therefore remains the same when the PRF changes.

The existence of an optimal signal signature/receiver filter combination when the axial length of the sample volume is fixed, has been indicated. It is not clear what this combination is, but a rectangular pulse and the corresponding optimal receiver filter yield a signal to noise ratio that closely approaches a bound derived in this paper for the optimal combination.

References

[1] B. A. J. Angelsen, "A theoretical study of the scattering of ultrasound from blood," *IEEE Trans. Biomed. Eng.*, vol. BME-27, No. 2, pp. 61–67, Feb. 1980.

[2] H. L. Van Trees, *Detection, Estimation, and Modulation Theory: Part I.* New York: John Wiley, 1968.

[3] P. A. Peronneau, J.-P. Bournat, A. Bugnon, A. Barbet, and M. Xhaard: "Theoretical and practical aspects of pulsed Doppler flowmetry: Real-time application to the measure of instantaneous velocity profiles *in vitro* and *in vivo*," in *Cardiovascular Applications of Ultrasound*, R. S. Reneman, Ed. Amsterdam: North Holland/American Elsevier, 1974, pp. 66–84.

[4] P. Atkinson and J. P. Woodcock, *Doppler Ultrasound and Its Use in Clinical Measurements.* London: Academic, 1982, p. 272.

[5] W. R. Brody, "Theoretical analysis of the Ultrasonic Blood Flowmeter," Ph.D. dissertation, Stanford Electronics Laboratories, Stanford University, California, Tech. Rep. 4958-1, 1971.

[6] B. A. J. Angelsen, "Transcutaneous measurement of blood velocity and flow in the thorax by ultrasound and the Doppler effect," Tech. Rep. 75-78-W, Inst. of. Eng. Cybern., Norwegian Institute of Technology, Trondheim, Norway, 1974.

[7] A. P. G. Hoeks, "On the development of a Multigate pulsed Doppler system with serial data-processing," Ph.D. dissertation, University of Maastricht, The Netherlands, 1982, p. 40.

[8] "Biological effects of ultrasonic energy on living mammals," Report from The Committee on Bioeffects of the American Institute of Ultrasound in Medicine, *Ultrasound Med. Biol.*, vol. 2, no. 4, p. 351. 1976.

[9] R. P. Kanval, *Linear Integral Equations.* New York: Academic, 1971, Chap. 7.

[10] D. W. Baker, S. L. Johnson, and D. E. Strandness, "Prospects for quantitation of transcutaneous pulsed Doppler techniques in cardiology and peripheral vascular desease," in *Cardiovascular Applications of Ultrasound*, R. S. Reneman, Ed. Amsterdam: North Holland/American Elsevier, 1974, pp. 108–124.

[11] L. Hatle and B. Angelsen: *Doppler Ultrasound in Cardiology-Physical Principles and Clinical Applications.* New York: Lea and Febiger, 1982.

[12] D. O. North, "Analysis of the Factors which Determine Signal/Noise Discrimination in Radar," *Proc. IEEE*, vol. 51, July 1963.

[13] T. Kailath, "Some Integral Equations with 'Nonrational' Kernels," *IEEE Trans. Inform. Theory*, no. 4, pp. 442–447, 1966.

[14] A. H. Nuttall, "Spectral estimation by means of overlapped FFT processing of windowed data," New London, CT: Naval Underwater Research Center, Rep. 4169, Oct. 13, 1971.

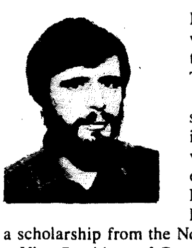

Kjell Kristoffersen was born in Karmøy, Norway, in 1952. He received the M.S. degree in electrical engineering from the Norwegian Institute of Technology, Trondheim, Norway, in 1978.

From 1978 to 1984 he was working with research and development in several areas of process identification and Doppler ultrasound, at the Division of Automatic Control, Foundation of Scientific and Industrial Research at the Norwegian Institute of Technology (SINTEF), Trondheim. During the period 1980 to 1982 he was funded by a scholarship from the Norwegian Institute of Technology. He is currently a Vice President of Development at Vingmed, Horten, Norway. His research interests are in the areas of medical ultrasound and signal processing.

Discrete Time Estimation of the Mean Doppler Frequency in Ultrasonic Blood Velocity Measurements

BJØRN A. J. ANGELSEN, SENIOR MEMBER, IEEE, AND KJELL KRISTOFFERSEN

Abstract—A new Doppler frequency estimator operating in the discrete time domain is derived from an analysis of the Doppler signal statistics. It is shown that the estimator gives a nearly unbiased estimate of the mean frequency of the signal spectrum, regardless of the spectrum shape. The discrete time implementation gives the advantage that, under specified conditions, the range-velocity product of a pulsed Doppler velocity meter can be increased.

Manuscript received April 28, 1982; revised September 29, 1982.
The authors are with the Division of Engineering Cybernetics, Norwegian Institute of Technology, University of Trondheim, N-7034, Trondheim, Norway.

I. INTRODUCTION

IN ULTRASONIC Doppler blood velocity measurements, the velocity v is coded in a frequency shift f_d of the backscattered ultrasound given by the Doppler effect. It is difficult to make the region of observation small in both pulsed and continuous wave measurements. It will therefore contain a distribution of blood velocities which gives a spectrum of Doppler-shifted frequencies in the signal. Full spectrum analysis retrieves all information in the backscattered signal, but is fairly costly to perform. Also, in many cases it is sufficient

0018-9294/83/0400-0207$01.00

to use a single spectral parameter like the mean [1]-[5], rms [6], [7], or maximum Doppler shift [8], [9]. In this paper, we derive a new mean frequency estimator that works in discrete time on samples of the Doppler signal. The estimator has the property that under certain conditions, the usual Nyquist rate can be exceeded.

The received RF signal in the continuous wave ultrasonic blood velocity instrument can be modeled by

$$e(t) = \mathrm{Re}\,\{\hat{x}(t)\, e^{i\omega_0 t}\} \tag{1}$$

where ω_0 is the transmitted angular frequency and $\hat{x}(t)$ is a complex signal called the complex envelope. It contains both amplitude and phase information of the RF signal and can be split into its real and imaginary parts by

$$\hat{x}(t) = x(t) + iy(t). \tag{2}$$

x and y are called the quadrature components of the process.

In the pulsed instrument, the situation is somewhat more complicated. However, by range gating we obtain time samples $\hat{x}(kT_s)$ of $\hat{x}(t)$ from a defined range cell, where T_s is the period between pulse transmissions. Using a low-pass filter, the continuous time signal $\hat{x}(t)$ can be regenerated from the samples, provided the maximum Doppler shift is less than the Nyquist rate $\omega_s/2$, where $\omega_s = 2\pi/T_s$.

The complex envelope $\hat{x}(t)$ is a complex Gaussian process since it is composed of the sum of contributions from a large number of uncorrelated scatterers [10]. For time-steady velocity fields, the process is stationary.

For the RF signal $e(t)$ in (2) to be stationary, the quadrature components must have the following property:

$$R_{xx}(\tau) = R_{yy}(\tau), \qquad R_{yx}(\tau) = -R_{xy}(\tau) \tag{3}$$

where we have defined

$$R_{pq}(\tau) = \langle p^*(t)\, q(t+\tau)\rangle \tag{4}$$

and $\langle\,\rangle$ denotes ensemble averaging. The autocorrelation function of $\hat{x}(t)$ then takes the form

$$R_{\hat{x}\hat{x}}(\tau) = 2\{R_{xx}(\tau) + iR_{xy}(\tau)\}. \tag{5}$$

The power spectrum of $\hat{x}(t)$ is defined by the Fourier transform of $R_{\hat{x}\hat{x}}(\tau)$

$$G_{\hat{x}\hat{x}}(\omega) = \int_{-\infty}^{\infty} d\tau\, R_{\hat{x}\hat{x}}(\tau)\, e^{i\omega_0\tau} \tag{6}$$

The *mean angular frequency* $\bar{\omega}$ of the process is defined as the first moment of $G_{\hat{x}\hat{x}}$, i.e.,

$$\bar{\omega} = \frac{\int_{-\infty}^{\infty} d\omega\, \omega\, G_{\hat{x}\hat{x}}(\omega)}{\int_{-\infty}^{\infty} d\omega\, G_{\hat{x}\hat{x}}(\omega)} = \frac{1}{i}\frac{\dot{R}_{\hat{x}\hat{x}}(0)}{R_{\hat{x}\hat{x}}(0)}. \tag{7}$$

Practical estimators based on (7) have been reported by several authors [1]-[5]. These estimators all operate on the continuous Doppler signal.

The mean frequency estimator derived in this paper works on samples of the Doppler signal. It can theoretically analyze frequencies in the interval $I(w) = (-\omega_s/2 + w,\ \omega_s/2 + w)$ where w is arbitrary. The mean frequency is obtained by an infinite series, which for the practical estimator, has to be truncated to a finite number of terms. By this, the estimator will be in error near the end points of $I(w)$, but the error can be made negligible over 90 percent of the interval. Using $w \neq 0$ in $I(w)$, a special version of the sampling theorem is obtained for complex signals. By this, angular frequencies above $\omega_s/2$, the Nyquist rate, can be analyzed.

In fact, by setting $w = \bar{\omega}$, the estimator will track the mean frequency for values well beyond the Nyquist frequency $\omega_s/2$, provided the signal bandwidth is less than ω_s.

II. Theory of the Estimator

A process $\hat{x}(t)$ is said to have spectral support in $\mathbb{S} \subset R$ if $\omega \notin \mathbb{S}$ implies $G_{\hat{x}\hat{x}}(\omega) = 0$.

Theorem 1: Suppose that a process $\hat{x}$ has spectral support in $I(w) = (-\omega_s/2 + w, \omega_s/2 + w)$. Then, for $T_s = 2\pi/\omega_s$

$$\dot{R}_{\hat{x}\hat{x}}(0) = \sum_{k=-\infty}^{\infty} a_k R_{\hat{x}\hat{x}}(kT_s)$$

$$a_0 = iw$$

$$a_k = \frac{(-1)^{k-1}}{kT_s} e^{-ikwT_s} \qquad k \neq 0. \tag{8}$$

Proof: We use similar techniques as in the proof of the sample theorem and define

$$\tilde{R}_{\hat{x}\hat{x}}(\tau) = R_{\hat{x}\hat{x}}(\tau) \sum_{k=-\infty}^{\infty} \delta(\tau - kT_s). \tag{9}$$

Then,

$$\mathcal{F}\{\tilde{R}_{\hat{x}\hat{x}}(\tau)\} = \frac{1}{T_s}\sum_{k=-\infty}^{\infty} G_{\hat{x}\hat{x}}(\omega - k\omega_s) \tag{10}$$

where $\mathcal{F}\{\ \}$ denotes the Fourier transform.

If $\hat{x}(t)$ is complex, its power spectrum can be asymmetrical around zero. We can then use an asymmetrical filter to smoothe the sampled function to obtain the continuous function

$$H(\omega) = \begin{cases} T_s & \omega \in I(w) \\ 0 & \omega \notin I(w). \end{cases} \tag{11}$$

Using this filter in (9), we obtain the interpolation formula for an asymmetrical spectrum

$$R_{\hat{x}\hat{x}}(\tau) = \sum_{k=-\infty}^{\infty} R_{\hat{x}\hat{x}}(kT_s)\, e^{iw(\tau - kT_s)}\, \frac{\sin \dfrac{\omega_s(\tau - kT_s)}{2}}{\dfrac{\omega_s(\tau - kT_s)}{2}}. \tag{12}$$

Differentiating term by term and setting $\tau = 0$, (8) is obtained.

Corollary: Suppose that $\hat{x}(t)$ has spectral support in $I(w)$.

Then, the mean frequency of $\hat{x}$ defined in (7) is given by

$$\bar{\omega} = w + \frac{2}{T_s} \sum_{k=1}^{\infty} \frac{(-1)^{k-1}}{k} \cdot [\rho_{xy}(kT_s) \cos kwT_s - \rho_{xx}(kT_s) \sin kwT_s] \tag{13}$$

where

$$\rho_{xx}(\tau) = R_{xx}(\tau)/R_{xx}(0)$$
$$\rho_{xy}(\tau) = R_{xy}(\tau)/R_{xx}(0).$$

Proof: From (3) and (5), we have $R_{\hat{x}\hat{x}}(0) = 2R_{xx}(0)$ and

$$R_{\hat{x}\hat{x}}(\tau) - R_{\hat{x}\hat{x}}(-\tau) = i4R_{xy}(\tau).$$

Since by (8), $a_{-k} = a_k^*$, we obtain

$$\dot{R}_{\hat{x}\hat{x}}(0) = i2\{wR_{xx}(0) + 2 \sum_{k=1}^{\infty} [\text{Im}\,(a_k) R_{xx}(kT_s) + \text{Re}\,(a_k) R_{xy}(kT_s)]\}. \tag{14}$$

Inserting this into (7) proves (13).

For practical estimation, we have to truncate the series to a finite number of terms. We shall then show that under specified assumptions, different coefficients $\hat{a}_k$ than those given above will give a better approximation of $\dot{R}_{\hat{x}\hat{x}}(0)$. We seek a representation of the form

$$\hat{\dot{R}}_{\hat{x}\hat{x}}(0) = \sum_{k=-n}^{n} \hat{a}_k R_{\hat{x}\hat{x}}(kT_s) \tag{15}$$

so that $\hat{\dot{R}}_{\hat{x}\hat{x}}(0)$ is a good approximation of $\dot{R}_{\hat{x}\hat{x}}(0)$ in some sense. To define the quality of the approximation, we study an ensemble of spectra $G_{\hat{x}\hat{x}}(\omega, \alpha)$, where α is the ensemble variable. We then minimize the mean square error over this ensemble, i.e.,

$$\min_{\hat{a}_k} E_\alpha\{|\hat{\dot{R}}_{\hat{x}\hat{x}}(0) - \dot{R}_{\hat{x}\hat{x}}(0)|^2\}. \tag{16}$$

From elementary properties of the Fourier transform, we obtain

$$\hat{\dot{R}}_{\hat{x}\hat{x}}(0) - \dot{R}_{\hat{x}\hat{x}}(0) = \frac{1}{2\pi} \int_{I(w)} d\omega\, D_n(\omega)\, G_{\hat{x}\hat{x}}(\omega) \tag{17}$$

where

$$D_n(\omega) = \sum_{k=-n}^{n} \hat{a}_k e^{-ik\omega T_s} - i\omega = iP_n(\omega) - i\omega. \tag{18}$$

The mean-square error of this ensemble of spectra will be

$$E_\alpha\{|\hat{\dot{R}}_{\hat{x}\hat{x}}(0) - \dot{R}_{\hat{x}\hat{x}}(0)|^2\} = \frac{1}{4\pi^2} \int_{I(w)} d\omega_1\, d\omega_2\, D^*(\omega_1) D(\omega_2) K(\omega_1, \omega_2) \tag{19}$$

where we have defined

$$K(\omega_1, \omega_2) = E_\alpha\{G_{\hat{x}\hat{x}}(\omega_1, \alpha)\, G_{\hat{x}\hat{x}}(\omega_2, \alpha)\}. \tag{20}$$

To proceed, we specify to a single frequency spectrum where the frequency is uniformly distributed in an interval $J \subset I(w)$, i.e., $G_{\hat{x}\hat{x}}(\omega, \alpha) = \delta(\omega - \alpha)$ and α has the probability density $p_\alpha(\alpha) = 1/l$ for $\alpha \in J$ and zero else. The length of J is l. This gives

$$K(\omega_1, \omega_2) = \frac{1}{l} \int_J d\alpha \delta(\omega_1 - \alpha)\, \delta(\omega_2 - \alpha) = \begin{cases} \frac{1}{l} \delta(\omega_1 - \omega_2) & \omega_1, \omega_2 \in J \\ 0 & \text{else.} \end{cases} \tag{21}$$

Inserting (21) into (19) gives, for this ensemble of spectra,

$$E_\alpha\{|\hat{\dot{R}}_{\hat{x}\hat{x}}(0) - \dot{R}_{\hat{x}\hat{x}}(0)|^2\} = \frac{1}{4\pi^2 l} \int_J d\omega\, |D_n(\omega)|^2. \tag{22}$$

This gives the following theorem.

Theorem 2: Let $\hat{x}(t)$ be a single frequency signal with frequency uniformly distributed in $J \subset I(w)$. Then, the coefficients in (15) which minimize the mean-square error in (16) correspond to the coefficients of the trigonometric polynomial which approximate $i\omega$ best in the mean-square sense in J.

The question now is how the $\hat{a}_k$'s are changed when $\hat{x}$ has a nonzero bandwidth. Given $K(\omega_1, \omega_2)$, we can determine the optimum $\hat{a}_k$'s by minimizing (19). In practice, it is difficult to specify $K(\omega_1, \omega_2)$ since the situations we are faced with vary. However, $G_{\hat{x}\hat{x}}(\omega)$ is a positive function and the error $D_n(\omega)$ in (18) will oscillate around zero. Due to the integration in (17), we see that the peak error is reduced when the signal has a nonzero bandwidth. We can therefore optimize the estimator for a single frequency signal, and we then know that the bias error is less for signals with nonzero bandwidths as is demonstrated below.

III. Numerical Determination of the Coefficients

$P_n(\omega)$ in (18) is periodic with period ω_s. The fundamental region in ω we define as $I(0) = (-\omega_s/2, \omega_s/2)$. We first derive approximations of $i\omega$ when $J = \{(-\omega_2, -\omega_1)\} \cap (\omega_1, \omega_2)\} \subset I(0)$ and then extend the result to arbitrary w.

Since ω is odd, $P_n(\omega)$ must be odd, which implies $\hat{a}_{-k} = -\hat{a}_k$, giving

$$P_n(\omega) = \sum_{k=1}^{n} b_k \sin k\omega T_s \tag{23}$$

where $b_k = 2\hat{a}_k$. The optimum coefficients are then obtained by minimizing

$$F = T_s^3 \int_{\omega_1}^{\omega_2} d\omega \left| \sum_{k=1}^{n} b_k \sin k\omega T_s - \omega \right|^2 = \int_{z_1}^{z_2} dz \left| \sum_{k=1}^{n} c_k \sin kz - z \right|^2 \tag{24}$$

where $z_i = \omega_i T_s$ and $c_k = T_s b_k$. This gives $\hat{a}_k = c_k / 2T_s$.

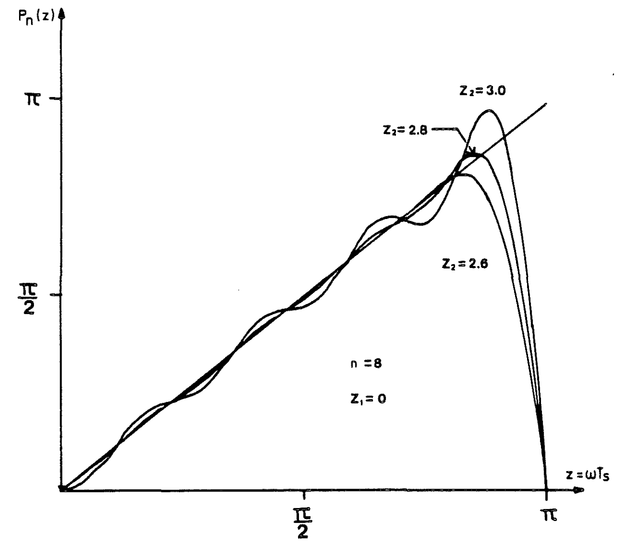

Fig. 1. Approximating polynomials $P_n(z)$ for $n = 8$ and various values of z_2.

We note that if $z_1 = 0$ and $z_2 = \pi$, c_k are the Euler coefficients of the Fourier series expansion of z on $(-\pi, \pi)$. These correspond to the coefficients in (8). Due to periodicity, P_n will approximate a sawtooth function equal to z when $z \in (-\pi, \pi)$ and make jumps of 2π for every $(2k+1)\pi$. The oscillations in the polynomials will be large near the discontinuities (Gibb's phenomenon). However, as our calculations will show, the error will be drastically decreased if we allow $z_2 < \pi$.

The approximating polynomials obtained for $n = 8$ with $z_1 = 0$ and various values of z_2 are shown in Fig. 1. Increasing z_1 from zero has little effect on the error in (z_1, z_2), while the error in $(0, z_1)$ increases. We see that good approximation may be obtained if we allow z_2 to be small enough. However, decreasing z_2 decreases the interval of frequencies that can be analyzed, so that a tradeoff has to be made.

The ratio of the estimated frequency to the actual mean frequency has been calculated for three different spectra

$$G_{\dot{x}\dot{x}}(\omega) = \begin{cases} \frac{1}{B} & \omega \in \left(\bar{\omega} - \frac{B}{2}, \bar{\omega} + \frac{B}{2}\right) \\ 0 & \text{else} \end{cases}$$

$$B = 0, 0.1\,\omega_s, 0.25\,\omega_s. \tag{25}$$

The results are shown in Fig. 2. We note that the error is drastically reduced when a signal of nonzero bandwidth is present.

The coefficients for actual values of n and z_2 are given in Table I for $w = 0$. When $w \neq 0$, the coefficients can be obtained from those with $w = 0$ as follows:

$$\begin{aligned} iP_n(\omega, w) &= iw + iP_n(\omega - w, 0) \\ &= iw + \sum \hat{a}_k(0)\, e^{-ikwT_s}\, e^{ik\omega T_s}. \end{aligned} \tag{26}$$

By this, we obtain

$$\begin{aligned} \hat{a}_0(w) &= iw \\ \hat{a}_k(w) &= \hat{a}_k(0)\, e^{-ikwT_s} \qquad k \neq 0. \end{aligned} \tag{27}$$

When $wT_s \neq p\pi$, $p = 0, 1, \cdots$, $\text{Im}\,\{a_k(w)\} \neq 0$ and in analogy with (13), we see that we have to estimate both $\rho_{xx}(kT_s)$ and $\rho_{xy}(kT_s)$. For $wT_s = p\pi$, $\text{Im}\,\{a_k(w)\} = 0$ and it is sufficient to estimate $\rho_{xy}(kT_s)$ only.

The trigonometric approximation to $f(\omega) = \omega$ is shown in Fig. 3. Due to the sampling with angular frequency ω_s it is possible to obtain a representation over a range ω_s only. For complex signals, whose spectrum is asymmetric around zero, we can offset the approximation as shown in the figure.

If we set $w = 0$ we can analyze frequencies in the range $(-\omega_s/2, \omega_s/2)$. This gives the well-known limit of the range-velocity product of a pulsed Doppler meter. For $w = \omega_s/2$, e.g., we can analyze frequencies in the range $(0, \omega_s)$, but we then need to be sure that we have only positive Doppler shifts present. If there are some negative Doppler shifts present, these will introduce errors in the estimate, so care has to be taken.

IV. Practical Estimator and Experiments

In analogy with (14), we obtain the following approximation to $\dot{R}_{\dot{x}\dot{x}}(0)$:

$$\hat{R}_{\dot{x}\dot{x}} = i2\left\{wR_{xx}(0) + 2\sum_{k=1}^{n} [\text{Im}\,(\hat{a}_k)\, R_{xx}(kT_s) + \text{Re}\,(\hat{a}_k)\, R_{xy}(kT_s)]\right\}. \tag{28}$$

The Doppler signal will be a Gaussian process [10], which implies [7]

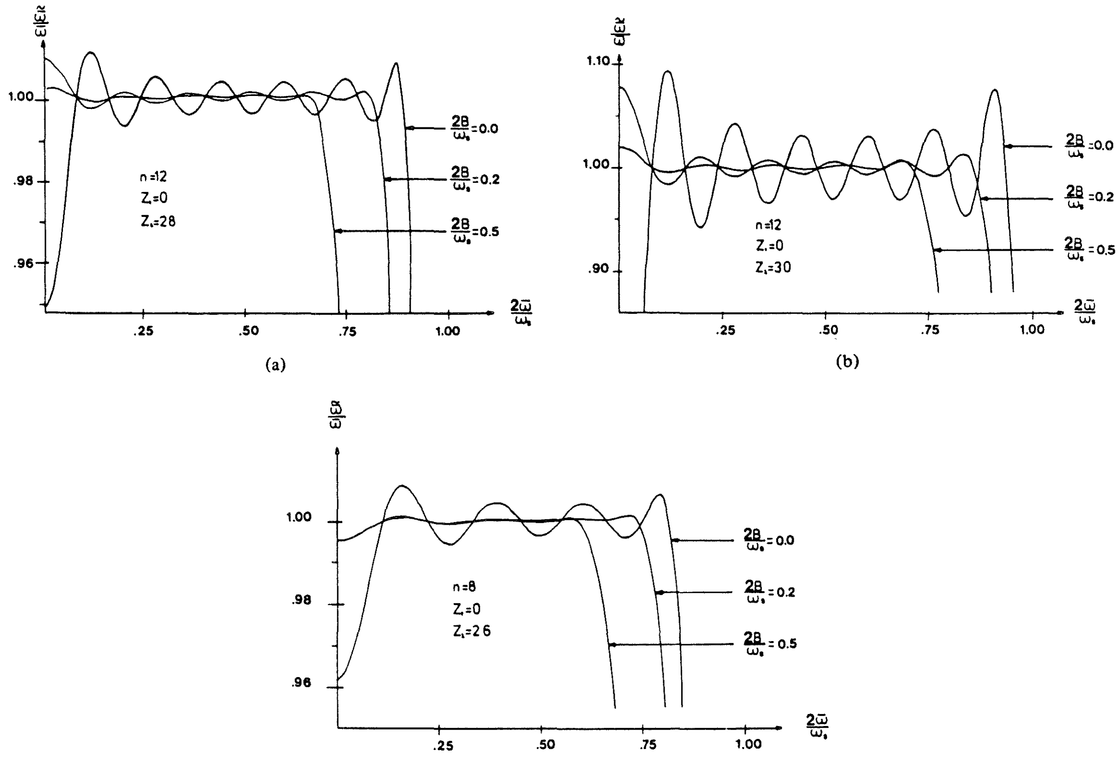

Fig. 2. Ratio of the expected value $\tilde{\bar{\omega}}$ of the estimated mean frequency to the true mean frequency $\bar{\omega}$ for the spectra in (27). B is the signal bandwidth.

TABLE I
COEFFICIENTS FROM MEAN-SQUARE ERROR MINIMIZATION

	N = 12		N = 8		N = 4
	z_2=2.9	z_2=2.8	z_2=2.8	z_2=2.6	z_2=2.2
c_1	1.9827E+0	1.9747E+0	1.9644E+0	1.9415E+0	1.8176E+0
c_2	-9.6574E-1	-9.5019E+1	-9.3018E-1	-8.8700E-1	-6.7319E-1
c_3	6.1605E-1	5.9377E-1	5.6514E-1	5.0678E-1	2.5766E-1
c_4	-4.3394E-1	-4.0610E-1	-3.7038E-1	-3.0345E-1	-7.3679E-2
c_5	3.1965E-1	2.8770E-1	2.4678E-1	1.7843E-1	
c_6	-2.4009E-1	-2.0563E-1	-1.6160E-1	-9.8530E-2	
c_7	1.8115E-1	1.4585E-1	1.0086E-1	4.8420E-2	
c_8	-1.3583E-1	-1.0133E-1	-5.7451E-2	-1.8996E-2	
c_9	1.0025E-1	6.8022E-2			
c_{10}	-7.2062E-2	-4.3375E-2			
c_{11}	4.9754E-2	2.5561E-2			
c_{12}	-3.2258E-2	-1.3174E-2			

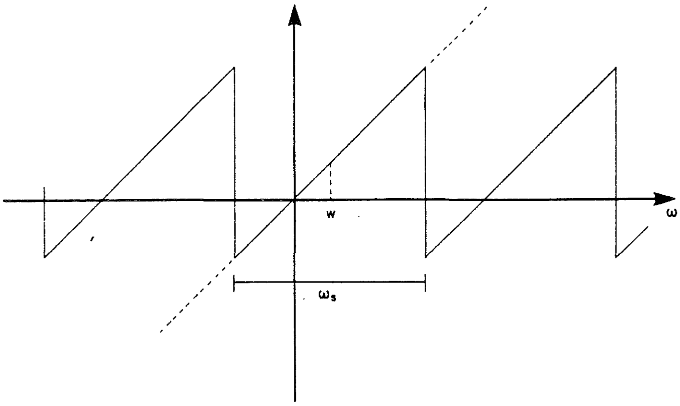

Fig. 3. Trigonometric approximation to $f(\omega) = \omega$. Due to the sampling with angular frequency ω_s, a representation is obtained over a range ω_s only.

$$\frac{R_{xy}(kT_s)}{R_{xx}(0)} = \frac{R_{(\mathrm{sgn}x)y}(kT_s)}{R_{(\mathrm{sgn}x)x}(0)}, \quad \frac{R_{xx}(kT_s)}{R_{xx}(0)} = \frac{R_{(\mathrm{sgn}x)x}(kT_s)}{R_{(\mathrm{sgn}x)x}(0)} \tag{29}$$

where $\mathrm{sgn}x = \pm 1$ for $x \gtrless 0$. By this, digital D-type flip-flops may be used to produce the delays in estimating $R_{(\mathrm{sgn}x)\substack{x\\y}}(kT_s)$ for $k \neq 0$.

For averaging, we use a first-order recursive low-pass filter. By this, we get the following equations:

$$\begin{aligned} \tilde{\omega}(j+1) &= w + \frac{T(j+1)}{N(j+1)} \\ T(j+1) &= \alpha T(j) + 2 \sum_{k=1}^{n} \hat{a}_k(0) \left[\cos (wkT_s) y(j+1) \right. \\ &\quad \left. - \sin (wkT_s) x(j+1)\right] \mathrm{sgn}x\,(j+1-k) \\ N(j+1) &= \alpha N(j) + |y(j+1)| \\ \alpha &= \exp(-T_s/T_f). \end{aligned} \tag{30}$$

T_f is the time constant of the low-pass filter. If T_f is sufficiently large, the variance in N will be small and

$$\begin{aligned} \langle\tilde{\omega}\rangle &\simeq w + \frac{\langle T\rangle}{\langle N\rangle} \\ &= w + 2 \sum_{k=1}^{n} \hat{a}_k(0) \left[\cos (wkT_s) \rho_{xy}(kT_s) \right. \\ &\quad \left. - \sin (wkT_s) \rho_{xx}(kT_s)\right]. \end{aligned} \tag{31}$$

Thus, the bias of the estimate is obtained through (17).

A block diagram of the estimator is shown in Fig. 4. Fig. 5 shows the output of this estimator and the estimator presented in [3] for a Doppler signal from the ascending aorta. Eight delays are used in the estimator and $z_2 = 2.8$. The discrete time estimator uses a first-order filter with $f_c = 1/(2\pi T_f) = 15$ Hz, while the continuous estimator uses a three-pole filter with $f_c \approx 22$ Hz for averaging. Taking this into account, both estimators have fairly equal performance in the systoli. In the diastole, the signal power is so low that both estimators give incorrect estimates of the frequency.

The variance of the estimator has been obtained by computer simulations for the following spectra [10]:

$$G_{\dot{x}\dot{x}}(\omega) = \begin{cases} \dfrac{4\omega}{\bar{\omega}} \dfrac{1}{p+2} \left(1 - \dfrac{p}{p+2} \dfrac{\omega}{\bar{\omega}}\right)^{(2/p)-1} & \omega \in \left[0, \dfrac{p+2}{p}\right)\bar{\omega} \\ 0 & \text{else.} \end{cases} \tag{32}$$

In the simulations, we chose $n = 12$, $z_2 = 2.8$, and $\alpha = 0.98$. The results are shown in Fig. 6.

V. Discussion

We can look upon (15) as an FIR transversal filter working in discrete time to perform differentiation. It uses both positive and negative lags. Using $\hat{a}_{-k} = \hat{a}_k^*$ and the properties of $R_{\dot{x}\dot{x}}$ given in (3) and (5), we are able to use only positive lags in (28), and this gives the simplified structure of the estimator in (30) and Fig. 4. The imaginary part of the frequency transfer function of the transversal filter in (30) approximates $i\omega$. Since we are using one-sided lags only, the frequency transfer function will also have a real part. However, the signal which is generated by the real part of the transfer function disappears in the correlation process. Therefore, the transversal filter in Fig. 4 is not a differentiator, but combined with the correlation process, the total effect is a differentiation. We could, of course, use both positive and negative lags in the filter, by which we would do a differentiation of the signal as in other continuous time estimators [1]-[4], but then it would not be sufficient to use the sign of x only in the filtering process to obtain the derivative of the signal.

The coefficients in the transversal filter will depend upon w. This introduces a delay in the triangular function in Fig. 3 and adding w at the output lifts the function so that it approximates $f(\omega) = \omega$. When $w = 0$, $\mathrm{Im}\,(a_k) = 0$ and we are left with the upper transversal filter only. This simplifies the estimator, but the possibility of analyzing signals with angular frequen-

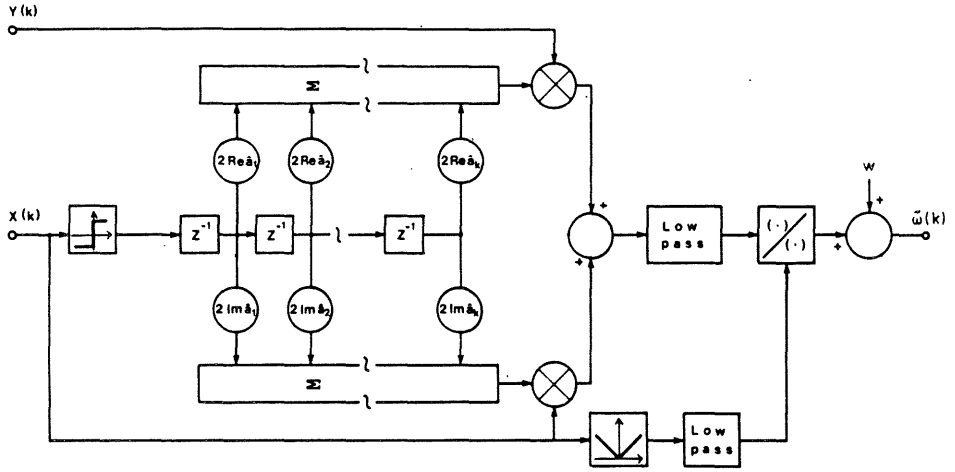

Fig. 4. Block diagram of the estimator.

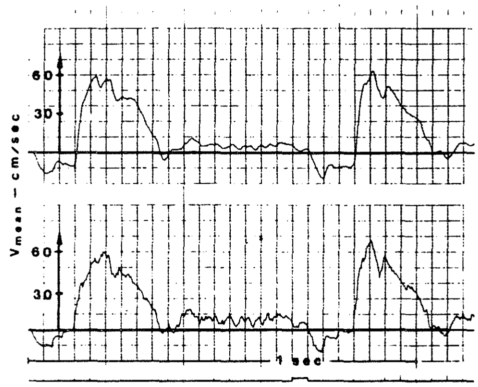

Fig. 5. Output of this estimator with $w = 0$ (lower trace) and estimator presented in [3] (upper trace) for a Doppler signal from the ascending aorta.

cies outside the range $(-\omega_s/2, \omega_s/2)$ emphasizes to leave the ability to use $w \neq 0$. The angular Doppler frequency often exceeds $\omega_s/2$ in flowjets in the heart and even in peripheral vessels.

We can either set w manually to a certain value or we can use feedback from $\tilde{\omega}$, say $w(k) = \tilde{\omega}(k - 1)$. Feedback has several advantages. If the blood velocity does not change too fast we will have $w(k) \approx \tilde{\omega}(k)$, and we are then analyzing signal frequencies in the range $(\tilde{\omega}(k) - \omega_s/2, \tilde{\omega}(k) + \omega_s/2)$. White noise will then give zero bias in the expectation value of the estimator since it is evenly distributed on both sides of the signal mean frequency. Also, if the total signal bandwidth is less than ω_s, we can theoretically track signal frequencies to unlimited range, if the frequencies increase continuously from low values. However, in practice, the signal bandwidth increases as $\tilde{\omega}$ increases and this sets a limit on the maximum frequency that can be tracked, depending on the practical situation. However, the tracking will at least enable us to measure signals with maximum frequencies up to ω_s instead of the Nyquist rate which is half that value, provided we have only one sign of Doppler shifts present.

As shown in Figs. 1 and 2, the estimator will have a bias error in its expected value depending on how many taps are used in the filter and how large a portion of $I(w)$ we want the estimator to cover. The trigonometric polynomial in (18) has a period of ω_s. Therefore, the best we can do is approximate $f(\omega) = \omega$ with a triangular function shown in Fig. 3. If we want a good representation of this triangular function with a trigonometric polynomial, we need a high order of the polynomial, due to the discontinuities in the triangular function. However, if we allow the polynomials to have a free variation in the vicinity of the discontinuity, we obtain a better approximation of the triangular function outside this vicinity, as discussed in Section III. This is demonstrated in Fig. 1 where we see that the error for $z < z_2$ is reduced when z_2 is decreased from π. However, the total mean-square error from 0 to π increases. For $z_2 = \pi$, we obtain the Fourier polynomials for the triangular function.

The bias is also largest for a single frequency signal and decreases with increasing signal bandwidth. In Fig. 2(a) and (c), we see that for a relative bandwidth of 0.2 the bias is less than 0.5 percent for $n = 8$, $z_2 = 2.6$, and for $n = 12$, $z_2 = 2.8$. Increasing z_2 to 3.0 for $n = 12$ increases the maximum bias for this signal to about 8 percent [Fig. 2(b)]. However, the maximum bias occurs for zero angular frequency and due to the instrument high-pass filter, we will not have angular frequency components below 0.05 ω_s to 0.1 ω_s. This reduces the maximum bias to 3-4 percent for $n = 12$, $z_2 = 3.0$, and a relative signal bandwidth of 0.2.

The output of this estimator is compared in Fig. 5 to the estimator in [3] for a Doppler signal from the ascending aorta. This last estimator uses a three-pole low-pass filter ($\approx$22 Hz) for averaging, while the present estimator uses a single-pole low-pass filter ($\approx$15 Hz). This is part of the reason why the present estimator has a noisier output than the other. Since we are using only one-sided lags in the transversal filter of the estimator, we introduce an unwanted signal part in the corre-

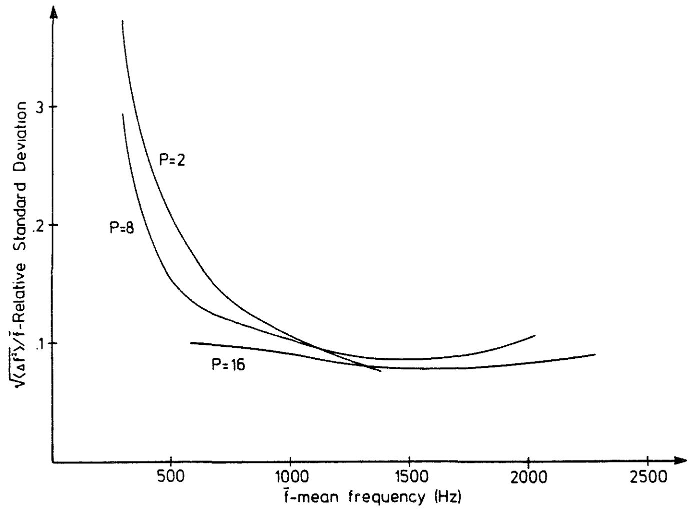

Fig. 6. Estimator variance from computer simulations for the spectra in (32). Nyquist frequency = 2500 Hz, $w = 0$.

lation from the real part of the filter frequency transfer function as discussed above. This signal part introduces no bias in the expectation value of the estimator, but will increase the variance in finite time estimation. Apart from the larger variance, the traces are very similar in systole. In diastole, the signal power is too low for both estimators to function properly.

From Fig. 6 we see that the relative standard deviation of the estimator is about 10 percent for signal frequencies above 600 Hz. This is larger than for the continuous time estimators calculated in [4]. Also, we note that the relative standard deviation does not have the typical $1/\sqrt{f}$ variation which is found for the continuous time estimators presented in [4]. The reason for this can partially be due to the single-sided lag used ih the transversal filter as discussed above, but using the sign in the correlation may also have an effect. The detailed explanation is left for a separate study.

References

[1] M.G.J. Arts and J.M.J.G. Roevros, "On the instantaneous measurement of blood flow by ultrasonic means," *Med. Biol. Eng.*, vol. 10, pp. 23-24, 1972.

[2] R. F. Pawula, "Analysis of center frequency of a power spectrum," *IEEE Trans. Inform. Theory*, vol. IT-14, pp. 669-675, Sept. 1968.

[3] B.A.J. Angelsen and A. O. Brubakk, "Transcutaneous measurement of blood velocity in the human aorta," *Card. Res.*, vol. X, pp. 368-379, May 1976.

[4] B.A.J. Angelsen, "Instantaneous frequency, mean frequency, and variance of mean frequency estimators for ultrasonic blood velocity Doppler signals," *IEEE Trans. Biomed. Eng.*, vol. BME-28, pp. 733-741, Nov. 1981.

[5] W. R. Brody and J. D. Meindle, "Theoretical analysis of the CW Doppler ultrasonic flowmeter," *IEEE Trans. Biomed. Eng.*, vol. BME-21, pp. 183-192, May 1974.

[6] R. S. Reneman, H. E. Clarke, N. Simmons, and M. P. Spencer, "*In vivo* comparison of electromagnetic and Doppler flowmeters: With special attention to the processing of the analog Doppler flow signal," *Card. Res.*, vol. VII, pp. 557-566, 1973.

[7] A. Papoulis, *Probability, Random Variables, and Stochastic Processes.* New York: McGraw-Hill, 1965, p. 487.

[8] B.A.J. Angelsen, "Analog estimation of the maximum frequency of Doppler spectra in ultrasonic blood velocity measurements," Dep. Eng. Cybern., Norwegian Inst. Technol., Trondheim, Norway, Rep. 76-21-W, 1976.

[9] A. O. Brubakk, B.A.J. Angelsen, and L. Hatle, "Diagnosis of valvular heart disease," *Card. Res.*, vol. XI, pp. 461-469, Sept. 1977.

[10] B.A.J. Angelsen, "A theoretical study of the scattering of ultrasound from blood," *IEEE Trans. Biomed. Eng.*, vol. BME-27, pp. 61-67, Feb. 1980.

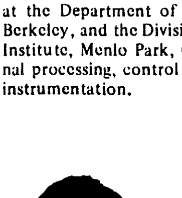

Bjørn A. J. Angelsen (M'79-SM'82) was born in Vestvågøy, Norway, in 1946. He received the M.S. and Dr.Techn. degrees from the Norwegian Institute of Technology, University of Trondheim, Trondheim, Norway, in 1971 and 1977, respectively.

From 1971 to 1972 he worked on infrared detectors at the Norwegian Defence Research Establishment, Kjeller, Norway. From 1972 to 1975 he held a stipend at the Norwegian Institute of Technology and from 1975 to the present he has been with the Division of Engineering Cybernetics, Norwegian Institute of Technology. From 1977 to 1978 he was on leave at the Department of Electrical Engineering, University of California, Berkeley, and the Division of Biomedical Engineering, Stanford Research Institute, Menlo Park, CA. His research interests include stochastic signal processing, control theory, ultrasonics, biomedical engineering, and instrumentation.

Kjell Kristoffersen was born in Karmøy, Norway, on November 21, 1952. He received the M.S. degree in electrical engineering from the Norwegian Institute of Technology, University of Trondheim, Trondheim, Norway, in 1978.

Since 1978 he has been working at the Division of Automatic Control, SINTEF (The Foundation of Scientific and Industrial Research), Norwegian Institute of Technology. He has been involved in research in the areas of process identification and medical and industrial applications of ultrasound. Further interests include biomedical engineering, digital signal processing, and stochastic control theory.

A Comparison Between Mean Frequency Estimators for Multigated Doppler Systems with Serial Signal Processing

K. KRISTOFFERSEN AND B. A. J. ANGELSEN, SENIOR MEMBER, IEEE

Abstract—**Eight different discrete time mean frequency estimators for complex Doppler signals are derived and analyzed. The estimators are well suited for use in multigated Doppler ultrasound measurements of blood velocity profiles. Approximate expressions for bias and variance of the estimators are derived. A general scheme for extending the analyzing range of discrete time Doppler frequency estimators above the Nyquist limit is also outlined.**

The estimators are evaluated by numerical computations of bias and variance, both for wide-band and narrow-band input signals. The performance of the best of the discrete time estimators is roughly equivalent to that of continuous time versions, provided frequency aliasing does not occur.

I. Introduction

MULTIGATED pulsed (PW) Doppler ultrasound instruments permit the real-time measurement of velocity profiles in blood vessels. An elegant way of designing a multigate system is to use serial signal processing [1]–[5]. Using serial design allows the signal processing units, e.g., the high-pass filter, to be shared between the signals from the different range gates in a time multiplexed system. Several investigators have reported efforts in developing discrete time Doppler frequency estimators for multigated systems. The detectors presented have estimated the mean frequency [5], [9] or other parameters relating similarly to the Doppler power spectrum [1]–[3], [7]. Frequency estimation is also an important issue in the development of real-time blood flow imaging systems [6].

The fractional bandwidth (the ratio between bandwidth and center frequency) of the Doppler spectrum varies greatly in different clinical situations. In a high-resolution system, the minimum value is typically 10–20 percent, limited by the transit time effect [8]. When there are velocity gradients in the sample volume, the fractional bandwidth may be much larger. A mean frequency estimator should ideally yield an unbiased, low-variance estimate of the mean Doppler shift, regardless of the signal bandwidth.

In a pulsed Doppler instrument, there is a limit on the magnitude of the maximum frequency that can be detected. This limit has been commonly recognized to be the Nyquist limit, i.e., half the pulse repetition frequency (PRF) of the instrument. However, in direction sensitive systems, the received RF Doppler signal is sampled in both amplitude and phase. A looser requirement is then sufficient to ensure unambiguous detection: the signal bandwidth must not exceed the PRF [9], [18]. Based on this looser requirement, Doppler frequency estimators that work for the asymmetric frequency interval $(-\omega_s/2 + w, \omega_s/2 + w)$ have been designed, where ω_s is the angular PRF of the system. The interval offset w may either be chosen constant (from prior knowledge of the Doppler spectrum) or varied adaptively by feedback from the Doppler frequency estimate itself. In the latter case, it is possible to track signals with time varying mean frequency over a frequency range larger than ω_s. Hoeks investigated an adaptive scheme based on a discrete time instantaneous frequency estimator [5]. This worked well for narrow to medium bandwidth signals (relative to ω_s). However, because the width of the probability distribution for the instantaneous frequency is considerably greater than the bandwidth of the corresponding signal spectrum, the tracking broke down when the signal bandwidth exceeded $\omega_s/2$. For optimal tracking performance, a discrete time frequency estimator should be able to handle a signal with (approximately) known center frequency w, as long as the total signal bandwidth is less than ω_s.

In an earlier paper [9], a discrete time estimator was derived that approximately satisfies the requirements stated above. There is, however, a number of different estimator structures that may be used to implement the ideas presented there. A simple structure is desirable in high-speed hardware implementations of the estimator. The aim of this work is to quantify the tradeoffs between complexity and estimator performance in terms of bias and variance. The implementation structure originally suggested is not a good choice since it may lead to excessive variance for narrow-band signals.

II. Discrete Time Estimation of the Mean Doppler Frequency

A. Estimators for Symmetrical Analyzing Intervals

The Doppler signal $\hat{x}(t)$, in Doppler ultrasound blood velocity measurements, is a zero mean complex Gaussian process [8]. In a PW instrument with discrete time signal processing, only samples $\{x(kT_s)\}$ are available where $T_s =$

Manuscript received December 18, 1983; revised March 25, 1985. This work was supported by grants from the Norwegian Institute of Technology.

The authors are with the Division of Engineering Cybernetics, Norwegian Institute of Technology, N 7034 Trondheim-NTH, Norway.

0018-9294/85/0900-0645$01.00 © 1985 IEEE

$1/f_s = 2\pi/\omega_s$ is the interval between pulse emissions. Without loss of generality, T_s is set to unity in the following. The Doppler signal can then be decomposed into its real quadrature components by

$$\hat{x}(k) = x(k) + jy(k). \tag{1}$$

The cross-correlation function between two stationary discrete time complex processes $\{p(k)\}$ and $\{q(k)\}$ is

$$R_{pq}(n) = \langle p^*(k)\, q(k+n)\rangle \tag{2}$$

where $*$ denotes a complex conjugate and $\langle\ \rangle$ denotes ensemble expectation. Stationarity of $\{x(k)\}$ is assumed throughout this work. Setting $p(k) = q(k) = \hat{x}(k)$, and combining (1) and (2), then yields the autocorrelation function of the complex Doppler signal

$$R_{\hat{x}\hat{x}}(n) = R_{xx}(n) + R_{yy}(n) + j[R_{xy}(n) - R_{yx}(n)]. \tag{3}$$

The power spectrum of the Doppler signal is the Fourier transform of the autocorrelation function of the continuous time Doppler signal $\hat{x}(t)$

$$G_{\hat{x}\hat{x}}(\omega) = \int_{-\infty}^{\infty} d\tau\, R_{\hat{x}\hat{x}}(\tau)\, e^{-j\omega\tau}. \tag{4}$$

If the continuous time Doppler signal has spectral support on the interval $(-\pi, \pi)$, the mean angular Doppler frequency is defined by

$$\overline{\omega} = \frac{\int_{-\pi}^{\pi} d\omega\, \omega G_{\hat{x}\hat{x}}(\omega)}{\int_{-\pi}^{\pi} d\omega\, G_{\hat{x}\hat{x}}(\omega)}. \tag{5}$$

Using elementary properties of the Fourier transform it has been shown that [10]

$$\overline{\omega} = -j\frac{\dot{R}_{\hat{x}\hat{x}}(0)}{R_{\hat{x}\hat{x}}(0)} = \frac{\dot{R}_{xy}(0) - \dot{R}_{yx}(0)}{R_{xx}(0) + R_{yy}(0)}. \tag{6}$$

The above equation forms the base for time domain analog mean frequency estimators [11], [12]. In [9], an odd-order finite impulse response (FIR) differentiator filter was used for approximate discrete time calculation of the derivatives in (6)

$$\dot{R}_{\substack{xy\\yx}}(0) \simeq \sum_{n=-N}^{N} a(n)\, R_{\substack{xy\\yx}}(n). \tag{7}$$

Appropriate differentiator coefficients $\{a(n)\}$ can be derived from a number of different criteria [9], [13]. For a given set of coefficients, the quality of the approximation depends on the signal bandwidth and the maximum frequency of the power spectrum. This problem is discussed at a later stage. Equations (6) and (7) now lead to the approximate equation

$$\overline{\omega} \simeq \frac{\sum_{n=-N}^{N} a(n)[R_{xy}(n) - R_{yx}(n)]}{R_{xx}(0) + R_{yy}(0)}. \tag{8}$$

Consequently, a discrete time mean frequency estimator is given by

$$\hat{\omega}_1 = \frac{\left\langle \left[x(k) \sum_{n=-N}^{N} a(n)\, y(k+n)\right] - \left[y(k) \sum_{n=-N}^{N} a(n)\, x(k+n)\right]\right\rangle}{\langle x^2(k) + y^2(k)\rangle}. \tag{9}$$

In a practical estimator, the ensemble averages must be substituted with time averages. The above estimator is then the discrete time equivalent of the continuous time "double correlator" mean frequency estimator originally proposed by Brody [11]. Its properties have been investigated by Gerzberg and Meindl [17] and Angelsen [10]. The properties of the discrete time estimator will differ from those of the continuous time version, due to both sampling effects and nonideal response of the discrete time differentiator filter when the signal has frequency components close to the Nyquist limit (e.g., when the signal-to-noise ratio is small).

It is possible to perform several simplifications of the expression (9). For time invariant velocity fields, the RF Doppler signal is stationary [8]. This is approximately true also for pulsatile velocity fields when the observation time is short compared to the rise time of the velocity. Then the relations $R_{xx}(\tau) = R_{yy}(\tau)$ and $R_{xy}(\tau) = -R_{yx}(\tau)$ hold [14]. Thereby (9) can be simplified to

$$\hat{\omega}_2 = \frac{\left\langle x(k) \sum_{n=-N}^{N} a(n)\, y(k+n)\right\rangle}{\langle x^2(k)\rangle} \tag{10}$$

which corresponds to the simplified analog single correlator estimator of Arts and Roevros [12].

The discrete time implementation allows for additional simplifications. One always has $a(n) = -a(-n)$ because the transfer function of an FIR differentiator filter is imaginary. Furthermore, both $R_{xy}(\tau)$ and $R_{yx}(\tau)$ are odd functions. This implies that the ratios (9) and (10) will not change if the differentiator filter is truncated by setting the upper limit of the summation to zero, if the remaining coefficients are multiplied by 2. The imaginary part of the transfer function of the truncated filter is still equal to that of the differentiator. However, the truncation generates a nonzero real part of the transfer function which contributes to the filter output with a component in phase with its signal input. This component will generate a zero mean term in the correlation process ($R_{xy}(0) = R_{yx}(0) = 0$). The truncation may therefore lead to increased estimation uncertainty when the averaging time is short.

The size of the real part of the transfer function of an odd-order FIR filter can be manipulated, without affecting the imaginary part, by varying the coefficient $a(0)$. One may thus tailor $a(0)$ to minimize the variance of the estimator for a signal with a known Doppler spectrum. When full length differentiator filters are used, one should choose $a(0) = 0$; this ensures a purely imaginary transfer function. With truncated filters a reasonable choice is

$$a(0) = -\sum_{n=-N}^{-1} a(n). \tag{11}$$

The transfer function of the truncated filter then has a zero for $\omega = 0$, which prevents low-frequency zero mean components from leaking through the correlator. This choice greatly reduces the variance of the estimate at low Doppler frequencies.

None of the above estimators is ideal for applications in multigated Doppler systems, because the FIR filter computations are fairly complex. Increased execution speed and calculation simplification result from using Bussgang's relation for Gaussian signals, stating [15]

$$\langle x(k) \operatorname{sgn} y(k+n) \rangle = \sqrt{\frac{2}{\pi}} \frac{R_{xy}(n)}{\sqrt{R_{yy}(0)}} \tag{12}$$

where sgn $(\cdot)$ is the signum function. This leads to the following alternative to the double correlator estimator (9):

$$\hat{\omega}_3 = \frac{\left\langle \left[x(k) \sum_{n=-N}^{N} a(n) \operatorname{sgn} y(k+n) \right] - \left[y(k) \sum_{n=-N}^{N} a(n) \operatorname{sgn} x(k+n) \right] \right\rangle}{\langle |x(k)| + |y(k)| \rangle}. \tag{13}$$

The continuous time version of this estimator was suggested by Angelsen [10]. The filter part of the above equation can be computed very efficiently using ROM arithmetics. Utilizing the symmetry of the coefficients, the first filter equation can be rewritten to

$$\sum_{n=1}^{N} a(n) \operatorname{sgn} y(k+n) - \sum_{n=1}^{N} a(n) \operatorname{sgn} y(k-n).$$

The sets $\{\operatorname{sgn} y(k+n)\}$ and $\{\operatorname{sgn} y(k-n)\}$ now form two N-bit binary words. These may form the addresses to ROM look-up tables where the two partial sums are tabulated. The same look-up tables may be multiplexed to also compute the second filter equation in (13).

The structure simplifications that were suggested for (9) can also be applied to (13). The resulting single correlator version is denoted $\hat{\omega}_4$. With the truncated differentiator filter and $a(0) = 0$, this corresponds to the original discrete time estimator evaluated in [9].

One is now left with a variety of discrete time mean frequency estimators that basically are variations over the same theme. In the following, it is assumed that the numerators and the denominators of all estimators are averaged by identical FIR low-pass filters of order K, with coefficients $\{b(k)\}$. The estimators under investigation are then described by

$$\hat{\omega}_i = \frac{N_i}{D_i}$$

$$N_i = \sum_{k=1}^{K} b(k)\, n_i(k)$$

$$D_i = \sum_{k=1}^{K} b(k)\, d_i(k) \qquad i = 1, 2, 3, 4. \tag{14}$$

The numerator kernels n_i are

$$n_1(k) = \left[1 - \frac{N'}{2N}\right] \sum_{n=-N}^{N'} a(n) \cdot [x(k)\, y(k+n) - y(k)\, x(k+n)] \tag{15a}$$

$$n_2(k) = 2\left[1 - \frac{N'}{2N}\right] \sum_{n=-N}^{N'} a(n)\, x(k)\, y(k+n) \tag{15b}$$

$$n_3(k) = \sqrt{\frac{\pi}{2}} \sqrt{R_{xx}(0)} \left[1 - \frac{N'}{2N}\right] \cdot \sum_{n=-N}^{N'} a(n)[x(k) \operatorname{sgn} y(k+n) - y(k) \operatorname{sgn} x(k+n)] \tag{15c}$$

$$n_4(k) = \sqrt{2\pi} \sqrt{R_{xx}(0)} \left[1 - \frac{N'}{2N}\right] \cdot \sum_{n=-N}^{N'} a(n)\, x(k) \operatorname{sgn} y(k+n). \tag{15d}$$

The two-valued parameter N' indicates whether the FIR differentiating filter is truncated or not. Allowed values are $N' = 0$ and $N' = N$. The numerators have, for convenience, been scaled to the same expectation value

$$\langle n_i(k) \rangle = \sum_{n-N}^{N} a(n) R_{xy}(n) \simeq \dot{R}_{xy}(0) \qquad i = 1, 2, 3, 4 \qquad N' = 0 \text{ or } N. \tag{16}$$

The corresponding denominator kernels d_i become

$$d_1(k) = \tfrac{1}{2}[x^2(k) + y^2(k)] \tag{17a}$$

$$d_2(k) = x^2(k) \tag{17b}$$

$$d_3(k) = \sqrt{\frac{\pi}{8}} \sqrt{R_{xx}(0)}\, [|x(k)| + |y(k)|] \tag{17c}$$

$$d_4(k) = \sqrt{\frac{\pi}{2}} \sqrt{R_{xx}(0)}\, |x(k)|. \tag{17d}$$

The expectation values of the denominators are normal-

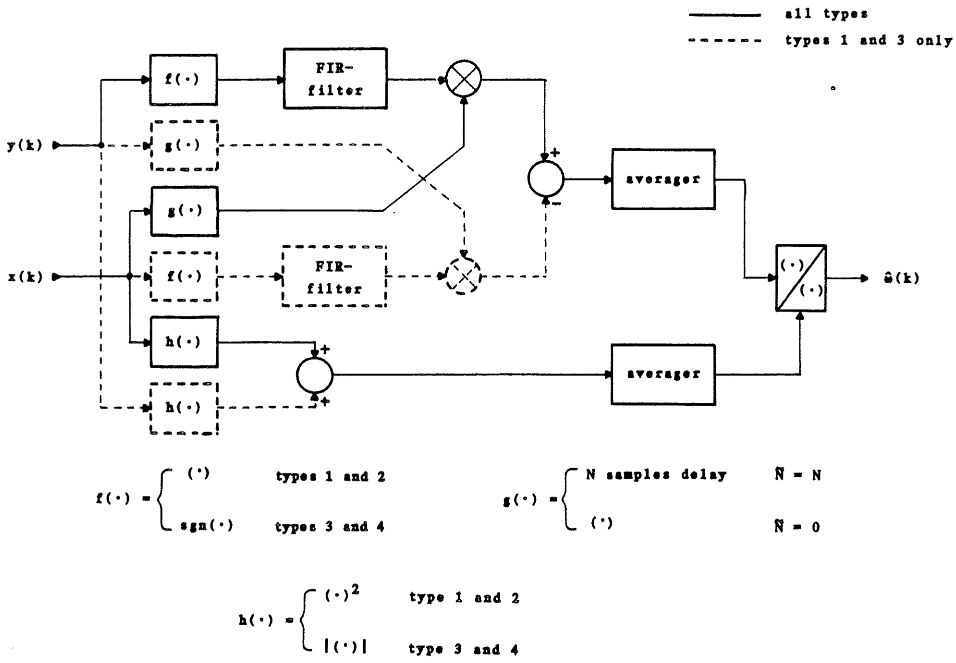

Fig. 1. Structures of different mean frequency estimators.

ized to

$$\langle d_i(k) \rangle = R_{xx}(0) \qquad i = 1, 2, 3, 4. \tag{18}$$

For a given set of coefficients, one has 8 possible ways of implementing the discrete time mean frequency estimator, as illustrated in Fig. 1. The letters t (truncated) or d (differentiator) behind the estimator-type number are used to indicate whether $N' = 0$ or $N' = N$. Estimator 3t thus denotes the double correlator estimator with sign multiplication and truncated differentiator filter. Unless otherwise stated, $a(0)$ is always given by (11) when the truncated filter is employed.

B. Extension to Arbitrary Analyzing Intervals

In [9], a more complex version of estimator 4t was derived that could analyze Doppler signals with spectral support on the asymmetric frequency interval $(-\pi + w, \pi + w)$. Using this version, signals with frequency components above the Nyquist limit could be analyzed without aliasing errors, provided that the total signal bandwidth was less than the sampling rate. By simple means, the same can be obtained also with the symmetric interval ($w = 0$) estimators outlined in the previous section. To show this, we initially define the normalized correlation functions.

$$\rho_{pq}(n) = \frac{R_{pq}(n)}{R_{xx}(0)} \tag{19}$$

where p, q can be x or y. Let $\tilde{\omega}$ denote the approximate mean frequency

$$\begin{aligned}\tilde{\omega} &= \frac{1}{2j} \sum_{n=-N}^{N} a(n) \rho_{\hat{x}\hat{x}}(n) \\ &= \sum_{n=-N}^{N} a(n) \rho_{xy}(n) \simeq \dot{\rho}_{xy}(0) = \bar{\omega}.\end{aligned} \tag{20}$$

Because of the symmetry $a(n) = -a(-n)$, the above equation may be rewritten as

$$\tilde{\omega} = -j \frac{\int_{-\pi}^{\pi} d\omega A(\omega) G_{\hat{x}\hat{x}}(\omega)}{\int_{-\pi}^{\pi} d\omega G_{\hat{x}\hat{x}}(\omega)} \tag{21}$$

where

$$A(\omega) = \sum_{n=-N}^{N} a(n) e^{jn\omega} \tag{22}$$

is the frequency response of the differentiator. Note that $A(\omega)$ is periodic with period 2π. An idealized differentiator frequency response is shown in Fig. 2(a).

Fig. 2(b) shows the spectrum of a stationary Doppler signal $\hat{x}(t)$. The spectrum of the sampled sequence $\{\hat{x}(k)\}$ becomes [16]

$$G^s_{\hat{x}\hat{x}}(\omega) = \sum_{n=-\infty}^{\infty} G_{\hat{x}\hat{x}}(\omega - 2n\pi) \tag{23}$$

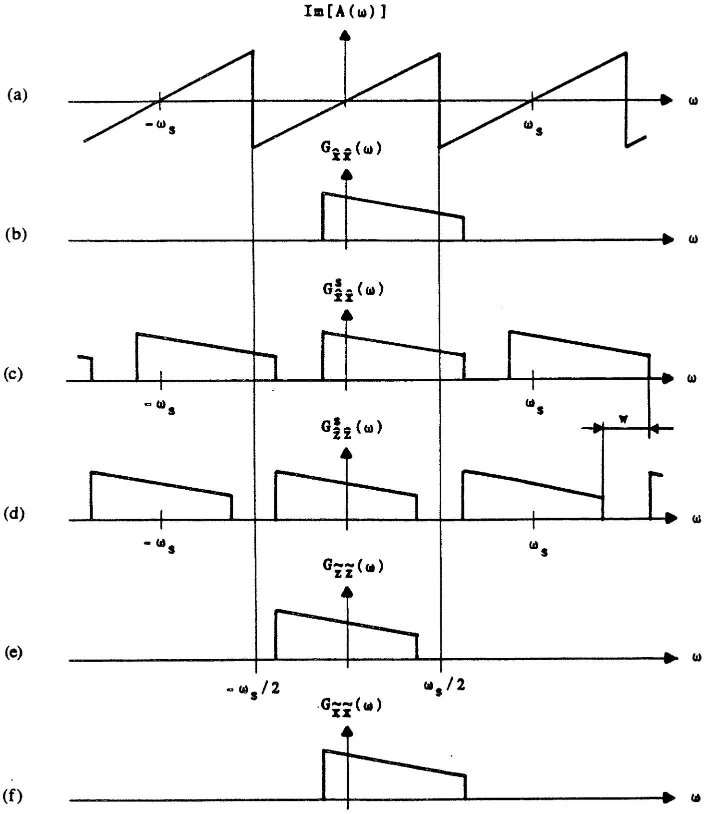

Fig. 2. Principles of mean frequency estimation when the signal contains frequency components exceeding the Nyquist limit.

as indicated in Fig. 2(c). In the example, the maximum frequency of $G_{\hat{x}\hat{x}}(\omega)$ exceeds the Nyquist limit $\omega_s/2$. Still, all information is contained in the power spectrum of the sampled signal because the partial spectra in the sum (23) do not overlap. However, $G_{\hat{x}\hat{x}}(\omega)$ also has spectral support outside the interval $(-\pi, \pi)$, and large aliasing errors will occur if $\{\hat{x}(k)\}$ is analyzed by an estimator with a differentiator filter of the type in Fig. 2(a). In [9], such errors were avoided by employing a differentiator filter with an asymmetric frequency response (FIR filter with complex coefficients). A simpler approach is to form a sampled sequence $\{\hat{z}(k)\}$, with power spectrum $G^s_{\hat{z}\hat{z}}(\omega) = G^s_{\hat{x}\hat{x}}(\omega + w)$, see Fig. 2(d). If the power spectrum of the continuous time Doppler signal $\hat{x}(t)$ has spectral support on $(-\pi + w, \pi + w)$, the power spectrum of the corresponding continuous time signal $\hat{z}(t)$ has spectral support on $(-\pi, \pi)$. One may, therefore, estimate the mean frequency of $G_{\hat{z}\hat{z}}(\omega)$ by analyzing the discrete time process $\{\hat{z}(k)\}$, using a symmetric interval estimator. The sequence $\{\hat{z}(k)\}$ is constructed by the simple transformation

$$\hat{z}(k) = \hat{x}(k)\, e^{-jkw}. \tag{24}$$

This leads to the analyzer structure in Fig. 3. The estimate of the mean frequency of $G_{\hat{x}\hat{x}}(\omega)$ is formed by adding w to the estimate of the mean frequency of $G_{\hat{z}\hat{z}}(\omega)$. The figure also shows how nonaliased audio Doppler information may be retrieved from the sampled Doppler signal. This is achieved by smoothing the quadrature components of $\{\hat{z}(k)\}$ by ordinary analog low-pass filters, with cutoff at the Nyquist frequency, and multiplying the smoothed signal $\tilde{z}(t)$ with the continuous time complex exponential exp (jwt). A signal $\tilde{x}(t)$ with true frequency (pitch) information is then generated [see Fig. 2(e) and (f)]. This operation is motivated by the fact that it is essential to use the audio Doppler signal as an aid in locating the Doppler sample volume [18].

III. Expressions for Estimator Bias and Variance

Expressions for estimator bias and variance may be derived using a time domain approach [10]. Following the method of Brody, (14) can be written on the form [11]

$$\hat{\omega}_i = \bar{\omega}\left(1 + \frac{\alpha_i - \beta_i}{1 + \beta_i}\right). \tag{25}$$

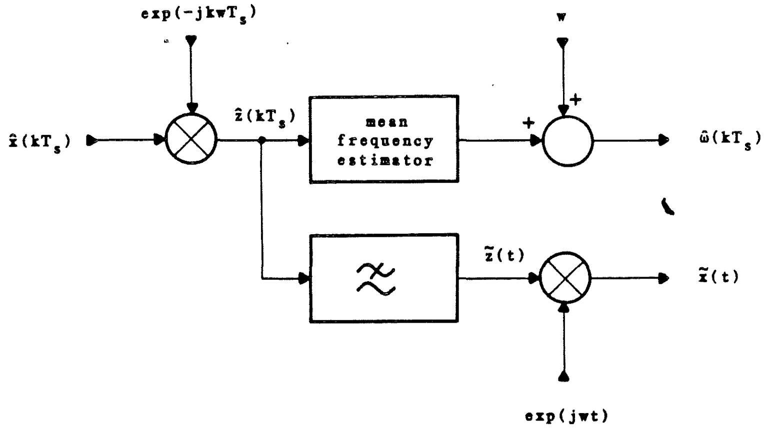

Fig. 3. Block diagram of estimator for asymmetric analyzing intervals. The lower part shows reconstruction of the continuous time Doppler signal.

The random variables α_i and β_i are the normalized excursions from the expectation values of the numerators and denominators, i.e.,

$$\alpha_i = \frac{N_i - \langle N_i \rangle}{\langle N_i \rangle}$$

$$\beta_i = \frac{D_i - \langle D_i \rangle}{\langle D_i \rangle} \tag{26}$$

D_i will be close to $\langle D_i \rangle$ when the low-pass filtering of the denominator is strong. The division can then be approximated with a first-order series expansion

$$\omega_i \simeq \bar{\omega}(1 + \alpha_i - \beta_i - \alpha_i\beta_i + \beta_i^2). \tag{27}$$

From this expression, one obtains approximate values for the fractional bias ϵ_i and fractional variance σ_i^2 of the estimators

$$\epsilon_i = \frac{\langle \omega_i - \overline{\omega} \rangle}{\overline{\omega}} \simeq \frac{\bar{\omega}}{\overline{\omega}} \cdot [1 + \langle \beta_i^2 \rangle - \langle \alpha_i\beta_i \rangle] - 1$$

$$\sigma_i^2 = \left\langle \left[\frac{\omega_i - \bar{\omega}}{\bar{\omega}}\right]^2 \right\rangle \simeq \langle \alpha_i^2 \rangle + \langle \beta_i^2 \rangle - 2\langle \alpha_i\beta_i \rangle. \tag{28}$$

The ratio $\bar{\omega}/\overline{\omega}$ in the bias accounts for the nonideal frequency response of the FIR differentiator, while the remaining terms represent bias due to the finite averaging interval.

Expressions for $\langle N_i^2 \rangle$ and $\langle N_i \rangle^2$ are needed to calculate $\langle \alpha_i^2 \rangle$. From (14), it follows that

$$\langle N_i^2 \rangle = \sum_{k=1}^{K} \sum_{n=1}^{K} b(k)\, b(n)\, \langle n_i(k)\, n_i(n) \rangle = \sum_{m=-(K-1)}^{K-1} \tilde{b}(m)\, \langle n_i(k)\, n_i(k+m) \rangle \tag{29}$$

where the coefficients $\{\tilde{b}(m)\}$ result from the convolution of $\{b(k)\}$ with itself

$$\tilde{b}(m) = \sum_{k=1}^{K-|m|} b(k)\, b(k + |m|). \tag{30}$$

The reduction to a single sum enters due to the stationarity, which makes $\langle n_i(k)\, n_i(n) \rangle$ a function of $k - n$ only. By direct calculation, one obtains the identity

$$\tilde{b}_s = \sum_{m=-(K-1)}^{K-1} \tilde{b}(m) = \left[\sum_{k=1}^{K} b(k)\right]^2. \tag{31}$$

It follows from (14) and (18) that

$$\langle N_i \rangle^2 = \tilde{b}_s \langle n_i \rangle^2 = \tilde{b}_s R_{xx}^2(0). \tag{32}$$

By combining (26), (29), and (32), the fractional variances of the numerators can be computed from the formula

$$\langle a_i^2 \rangle = \tilde{b}_s^{-1} \sum_{m=-(K-1)}^{K-1} \tilde{b}(m)\, \xi_{n_in_i}(m) \tag{33a}$$

where

$$\xi_{n_in_i}(m) = R_{xx}^{-2}(0)\, \bar{\omega}^{-2}\, \langle n_i(k)\, n_i(k+m) \rangle - 1. \tag{33b}$$

Similar expressions may be derived for the fractional variances of the denominators and the cross correlations between the numerators and the denominators

$$\langle \beta_i^2 \rangle = \tilde{b}_s^{-1} \sum_{m=-(K-1)}^{K-1} \tilde{b}(m)\, \xi_{d_id_i}(m) \tag{34a}$$

where

$$\xi_{d_id_i}(m) = R_{xx}^{-2}(0)\, \langle d_i(k)\, d_i(k+m) \rangle - 1 \tag{34b}$$

and

$$\langle \alpha_i\beta_i \rangle = \tilde{b}_s^{-1} \sum_{m=-(K-1)}^{K-1} \tilde{b}(m)\, \xi_{n_id_i}(m) \tag{35a}$$

where

$$\xi_{n_id_i}(m) = R_{xx}^{-2}(0)\,\bar{\omega}^{-1}\,\langle n_i(k)\,d_i(k+m)\rangle - 1. \quad (35b)$$

The normalized covariance functions $\xi_{pq}(m)$ are needed to solve the above equations. Finding these involves calculations with fourth-order moments of the Doppler signal probability distribution. Some of the expressions are rather complex, and the derivation is left for the Appendix.

IV. Numerical Calculations of Estimator Bias and Variance

A. Selection of Estimator and Signal Parameters

In the following, the performance of the estimators will be compared for signals with specified power spectra. Before doing this, one must select proper differentiator filter coefficients. The fractional bias due to nonideal differentiation follows from (6) and (21)

$$\left|\frac{\tilde{\omega}-\bar{\omega}}{\bar{\omega}}\right| = \left|\frac{\int_{-\pi}^{\pi} d\omega\, A_r(\omega)\,\omega G_{\xi\xi}(\omega)}{\int_{-\pi}^{\pi} d\omega\, \omega G_{\xi\xi}(\omega)}\right| \le \max_{\omega\in\Omega}\{|A_r(\omega)|\} \quad (36)$$

where

$$A_r(\omega) = \frac{A(\omega) - j\omega}{j\omega} \quad (37)$$

is the fractional differentiating error for a single frequency input to the differentiator, and Ω is the interval where $G_{\xi\xi}(\omega)$ has spectral support. Thus, the peak fractional bias for a general signal spectrum with spectral support on Ω is less or equal to the peak fractional differentiating error for a single frequency $\omega \in \Omega$ input to the differentiator filter. It is, therefore, reasonable to select the coefficients $\{a(n)\}$ that minimize the peak fractional differentiating error for single frequency inputs. Such coefficients can be calculated using the Remez exchange algorithm [13], which makes $A_r(\omega)$ a minimum amplitude equiripple function over a specified frequency interval. Selecting $N = 8$ and the interval $(-0.84\pi, 0.84\pi)$ then yields the response shown in Fig. 4(a). The peak fractional error is seen to be approximately 1 percent over the specified interval. From (36) and Fig. 4(a), it can be seen that the fractional bias due to nonideal differentiation decreases with increasing signal bandwidth [9]. A greater analyzing range can be obtained by allowing a larger peak error, or by increasing N.

Fig. 4(b) shows the transfer function of the corresponding truncated differentiator filter, both with $a(0) = 0$ and when $a(0)$ is calculated from (11). The real part of the transfer function of the latter has the smallest absolute value for angular frequencies less than approximately 0.5π.

In [9], it was argued for the use of differentiator coefficients $\{a(n)\}$ that minimized the mean square differentiator error $|A(\omega) - j\omega|^2$ over a specified interval. This yielded a relatively large fractional bias for low frequencies. However, the Doppler signal is always high-pass filtered, and the practical difference between the two approaches will be small in most clinical situations.

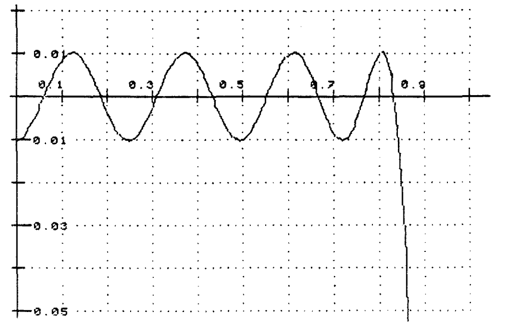

(a)

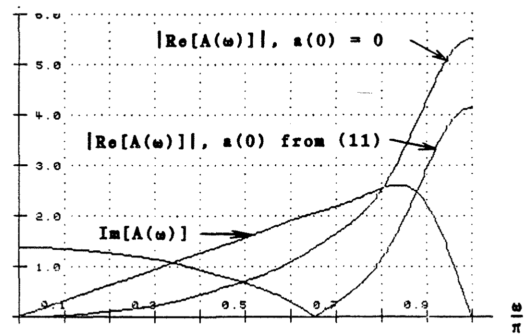

(b)

Fig. 4. FIR differentiator characteristics. (a) Fractional differentiating error function for sinewave input. (b) Transfer function for the truncated differentiator filter.

In the following, smoothing of the numerators and denominators of the estimators by pure averaging filters is assumed, i.e.,

$$b(m) = \frac{1}{K} \qquad m = 1, 2, \cdots, K. \quad (39)$$

The resulting $\{\tilde{b}(m)\}$ and $\tilde{b}_s$ become from (30) and (31)

$$\tilde{b}(m) = \frac{1}{K^2}[K - |m|] \qquad -K < m < K$$
$$\tilde{b}_s = 1. \quad (40)$$

In the calculations, $K = 50$ was selected. The spectrum of the input signal was assumed to be rectangular

$$G(\omega) = \begin{cases} \dfrac{2\pi}{B\bar{\omega}} & \bar{\omega}\left(1 - \dfrac{B}{2}\right) < \omega < \bar{\omega}\left(1 + \dfrac{B}{2}\right) \\ 0 & \text{elsewhere.} \end{cases} \quad (41)$$

The parameter B is the fractional bandwidth of the spectrum. By adding white noise to the Doppler signal and

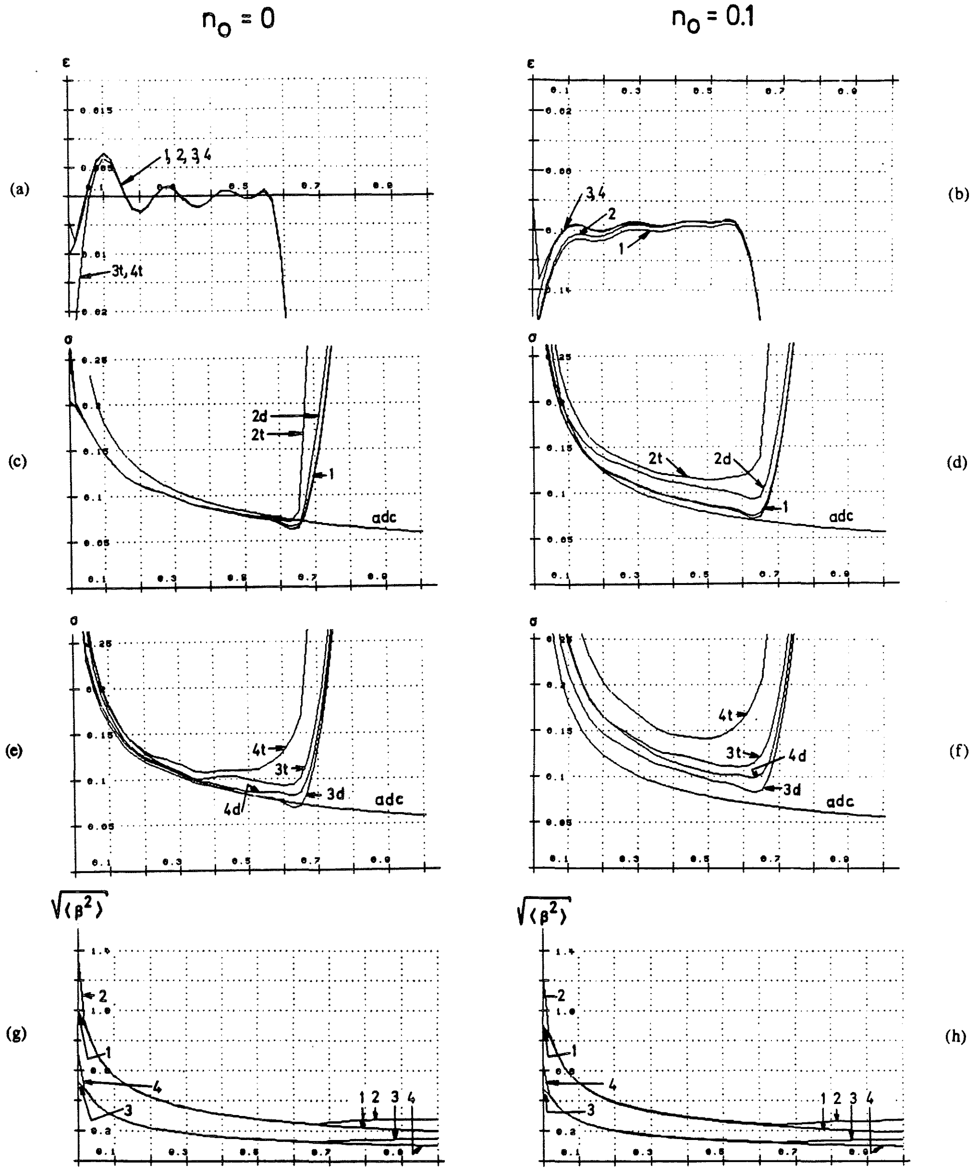

Fig. 5. Comparison between estimator performances when $B = 1$. The x axes are scaled relative to the Nyquist frequency. Left column: noiseless Doppler signal. Right column: $S/N = 10$ dB ($n_o = 0.1$).

assuming a signal-to-noise ratio n_o, the following normalized correlation functions are obtained:

$$\rho_{xx}(n) = \rho_{yy}(n) = (1 + n_o)^{-1} \cdot \left(n_o \delta_{n0} + \operatorname{sinc} \frac{n\bar{\omega}B}{2} \cos n\bar{\omega} \right)$$

$$\rho_{xy}(n) = -\rho_{yx}(n) = (1 + n_o)^{-1} \cdot \operatorname{sinc} \frac{n\bar{\omega}B}{2} \sin n\bar{\omega} \tag{42}$$

where $\operatorname{sinc} z = \sin z/z$ and δ_{nm} is the Kronecker delta. The covariances $\xi_{pq}(m)$ can now be computed from the expressions in the Appendix. The variances and biases for the estimators follow from (28) and (33)–(35).

B. Numerical Results

Four sets of calculations have been performed. Fig. 5 shows results for a signal with large fractional bandwidth ($B = 1$). The left column applies with no noise present. In the right column, the signal-to-noise ratio is 10 dB ($n_o = 0.1$). From top to bottom the figure shows fractional

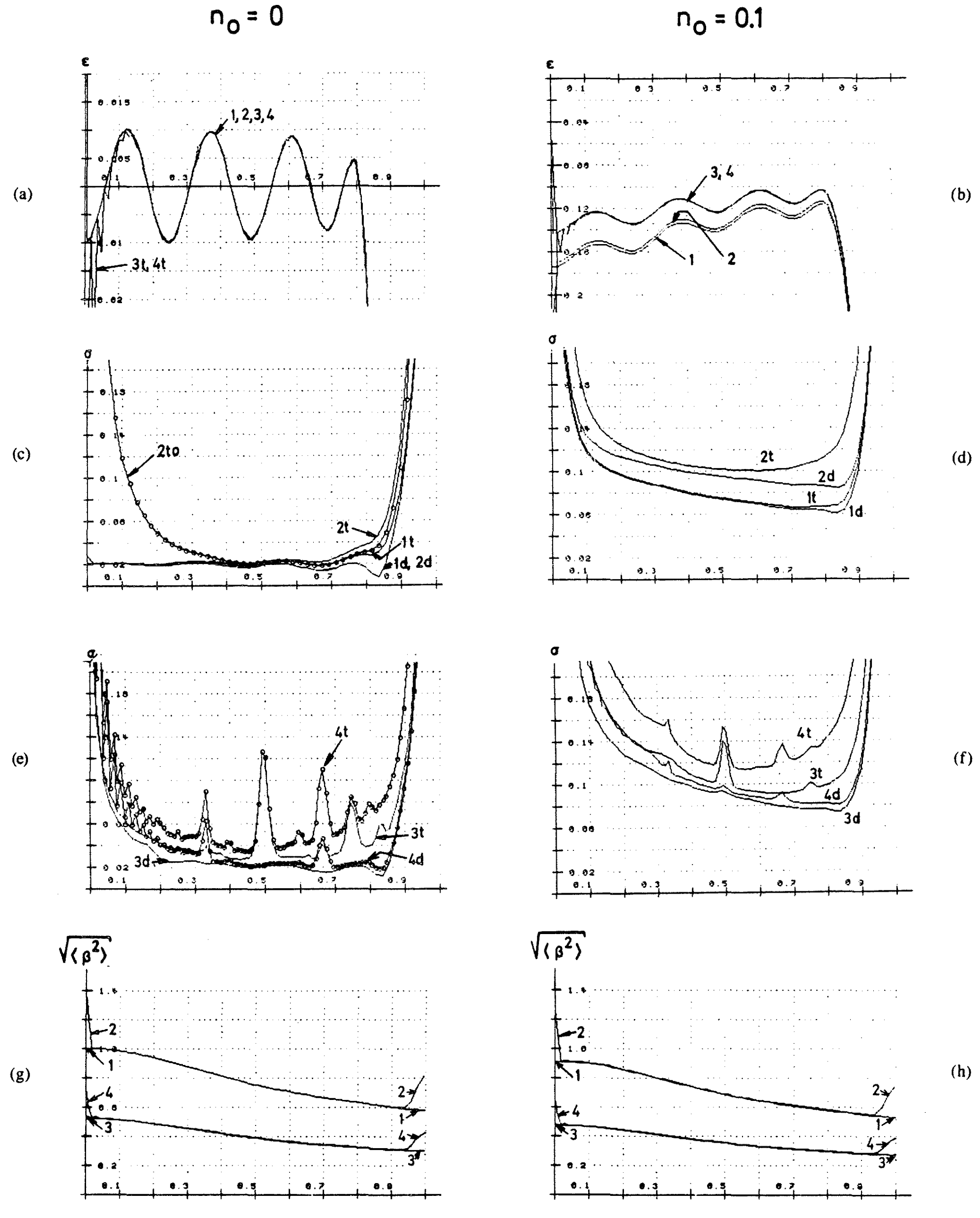

Fig. 6. Comparison between estimator performances when $B = 0.1$. The figure is organized the same way as Fig. 5.

biases, fractional standard deviations for estimators 1 and 2, fractional standard deviations for estimators 3 and 4, and finally, fractional standard deviations $\sqrt{\langle \beta_i^2 \rangle}$ for the denominators. The traces labeled *adc* are the corresponding fractional standard deviations for the analog double correlator (see the Discussion).

Fig. 6 is organized in the same way as Fig. 5 and shows the results when the fractional bandwidth $B = 0.1$. The curve labeled 2*to* in Fig. 6(c) is the fractional variance of estimator 2 with truncated differentiator filter and $a(0) = 0$.

In the noiseless case with strong filtering, the biases of all estimators are practically the same. The peak fractional bias is small (~ 1 percent), decreasing with increasing absolute signal bandwidth $\bar{\omega} B$. A closer investigation shows that ϵ_i is nearly equal to $\tilde{\omega}/\bar{\omega} - 1$ [(36)]. The bias is, therefore, mainly caused by the ripple in the frequency response of the differentiator. With 10 dB signal-to-noise ratio one should, from (20) and (42), expect the fractional bias to be -9 percent ($\epsilon = 1/(1 + n_o) - 1$). Some deviations from this value are seen when the absolute signal bandwidth is small. This type of bias may be heavily reduced by controlling the analyzing interval offset w adaptively from the estimate itself, i.e., $w(k + 1) = \omega_i(k)$ [9].

The variances of the estimators increase with increasing fractional bandwidth B when the mean frequency is constant. For the group employing full multiplication, there is little difference in performance between the types $1d$ and $2d$, provided the maximum signal frequency does not exceed the Nyquist limit [see Figs. 5(c) and 6(c)]. When the differentiator limit 0.84π is exceeded, the fractional variances of all estimators increase abruptly. Note that, in the presence of noise, the single correlators in this group have higher variances than the double correlators, especially when the differentiator filter is truncated (σ_{2t}). Reducing B from 1 to 0.1 when the signal-to-noise ratio is 10 dB hardly affects the variance of the estimators. This is not surprising; the signal is relatively wideband at this noise level, regardless of B.

The result of using a nonzero $a(0)$ when the differentiator filter is truncated is illustrated in Fig. 6(c). The large reduction in variance for low mean frequencies is apparent. However, $\sigma_{2to} < \sigma_{2t}$ for high mean frequencies. The crossover point is approximately 0.5π, which corresponds well with the frequency responses in Fig. 4(b).

The estimators employing sign multiplication have invariably higher variances than the corresponding full multiplication types, and there are considerable differences in performance between the individual estimators in this group. A common characteristic is that their fractional variances increase heavily for the combination of low mean frequencies and narrow-band signals. The reason is that when a hard limited signal is differentiated, the differentiator output is nonzero only in the vicinity of a zero-crossing of the signal. When the number of zero-crossings during the averaging time KT_s is small, the smoothing of the numerator becomes insufficient and the variance increases.

The full differentiator filter estimators $3d$ and $4d$ perform fairly equally except for some small peaks in the plot of σ_{2d} for $B = 0.1$. In the noiseless case, their variances are approximately equal to that of the "full" double correlator $1d$. Type $3d$ is, however, somewhat more sensitive to noise than type d, having approximately 13 percent higher standard deviation in the mid-frequency range when $S/N = 10$ dB. In contrast, the variances of the single correlators $2d$ and $4d$ are fairly equal also when noise is present.

The truncated filter estimators in the group using sign multiplication suffer from deficiencies: their fractional variances do not decrease monotonically with increasing mean frequency, and in the narrow-band case σ_{3t} and σ_{4t} show large peaks, most severe at $\bar{\omega} = 0.5\pi$ (this phenomenon will be explained in the next section). The noise immunity of estimator $4t$ is also poor [Figs. 5(f) and 6(f)].

Fig. 5(g) and (h) shows that the denominators with squared terms have larger excursions from their means than the denominators using absolute values. In spite of this, the estimators with ordinary multiplication have lower variances than the estimators with sign multiplication. This is due to the higher correlation between numerators and denominators for these types. Note that the variances of the single term denominators D_2 and D_4 increase when the maximum frequency increases to the point where aliasing occurs ($\bar{\omega} = 0.67\pi$ when $B = 1$, $\bar{\omega} = 0.95\pi$ when $B = 0.1$). This is of no practical importance since the differentiating error starts to increase at a much earlier stage.

V. Discussion

It is interesting to compare the results to corresponding calculations for continuous time estimators. Gerzberg and Meindl [17] analyzed the double correlator estimator using a frequency domain technique due to Brody [11]. Under the assumption of strong filtering, they derived the following approximation to its variance:

$$\bar{\omega}^2 \sigma^2 = \frac{2\pi}{T_a} \frac{\int_{-\infty}^{\infty} d\omega (\omega - \bar{\omega})^2 \, G_{\dot{\xi}\xi}^2(\omega)}{\left[\int_{-\infty}^{\infty} d\omega \, G_{\dot{\xi}\xi}(\omega)\right]^2} \tag{43}$$

where T_a is the averaging time of the estimator. Thus, in the continuous time case, the variance of the double correlator estimator depends only on the shape and bandwidth of the Doppler spectrum, not on the mean frequency itself. If the above equation is solved for the spectrum family described by (42), one obtains

$$\sigma^2 = \frac{1}{12(1 + n_o)^2 K\omega_r^2} \cdot [(1 + B\omega_r n_o)^2 B\omega_r + n_o^2(1 - (B\omega_r)^3)] \tag{44}$$

where $\omega_r = \bar{\omega}/\omega_s$. For comparison, the fractional standard deviations resulting from the above expression when $B = 1$ and $n_o = 0$, $n_o = 0.1$ are plotted in Fig. 5 (labeled *adc*). When the filtering is strong and the Nyquist limit is not exceeded, the variance of the discrete time double correlator $1d$ is seen to be nearly identical to that of the corresponding continuous time estimator. Note that the fractional standard deviations of most of the discrete time estimators show the same falloff rate as predicted by (44) ($\sigma^2 \sim 1/\bar{\omega}$ for medium or high signal-to-noise ratios). It is therefore likely that their variances depend on the signal bandwidth only. When this holds, the variance becomes independent of the analyzing interval offset w.

Gerzberg and Meindl stated, without proof, that the variance of the analog single correlator estimator was twice that of the double correlator. In contrast, Angelsen found that their variances were equal under strong filtering [10]. This was confirmed by our results because $\sigma_{1d} \simeq \sigma_{2d}$ as long as the maximum frequency of the signal spectrum does not exceed the differentiator limit. The discrete time single correlator estimator has, however, less noise immunity than the double correlator.

It is also possible to compare our calculations to the results of Hoeks [5]. He showed, by simulations, that the variance of the discrete time instantaneous frequency estimator closely obeyed the expression (43) for signal-to-noise ratios greater than or equal to 10 dB. For lower signal-to-noise ratios, its variance was considerably larger than predicted by (44).

It has been shown that the bias of the discrete time mean frequency estimators mainly is caused by differentiating error. Equation (28) then implies that $\langle \beta_i^2 \rangle \simeq \langle \alpha_i \beta_i \rangle$. It follows from (28) that [11], [17]

$$\sigma_i^2 = \langle \alpha_i^2 \rangle - \langle \beta_i^2 \rangle. \tag{45}$$

Fig. 5(g) and (h) reveals that $\langle \beta_1^2 \rangle \simeq \langle \beta_2^2 \rangle$ and $\langle \beta_3^2 \rangle \simeq \langle \beta_4^2 \rangle$ in the interesting frequency ranges. Thus, differences between estimator variances within each group {1, 2} and {3, 4} are related to differences in numerator variances only. The reason for the large variance of the truncated type 2 estimator at high frequencies is increased numerator variance, due to leakage of the input signal through the rapidly increasing real part of the transfer function of the truncated differentiator filter [compare to Fig. 4(b)]. The leakage generates a zero mean term at the correlator's output which oscillates with twice the signal frequency. The relative contribution of this term reduces if K is increased.

The variance peaks for most of the estimators employing sign multiplication are caused by aliasing that occurs when discrete time filtering is performed on a hard limited signal. The aliasing becomes particularly disturbing for narrow-band signals, when strong harmonics of the hard limited signal are mapped down to frequencies in the vicinity of the signal frequency itself. This generates a low-frequency beat at the correlator outputs which is difficult to suppress by low-pass filtering. When the signal bandwidth increases, the peaks are smeared out, but they still give an overall increase in variance. This explains why σ_{4t} increases in the mid-frequency range in the noiseless case with $\mathcal{B} = 1$.

The validity of the results in the narrow-band case may be questioned, as the requirement $\langle \beta_i^2 \rangle << 1$ is poorly met, especially for estimators 1 and 2 [see Fig. 6(g) and (h)]. Averaging 50 samples is hardly strong filtering unless the signal bandwidth $\bar{\omega} B$ exceeds $\sim 0.1\pi$. However, the differences between the estimators within each group {1, 2} and {3, 4} are caused by differences in numerator variances only. The relative results within each group of estimators are, therefore, still approximately correct.

The variances calculated for estimator $4t$ are considerably lower than those obtained from computer simulations in [9]. The reason is the use of the nonzero filter coefficient $a(0)$, which was not included in our first work. The peaks in the variance plot for narrow-band signals were not revealed by the initial simulations.

In conclusion, all of the estimators in the group using full multiplication yield good results. The single correlator estimators have somewhat less noise immunity than the double correlators, especially with a truncated FIR filter. For the double correlator, a truncation gives negligible deterioration. In the group using sign multiplication, both estimators with full length differentiator filters show performances similar to that of the corresponding single correlator estimator using full multiplication. It is not advisable to truncate the differentiator filters in this group. This may result in large variances for narrow-band signals and also the noise immunity deteriorates. For cost-effective hardware implementations in multigated Doppler instruments, the types $3d$ or $4d$ are good solutions. Their variances are not much larger than the "full" estimator $1d$, whereas an implementation of these estimators requires modest amounts of hardware, compared to any estimator from the group using full multiplication.

Appendix
Calculation of the Normalized Autocovariance Functions

A. Estimators Using Ordinary Multiplication

When p, q, r, and s are zero mean, jointly Gaussian variables, the following relation holds [16]:

$$\langle pqrs \rangle = \langle pq \rangle \langle rs \rangle + \langle pr \rangle \langle qs \rangle + \langle ps \rangle \langle qr \rangle. \tag{A1}$$

Equations (15b) and (33b) yield

$$\begin{aligned} R_{xx}^2(0)\, \bar{\omega}^2\, \xi_{n_2 n_2}(m) = 4\left[1 - \frac{N'}{2N}\right]^2 &\cdot \sum_{j=-N}^{N'} \sum_{n=-N}^{N'} a(j)\, a(n) \\ &\cdot \langle x(k)\, y(k+j)\, x(k+m) \\ &\cdot y(k+m+n) \rangle \\ &- R_{xx}^2(0)\, \bar{\omega}^2. \end{aligned} \tag{A2}$$

Setting $p = x(k)$, $q = y(k + j)$, $r = x(k + m)$, and $s = y(k + m + n)$ in (A1) yields directly

$$\xi_{n_2 n_2}(m) = 4\bar{\omega}^{-2}\left[1 - \frac{N'}{2N}\right]^2 \sum_{j=-N}^{N'} \sum_{n=-N}^{N'} \cdot\, a(j)\, a(n)\, \tilde{n}_2(m, n, j) \tag{A3}$$

where

$$\tilde{n}_2(m, n, j) = \rho_{xx}(m + n - j)\, \rho_{xx}(m) - \rho_{xy}(m + n)\, \rho_{xy}(m - j).$$

Similarly,

$$\xi_{n_1 n_1}(m) = 4\bar{\omega}^{-2}\left[1 - \frac{N'}{2N}\right]^2 \sum_{j=-N}^{N'} \sum_{n=-N}^{N'} \cdot\, a(j)\, a(n)\, \tilde{n}_1(m, n, j) \tag{A4}$$

where

$$2\tilde{n}_1(m, n, j) = \rho_{xx}(m + n - j)\,\rho_{xx}(m) - \rho_{xy}(m + n)\,\rho_{xy}(m - j) + \rho_{xy}(m + n - j)\,\rho_{xy}(m) - \rho_{xx}(m + n)\,\rho_{xx}(m - j).$$

The numerator covariances can be computed efficiently for type 2 by observing that the first term in $\tilde{n}_2$ depends on $n - j$ only; while the second term is a product of functions of n and j. In analogy with (29) and (30), one obtains

$$\sum_{j=-N}^{N'} \sum_{n=-N}^{N'} \tilde{n}_2(m, n, j) = \rho_{xx}(m) \cdot \sum_{k=-N-N'}^{N+N'} \tilde{a}(k)\,\rho_{xx}(m + k) - \left[\sum_{n=-N}^{N'} a(n)\,\rho_{xy}(m + n)\right] \cdot \sum_{j=-N}^{N'} a(j)\,\rho_{xy}(m - j) \quad \text{(A5)}$$

where

$$\tilde{a}(k) = \sum_{j=-N}^{N+N'-|k|} a(j)\,a(j + |k|)$$

$$k = -N - N', \cdots, N + N'.$$

$\xi_{n_2n_2}(m)$ is, from (A6), an even function. This can be used for reducing the number of terms in the sum (33a). Similar simplifications can also be made to speed up the computations for estimator 2.

The autocovariance function of the denominator and the cross covariance between the numerator and the denominator can also be computed following the procedure outlined above. The results are

$$\xi_{d_1d_1}(m) = \rho_{xx}^2(m) + \rho_{xy}^2(m) \quad \text{(A6a)}$$

$$\xi_{d_2d_2}(m) = 2\rho_{xx}^2(m) \quad \text{(A6b)}$$

$$\xi_{n_id_1}(m) = 2\bar{\omega}^{-1}\left[1 - \frac{N'}{2N}\right] \cdot \sum_{n=-N}^{N'} a(n)\,\tilde{c}_i(m, n) \qquad i = 1, 2 \quad \text{(A7a)}$$

where

$$\tilde{c}_1(m, n) = \rho_{xy}(m)\,\rho_{xx}(m - n) - \rho_{xx}(m)\,\rho_{xy}(m - n) \quad \text{(A7b)}$$

$$\tilde{c}(m, n) = -2\rho_{xx}(m)\,\rho_{xy}(m - n). \quad \text{(A7c)}$$

B. Estimators Using Sign Multiplication

The covariance functions for this group can be computed using a theorem proven in [10]. It states that when x_1, x_2, y_1, and y_2 are zero mean, jointly Gaussian distributed variables, then

$$\langle x_1x_2 \operatorname{sgn} y_1 \operatorname{sgn} y_2\rangle = \frac{2}{\pi}\langle x_1x_2\rangle \sin^{-1}\langle \tilde{y}_1\tilde{y}_2\rangle + \frac{\tilde{p} - \tilde{q}\langle \tilde{y}_1\tilde{y}_2\rangle}{\sqrt{1 - \langle \tilde{y}_1\tilde{y}_2\rangle^2}} \quad \text{(B1)}$$

where

$$\tilde{p} = \langle x_1\tilde{y}_1\rangle\langle x_2\tilde{y}_2\rangle + \langle x_1\tilde{y}_2\rangle\langle x_2\tilde{y}_2\rangle$$

$$\tilde{q} = \langle x_1\tilde{y}_1\rangle\langle x_2\tilde{y}_1\rangle + \langle x_1\tilde{y}_2\rangle\langle x_2\tilde{y}_2\rangle$$

$$\tilde{y}_i = \frac{y_i}{\sqrt{\langle y_i^2\rangle}} \qquad i = 1, 2.$$

This formula can be applied in the same way as (A1) in Section A to calculate the fourth-order moments involved in the covariances of estimator 3 and 4. The numerator covariances become

$$\xi_{n_in_i}(m) = 4\bar{\omega}^{-2}\left[1 - \frac{N'}{2N}\right] \cdot \sum_{j=-N}^{N'} \sum_{n=-N}^{N'} a(j)\,a(n)\,\tilde{n}_i(m, n, j) - 1 \qquad i = 3, 4 \quad \text{(B2a)}$$

where

$$2\tilde{n}_3(m, n, j) = \rho_{xx}(m) \sin^{-1}\rho_{xx}(m + n - j) + \rho_{xy}(m) \sin^{-1}\rho_{xy}(m + n - j) + R(m, n, j) - S(m, n, j) \quad \text{(B2b)}$$

$$\tilde{n}_4(m, n, j) = \rho_{xx}(m) \sin^{-1}\rho_{xx}(m + n - j) + R(m, n, j) \quad \text{(B2c)}$$

$$R(m, n, j) = \frac{\rho_{xy}(j)\,\rho_{xy}(n) - \rho_{xy}(m + n)\,\rho_{xy}(m - j) - Q(m, n, j)\,\rho_{xx}(m + n - j)}{\sqrt{1 - \rho_{xx}^2(m + n - j)}}$$

$$Q(m, n, j) = \rho_{xy}(m + n)\,\rho_{xy}(n) - \rho_{xy}(j)\,\rho_{xy}(m - j)$$

$$S(m, n, j) = \frac{-\rho_{xy}(j)\,\rho_{xy}(n) + \rho_{xx}(m + n)\,\rho_{xx}(m - j) + T(m, n, j)\,\rho_{xy}(m + n - j)}{\sqrt{1 - \rho_{xy}^2(m + n - j)}}$$

$$T(m, n, j) = \rho_{xy}(j)\,\rho_{xy}(m - j) - \rho_{xx}(m + n)\,\rho_{xx}(n).$$

Unfortunately, no simplifications similar to (A5) seem possible in this case. Computation of (B2) is therefore fairly time consuming. There is also a problem when $m + n - j = 0$. $R(m, n, j)$ is then not defined, since $\rho_{xx}(0) = 1$. By setting $m + n - j = \tau$ and substituting the approximation $\rho_{xx}(\tau) \simeq 1 + \ddot{\rho}_{xx}(0)\, \tau^2/2$, it can be shown that $R(m, n, j) = 0$ in the limit when τ goes to zero.

For the rest of the covariance functions, we obtain

$$2\xi_{d_3d_3}(m) = \rho_{xx}(m) \sin^{-1} \rho_{xx}(m) + \rho_{xy}(m) \sin^{-1} \rho_{xy}(m) + \sqrt{1 - \rho_{xx}^2(m)} + \sqrt{1 - \rho_{xy}^2(m)} - 2 \tag{B3a}$$

$$\xi_{d_4d_4}(m) = \rho_{xx}(m) \sin^{-1} \rho_{xx}(m) + \sqrt{1 - \rho_{xx}^2(m)} - 1 \tag{B3b}$$

$$\xi_{n_id_i}(m) = 2\tilde{\omega}^{-1} \left[1 - \frac{N'}{2N}\right] \sum_{n=-N}^{N'} \cdot\, a(n)\, \tilde{c}_i(m, n) - 1 \qquad i = 3, 4 \tag{B4a}$$

where

$$\begin{aligned} 2\tilde{c}_3(m, n) = {} & \rho_{xy}(m) \sin^{-1} (m - n) \\ & - \rho_{xx}(m) \sin^{-1} \rho_{xy}(m - n) \\ & + \rho_{xy}(n) \sqrt{1 - \rho_{xx}^2(m - n)} \\ & + \rho_{xy}(n) \sqrt{1 - \rho_{xy}^2(m - n)} \end{aligned} \tag{B4b}$$

$$\tilde{c}_4(m, n) = - \rho_{xx}(m) \sin^{-1} \rho_{xy}(m - n) + \rho_{xy}(n) \sqrt{1 - \rho_{xy}^2(m - n)}. \tag{B4c}$$

References

[1] P. A. Grandchamp, "A novel pulsed directional Doppler velocimeter: The phase detection profilometer," in *Proc. 2nd Eur. Congr. Ultrason. Med.* Amsterdam, The Netherlands: Exerpta Medica, 1975, pp. 137-143.

[2] M. Brandestini, "Applications of the phase detection principle in a transcutaneous velocity profile meter," in *Proc. 2nd Eur. Congr. Ultrason.. Med.* Amsterdam, The Netherlands: Exerpta Medica, 1975, pp. 144-152.

[3] —, "Signalverarbeitung in perkutanen Ultraschall Doppler Blutfluss Messgeraten," Ph.D. dissertation, ETH5711, Eidgenossischen Technischen Hochschule, Zurich, Switzerland, 1976.

[4] —, "Topoflow—A full range Doppler velocity meter," *IEEE Trans. Sonics Ultrason.*, vol. SU-25, pp. 287-293, 1978.

[5] A. P. G. Hoeks, "On the development of a multi-gate pulsed Doppler system with serial data-processing," Ph.D. dissertation, Univ. Maastricht, Maastricht, The Netherlands, 1982.

[6] K. Namekawa, C. Kasai, M. Tsukamoto, and A. Koyano, "Realtime bloodflow imaging system utilizing auto-correlation techniques," in *Proc. 3rd Conf. World Fed. Ultrason. Med. Biol.*, R. A. Lersky and P. Morley, Eds. Elmsford, NY: Pergamon, 1982, pp. 203-208.

[7] B. A. J. Angelsen and K. Kristoffersen, "On ultrasonic MTI measurements of velocity profiles in blood flow," *IEEE Trans. Biomed. Eng.*, vol. BME-26, pp. 665-671, Dec. 1979.

[8] B. A. J. Angelsen, "A theoretical study of the scattering of ultrasound from blood," *IEEE Trans. Biomed. Eng.*, vol. BME-27, pp. 61-67, Feb. 1980.

[9] B. A. J. Angelsen and K. Kristoffersen, "Discrete time estimation of the mean Doppler frequency in ultrasonic blood velocity measurements," *IEEE Trans. Biomed. Eng.*, vol. BME-30, pp. 207-214, Apr. 1983.

[10] B. A. J. Angelsen, "Instantaneous frequency, mean frequency and variance of mean frequency estimators for ultrasonic blood velocity Doppler signals," *IEEE Trans. Biomed. Eng.*, vol. BME-28, pp. 733-741, Nov. 1981.

[11] W. R. Brody, "Theoretical analysis of the ultrasonic blood flowmeter," Ph.D. dissertation, Stanford Electronics Laboratories, Stanford University, CA, 1971, Tech. Rep. 4958-1.

[12] M. G. J. Arts and J. M. J. G. Roevros, "On the instantaneous measurements of blood flow by ultrasonic means," *Med. Biol. Eng.*, vol. 10, pp. 23-24, 1972.

[13] L. R. Rabiner and B. Gold: *Theory and Application of Digital Signal Processing.* Englewood Cliffs, NJ: Prentice-Hall, 1975, pp. 123-204.

[14] A. Papoulis, *Probability, Random Variables and Stochastic Processes.* Tokyo, Japan: McGraw-Hill, 1965, pp. 336-381.

[15] J. L. Brown, Jr., "On a cross correlation property for stationary processes," *IEEE Trans. Inform. Theory*, vol. IT-3, pp. 28-31, Mar. 1957.

[16] S. A. Tretter, *Introduction to Discrete Time Signal Processing* New York: Wiley, 1976, p. 307.

[17] L. Gerzberg and J. D. Meindl, "Power-spectrum centroid detection for Doppler systems applications," *Ultrason. Imaging*, vol. 2, pp. 232-261, 1980.

[18] L. Hatle and B. Angelsen: *Doppler Ultrasound in Cardiology—Physical Principles and Clinical Applications.* New York: Lea and Fabiger, 1982.

K. Kristoffersen, photograph and biography not available at the time of publication.

B. A. J. Angelsen (M'79-SM'82), photograph and biography not available at the time of publication.

Time Domain Estimation of the Center Frequency and Spread of Doppler Spectra in Diagnostic Ultrasound

K. Kristoffersen, M.Sc.
VINGMED SOUND A/S
Box 141, 3191 Horten
Norway

ABSTRACT

Two sets of estimators of the center frequency and mean square bandwidth of a Doppler spectrum are analyzed. The first set is based on a linear combination of the complex autocorrelation of the Doppler signal for different lags. It is then shown that the argument (phase angle) of the complex autocorrelation function at unity sample lag is a close approximation to the mean Doppler shift, whereas its modulus (magnitude) gives information about the mean square bandwidth of the spectrum. Approximate expressions for the bias and variance of the estimators are derived, valid for long averaging times. The performances of the estimators are compared for signals with rectangular spectra and different signal-to-noise ratios.

1. INTRODUCTION

In the early phase of diagnostic Doppler ultrasound, a number of workers investigated time-domain methods for extracting frequency or, equivalently, blood velocity information from the backscattered Doppler signal. Continuous time-domain methods were developed for the estimation of mean [1]-[5], RMS [6], and maximum Doppler shift [7]. When relatively low-cost, real-time spectrum analyzers became available, these methods lost most of their importance. With the advent of cardiac color-flow mapping, the time-domain techniques have got a renewed actuality.

Real-time flow mapping systems based on the combined use of multigated pulsed Doppler instruments and phased-array sector scanners have recently become available [8][9][24]. The principle of operation is the following: A soundbeam is swept rapidly across the imaged sector in a stepwise manner. Each radial vector in the sector image is examined with a small number of soundbursts, so that estimates of the velocity parameter(s) to be mapped are obtained for a large number of range gates. These parameters are coded into color, and displayed as an overlay to a gray-scale echo image of the surrounding tissue. The parameters mapped in [8][9][24] were related to the center frequency and the bandwidth of the Doppler spectrum.

A parameter estimator for flow-map systems needs to be simple, as the time available for processing is scarce (on the order of 1 μs per sample of the complex Doppler signal). Moreover, it is important that the estimator has a low stochastic uncertainty: The variance of a spectral parameter estimate is inversely related to the measurement time, so a high-variance parameter estimator translates directly to a low frame rate flow image. A moderate bias of the estimator, on the other hand, is not as harmful, because the color image has a relatively coarse parameter resolution.

Serial signal-processing is an efficient scheme for implementing multigated Doppler systems with a large number of range gates. In this concept, all signal-processing units (e.g., the frequency detector) are timeshared between the signals from the different range gates. The method was developed in the mid 70's: Inspired by the well-known Radar concept of Moving Target Indication [10], Grandchamp [11] and Brandestini [12] developed experimental devices, capable of measuring velocity profiles **in vitro**. The devices employed an RF signal-processing scheme with severely limited ability to remove the strong, low frequency Doppler shift from tissue that occur in **in vivo** measurements. Brandestini later improved the technique, using discrete-time signal processing in the baseband [13][14].

The success of the serial signal-processing scheme relies heavily on the quality of the parameter estimator. Brandestini's original device employed a phase-detection method that essentially averaged a discrete-time approximation to the instantaneous Doppler frequency over a time interval [13][15]. He later converted this technique to equivalent baseband processing [14]. This **instantaneous frequency estimator** exhibits aliasing type of phenomena for Doppler spectra with maximum frequency well below the Nyquist frequency [15]. Hoeks later overcame these limitations by employing an adaptive interpretation of the instantaneous frequency, based upon the temporal evolution of the Doppler shift from arteries [16]. His scheme, which is briefly discussed in this paper, also enables the measurement of Doppler frequencies exceeding the Nyquist frequency. The same holds for the discrete-time **mean frequency estimator** developed by Angelsen and Kristoffersen [17][18].

In a recent work [19], Barber et al. presented a new 'instantaneous' frequency estimator, which turns out to be identical to the detector employed in a commercially available real-time flow-map system [9][24]. This detector differs, however, from the instantaneous frequency estimator previously discussed, and to avoid ambiguity, it will be referred to as the **correlation-angle estimator** in the subsequent parts of this paper. On the basis of experiments, Barber et al. concluded that a 'hybrid' estimator, consisting of the correlation angle estimator for high frequencies and an 'approximate mean' frequency estimator for low frequencies, outperformed the ordinary mean frequency estimator under adverse signal-to-noise ratios. However, a number of questions remains unanswered: Neither of the papers [19],[24] showed how the the output of the correlation-angle estimator was related to the spectrum in the general case, and its statistical properties (bias, variance) are still unknown.

When it comes to time-domain estimation of the Doppler signal bandwidth, little work seems to have been published. Recently, an estimator of mean-square bandwidth was proposed by Kasai et al. [24], but otherwise the subject has merely been touched upon in a few papers [4][8].

The objectives of this paper are the following;

i) on theoretical grounds, to develop a general framework for evaluation of a class of discrete-time spectral parameter estimators;

ii) apply this framework to compare the performances of the correlation-angle estimator to the 'true' mean frequency estimator for arbitrary signal inputs;

ii) and, finally, apply the framework to establish and evaluate estimators of spectral spread.

The paper is organized in the following way: Basic definitions and notational conventions are stated in the next section, whereas the concept of spectral parameter estimation is discussed in a general context in Section 3. The results derived are then applied to evaluate estimators of the mean, bandwidth, and the variance (i.e., mean-square bandwidth) of the Doppler spectral density. In Section 5, simplified estimators for the mean and the variance of the spectral density are derived. The simplified mean frequency estimator coincides with the correlation-angle estimator of Barber et al., and that of the bandwidth is the same as the estimator of Kasai et al. Quantitative comparisons between the 'full' and the simplified estimators are performed for signals with specified spectra and signal-to-noise ratios. Finally, a relation between the correlation-angle estimator and the discrete-time instantaneous frequency estimator is established.

2. DEFINITIONS AND NOTATIONAL CONVENTIONS

Let $\hat{x}(t)$ denote the complex envelope of the received signal in Doppler ultrasound blood velocity measurements. In a single-gate pulsed system, the signal available for analysis is $\{\hat{x}(kT_s)\}$, k integer, where T_s is the time interval between the emission of two ultrasound bursts. In the following, T_s is set to unity, and it is assumed that the signal originates from a time steady velocity field. The sequence $\{\hat{x}(k)\}$ is then a stationary complex Gaussian process [20]. As such, it is entirely characterized by its autocorrelation function,

$$R(n) = \langle \hat{x}^*(k)\hat{x}(k+n) \rangle \tag{2.1}$$

where the brackets denote ensemble expectation value and the asterisk denotes complex conjugate. The auto-correlation satisfies the symmetry relation

$$R(n) = R^*(-n) \tag{2.2}$$

The power spectrum $G(\omega)$ of the sampled Doppler signal is defined as the Fourier transform of $R(n)$,

$$G(\omega) = \sum_n R(n)e^{-jn\omega} \tag{2.3}$$

Note that due to the sampled nature of a PW Doppler instrument, $G(\omega)$ is periodical with period 2π. In the following it is assumed that, unless otherwise specified, all summation indices run from $-\infty$ to ∞. Similarly, where no integration limits are specified, it is assumed that the integration extends over the entire Nyquist interval $-\pi$ to π.

The angular **mean frequency** of the Doppler signal is defined as the first-order moment of the spectral density, i.e.,

$$\bar{\omega} = \frac{\int d\omega\ \omega G(\omega)}{\int d\omega\ G(\omega)} \tag{2.4}$$

The second order moment of the spectral density (denoted mean-square (MS) frequency in subsequent parts of this paper) is the square of what is commonly referred to as the angular **RMS frequency** of the spectrum,

$$\omega_{rms}^2 = \frac{\int d\omega\ \omega^2 G(\omega)}{\int d\omega\ G(\omega)} \tag{2.5}$$

The RMS frequency does not resolve the sign of the Doppler shift. It is well known that the continuous time zero-crossing detector yields an output that is an estimate of ω_{rms} [21]. This is generally not the case for the discrete-time zero-crosser [15].

The angular **variance** of the Doppler spectral density is a measure of spectral spread [4][8] . It is defined as

$$v = \frac{\int d\omega\ (\omega - \bar{\omega})^2 G(\omega)}{\int d\omega\ G(\omega)} = \omega_{rms}^2 - \bar{\omega}^2 \tag{2.6}$$

The spectral variance can be calculated as the difference between the mean-square frequency and the square of the mean frequency. To avoid confusion with the variance of a parameter estimate (stochastic uncertainty), the term **mean-square (MS) angular bandwidth** will be used instead of spectral variance troughout this paper.

The **instantaneous angular frequency** of the Doppler signal is defined as the time derivative of $\arg\{\hat{x}(t)\}$, where $\arg\{\cdot\}$ denotes phase angle [5]. A discrete-time approximation to the instantaneous frequency is given by [15][16],

$$\hat{\omega}_i(k) = \arg\{\hat{x}(k)\} - \arg\{\hat{x}(k-1)\} \qquad -\pi + w_o < \omega_i \le \pi + w_o \tag{2.7}$$

where w_o is an interval offset that can be chosen to determine the desired range of variation (domain) for ω_i. If the interval offset is zero, the range of variation becomes symmetrical around zero (the Nyquist interval $-\pi$ to π).

3. GENERAL FRAMEWORK FOR ESTIMATION OF SPECTRAL PARAMETERS

3.1 Derivation of a spectral parameter estimator

Both the mean and the MS frequencies are spectral parameters of the general class

$$\omega_p = \frac{\int d\omega\ \mathrm{Re}\{A_1(\omega)\}G(\omega)}{\int d\omega\ \mathrm{Re}\{A_2(\omega)\}G(\omega)} = \frac{\mathrm{Re}\{\int d\omega\ A_1(\omega)G(\omega)\ \}}{\mathrm{Re}\{\int d\omega\ A_2(\omega)G(\omega)\ \}} \tag{3.1}$$

where $Re\{A_i(\omega)\}$, $i = 1,2$, are appropriate spectral weighting functions ($Re\{A_2(\omega)\}$ is unity for both examples given). Alternately, such a parameter may be expressed as the solution of an integral equation on the form

$$\int d\omega\ G(\omega)(Re\{A_1(\omega)\} - \omega_p Re\{A_2(\omega)\}) = 0 \tag{3.2}$$

In the time domain, ω_p can be expressed as the ratio between the real parts of two linear combinations of samples of the auto-correlation function. This is realized by rewriting Eq. (3.1), using the inverse Fourier transform, and interchange the order of integration and summation,

$$\omega_p = \frac{Re\{\int d\omega\ A_1(\omega)\ \sum_n R(n)e^{-jn\omega}\}}{Re\{\int d\omega\ A_2(\omega)\ \sum_n R(n)e^{jn\omega}\}} = \frac{Re\{\sum_n a_1(-n)R(n)\}}{Re\{\sum_n a_2(-n)R(n)\}} \tag{3.3}$$

where $\{a_i(n)\}$ and $A_i(\omega)$ are Fourier transform pairs.

A time-domain estimator $\hat{\omega}_p$ for the frequency parameter ω_p can be established directly on the basis of Eq. (3.3), using the definition Eq. (2.1). The estimator becomes

$$\hat{\omega}_p = \frac{z_1}{z_2} \tag{3.4}$$

where

$$z_i = Re\{\sum_k b(k) \sum_n a_i(n)\hat{x}^*(k)\hat{x}(k-n)\}$$

$$= Re\{\sum_k b(k)\hat{x}^*(k) \sum_n a_i(n)\hat{x}(k-n)\} \qquad i = 1,2 \tag{3.5}$$

The kernel of Eq. (3.5) is the cross correlation between one version of the Doppler signal that is filtered through a filter with impulse response $\{a_i(n)\}$, and the signal itself. The set $\{b(k)\}$ is the real impulse response of the smoothing (averaging) filters for the numerator and the denominator (identical filtering is assumed). A practical estimator will normally use running averages, to allow for updating of the parameter estimate when the Doppler signal is nonstationary.

The choice of coefficients $\{a_i(n)\}$ for the estimator is not unique, because only the real part of $A_i(\omega)$ contributes to the integrals in Eq. (3.1). In general, the lowest variance of the estimator is guaranteed if the coefficients are selected such that $Im\{A_i(\omega)\} = 0$ [18]. The symmetry relation

$$a_i(n) = a_i^*(-n) \tag{3.6}$$

then holds, which implies that any nonconstant real valued transfer function $A_i(\omega)$ yields a filter with a noncausal impulse response $\{a_i(n)\}$. In a practical estimator the duration of the impulse response must be finite, say **2N + 1** samples. The lack of causality then requires the direct doppler signal to be delayed **N** samples prior to the correlation in Eq. (3.5). However, the spectral weighting function can always be rewritten on the form

$$\mathrm{Re}\{A_i(\omega)\} = \mathrm{Re}\{\ \Sigma\ a_i'(n)e^{-jn\omega}\ \} \tag{3.7}$$

where

$$a_i'(n) = \begin{cases} a_i(n) + a_i^*(-n) & n < 0 \\ a_i(0) & n = 0 \\ 0 & n > 0 \end{cases} \tag{3.8}$$

Any type of spectral weighting function may, therefore, be constructed with a causal coefficient set, i.e. $a_i(n) \equiv 0$ for $n > 0$, at the expense of adding a nonzero imaginary part to $A_i(\omega)$. Eq. (3.7) also shows that when $A_i(\omega)$ is an odd function (e.g., $A_1(\omega) = \omega$), the corresponding coefficients become purely imaginary. If $A_i(\omega)$ is even (e.g., $A_1(\omega) = \omega^2$), the coefficients become real.

The expectation value for the numerator and the denominator of the estimator becomes

$$\langle z_i \rangle = (\sum_k b(k))\mathrm{Re}\{\sum_n a_i(-n)R(n)\} = B(0)\ \frac{1}{2\pi}\int d\omega\ G(\omega)\mathrm{Re}\{A_i(\omega)\} \tag{3.9}$$

where B(0) is the frequency response of the smoothing filter at zero frequency. The frequency response $B(\omega)$ is defined as

$$B(\omega) = \sum_k b(k)e^{-jk\omega} \tag{3.10}$$

The ratio between the expected values of the numerator and the denominator is an unbiased estimate for the frequency parameter ω_p. When the averaging time is finite, it is still possible that $\hat{\omega}_p$ be biased, because of the nonzero variance of z_i. Whether or not depends on how its numerator and denominator are correlated.

3.2 Bias and variance of the parameter estimate

Under strong filtering, the standard deviation of the denominator Eq. (3.4) is small compared to its expected value. It is then a good approximation to substitute the division with a second-order linearization [1],

$$\langle z_2\rangle^2 \left[\frac{z_1}{z_2} - \frac{\langle z_1\rangle}{\langle z_2\rangle} \right] \approx [(z_1 - \langle z_1\rangle) - \omega_p(z_2 - \langle z_2\rangle] \qquad (3.11)$$

$$- (z_2 - \langle z_2\rangle)[(z_1 - \langle z_1\rangle) - \omega_p(z_2 - \langle z_2\rangle]$$

Eq. (3.11) leads to the following expressions for the bias and variance of the parameter estimate,

$$\mathrm{Bias}\{\hat{\omega}_p\} = \hat{\omega}_p - \omega_p \approx \frac{1}{\langle z_2\rangle^2} \left[\omega_p \, \mathrm{Var}\{z_2\} - \mathrm{Cov}\{z_1,z_2\}\right] \qquad (3.12)$$

$$\mathrm{Var}\{\hat{\omega}_p\} \approx \frac{1}{\langle z_2\rangle^2} \left[\mathrm{Var}\{z_1\} - 2\omega_p \, \mathrm{Cov}\{z_1,z_2\} + \omega_p^2 \, \mathrm{Var}\{z_2\}\right] \qquad (3.13)$$

where the covariance between the sequences z_i and z_j is defined as

$$\mathrm{Cov}(z_i,z_j) = \langle (z_i - \langle z_i\rangle)(\langle z_j - \langle z_j\rangle)\rangle \qquad i,j = 1,2 \qquad (3.14)$$

The expression Eq. (3.13) for the variance was derived neglecting the second-order terms in Eq. (3.11). The bias expression, therefore, is valid for a somewhat larger variance of the denominator than that for the variance.

Note that $\mathrm{Var}\{z_i\} = \mathrm{Cov}\{z_i,z_i\}$. In the appendix it is shown that when $\{\hat{x}(k)\}$ is a complex Gaussian process, the covariance between z_1 and z_2 is given by the following frequency domain expression,

$$\mathrm{Cov}\{z_1,z_2\} = \frac{1}{4(2\pi)^2} \int d\omega \int d\Omega \; G(\omega)G(\omega-\Omega)\,|B(\Omega)|^2\{A_1(\omega-\Omega)A_2^*(\Omega)$$

$$+ A_1(\omega-\Omega)A_2(\omega) + A_1^*(\omega)A_2^*(\omega-\Omega) + A_1^*(\omega)A_2(\omega)\} \qquad (3.15)$$

Under strong filtering, the bandwidth of the smoothing filter is much smaller than the bandwidth of the weighted Doppler spectrum $\mathrm{Re}\{A_i(\omega)\}G(\omega)$. The magnitude-squared frequency response of the smoothing filter then behaves essentially as a delta function in the integral (3.15). This approximation yields

$$(2\pi)^2\mathrm{Cov}\{z_1 z_2\} \simeq \frac{1}{4} \int d\Omega |B(\Omega)|^2 \int d\omega \; G^2(\omega)(A_1(\omega)+A_1^*(\omega))(A_2(\omega)+A_2^*(\omega))$$

$$= B^2(0) \quad W_b \int d\omega \; G^2(\omega)\mathrm{Re}\{A_1(\omega)\}\mathrm{Re}\{A_2(\omega)\} \qquad (3.16)$$

where W_b is the equivalent angular noise bandwidth (ENBW) of the smoothing filter,

$$W_b = \frac{\int d\omega \ |B(\omega)|^2}{B^2(0)} = 2\pi \frac{\sum_k b^2(k)}{(\sum_k b(k))^2} \tag{3.17}$$

The latter form of the equation follows from Parseval's theorem. For a Doppler spectrum with bandwidth B and a spectral weighting function of unity, strong filtering is obtained when $W_b << 2\pi B$.

Inserting Eqs. (3.16) into Eqs. (3.12),(3.13), combining with Eq. (3.9) and rearranging terms finally yields

$$\text{Bias}\{\hat{\omega}_p\} \simeq - W_b \frac{\int d\omega \ G^2(\omega)\text{Re}\{A_2(\omega)\}(\text{Re}\{A_1(\omega)-\omega_p\text{Re}\{A_2(\omega)\})}{[\int d\omega \ G(\omega)\text{Re}\{A_2(\omega)\}]^2} \tag{3.18}$$

$$\text{Var}\{\hat{\omega}_p\} \simeq W_b \frac{\int d\omega \ G^2(\omega)(\text{Re}\{A_1(\omega)\} - \omega_p\text{Re}\{A_2(\omega)\})^2}{[\int d\omega \ G(\omega)\text{Re}\{A_2(\omega)\}]^2} \tag{3.19}$$

Under strong filtering both bias (if nonzero) and variance become proportional to the ENBW of the smoothing filter, which reduces in direct proportion with the averaging time (see next section). Eqs. (3.18), (3.19) thus imply that the estimator $\hat{\omega}_p$ is consistent and asymptotically unbiased, regardless of the spectrum shape. Moreover, neither bias nor variance of the estimator is affected by a nonzero imaginary part of the filter transfer funtions $A_i(\omega)$ (this is not necessarily true when the filtering is light). The condition for $\hat{\omega}_p$ to be unbiased for relatively short averaging times follows from Eq. (3.18),

$$\int d\omega G(\omega)\text{Re}\{A_2(\omega)\} \int d\omega G^2(\omega)\text{Re}\{A_1(\omega)\}\text{Re}\{A_2(\omega)\}$$
$$= \int d\omega G^2(\omega)\text{Re}^2\{A_2(\omega)\} \int d\omega \ G(\omega)\text{Re}\{A_1(\omega)\} \tag{3.20}$$

This equation is approximately satisfied when the spectrum is so narrow-band that both $\text{Re}\{A_1(\omega)\}$ and $\text{Re}\{A_2(\omega)\}$ changes little over its bandwidth. In the special case where the denominator weighting function $\text{Re}\{A_2(\omega)\}$ is constant (e.g., in mean or MS frequency estimation), the equation is satisfied for rectangular spectra.

Equations (3.18) and (3.19) are discussed in greater detail for some important special cases of the spectral weighting functions later in this paper.

3.3 Properties of the smoothing filter

The smoothing filters reduce the variance of the parameter estimate by averaging 'raw' estimates of the numerator and denominator over a time period equal to the duration of their impulse responses. This has the undesired side effect of slowing down the response of the estimator when the signal frequency is changing rapidly, e.g., in the case of Doppler signals from the human arterial system. The optimal smoothing filter is the one with the smallest ENBW for a given duration of its impulse response. If the duration of the impulse response is M samples (FIR filtering), the following relation holds,

$$W_b = 2\pi \frac{\sum_{k=1}^{M} b^2(k)}{\left(\sum_{k=1}^{M} b(k)\right)^2} \geq 2\pi \frac{\sum_{k=1}^{M} b^2(k)}{M\left(\sum_{k=1}^{M} b(k)\right)^2} = 2\pi \frac{1}{M} \tag{3.21}$$

The Schwarz inequality was used on the denominator. By inspection, equality is attained when all of the coefficients $\{b(k)\}$ are equal. The optimal shape of the smoothing filter impulse response is, therefore, rectangular, and its ENBW is inversely proportional to the duration of its impulse response.

A commonly used smoothing filter in multigated Doppler systems with discrete-time signal processing is a first-order recursive low-pass filter of the form

$$v(k+1) = a\, v(k) + u(k) \qquad 0 < a < 1 \tag{3.22}$$

where $\{u(k)\}$ is the input and $\{v(k)\}$ is the filtered sequence [13][16][17][19]. This filter has become popular because of its ease in implementation. Its impulse response is a decaying exponential,

$$b_r(k) = \begin{cases} a^k & k \geq 0 \\ 0 & \text{elsewhere} \end{cases} \tag{3.23}$$

The angular ENBW of the first-order recursive low-pass filter can be computed from (3.17). The result is

$$W_{b,r} = 2\pi \frac{1-a}{1+a} \tag{3.24}$$

The bandwidths of the recursive and the optimal smoothing filters are the same when the above expression is equal to $2\pi/M$. This is satisfied if

$$W_{b,r} = \frac{2\pi}{M} \qquad \Leftrightarrow \qquad a = \frac{M-1}{M+1} \simeq \frac{1}{(1+\frac{1}{M})^2} \tag{3.25}$$

where the latter approximation is valid when M is large. After M samples, the impulse response of the recursive filter has decayed to

$$\frac{(M-1)^M}{(M+1)^M} \simeq \frac{1}{[(1+\frac{1}{M})^M]^2} \simeq e^{-2} = 0.135 \qquad M \gg 1 \tag{3.26}$$

i.e., 13.5 percent of its initial value. This is a very small reduction in time resolution compared to that of an optimal filter with the same noise reduction properties.

4. ESTIMATORS OF SPECTRUM MEAN, MS BANDWIDTH, AND BANDWIDTH

4.1 Estimation of mean frequency

According to the definition (2.4), the general parameter estimator (3.4) becomes an estimator $\hat{\omega}_m$ of the mean frequency if its numerator coefficients are chosen equal to $\{a_{1m}(n)\}$, such that the corresponding spectral weighting function $Re\{A_{1m}(\omega)\}$ approximates the ideal sawtooth function

$$\begin{aligned} A_s(\omega) &= \omega \qquad && -\pi < \omega < \pi \\ A_s(\omega+2\pi) &= Re\{A_s(\omega)\} \qquad && \forall\ \omega \end{aligned} \tag{4.1}$$

The denominator weighting function is unity in mean frequency estimation, which yields only one nonzero denominator coefficient,

$$\{z_2(k)\} = \{a_{2m}(k)\} = \delta_{no} \tag{4.2}$$

where δ_{nk} is the Kronecker delta symbol. The ideal numerator coefficient set can be calculated by taking the inverse Fourier transform of $A_s(\omega)$ over the interval $(-\pi,\pi)$. This yields the doubly infinite series

$$a_s(n) = \frac{1}{2\pi} \int d\omega \, \omega e^{jn\omega} = \begin{cases} -j \frac{1}{n} (-1)^n & |n| > 0 \\ 0 & n = 0 \end{cases} \tag{4.3}$$

which are recognized as the coefficients of an ideal differentiator filter [17]. According to (3.8), the spectral weighting function does not change if the coefficient set is made one sided by setting

$$a_s'(n) = \begin{cases} 2\, a_s(n) & n > 0 \\ 0 & n \leq 0 \end{cases} \tag{4.4}$$

To form a practical estimator, the set $\{a_m(n)\}$ needs to be nonzero on a finite interval only. The series (4.4) decays slowly when n increases, so that an abrupt truncation after a small number of terms gives large errors in the spectral weighting function [17]. A better approach is to determine $\{a_m(n)\}$ directly, so that $Re\{A_m(\omega)\}$ is an optimal approximation to $A_s(\omega)$ according to some performance index. One criterion which has been used is minimum average of the squared error $|Re\{A_m(\omega)\}-\omega|^2$ over a specified interval $-P < \omega < P$, where $0 < P \leq \pi$ [17]; another is minimization of the peak fractional differentiation error $\max|(Re\{A_m(\omega)\}-\omega)/\omega|$ over a specified interval [18]. The latter method yields a peak fractional error equal to 1 percent over an interval that spans 84 percent of the Nyquist range when 8 nonzero coefficients are employed in (4.4).

Assume that the spectral weighting function is chosen as a good approximation to ω over the frequency range where $G(\omega)$ has spectral support. It follows then from (3.18) and (3.19) that under strong filtering, the following relations hold for the bias and variance,

$$Bias\{\hat{\omega}_m\} \simeq - W_b \frac{\int d\omega \, G^2(\omega)(\omega - \bar{\omega})}{(\int d\omega \, G(\omega))^2} \tag{4.5}$$

$$Var\{\hat{\omega}_m\} \simeq W_b \frac{\int d\omega \, G^2(\omega)(\omega - \bar{\omega})^2}{(\int d\omega \, G(\omega))^2} \tag{4.6}$$

The mean frequency estimate is unbiased for any spectrum that is symmetrical around its mean. Both bias (if nonzero) and variance are solely dependent on the spectrum shape; as long as aliasing does not occur, they do not change if a spectrum is translated along the frequency axis.

The above results are not surprising. Eqs. (4.5),(4.6) have previously been derived in the continuous-time domain by Gerzberg and Meindl, under the assumption of an ideal differentiator filter and a smoothing filter with a rectangular impulse response

[4]. It has also been shown previously that discrete-time estimation gives results that compare well with continuous-time estimation [18].

4.2 Adaptive mean frequency estimation

Fig. 4.1 shows a rectangular Doppler spectrum with bandwidth **B**, in the presence of additive white noise. The spectra are scaled such that the signal-to-noise ratio is **S**. The mean angular frequency of the composite signal/noise spectrum can be calculated from the definition formula (2.4). The result is

$$\bar{\omega} = \bar{\omega}_s \frac{S}{1 + S} \tag{4.7}$$

Therefore, an estimator of the true spectrum mean will produce a severely biased estimate of the signal mean frequency when the signal-to-noise ratio is low. According to (4.6), additional bias may be present for short averaging times, since the composite spectrum is not symmetrical around its mean.

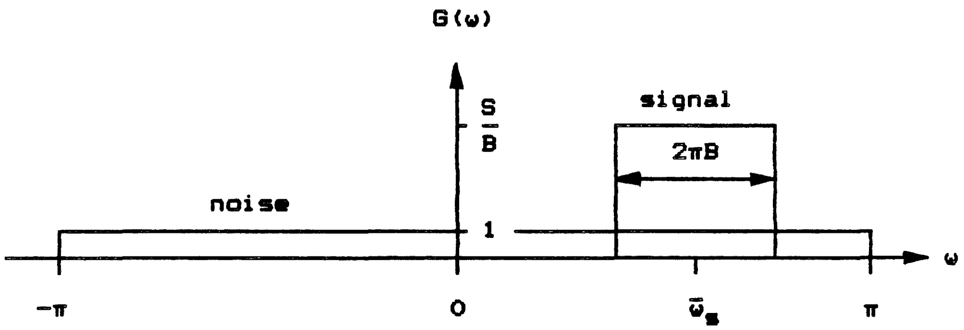

Fig. 4.1 Additive signal and white noise spectra.

There are several ways to correct for the bias when the signal-to-noise ratio is finite. Gerzberg has shown that if the mean frequency and the power of the noise is known or can be estimated, e.g., in time slots when there is no signal present, the contribution from the noise can be subtracted away from the numerator and the denominator of the mean frequency estimator [4]. When feasible, this technique greatly improves the noise immunity of the estimator. This approach has also been explored by Barber et al. [19].

An alternate approach is to employ an adaptive premixing of the signal [17][18], as shown in Fig. 4.2. The underlying philosophy is to shift the composite spectrum down to zero mean frequency prior to analysis. The lower integrator and the loop gain A_1 form an integral controller, while the upper integrator converts frequency to phase of the premixing signal. Equilibrium of the feedback loop is obtained when

$$\langle\hat{\omega}_z(k)\rangle = 0 \qquad \Longleftrightarrow \qquad \int d\omega\ G(\omega+\langle\hat{\omega}_{ma}\rangle)\mathrm{Re}\{A_m(\omega)\} = 0 \tag{4.8}$$

where the second form of the equation follows from (3.2) with $A_1 = A_m$, $A_2 = 1$, and $\omega_p = 0$. By changing variables of integration, the expected adaptive mean frequency estimate $\omega_{ma} = \langle\hat{\omega}_{ma}\rangle$ becomes the solution of the following integral equation,

$$0 = \int d\omega\ G(\omega)\mathrm{Re}\{A_m(\omega - \omega_{ma})\} \approx \int d\omega\ G(\omega)(\omega - \omega_{ma}) \tag{4.9}$$

where the second form is valid when $G(\omega)$ has spectral support in the frequency range where $\mathrm{Re}\{A_m(\omega)\} \approx \omega$. Note the difference from (3.2), in that a closed form solution does not exist for the left version of (4.9) in the general case.

The adaptive scheme has three favourable effects:

a) The mean frequency of the signal input to the estimator becomes zero. According to (4.7), any bias due to a finite signal to (white) noise ratio will then disappear. This can be realized from (4.8) also, because the integral of $G(\omega)\mathrm{Re}\{A_m(\omega)\}$ over the Nyquist interval does not change if a constant component is added to $G(\omega)$.

b) For spectra of the class shown in Fig. 4.1, the spectrum of the input signal to the estimator becomes symmetrical around its mean, even in the case of a finite signal-to-noise ratio. According to (4.6), any bias caused by a finite averaging interval then vanishes.

c) When the mean frequency of the signal is time varying, the feedback forms a tracking mechanism that allows for estimation of frequencies exceeding the Nyquist frequency. The tracking breaks down when the bandwidth of the signal exceeds unity (i.e., the sampling rate).

For the feedback scheme to work properly, it is important that the loop be made fast enough to track fast variations that may occur in the mean frequency of the Doppler signal from blood, e.g., during the upstroke of an arterial velocity waveforms. On the other hand, modulation effects that broaden the spectrum of the signal $\{\hat{z}(k)\}$ may occur if the loop is made so fast that the standard deviation of the mean frequency estimate $\hat{\omega}_{ma}$ becomes comparable to the bandwidth of the input signal. The loop gain must, therefore, be designed as a compromize between these two requirements. Note that when the feedback is efficient, the MS frequency of the sequence $\{\hat{z}(k)\}$ coincides with the MS bandwidth of the Doppler signal.

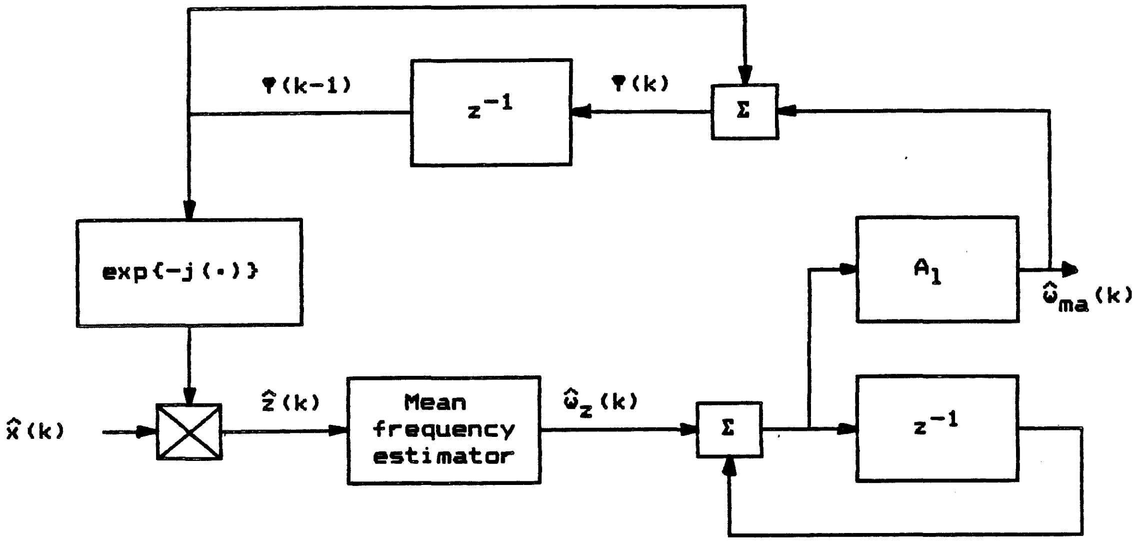

Fig. 4.2. Block schematics of adaptive mean frequency estimation.

4.3 Estimation of the mean square bandwidth

An estimator $\hat{V}_r$ of the mean-square angular bandwidth of the Doppler spectrum can be established from the definition formula (2.6),

$$\hat{V}_r = \hat{\omega}_r - \hat{\omega}_m^2 \qquad (4.10)$$

where $\hat{\omega}_m$ is the mean frequency estimate previously defined, and $\hat{\omega}_r$ is an estimate of the MS frequency. The general estimator (3.4) becomes an estimator of the latter variable if its numerator coefficients $\{a_{1r}(k)\}$ are chosen such that the corresponding weighting function $\mathrm{Re}\{A_{1r}(\omega)\}$ approximates the periodic parabolic function (compare with (2.5))

$$A_p(\omega) = \omega^2 \qquad -\pi < \omega < \pi$$

$$A_p(\omega+2\pi) = A_p(\omega) \tag{4.11}$$

As is the case in mean frequency estimation, the denominator weighting function is unity. Solving for the ideal numerator coefficients yields

$$a_p(n) = \frac{1}{2\pi} \int d\omega\, \omega^2 e^{jn\omega} = \begin{cases} \frac{2}{n^2}(-1)^n & |n| > 0 \\ \frac{\pi^2}{3} & n = 0 \end{cases} \tag{4.12}$$

These coefficients decay rapidly when n increases, and an estimator with a relatively small number of nonzero terms may, therefore, yield a weighting function that is a close approximation to ω^2 over the entire Nyquist range.

Eq. (4.10) can be rewritten on the form

$$\hat{v}_r - v_r \equiv (\hat{\omega}_r - \omega_r) - 2\omega_m(\hat{\omega}_m - \omega_m) - (\hat{\omega}_m - \omega_m)^2 \tag{4.13}$$

where v_r, ω_r, ω_m are the expectation values of the MS bandwidth and frequency, and the mean frequency in the case of an infinite averaging interval,

$$v_r = \omega_r - \omega_m^2 \simeq \omega_{rms}^2 - \bar{\omega}^2 = v \tag{4.14}$$

Eqs. (4.13) and (3.18) now yield directly

$$\mathrm{Bias}\{\hat{v}_r\} = \mathrm{Bias}\{\hat{\omega}_r\} - 2\omega_m\, \mathrm{Bias}\{\hat{\omega}_m\} - \mathrm{Var}\{\hat{\omega}_m\}$$

$$\simeq - W_b \frac{\int d\omega\, G^2(\omega)[(\mathrm{Re}\{A_r(\omega)-\omega_r) - (\mathrm{Re}\{A_m(\omega)\}-\omega_m)(\mathrm{Re}\{A_m(\omega)\}-3\omega_m)]}{[\int d\omega\, G(\omega)]^2}$$

$$\simeq - W_b \frac{\int d\omega\, G^2(\omega)[2(\omega-\bar{\omega})^2 - v]}{[\int d\omega\, G(\omega)]^2} \tag{4.15}$$

where the latter version is valid in the frequency range where $\mathrm{Re}\{A_r(\omega)\} \simeq \omega^2$ and $\mathrm{Re}\{A_m(\omega)\} \simeq \omega$. It is assumed that the smoothing filters for both $\hat{\omega}_m$ and $\hat{\omega}_r$ are identical. The above equation reveals that the estimate of the mean-square bandwidth is negatively biased, even when the estimates of the MS and the mean frequencies both are unbiased (as is the case when the spectrum is rectangular). This unfortunate effect is caused by the square operator in (4.10); when the variance of the mean frequency estimate is large, the center of the probability distribution of the squared mean frequency estimate becomes offset from the squared mean frequency. The bias becomes significant when the averaging time is so short that the variance of the mean frequency estimate becomes comparable to the MS bandwidth of the Doppler spectrum. Note that as long as aliasing does not occur, the bias is constant under a translation of the spectrum along the frequency axis.

Under strong filtering, the variance of the MS bandwidth estimate becomes (from (4.13), neglecting second order terms),

$$\mathrm{Var}\{\hat{v}_r\} \simeq \mathrm{Var}\{\hat{\omega}_r\} - 4\omega_m \,\mathrm{Cov}\{\hat{\omega}_r,\hat{\omega}_m\} + 4\omega_m^2 \,\mathrm{Var}\{\hat{\omega}_m\} \tag{4.16}$$

The first and the last term can be written up directly from (3.16) when the spectral weighting functions $\mathrm{Re}\{A_r(\omega)$ and $\mathrm{Re}\{A_m(\omega)\}$ have been chosen. The covariance term is somewhat more cumbersome to derive. Using the first order part of the linearization (3.11) for both the mean and the MS frequency estimation yields after some manipulations

$$\mathrm{Cov}\{\hat{\omega}_r,\hat{\omega}_m\} = \langle(\hat{\omega}_r-\omega_r)(\hat{\omega}_m-\omega_m)\rangle$$

$$\simeq \frac{1}{\langle z_2\rangle^2}\left[\mathrm{Cov}\{z_{1m},z_{1r}\}-\omega_m\mathrm{Cov}\{z_{1r},z_2\}-\omega_r\mathrm{Cov}\{z_{1m},z_2\}+\mathrm{Var}\{z_2\}\right] \tag{4.17}$$

Insertion into (3.16) and (4.16) and rearranging terms finally yields the variance of the MS bandwidth estimate under strong filtering,

$$\mathrm{Var}\{\hat{v}_r\} \simeq W_b \frac{\int d\omega\; G^2(\omega)[(\mathrm{Re}\{A_r(\omega)\}-\omega_r)-2\omega_m(\mathrm{Re}\{A_m(\omega)\}-\omega_m)]^2}{[\int d\omega\; G(\omega)]^2}$$

$$\simeq W_b \frac{\int d\omega\; G^2(\omega)[(\omega-\bar{\omega})^2 - v]^2}{[\int d\omega\; G(\omega)]^2} \tag{4.18}$$

where the latter version, as usual, is valid in the frequency interval where $\mathrm{Re}\{A_r(\omega)\} \simeq \omega^2$ and $\mathrm{Re}\{A_m(\omega)\} \simeq \omega$. As was the case for the bias, the variance does not change if a given spectrum is translated along the frequency axis.

4.4 Estimation of bandwidth

According to the definition (2.6), a rectangular spectrum with angular bandwidth **$2\pi B$** has the MS angular bandwidth

$$v = (2\pi)^2 \frac{B^2}{12} \tag{4.19}$$

Based on this model, (4.19) suggests the following estimator of spectrum bandwidth,

$$\hat{B}_r = \sqrt{12\hat{v}_r}/2\pi \qquad \Leftrightarrow \qquad B_r = \sqrt{12\, v_r}/2\pi \tag{4.20}$$

Linearization of the square root to the second order gives a quadratic approximation,

$$2\pi(\hat{B}_r - B_r) \approx \sqrt{\frac{3}{v_r}}\,(\hat{v}_r - v_r) - \sqrt{\frac{3}{16v_r^3}}\,(\hat{v}_r - v_r)^2 \tag{4.21}$$

Under strong filtering, the bias and standard deviation of the bandwidth estimate therefore becomes approximately

$$2\pi \mathrm{Bias}\{\hat{B}_r\} \approx \sqrt{\frac{3}{v_r}}\,\mathrm{Bias}\{\hat{v}_r\} - \sqrt{\frac{3}{16v_r^3}}\,\mathrm{Var}\{\hat{v}_r\} \tag{4.22}$$

$$(2\pi)^2 \mathrm{Var}\{\hat{B}_r\} \approx \frac{3}{v_r}\,\mathrm{Var}\{\hat{v}_r\} \tag{4.23}$$

Combining with (4.15) reveals that both terms in the expression for the bias give negative contributions for rectangular spectra; hence the bandwidth tends to be underestimated when the averaging time is short.

5. ESTIMATION OF SPECTRUM MEAN AND BANDWIDTH FROM THE CORRELATION FUNCTION AT ZERO AND UNITY LAG

5.1 Derivation of simplified time-domain expressions for the mean and MS bandwidth

The auto-correlation function for the Doppler signal at n samples lag can be written as

$$R(n) = \frac{1}{2\pi} e^{jn\omega_\varphi} \int d\omega \; G(\omega) e^{jn(\omega-\omega_\varphi)} \tag{5.1}$$

where ω_φ is an arbitrary frequency. Expanding the complex exponential of the integrand in series to the second order of its arguments yields the approximation

$$2\pi R(n) e^{-jn\omega_\varphi} \simeq \int d\omega G(\omega) + j\, n \int d\omega G(\omega)(\omega-\omega_\varphi) - \frac{n^2}{2} \int d\omega G(\omega)(\omega-\omega_\varphi)^2 \tag{5.2}$$

For a unity sample lag ($n = 1$), the imaginary part of this equation becomes

$$\frac{1}{2\pi} \int d\omega \; G(\omega)(\omega-\omega_\varphi) \simeq \mathrm{Im}\{R(1) e^{-j\omega_\varphi}\} = \frac{1}{2\pi} \int d\omega \; G(\omega) \sin(\omega-\omega_\varphi) \tag{5.3}$$

It follows that ω_φ becomes an approximation to the mean frequency if it is chosen such that the right integral becomes zero. This holds if

$$\omega_\varphi = \arg\{R(1)\} \qquad \Longleftrightarrow \qquad \int d\omega \; G(\omega) \sin(\omega-\omega_\varphi) = 0 \tag{5.4}$$

This suggests that the argument (phase angle) of the autocorrelation function at unity lag may serve as an estimator of the mean Doppler shift. This quantity was referred to as the **correlation-angle** in the introduction. An estimator of the correlation-angle is simple to implement, since only one sample of the auto-correlation function needs to be estimated. Eq. (5.4) indicates that $\omega_\varphi = \bar{\omega}$ when $G(\omega)$ is symmetrical around its mean. Moreover, according to (5.4), the correlation-angle does not change if a white noise component is added to the signal.

When the spectrum is narrow-band, the sine can be linearized to give

$$\int d\omega \; G(\omega)(\omega-\omega_\varphi) \simeq 0 \tag{5.5}$$

The linearization gives less than 10 percent peak error for bandwidths less than 0.5π. So long as the bandwidth of the Doppler spectrum does not exceed 25 percent of the sampling frequency, ω_φ becomes essentially identical to the mean frequency, regardless of the spectrum shape. However, a closer investigation shows that even for very wideband, assymetric spectra (triangular shape), the correlation-angle is a good approximation to the mean frequency.

Equating the real part of (5.2) with ω_φ as chosen in (5.4) and rearranging terms yields similarly an estimate of the mean-square bandwidth,

$$v_\varphi = 2\,\frac{R(0) - R(1)e^{-j\omega_\varphi}}{R(0)} = \frac{\int d\omega G(\omega) 4\sin^2(\frac{\omega - \omega_\varphi}{2})}{\int d\omega\, G(\omega)} \tag{5.6}$$

In the following, the quantity v_φ shall be referred to as the **correlation-decay** approximation to the MS bandwidth, motivated by the fact that it is twice the normalized distance between the magnitudes of $R(1)$ and $R(0)$. For spectra with bandwidths smaller than approx 36 percent of the sampling frequency the below approximation gives less than 10 percent error in the MS bandwidth estimate (and less than 5 percent in the RMS bandwidth),

$$v_\varphi \simeq \frac{\int d\omega\, G(\omega)(\omega-\omega_\varphi)^2}{\int d\omega\, G(\omega)} \tag{5.7}$$

This equation shows that the correlation-decay is an approximation to the second-order moment centered around ω_φ rather than the true spectrum mean. For most well-behaved spectra the correlation-angle is close to the mean frequency, so the correlation-decay is, therefore, a good approximation to the MS bandwidth-for narrow to medium bandwidth spectra.

5.2 Properties of the correlation-angle estimator

It follows from (5.4) that an estimator of the correlation-angle can be written as

$$\hat{\omega}_\varphi = \tan^{-1}\hat{\omega}_a \tag{5.8}$$

where $\hat{\omega}_a$ is the fraction

$$\hat{\omega}_a = \frac{z_{1\varphi}}{z_{2\varphi}} \tag{5.9}$$

The numerator and the denominator can both be written on the form (3.5),

$$z_{1\varphi} = \sum_k b(k)\ \mathrm{Im}\{\hat{x}^*(k)\hat{x}(k+1)\}$$

$$= \mathrm{Re}\{\sum_k \sum_n b(k) a_{1\varphi}(n)\hat{x}^*(k)\hat{x}(k-n)\} \tag{5.10}$$

$$z_{2\varphi} = \sum_k b(k)\ \mathrm{Re}\{\hat{x}^*(k)\hat{x}(k+1)\}$$

$$= \mathrm{Re}\{\sum_k \sum_n b(k)a_{2\varphi}(n)\hat{x}^*(k)\hat{x}(k-n)\} \qquad (5.11)$$

where the coefficients and the corresponding weighting functions are given as

$$a_{1\varphi}(n) = \begin{cases} j & n = -1 \\ 0 & \text{elsewhere} \end{cases} \quad \Leftrightarrow \quad \mathrm{Re}\{A_{1\varphi}(\omega)\} = \sin\omega \qquad (5.12)$$

$$a_{2\varphi}(n) = \begin{cases} 1 & n = -1 \\ 0 & \text{elsewhere} \end{cases} \quad \Leftrightarrow \quad \mathrm{Re}\{A_{2\varphi}(\omega)\} = \cos\omega \qquad (5.13)$$

Therefore, the argument $\hat{\omega}_a$ of the inverse tangent in (5.8) is an estimator of the class discussed in Section 3. The estimator described by (5.8)-(5.13) was referred to as the correlation-angle estimator in the introduction, and it has previously been investigated experimentally by Barber et al. [19].

Now assume that two sets of data $\{\hat{x}_1(k)\}$ and $\{\hat{x}_2(k)\}$ are available, the second set formed as a frequency shift transformation of the first,

$$\hat{x}_2(k) = \hat{x}_1(k)e^{jk\omega_o} \qquad (5.14)$$

Substitition into (5.8) - (5.11) then yields

$$\hat{\omega}_{\varphi 2} \equiv \hat{\omega}_{\varphi 1} + \omega_o \qquad (5.15)$$

This implies that the statistical properties of $\hat{\omega}_\varphi$ are solely determined by the shape of the Doppler spectrum; the stochastic fluctuations of the estimate are not affected by a change in mean frequency for a given spectrum.

It is interesting to compare the correlation-angle estimator to the 'true' mean frequency estimator in the feedback configuration outlined in Section 4.2. Eqs. (4.9) and (5.4) reveal that $\omega_\varphi = \omega_{ma}$ if the coefficients $\{a_m(n)\}$ of the mean frequency estimator are chosen according to (5.12). The instantaneous frequency estimator is therefore 'autoadaptive', in the sense that it in many respects behaves similar to the true mean frequency estimator in a feedback configuration. Eq. (5.15) is a manifestation of this property. For signals with continuously varying frequency contents (Doppler signal from arteries), it is, apparently, possible to track the evolution of the correlation-angle versus time, so that its range of variation can be extended beyond the Nyquist range $(-\pi,\pi)$.

Note that a better approximation to (5.2) can be obtained by including higher order central moments of the spectrum. If two lags of the correlation function are known, e.g., the additional information may be used to eliminate errors from the third and fourth order central moments. Wideband autoadaptive estimators for the mean frequency and MS bandwidth may be derived in that way.

Approximate statistical properties of the instantaneous frequency estimator can be derived by linearization of (5.8) and (5.9) around ω_φ. This yields

$$\hat{\omega}_\varphi - \omega_\varphi \simeq \cos^2\omega_\varphi \; (\hat{\omega}_a - \omega_a) + \cos\omega_\varphi \sin\omega_\varphi \; (\hat{\omega}_a - \omega_a)^2$$

$$\simeq \hat{\omega}_a - \omega_a \qquad\qquad |\omega_\varphi| << 1 \qquad\qquad (5.16)$$

where, as usual, ω_a is the expected value of $\hat{\omega}_a$ when the averaging interval is infinite, and the latter approximation is valid when $|\omega_\varphi|$ is small. According to (5.15), neither variance nor bias are affected of a change of center frequency for a given spectrum. The variance and the bias of $\hat{\omega}_\varphi$ for the spectrum $G(\omega)$, therefore, coincide with the same quantities of $\hat{\omega}_a$ for the spectrum $G(\omega+\omega_\varphi)$. With a proper shift of integration variables, the bias and the variance can then be written up directly from (3.18) - (3.19), with weighting functions as specified in (5.12) and (5.13). This yields

$$\mathrm{Bias}\{\hat{\omega}_\varphi\} \simeq -W_b \frac{\int d\omega \; G^2(\omega)\cos(\omega-\omega_\varphi)\sin(\omega-\omega_\varphi)}{[\int d\omega \; G(\omega)\cos(\omega-\omega_\varphi)]^2}$$

$$= -W_b \frac{\int d\omega \; G^2(\omega)\sin 2(\omega-\omega_\varphi)}{2|\int d\omega \; G(\omega)e^{j(\omega-\omega_\varphi)}|^2} \qquad (5.17)$$

$$\mathrm{Var}\{\hat{\omega}_\varphi\} \simeq W_b \frac{\int d\omega \; G^2(\omega)\sin^2(\omega-\omega_\varphi)}{|\int d\omega \; G(\omega)e^{j(\omega-\omega_\varphi)}|^2} \qquad (5.18)$$

The change of denominators between the two different versions of (5.17) follows because of the relation (5.4).

The correlation-angle estimator becomes unbiased when the spectrum is symmetrical around ω_φ. For narrow-band spectra, the trigonometrical functions in (5.17) and (5.18) can be expanded in series to the first order of their arguments. The equations then coincide with the corresponding expressions for the 'true' mean frequency estimator ((4.5) and (4.6)).

5.3 Properties of the correlation-decay estimator

An estimator of the correlation-decay can be written up from (5.6),

$$\hat{v}_\varphi = 2\,\frac{\hat{R}(0) - \hat{R}(1)e^{-j\hat{\omega}_\varphi}}{\hat{R}(0)} = 2\,\frac{\hat{R}(0) - |\hat{R}(1)|}{\hat{R}(0)} \tag{5.20}$$

where the autocorrelation estimates can be formed in analogy with (3.5). This estimator has previously been used in a commercially available flow-map system [24]. The question that remains to be answered is how the performance of this simple estimator compares to that of the 'true' mean-square bandwidth estimator discussed in Section 4.2. Using the technique that led to (5.15), it is straightforward to show that also $\hat{v}_\varphi$ is auto-adaptive; its stochastic properties remain unchanged under a shift of mean frequency for a given signal. It is, therefore, sufficient to study the estimator for spectra that satisfy $\omega_\varphi = 0$. In this case, the numerator of (5.20) can be approximated with

$$\hat{R}(0) - |\hat{R}(1)| \simeq \hat{R}(0) - \mathrm{Re}\{\hat{R}(1)\}\left[\,1 + \frac{\mathrm{Im}\{\hat{R}(1)\}^2}{2\,\mathrm{Re}\{\hat{R}(1)\}^2}\,\right]$$

$$\simeq R(\hat{0}) - \mathrm{Re}\{\hat{R}(1)\} \qquad \mathrm{Im}\{\hat{R}(1)\} << \mathrm{Re}\{\hat{R}(1)\} \tag{5.21}$$

where the approximation is valid under strong filtering. Hence, the properties of the estimator (5.20) for a signal with spectrum $G(\omega)$ coincide with those of an estimator with the simpler numerator (5.21) for a signal with the spectrum $G(\omega+\omega_\varphi)$. The latter estimator is on the standard form (3.5), with coefficients and spectral weighting functions given as

$$a_1(n) = \begin{cases} 2 & n = 0 \\ -2 & n = -1 \\ 0 & \text{elsewhere} \end{cases} \quad \Longleftrightarrow \quad \mathrm{Re}\{A_1(\omega)\} = 4\sin^2\frac{\omega}{2} \tag{5.22}$$

$$a_2(n) = \delta_{n0} \quad \Longleftrightarrow \quad \mathrm{Re}\{A_2(\omega)\} = 1 \tag{5.23}$$

It follows immediately that under strong filtering, the following relations hold,

$$\text{Bias}\{\hat{v}_\varphi\} \simeq - W_b \frac{\int d\omega\, G^2(\omega)\,(4\sin^2(\frac{\omega-\omega_\varphi}{2}) - v_\varphi)}{[\int d\omega\, G(\omega)]^2} \tag{5.24}$$

$$\text{Var}\{\hat{v}_\varphi\} \simeq W_b \frac{\int d\omega\, G^2(\omega)\,[4\sin^2(\frac{\omega-\bar{\omega}_\varphi}{2}) - v_\varphi)^2}{[\int d\omega\, G(\omega)]^2} \tag{5.25}$$

In its linearized form, the expression for the variance becomes equivalent to the corresponding expression for $\hat{v}_r$ (Eq. (4.18)). This is, however, not the case for the bias. Unlike $\hat{v}_r$, the estimator $\hat{v}_\varphi$ becomes completely unbiased in the case of rectangular spectra. The linearized expression for the bias is identical to the bias of the MS frequency estimate alone (the first term in (4.12)).

5.4 Estimation of bandwidth

The bandwidth may also be estimated on the basis of the simplified MS bandwidth estimation scheme. From direct analogy with (4.20), this estimator becomes

$$\hat{B}_\varphi = \sqrt{12\hat{v}_\varphi}/2\pi \qquad \Leftrightarrow \qquad B_\varphi = \sqrt{12\, v_\varphi}/2\pi \tag{5.26}$$

Under strong filtering, the bias and standard deviation of the bandwidth estimate therefore become

$$2\pi\text{Bias}\{\hat{B}_\varphi\} \approx \sqrt{\frac{3}{v_\varphi}}\,\text{Bias}\{\hat{v}_\varphi\} - \sqrt{\frac{3}{16v_\varphi^3}}\,\text{Var}\{\hat{v}_\varphi\} \tag{5.27}$$

$$(2\pi)^2\text{Var}\{\hat{B}_\varphi\} \approx \frac{3}{v_\varphi}\,\text{Var}\{\hat{v}_\varphi\} \tag{5.28}$$

6. NUMERICAL COMPARISONS BETWEEN THE ESTIMATORS

6.1 Mean frequency estimation

A comparison between the mean frequency and the correlation-angle estimators has been performed for signals with specified spectra and signal-to-noise ratios. For this purpose, the spectrum model in Fig. 4.2 was used, i.e. rectangular spectra with bandwidth B and signal-to-noise ratio S. It was assumed that the averaging filters had rectangular impulse responses of M samples duration.

It has previously been shown that the correlation-angle estimator yields an unbiased estimate of the mean angular Doppler frequency for spectra of the type shown in Fig. 4.2. According to (4.7) and (4.5), the mean frequency estimator will give more than 50 percent underestimation for $S = 1$. This bias vanishes entirely if the adaptive scheme is used.

Eqs. (3.17),(4.6) and (5.18) yield the following results for the variances, valid under strong filtering ($MB >> 1$),

$$M \, \mathrm{Var}\{\hat{f}_m\} = M \, \mathrm{Var}\{\hat{\omega}_m/2\pi\} = \frac{S^2B + 2SB^2 + 1}{12(1 + S)^2} \tag{6.1}$$

$$M \, \mathrm{Var}\{\hat{f}_\varphi\} = M \, \mathrm{Var}\{\hat{\omega}_\varphi/2\pi\} = \frac{(S^2 + 2SB)(B - \frac{1}{2\pi}\sin 2\pi B) + B^2}{8 \, S^2 \sin^2 \pi B} \tag{6.2}$$

The standard deviations of the estimates are plotted versus bandwidth in Fig. 6.1 for $S = \infty$ (noiseless case) and $S = 1$. The plots show that the mean frequency estimator has a much smaller variance than the correlation-angle estimator when $B > 0.5$; its noise immunity is therefore superior also. The reason for the difference is that the fractional uncertainty of the denominator of $\hat{\omega}_\varphi$ becomes larger when its expected value is reduced; this effect enters in the denominator of (5.18), which is recognized as the squared magnitude of the correlation function at unity lag. This quantity decreases rapidly when the bandwidth increases.

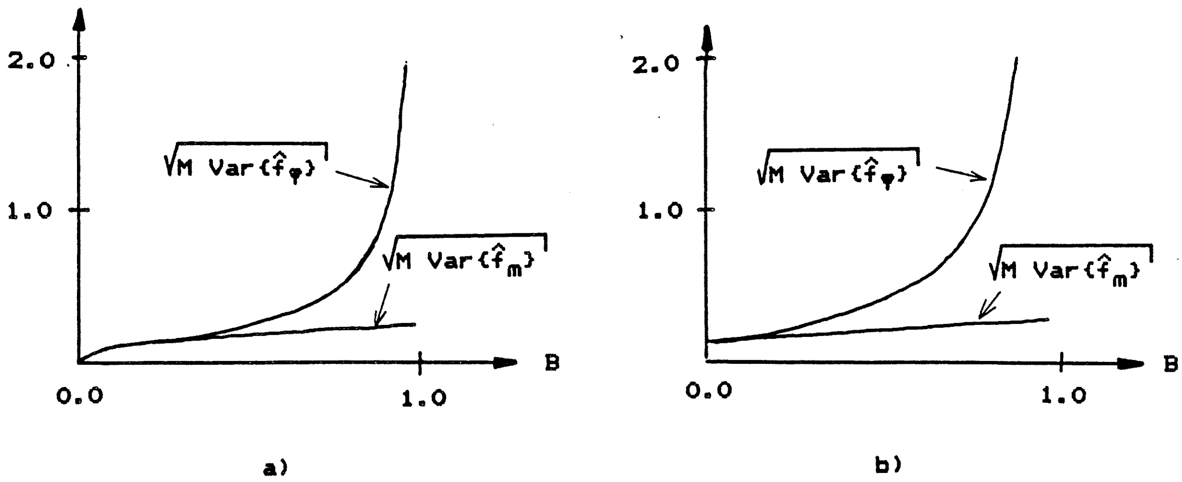

Fig. 6.1 Standard deviations of mean frequency and correlation-angle estimators in units of $\sqrt{M}$, plotted vs. signal bandwidth.

a) Noiseless case.

b) S/N = 0 dB

6.2 Bandwidth estimation

A corresponding comparison has been done also for the bandwidth estimators. The following results have been derived for B_r and B_φ,

$$B_r = \sqrt{\frac{(SB^2 + 1)}{S + 1}} \tag{6.3}$$

$$B_{\varphi} = \sqrt{\frac{12[S(1 - \frac{1}{\pi B}\sin \pi B) + 1]}{2\pi^2(1 + S)}} \tag{6.4}$$

Note that the above results, as well as all of the subsequent results for the 'true' bandwidth estimator $\hat{B}_r$, are valid only when one of the two following conditions are met,

a) both $\hat{\omega}_m$ and $\hat{\omega}_r$ are estimated from the translated signal $\{\hat{z}(k)\}$ in the adaptive scheme in Fig. 4.2;

b) noiseless case with mean frequency so small that aliasing does not occur (i.e, $|\bar{F} + 0.5B| \leq 0.5$).

Eqs. (6.3),(6.4) are plotted in Fig. 6.2 for the noiseless case and when S = 10 (S/N = 10 dB). The correlation-decay estimator $\hat{B}_{\varphi}$ gives some underestimation for very wide-band signals; its maximum output is 0.78B. The minimum signal bandwidth that can be resolved is determined by the signal-to-noise ratio. Consequently, both $\hat{B}_r$ and $\hat{B}_{\varphi}$ become very different from the bandwidth of the Doppler signal when the signal-to-noise ratio is low and the signal is narrow-band.

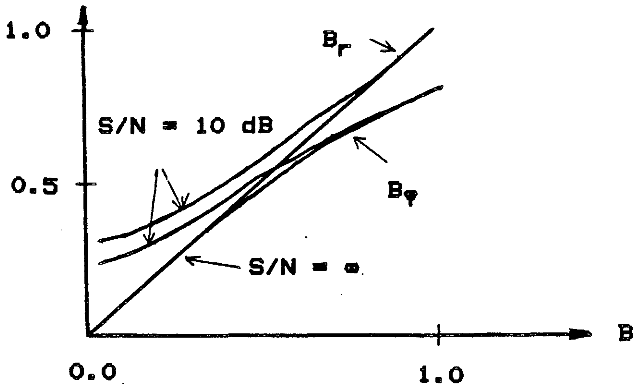

Fig. 6.2 Expectation values of bandwidth estimates for an infinite averaging interval, as a function of the true signal bandwidth B.

When the averaging interval is short, $\hat{B}_r$ and $\hat{B}_{\varphi}$ become biased estimators of B_r and B_{φ}, respectively. In the noiseless case, the following result is obtained from (4.18) and (4.22),

$$\mathrm{Bias}\{B_r\} = -0.6\,\frac{1}{M} \tag{6.5}$$

The bias is constant, regardless of B. However, the above relation is valid only under strong filtering, which requires

$MB >> 1$. The bias is then always small compared to the bandwidth itself.

The same calculation has been carried out also for the bias of $\hat{B}_\varphi$. For small bandwidths its bias is $-0.1/M$, decreasing to approx. $-0.05/M$ when B approaches unity. The reason why the bias of $\hat{B}_r$ is so much larger is the squaring of the mean frequency estimate.

The variances of the bandwidth estimators follow from (4.23) and (5.27). In the noiseless case, the results are

$$M \, Var\{\hat{B}_r\} = \frac{B}{5} \tag{6.6}$$

$$M \, Var\{\hat{B}_\varphi\} =$$

$$\frac{6}{(2\pi)^2 B} \left[\frac{\frac{3}{2} - \frac{2}{\pi B} \sin \pi B + \frac{1}{4\pi B} \sin 2\pi B}{1 - \frac{1}{\pi B} \sin \pi B} - (1 - \frac{1}{\pi B} \sin \pi B)\} \right] \tag{6.7}$$

The corresponding expressions for a finite signal-to-noise ratio have been omitted, as they are complicated and give little additional insight.

The standard deviations of the bandwidth estimates are plotted versus signal bandwidth in Fig. 6.3, together with the corresponding quantities when S/N = 10 dB. The simple estimator has a lower variance for large bandwidths and/or low signal-to-noise ratio. On the other hand, its mean is smaller in these situations, so if the fractional standard deviations of the estimators are compared (ratio between standard deviation and mean), the difference between the estimators becomes smaller. Nevertheless, the simple estimator has a somewhat better noise immunity than the full-bandwidth estimator. This is not surprising, as its spectral weighting function is considerably more narrow-band than the quadratic one.

Note that the variances of the both estimates increase with decreasing signal bandwidth for small signal-to-noise ratios. The reason is the large derivative of square root in (4.20), which, for small values of its argument, maps small fractional fluctuations in the MS bandwidth estimate to larger fractional fluctuations in the bandwidth estimate.

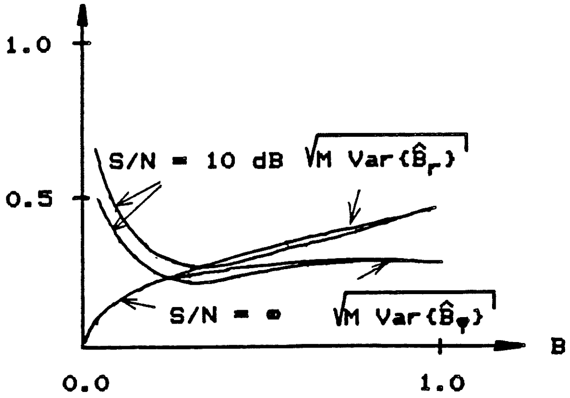

Fig. 6.3 Standard deviation of bandwidth estimates in units of $\sqrt{M}$ in the noiseless case and when S/N = 10 dB.

7. COMPARISONS BETWEEN THE INSTANTANEOUS FREQUENCY AND THE CORRELATION-ANGLE

It is interesting to compare the correlation-angle estimator to a scheme that averages the discrete-time instantaneous frequency. The latter estimator has been investigated by Angelsen and Kristoffersen [15] and Hoeks [16]. Using a basic result from [22], it was shown that that the probability distribution of the discrete-time instantaneous frequency is

$$p(\omega_i) = D\,h(A) \qquad -\pi + w_o < \omega_i \le \pi + w_o \tag{7.1}$$

where w_o is the interval offset previously discussed in Section 2, and $h(A)$ is

$$h(A) = \frac{\sqrt{(1 - A^2)} + A(\pi - \cos^{-1}A)}{2\pi\,(1 - A^2)^{1.5}} \tag{7.2}$$

The quantities A and D are functions of the correlation function at unity lag,

$$A = \left[R_{xx}(1)\cos\omega_i + R_{xy}(1)\sin\omega_i\right]/R_{xx}(0) \qquad -1 \le A \le 1 \tag{7.3}$$

$$D = \left|1 - \frac{R_{xx}^2(1)}{R_{xx}^2(0)} - \frac{R_{xy}^2(1)}{R_{xx}^2(0)}\right| \tag{7.4}$$

The quantities $R_{xx}(\cdot)$, $R_{xy}(\cdot)$ are the auto- and cross-correlation function of the quadrature components $\{x(k)\}$, $\{y(k)\}$ of

$\{\hat{x}(k)\}$. For a complex Gaussian process, the following relation holds,

$$R(k) = 2(R_{xx}(k) + j\ R_{xy}(k)) \tag{7.5}$$

Consequently, the variable A in (7.1) can be rewritten as

$$A = \frac{\mathrm{Re}\{R(1)e^{-j\omega_i}\}}{\mathrm{Re}\{R(0)\}} \tag{7.6}$$

It can be shown that the function $h(\cdot)$ is a monotonically increasing function of its argument. The mode of the distribution $p(\omega_i)$ is, therefore, the angular frequency where A is maximum. From inspection of (7.6), this occurs when

$$\mathrm{mode}\{p(\omega_i)\} = \arg\{R(1)\} = \omega_\varphi \tag{7.7}$$

Therefore, the expectation value of the correlation-angle estimator coincides with the mode of the distribution of the discrete-time instantaneous frequency.

Eq. (7.6) shows that $A(\omega_{im}+\omega) = A(\omega_{im}-\omega)$. Hence, the probability distribution for the instantaneous frequency is symmetric around its mode, i.e

$$p(\omega_\varphi + \omega) = p(\omega_\varphi - \omega) \qquad -\pi < \omega \le \pi \tag{7.8}$$

It is also well known that for narrow-band spectra, the distribution of the instantaneous frequency is considerably wider than the spectral density [16].

Hoeks proposed an estimator that averages the discrete-time approximation to the instantaneous frequency, Eq. (2.7). In its basic version, it can be written as

$$\hat{\omega}_{im} = \Sigma\ b(k)\ (\arg\{\hat{x}(k)\} - \arg\{\hat{x}(k-1\})) \tag{7.9}$$

One problem with this scheme is to determine the interval offset w_o. According to (7.8), the following relation holds when $w_o = \omega_\varphi$,

$$\langle\hat{\omega}_{im}\rangle = \omega_\varphi \tag{7.10}$$

If the Brandestini scheme is employed ($w_o = 0$), (7.8) indicates severe errors due to mapping or 'aliasing' of the instantaneous frequency in the cases when the ω_φ is significantly different from zero and the width of $p(\omega_i)$ is large. This effect has been quantified previously [15]. Hoeks overcame this limitation by selecting the interval offset adaptively, i.e

$$w_o(k+1) = \hat{\omega}_{im}(k) \tag{7.11}$$

where $\hat{\omega}_{im}(k)$ was estimated on the basis of a running average of the instantaneous frequency. He demonstrated that the adaptive scheme worked well for S/N's above −6 dB and signal bandwidths less than one half of the sampling frequency.

One question that remains to be answered is how the variance of the averaged instantaneous frequency compares to that of the correlation-angle and the mean frequency estimators. Hoeks simulated the instantaneous frequency estimator on a computer, using signals with rectangular spectra of bandwidths 0.01, 0.1, and 0.3, and different S/N's [16]. In two different sets of simulations, he smoothed the instantaneous frequency with a recursive filter of the type (3.24), using the feedback coefficient $a_1 = 15/16$ and $a_2 = 31/32$, respectively. He concluded that $Var\{\hat{\omega}_{im}\}$ obeyed the relation (4.6) for signal-to-noise ratios above 10 dB; for lower S/N's it was considerably larger. However, Hoeks conclusions were based on the assumption that the angular bandwidths of his smoothing filters were $W_{b1} = 2\pi/16$ and $W_{b2} = 2\pi/32$, whereas the correct ENBWs according to (3.24) were nearly one half of this magnitude. It follows then from his results that the variance of the averaged instantaneous frequency estimator is twice that of the true mean frequency estimator for signals with bandwidths less than 0.3 and S/N's higher than 10 dB. This seems not unlikely, as the probability distribution of the instantaneous frequency is much wider than the power spectrum in these cases. On the other hand, the distribution of the instantaneous frequency and the power spectrum coincides in the case of white noise, so it is harder to explain the deteriorating performance of the instantaneous frequency estimator for low S/N's. The increased variance in the latter situation was probably caused by the adaptive determination of w_o.

The variance increase of the instantaneous frequency estimator for low S/N's was not quite as bad as that predicted in this paper for the correlation-angle estimator: A detailed comparison to Hoeks results reveals that the instantaneous frequency estimator performs slightly better than the correlation-angle estimator for S/N = −10 dB.

8. CONCLUDING REMARKS

An important result of this paper is that the correlation-angle estimator has a higher variance than the adaptive mean frequency estimator for wide-band signals or/and poor signal-to-noise ratios. This explains why Barber et al. [19] got better results with their time-domain mean frequency estimator than with the correlation-angle estimator for the lowest Doppler shifts, where their system had the smallest signal-to-noise ratio. The reason why they got better results with the correlation-angle for higher frequencies is harder to explain. Two reasons seem possible: Their time-domain mean frequency estimator was different than the corresponding detector investigated in this paper; it was based on only one lag of the correlation function, and it must be expected to deteriorate for Doppler shifts larger than about one third of the sampling frequency. Secondly, they did not use the adaptive method to correct for bias under poor signal-to-noise.

Most of the results derived in this paper are valid for strong filtering only, a condition which is rarely met in real-time flow mapping. However, there is no reason to believe that the individual ranking of the estimators will be very different in the case of short averaging intervals.

The low bias of the correlation-decay bandwidth estimator for short averaging intervals makes it well suited for flow-map applications. Its primary feature is that the MS bandwidth is estimated directly, not as the difference between two high-variance quantities, as is the case with the 'ordinary' estimator. Bias that occurs because of the squaring of the mean frequency in the ordinary estimator is, therefore, avoided.

It should finally be mentioned that there exists a number of ways to simplify the calculations in the estimation of correlations between Gaussian processes. Hard limiting of one or even both of the processes may reduce the hardware complexity strongly in a high-speed implementation. The tradeoffs involved are hardware complexity versus an increased variance of the correlation estimate [5][18].

REFERENCES

[1] W. R. Brody, "Theoretical analysis of the ultrasonic blood flowmeter," Ph. D. dissertation, Stanford Electronics Laboratories, Stanford University, CA, 1971, Tech. Rep. 4958-1.

[2] M. G. J. Arts and J. M. J. G. Roevros, "On the instantaneaous measurements of blood flow by ultrasonic means," **Med. Biol. Eng.**, vol. 10, pp. 23-24, 1972.

[3] R. F. Pawula, "Analysis of the center frequency of a power spectrum," **IEEE Trans. Inform. Theory**, vol. IT-14, pp. 669-675, Sept. 1968.

[4] L. Gerzberg and J. D. Meindl, "Power spectrum centroid detection for Doppler systems applications," **Ultrason. Imaging**, vol. 2, pp. 232-261, 1980.

[5] B. A. J. Angelsen, "Instantaneous frequency, mean frequency, and variance of mean frequency estimators for ultrasonic blood velocity Doppler signals," **IEEE Trans. Biomed. Eng.**, vol. BME-28, No. 11., Nov. 1981.

[6] R. S. Reneman, H. E. Clarke, N. Simmons, and M. P. Spencer, "In vivo comparison of electromagnetic and Doppler flowmeters: With special attention to the processing of the analog Doppler signal," **Card. Res.**, vol. VII, pp. 557-556, 1973.

[7] B. A. J. Angelsen, "Analog estimation of the maximum frequency of Doppler spectra in ultrasonic blood velocity measurements," Dep. Eng. Cybern., Norwegian Inst. Tech., Trondheim, Norway, Rep. 76-21-W, 1976.

[8] K. Namekawa, C. Kasai, M. Tsukamoto, and A. Koyano, "Real-time bloodflow imaging system utilizing auto-correlation techniques," in **Proc. Ultrasound '82**, R. A. Lerski, P. Morley (eds.). Pergamon Press, 1982, pp. 203-208.

[9] R. Omoto, ed., **Color atlas of real-time two-dimentional Doppler echocardiography**, Tokyo: Shindan-To-Chiryo Co., Ltd, 1984, p. 11.

[10] M. I. Skolnik, **Introduction to Radar Systems.** New York: McGraw-Hill, 1962, pp. 113-154.

[11] P.A. Grandchamp, "A novel pulsed directional Doppler velocimeter; The phasedetection profilometer," in **Proc. 2nd Eur. Congr. Ultrasonics. Med.** Amsterdam, The Netherlands: Exerpta Medica, 1975, pp. 137-143.

[12] M. Brandestini, "Applications of the phase detection principle in a transcutaneous velocity profile meter," in **Proc. 2nd Eur. Congr. Ultrasonics. Med.** Amsterdam, The Netherlands: Exerpta Medica, 1975, pp. 144-152.

[13] -, "Signalverarbeitung in perkutanen Ultraschall Doppler Blutfluss Messgeräten," Eidgenössischen Technischen Hochscule, Ph.D. Dissertation ETH 5711, Zürich, Switzerland, 1976.

[14] -, "Topoflow - A full range Doppler velocity meter," **IEEE Trans. Sonics Ultrason.**, vol. SU-25, pp. 287-293, 1978.

[15] B. A. J. Angelsen and Kjell Kristoffersen, "On ultrasonic MTI measurements of velocity profiles in blood flow," **IEEE Trans. Biomed. Eng.**, vol. BME-26, pp. 665-671, no. 12, Dec. 1979.

[16] A. P. G. Hoeks, "On the development of a multi-gate pulsed Doppler system with serial data processing," Ph.D. dissertation, Univ. Maastricht, The Netherlands, 1982.

[17] B. A. J. Angelsen and Kjell Kristoffersen, "Discrete time estimation of the mean Doppler frequency in ultrasonic blood velocity measurements," **IEEE Trans. Biomed. Eng.**, vol. BME-30, pp. 207-214, Apr. 1983.

[18] K. Kristoffersen, B. A. J. Angelsen, "A comparison between mean frequency estimators for multigated Doppler systems with serial signal processing," **IEEE Trans. Biomed. Eng.**, vol. BME-32, Sept. 1985.

[19] W. D. Barber, J. W. Eberhard, S. G. Carr, "A new time domain technique for velocity measurements using Doppler ultrasound," **IEEE Trans. Biomed. Eng.**, vol. BME-32, pp. 213-229, March 1985.

[20] B. A. J. Angelsen, "A theoretical study of the scattering of ultrasound from blood," **IEEE Trans. Biomed. Eng.**, vol. BME-27, pp. 61-67, Feb. 1980.

[21] A. Papoulis, **"Probability, random variables, and stochastic processes"**. New York: McGraw-Hill, 1965, p. 487.

[22] W. B. Davenport, Jr., and W. L. Root, **"An introduction to the theory of random signals and noise"**. New York: McGraw-Hill, 1958, p. 164.

[23] H. L. Van Trees, **"Detection, estimation, and modulation theory, Part III"**. New York: John Wiley, 1971.

[24] C. Kasai, K. Namekawa, A. Koyano, R. Omoto, "Real-Time Two-Dimensional Blood Flow Imaging Using an Autocorrelation Technique," **IEEE Trans. Sonics Ultras.**, vol. SU-32, pp. 458-464, May 1985.

APPENDIX

The following formula holds for the 4th order moment of the jointly Gaussian complex processes q,r,s,t [23],

$$\langle q^* r s^* t\rangle = \langle q^* r\rangle\langle s^* t\rangle + \langle q^* t\rangle\langle s^* r\rangle \tag{A1}$$

The above relation can be used to calculate the covariance between two filtered cross correlation function estimates as defined in (3.5). The covariance becomes

$$4\,\mathrm{Cov}\{z_1,z_2\} = 4\,\langle (z_1 - \langle z_1\rangle)(z_2 - \langle z_2\rangle)\rangle$$

$$\begin{aligned}
= \sum_k \sum_l \sum_m \sum_n b(k)b(l)\{&[a_1(n)\hat{x}^*(k)\hat{x}(k-n) + a_1^*(n)\hat{x}(k)\hat{x}^*(k-n)]\\
&[a_2^*(m)\hat{x}(l)\hat{x}^*(l-m) + a_2(m)\hat{x}^*(l)\hat{x}(l-m)]\\
- [a_1(n)R(-n)+a_1^*(n)R^*(-n)]R(m)][a_2(m)R(-m)+a_2^*(m)R^*(-m)]\}
\end{aligned}$$

$$\begin{aligned}
= \sum_k \sum_l \sum_m \sum_n b(k)b(l)\{&a_1(n)a_2^*(m)\langle\hat{x}^*(k)\hat{x}(k-n)\hat{x}(l)\hat{x}^*(l-m)\rangle\\
&+ a_1(n)a_2(m)\langle\hat{x}^*(k)\hat{x}(k-n)\hat{x}^*(l)\hat{x}(l-m)\rangle\\
&+ a_1^*(n)a_2^*(m)\langle\hat{x}(k)\hat{x}^*(k-n)\hat{x}(l)\hat{x}^*(l-m)\rangle\\
&+ a_1^*(n)a_2(m)\langle\hat{x}(k)\hat{x}^*(k-n)\hat{x}^*(l)\hat{x}(l-m)\rangle\\
- [a_1(n)R(-n) + a_1^*(n)R^*(-n)][a_2(m)R(-m) + a_1^*(m)R^*(-m)]\}
\end{aligned}$$

$$\begin{aligned}
= \sum_k \sum_l \sum_m \sum_n b(k)b(l)\{&a_1(n)a_2^*(m)\{R(l-k)R^*(l-k-m+n)\\
&+ a_1(n)a_2(m)R(l-k-m)R^*(l-k+n)\\
&+ a_1^*(n)a_2^*(m)R(l-k+n)R^*(l-k-m)\\
&+ a_1^*(n)a_2(m)R(l-k-m+n)R^*(l-k)\}
\end{aligned} \tag{A.2}$$

This equation can be transformed to the frequency domain by first rewriting the autocorrelation function as the inverse Fourier transform of the power spectrum, and then interchanging the order of summations and integrations. This yields

$$4\,\mathrm{Var}\{N_p\} =$$

$$\sum_k \sum_l \sum_m \sum_n b(k)b(l)\int d\omega \int d\Omega\; G(\Omega)G(\omega)\{a_1(n)a_2^*(m)e^{j\omega(l-k)}e^{-j\Omega(l-k-m+n)}$$
$$+ a_1(n)a_2(m)e^{j\omega(l-k-m)}e^{-j\Omega(l-k+n)}$$
$$+ a_1^*(n)a_2^*(m)e^{j\omega(l-k+n)}e^{-j\Omega(l-k-m)}$$
$$+ a_1^*(n)a_2(m)\; e^{j\omega(l-k+n-m)}e^{-j\Omega(l-k)}\}$$

$$= \int d\omega \int d\Omega G(\Omega)G(\omega)\sum_k b(k)e^{-jk(\omega-\Omega)}\sum_l b(l)e^{jl(\omega-\Omega)}\{\sum_n a_1(n)e^{-jn\Omega}\sum_m a_2^*(m)e^{jm\Omega}$$
$$+ \sum_n a_1(n)e^{-jn\Omega}\sum_m a_2(m)e^{-jm\omega} + \sum_n a_1^*(n)e^{jn\omega}\sum_m a_2^*(m)e^{jm\Omega}$$
$$+ \sum_n a_1^*(n)e^{jn\omega}\sum_m a_2(m)e^{-jm\omega}\}$$

$$= \int d\omega \int d\Omega\; G(\Omega)G(\omega)\,|B(\omega-\Omega)|^2\{A_1(\Omega)A_2^*(\Omega) + A_1(\Omega)A_2(\omega)$$
$$+ A_1^*(\omega)A_2^*(\Omega) + A_1^*(\omega)A_2(\omega)\}$$

$$= \int d\omega \int d\Omega\; G(\omega)G(\omega-\Omega)\,|B(\Omega)|^2\{A_1(\omega-\Omega)A_2^*(\Omega) + A_1(\omega-\Omega)A_2(\omega)$$
$$+ A_1^*(\omega)A_2^*(\omega-\Omega) + A_1^*(\omega)A_2(\omega)\} \qquad (A.3)$$

The final version was formed using the substitution $\Omega := \omega - \Omega$.

RAPPORTNUMMER

STF48 A84030

TILGJENGELIGHET

Accessible

SINTEF RAPPORT

STIFTELSEN FOR INDUSTRIELL OG TEKNISK FORSKNING VED NORGES TEKNISKE HØGSKOLE

7034 TRONDHEIM — NTH

TLF.: (07) 59 30 00

TELEX: 55620 SINTF N

RAPPORTENS TITTEL	DATO
REAL TIME SPECTRUM ANALYSIS IN DOPPLER ULTRASOUND BLOOD VELOCITY MEASUREMENTS	November 1984
	ANTALL SIDER OG BILAG: 138
SAKSBEARBEIDER/FORF.: Kjell Kristoffersen	ANSV. SIGN.: B. Angelsen
AVDELING: 48, Reguleringsteknikk	PROSJEKTNUMMER: 481096.06

OPPDRAGSGIVER	OPPDR. GIVERS REF.
VINGMED A/S	

EKSTRAKT

This report covers aspects of spectrum analysis in Doppler ultrasound blood velocity measurements. The properties of the modified periodogram spectrum estimator are derived, and the stabilizing effect of averaging periodograms from overlapping signal segments is discussed. It is shown that averaging weakly compressed periodograms may reduce the dynamic range requirements to the spectrum averager device significantly, at the cost of a modest increase in variance.

An architecture for a real time hardwired spectrum analyzer is proposed. The modified periodogram is calculated by passing the signal segment to be Fourier-transformed twice through a Chirp Z-transformer based on Bucket Brigade Devices. This approach should allow for a 64 point spectrum to be calculated in 128 μs.

3 STIKKORD PÅ NORSK	KEYWORDS IN ENGLISH
	Spectrum analysis
	Doppler ultrasound
	Blood velocity

Table of contents

Table of contents, continued

1. INTRODUCTION

The received signal in Doppler ultrasound blood velocity measurements is formed by the scattering of ultrasound from a large number of randomly located red blood cells. The Doppler signal therefore becomes a zero mean Gaussian process [5]. As such, all information is contained in its autocorrelation function. When the velocity field in the blood vessel is time steady, the Doppler signal becomes stationary [5], and it follows from the Wiener-Kintchine Theorem that all available information is also contained in its power spectrum. From a signal processing point of view, this explains why spectral analysis plays such an important role in the interpretation of Doppler signals in blood velocity measurements.

The power spectrum of the Doppler signal has a physical interpretation. The spectral density at a frequency f_d is a rough measure of the fractional blood volume in the sensitivity region (sample volume) of the Doppler instrument that travels with velocity v, such that v and f_d are proportionally interrelated via the Doppler equation. Rescaling the frequency axis of a power spectral density plot into velocity units therefore yields essentially the velocity distribution in the sample volume. Spectral analysis thus provides information about the entire velocity distribution. In contrast, widely used single frequency estimators only estimate a single parameter of this distribution (mean [39], maximum [40] or root mean square frequency [41]).

The clinically most important parameter of the velocity distribution is probably its maximum velocity. This parameter may be applied to estimate the pressure drop across obstructions to flow, via the Bernoulli equation [42][43]. If some minor spectral broadening effects are neglected, the maximum velocity corresponds to the maximum frequency of the Doppler spectrum, which can be detected using spectrum analysis.

The velocity profiles in human arteries have pulsatile time variations, caused by the beating of the heart. The Doppler signal therefore becomes a nonstationary (evolutionary) Gaussian process. If the estimate of the power spectrum is formed over a so short signal segment that the velocity profile is essentially constant (~ 10 ms), the expected value of this 'shorttime spectrum' approximates the instantaneous velocity distribution. However, the short time available for signal analysis leaves errors (bias, variance) in the estimate. Frequently the signal to noise ratio of the measurements may be poor. The estimated velocity distribution therefore always has a stochastic uncertainty, which may be reduced by properly parametrized spectral analysis.

Spectral analysis has a number of advantages compared to the use of single frequency estimators. These are

- The ratio between the signal and the noise spectral intensities (the 'spectral signal to noise ratio') for a narrowband signal in wideband noise is much larger than the total signal to noise power ratio. This makes a spectral estimator less sensitive to noise than, for example, a time domain implementation of a mean frequency estimator, which responds to the entire noise power spectrum.

- It is well known that narrowband noise, such as electronic RF interference, may cause serious problems for single frequency estimators [44]. In spectral analysis, this type of noise only generates stationary spectral lines. These are easily discerned from the more wideband, time varying Doppler spectrum.

- Doppler signals from different vessels within the same sample volume (especially actual using continuous wave Doppler with no range resolution) can often be seperated using spectrum analysis. The output from single frequency estimators in such a case is related to the sum of the individual Doppler spectra from the vessels. The presence of an interfering vessel may not be recognized by the operator, and erroneous interpretations may result [44].

- Aliasing errors in pulsed Doppler systems are immediately revealed using spectral analysis, while normally causing large errors in the output from single frequency estimators. Unless the ultrasonographer is skilled, this may be overlooked and, again, misinterpretations are likely.

- When the velocity field is unidirectional, sampled data spectrum analysis of the complex Doppler signal increases the frequency limit of pulsed Doppler systems with a factor 2 compared to the Nyquist limit PRF/2 [13]; PRF denotes the pulse repetition frequency (sampling frequency) of the instrument. In this report it shall be demonstrated that in some situations, frequencies even exceeding the PRF can be quantified.

The major drawback of spectrum analysis is that it traditionally has been rather costly, both to perform and to display. Developments in technology are now changing this picture.

A good spectrum estimator should yield low bias/ low variance spectrum estimates. It should also be consistent, i.e. the variance of the estimate should tend to zero as the length of the available data record increases to infinity. A nonzero bias in spectrum analysis means either finite resolution, sidelobes, or spurious spectral responses. Due to the transit time effect, the Doppler signal always has a finite bandwidth, even when measuring on a vessel with a flat velocity profile (plug flow) [45]. Typically, the correlation time of the interesting frequency components in the signal is shorter than the allowable data collecting time for one spectrum estimate (~ 10 ms). The Doppler signal may in fact be modeled as a relatively low order MA process [34]. This means that computationally efficient Fourier transform based spectrum estimators are well suited for our purpose, as these model the signal as an all-zero process. All-pole (AR) or mixed pole/zero (ARMA) models may have lower bias when the available data record is shorter than the correlation time of the signal [46], but this is rarely the case in our situation.

A variety of types of spectrum analysers have earlier been designed for dedicated use in Doppler ultrasound applications: Banks of parallel filters [23][47], sweeping filters (off line analysis) [48], time compression plus sweeping filter [49]. A review of their principles is given by Atkinson and Woodcock [24]. The modified periodogram is the most commonly used estimator in Doppler signal analysis today [20][21][26][33][50]. It is defined as the normalized magnitude squared Fourier transform of a sequence of samples, which is the product of the Doppler signal and a suitable window function. The standard deviation of this estimate equals its mean, regardless of the length of the data record (see Section 2.2.2). The modified periodogram thus is a high variance, nonconsistent spectrum estimator.

Two basic principles exist for improving the consistency of the modified periodogram. One is to compute the periodogram of the entire data record available, and smooth this 'raw' estimate in the frequency domain (the smoothed periodogram estimator) [2]. Traditionally, this operation has been carried out in the time domain by estimating the sample autocorrelation function, multiply it with a 'lag window', and Fourier transform to obtain the power spectrum (the Blackman and Tukey method) [27]. A different approach is to partition the data record into a number of sub-sequences, possibly overlapping, compute the modified periodograms of each signal segment and then average to reduce the variance [7][56]. The result of this operation is denoted the averaged modified periodogram, and the method is often referred to as the Windowed Overlap Segment Average (WOSA) method. The performances of both methods are roughly the same, but the WOSA method is computationally more efficient. More recently, Yuen has advocated a method that is a combination of the above ones, employing averaged periodograms from rectangular windowed, non-overlapping signal segments, and additional smoothing in the frequency domain [51][52]. This method has been further elaborated by Nuttall and Carter; they have shown that it can attain the same statistical stability as the two traditional methods at a lower computational cost [53]. Common for all methods is that a reduction in variance always leads to reduced resolution, i.e an increase of the bias.

The objectives of this report are:

a) To give a comprehensive discussion of spectrum analysis applied in Doppler blood velocity measurements. This includes
   - understanding the properties of the spectrum estimator;
   - relating these to the measurement situation to determine how the spectrum estimator should be parametrized for optimal results.

b) Pay attention to some special problems that occur in pulsed Doppler measurements. These are
   - frequency aliasing;
   - the application of analog, continuous time filters as an integral part of an intrinsicly discrete time system.

c) Apply the above information to establish the system architecture of a real time spectrum analyser for the processing of complex Doppler signals.

The properties of the Doppler spectrum (center frequency, bandwidth and their rate of change, spectral dynamic range) vary between different clinical situations. The analyser design should contain flexibility to be used with near optimal qualities in all of these situations. To obtain this, it has been chosen to concentrate on the averaged modified periodogram spectrum estimator. This approach allows for the use of a Discrete Fourier Transform (DFT) computer with a relatively small number of points, which strongly reduces the complexity and speed requirements for the hardware.

The report is organized as follows: Initially, the statistical properties of the spectrum estimator are derived, assuming it is being applied to a stationary complex Gaussian process. It will also be focused on issues which lead to simpler hardware realizations (averaging of individually compressed periodograms), or improved display of the spectrum estimate (suppression of white noise by thresholding). These properties are related to the practical measurement situation in Chapter 3, which also contains a discussion on frequency aliasing in pulsed Doppler systems. Different hardware implementation schemes are then evaluated. Finally, the system architecture for a fast spectrum analyser is proposed in Chapter 5 (128 μs minimum computing time). The solution employs mixed analog/digital signal processing, based on Bucket Brigade Devices. It is both inexpensive and compact relative to the performance. Appendix I contains a discussion on the design of smoothing lowpass filters for pulsed Doppler instruments employing discrete time signal processing.

The speed of the outlined spectrum analyser makes it suited for both conventional single gate pulsed and/or continuous wave Doppler systems, as well as multigated systems. In the latter case, the high speed allows a single spectrum analyser to be timeshared between independent signals from a large number of range gates.

A summary of the most important results of each chapter is given at the end of the chapter.

2. MODIFIED PERIODOGRAM SPECTRUM ESTIMATION APPLIED TO A STATIONARY COMPLEX GAUSSIAN PROCESS

The chapter contains the theory of the averaged modified periodogram spectrum estimator. Numerous investigators have analysed the periodogram as a spectrum estimator for real signals [1][2][3][4][7][56][57]. By far, the best analysis available on the subject seem to be the reports written by A. H. Nuttall [56][57]. His analysis were made under the assumption that the signal was a continuous time, real Gaussian process. In our situation it is dealt with a signal acquisition process that is intrinsicly sampled, i.e. pulsed Doppler measurements. Rather than giving a direct review of Nuttall's results, it has been chosen to derive discrete time equivalents to these, under the constraint that the signal is a stationary complex Gaussian process. The latter assumption greatly simplifies the derivation of expressions for estimator variance. Some well known properties of the periodogram, having approximate validity for real signals, in fact become exact for this class of signals (this was also realized by Nuttall). The majority of the results in Sections 2.2, 2.3 and 2.6 are therefore not new, although the approach to the derivations may differ from the other works cited.

2.1 Definition of terms

The cross correlation function between two complex, stationary processes $p(t)$ and $q(t)$ is defined as

$$R_{pq}(\tau) = \langle p^*(t)q(t+\tau)\rangle \tag{2.1}$$

where $\langle\ \rangle$ denotes ensemble expectation and * denotes complex conjugate. The Doppler signal $\hat{x}(t)$ in ultrasonic blood velocity measurements is a complex, zero mean Gaussian process [5]. It can be decomposed into its real quadrature components by

$$\hat{x}(t) = x(t) + jy(t) \tag{2.2}$$

When the velocity field in the blood vessel is time invariant, $\hat{x}(t)$ will be stationary, and the following correlation properties hold for its quadrature components [5]:

$$R_{xx}(\tau) = R_{yy}(\tau) = R_{xx}(-\tau) \tag{2.3}$$

$$R_{xy}(\tau) = -R_{yx}(\tau) = -R_{xy}(-\tau) \tag{2.4}$$

The definitions of the correlation functions follow from (2.1). It is assumed that the above relations are satisfied throughout the rest of Chapter 2.

The power spectrum of the stochastic process $\hat{x}(t)$ is defined as the Fourier transform of its autocorrelation function $R_{\hat{x}\hat{x}}(\tau)$:

$$G_{\hat{x}\hat{x}}(\omega) = \int_{-\infty}^{\infty} d\tau \; R_{\hat{x}\hat{x}}(\tau) e^{-j\omega\tau} \tag{2.5}$$

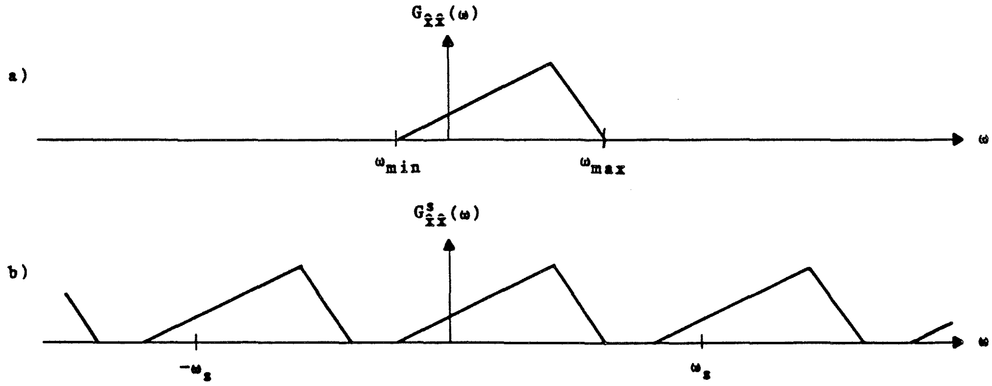

Fig. 2.1 Power spectra of
a) continuous process $\hat{x}(t)$
b) discrete process $\{\hat{x}(kT_s)\}$

When $\hat{x}(t)$ is sampled with angular sampling rate $\omega_s = 2\pi/T_s$, the power spectrum of the discrete time process $\{\hat{x}(kT_s)\}$ is similarly given by

$$G^s_{\hat{x}\hat{x}}(\omega) = \sum_{n=-\infty}^{\infty} R_{\hat{x}\hat{x}}(nT_s) e^{-jn\omega T_s} \tag{2.6}$$

Thus, the sampled power spectrum $G^s_{\hat{x}\hat{x}}(\omega)$ is periodic with period ω_s. When $\hat{x}(t)$ is stationary, the following relation holds [2]:

$$G^s_{\hat{x}\hat{x}}(\omega) = \frac{1}{T_s} \sum_{n=-\infty}^{\infty} G_{\hat{x}\hat{x}}(\omega-n\omega_s) \tag{2.7}$$

The significance of this well known equation is shown schematically in Fig. 2.1. The sampled power spectrum is formed by multiple translations of $G_{\hat{x}\hat{x}}(\omega)$ along the ω-axis. Note that since $\hat{x}(t)$ is a complex process, its power spectrum is generally <u>not</u> a symmetric function in ω. As long as its angular bandwidth does not exceed ω_s, i.e.

$$\omega_{max} - \omega_{min} < \omega_s \tag{2.8}$$

the partial spectra in Fig. 2.1.b will not overlap. Then $G_{\hat{x}\hat{x}}(\omega)$ can be determined unambiguously from $G^s_{\hat{x}\hat{x}}(\omega)$, if one from prior information knows which part of the sampled power spectrum that contains the spectrum of the continuous time signal. For example, if one from physical reasons knows that $G_{\hat{x}\hat{x}}(\omega)$ only can have spectral support on positive frequencies with maximum frequency less than ω_s, the relation $G_{\hat{x}\hat{x}}(\omega) = T_s G^s_{\hat{x}\hat{x}}(\omega)$, $\omega \in [0,\omega_s]$, holds.

Unless otherwise stated, T_s shall be set to unity in the rest of the report. Since the spectrum estimation described in the following is carried out in the discrete time domain, the unprecise but convenient term "spectrum" will be used to denote both $G_{\hat{x}\hat{x}}(\omega)$ and $G^s_{\hat{x}\hat{x}}(\omega)$. The only situation where one needs to distinguish between these is when (2.8) is violated.

2.2 The averaged modified periodogram spectrum estimator

2.2.1 Definition and expectation value

An estimator of the sampled power spectrum $G^s_{\hat{x}\hat{x}}(\omega)$, based on K signal samples centered around sample k, is given by

$$\tilde{G}(k,\omega;K) = \frac{1}{K} |\tilde{X}(k,\omega;K)|^2 \tag{2.9}$$

where

$$\tilde{X}(k,\omega;K) = \sum_{n=1}^{K} w(n;K)\hat{x}(k+n-K/2)e^{-jn\omega} \tag{2.10}$$

This estimator is commonly referred to as the modified periodogram. The smooth, real window function $\{w(n;K)\}$ is assumed to be nonzero only for $0 < n \leq K$. The limits of the summation in (2.10) can therefore be extended to infinity, without changing the result. The window improves the dynamic range of the periodogram; details will be discussed later. To simplify the notation, the parameters k and/or K shall be omitted from $\tilde{G}$, $\tilde{X}$ and w in situations where no ambiguity is introduced. For example, all of the forms $\tilde{G}(\omega)$, $\tilde{G}(k,\omega)$ and $\tilde{G}(k,\omega;K)$ may be used when the signal is stationary. In the following, the short form $G(\omega)$ is used instead of $G^{s}_{\hat{x}\hat{x}}(\omega)$ to denote the sampled power spectrum.

The correlation between $\tilde{X}(k,\omega)$ and $\tilde{X}(k,\omega+\Delta)$ is from (2.1)

$$\begin{aligned} \langle \tilde{X}^*(\omega)\tilde{X}(\omega+\Delta)\rangle &= \langle \sum_{n=-\infty}^{\infty} \sum_{m=-\infty}^{\infty} w(n)w(m)\hat{x}^*(n)\hat{x}(m)e^{-j(m-n)\omega}e^{-jm\Delta}\rangle \\ &= \sum_{n=-\infty}^{\infty} \sum_{m=-\infty}^{\infty} w(n)w(m)R_{\hat{x}\hat{x}}(m-n)e^{-j(m-n)\omega}e^{-jm\Delta} \end{aligned} \tag{2.11}$$

This expression can be simplified by transforming into the frequency domain, using the substitution $m - n = k$ and the Fourier transform relations

$$w(k+m;K) = \frac{1}{2\pi}\int_{-\pi}^{\pi} d\omega \; W(\omega;K)e^{j(k+m)\omega} \tag{2.12}$$

$$W(\omega;K) = \sum_{k=1}^{K} w(k;K)e^{-jk\omega} \tag{2.13}$$

$W(\omega;K)$ is the frequency response of the window. Using the above relations and (2.6), the following frequency domain expression is obtained for the correlation:

$$\langle \tilde{X}^*(\omega)\tilde{X}(\omega+\Delta)\rangle = \frac{1}{2\pi}\int_{\pi}^{\pi} d\lambda \; W(\lambda)W^*(\lambda-\Delta)G(\omega-\lambda+\Delta) \tag{2.14}$$

The expected value of the periodogram follows immediately from (2.9) and (2.14) with $\Delta = 0$:

$$\langle \tilde{G}(\omega;K) \rangle = \frac{1}{K} \langle \tilde{X}(\omega)\tilde{X}^*(\omega) \rangle = \frac{1}{2\pi} \int_{-\pi}^{\pi} d\lambda \; W_s(\lambda;K) G(\omega-\lambda) \tag{2.15}$$

where

$$W_s(\omega;K) = \frac{1}{K} |W(\omega;K)|^2 \tag{2.16}$$

Hence, the expected value of the periodogram is the convolution between the true spectrum $G(\omega)$ and the <u>spectral window</u> $W_s(\omega)$, i.e. the expected value is a smoothed version of the true power spectrum. Therefore, the periodogram is a <u>biased</u> estimator of the sampled power spectrum, unless the power spectrum is completely flat (white noise). In the latter case, the following scaling condition is required for the periodogram to be unbiased (from eq. (2.15)):

$$\frac{1}{2\pi} \int_{-\pi}^{\pi} d\omega \; W_s(\omega;K) = \frac{1}{K} \sum_{k=1}^{K} w^2(k;K) = 1 \tag{2.17}$$

The first identity follows from Parseval's theorem [2]. The above equation states that the area under the spectral window must equal unity.

Good windows have real frequency responses with a narrow main lobe centered around $\omega = 0$, and small side lobes. The amount of bias in spectrum estimation is determined both from the width of the main lobe and the size of the side lobes. Generally spoken, a window with small side lobes tends to have a broad main lobe, and vice versa. The 6 dB angular bandwidth of the main lobe is related to K by [6]

$$\Delta\omega_a = k_w \frac{2\pi}{KT_s} \tag{2.18}$$

where k_w is a characteristic constant for each type of window. Thus, increasing the length of the data record decreases the width of the main lobe of $W_s(\omega)$, and reduces the bias. In combination, eqs. (2.17) and (2.18) indicate that the spectral window will converge to a delta function in the limit when $K \rightarrow \infty$. The periodogram is therefore an asymptotically unbiased spectrum estimator [4].

A large number of window types have been proposed in the literature. Surveys are given in [6] and [9]. The time domain versions of the rectangular and the Hamming windows are listed below:

$$w_r(k;K) = \begin{cases} 1 & 0 < k \leq K \\ 0 & \text{elsewhere} \end{cases} \tag{2.19}$$

$$w_h(k;K) = \begin{cases} 1.586[0.54 + 0.46 \cos \frac{2\pi}{K}(k-\frac{K+1}{2})] & 0 < k \leq K \\ 0 & \text{elsewhere} \end{cases} \tag{2.20}$$

These window types will be used in some examples later in this report. The rectangular window has an even time domain weighting of the signal. It is useful to include, since it establishes a reference for the yield of noneven data weighting. The choice of the Hamming window as a second example was done since it is incorporated in commercially available analog charge transfer devices intended for use in spectrum analysis. These devices are discussed in Chapters 4 and 5.

The spectral windows $W_s(\omega)$, eq. (2.16), for the above time windows have been plotted in dB scale in Fig. 2.2 for $K = 32$ and $K = 64$. The smaller side lobes and broader main lobe of the Hamming window are apparent. From [6], $k_w = 1.21$ for the rectangular window, while $k_w = 1.81$ for the Hamming window. The peak side lobe level of the Hamming window is -43 dB, vs. -13 dB for the rectangular type (valid for continuous time versions of the windows, but since aliasing effects are small for actual values of K, the numbers are good approximations).

When Fig. 2.2 is related to eq. (2.15), it becomes clear that the resolution of the periodogram is determined from the width of the main lobe. The side lobes affect the dynamic range of the periodogram, as side lobes of a strong frequency component may totally obscure weaker frequency components. The choice of window type therefore becomes a tradeoff in resolution vs. dynamic range.

2.2.2 Correlation properties and variance

We shall now analyse the variance and consistency properties of the modified periodogram. Observe from (2.2)-(2.4) that

$$\begin{aligned} \langle \tilde{x}(k)\tilde{x}(n)\rangle &= R_{xx}(n-k) - R_{yy}(n-k) + j[R_{xy}(n-k) - R_{yx}(n-k)] \\ &= 0 \end{aligned} \tag{2.21}$$

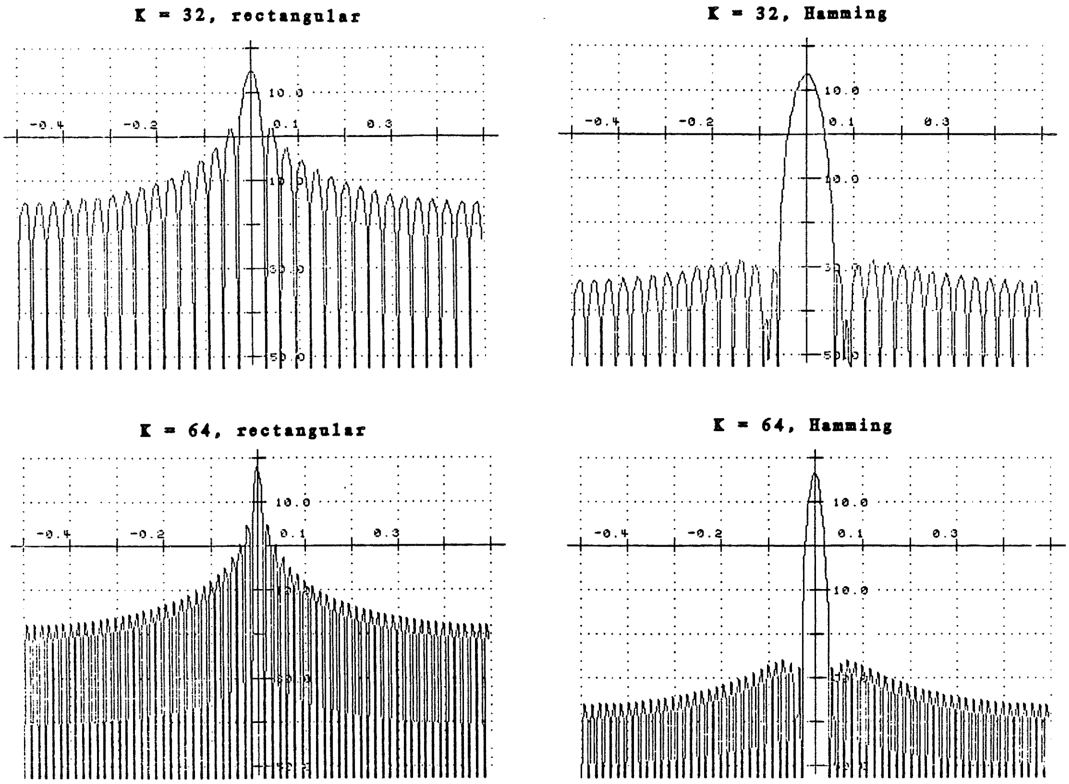

Fig. 2.2 dB plots of Hamming and rectangular spectral windows for $K = 32$ and $K = 64$. The x-axis are scaled relative to $\omega_s/2$.

The above property may equivalently to (2.3),(2.4) be taken as a definition of a stationary complex Gaussian process [10]. Since $\tilde{X}(k,\omega)$ at a fixed ω is a linear combination of zero mean complex Gaussian processes, it becomes itself a zero mean complex Gaussian process. It follows immediately that also the correlation

$$\langle \tilde{X}(k,\omega_1)\tilde{X}(n,\omega_2)\rangle = 0 \tag{2.22}$$

for all k,n and ω_1,ω_2. The 4 th order moment of the complex zero mean jointly Gaussian variables q,r,s,t is then given by [10]:

$$\langle q^*r^*st\rangle = \langle q^*s\rangle\langle r^*t\rangle + \langle r^*s\rangle\langle q^*t\rangle \tag{2.23}$$

Note that if the variables had been real, there would have been one additional term on the right side. Using this formula, the covariance between the periodogram estimate at the angular frequencies ω and $\omega + \Delta$ becomes

$$\mathrm{Cov}(\tilde{G}(\omega),\tilde{G}(\omega+\Delta)) = \frac{1}{K^2}\langle\tilde{X}(\omega)\tilde{X}^*(\omega)\tilde{X}(\omega+\Delta)\tilde{X}^*(\omega+\Delta)\rangle - \tilde{G}(\omega)\tilde{G}(\omega+\Delta)$$

$$= \frac{1}{K^2}|\langle\tilde{X}(\omega)\tilde{X}^*(\omega+\Delta)\rangle|^2 \qquad (2.24)$$

Using eq.(2.14), this expression can be converted to the form

$$\mathrm{Cov}(\tilde{G}(\omega)\tilde{G}(\omega+\Delta)) = \frac{1}{K^2}\frac{1}{(2\pi)^2}\left|\int_{-\pi}^{\pi}d\lambda\ W(\lambda)W^*(\lambda-\Delta)G(\omega-\lambda-\Delta)\right|^2 \qquad (2.23)$$

The only way one can get a sizable value of the above integral is to make Δ so small that the main lobes of $W(\lambda)$ and $W^*(\lambda-\Delta)$ overlap. Fig. 2.2 then reveals that two point estimates of the periodogram for practical purposes are uncorrelated when they are spaced more than one main lobe width apart.

The variance of the periodogram at a fixed frequency is obtained by setting $\Delta = 0$ in eq. (2.24). Comparing with (2.15) leads to the simple result

$$\mathrm{Var}(\tilde{G}(\omega)) = \langle\tilde{G}(\omega)\rangle^2 \qquad (2.26)$$

It is convenient to introduce the normalized term <u>fractional variance</u>, defined as the ratio between the variance and the square of the mean of a stochastic variable:

$$\mathrm{Fracvar}[\tilde{G}(\omega)] = \frac{\mathrm{Var}(\tilde{G}(\omega))}{\langle\tilde{G}(\omega)\rangle^2} = 1 \qquad (2.27)$$

The equation illustrates the well known fact that the modified periodogram is a poor estimator of the power spectrum: In addition to having a large bias for short data records, also its fractional variance is very large. Furthermore, since two periodogram ordinates are uncorrelated when their frequency arguments are spaced more than one main lobe width apart, the periodogram tends to fluctuate wildly around its mean [4]. These properties are valid regardless of K, and the modified periodogram is therefore a highly nonconsistent estimator of the power spectrum. When K increases, the width of the main lobe of $W_s(\omega)$ decreases, and consequently, the periodogram will fluctuate more rapidly around its mean.

The simple expression (2.27) is not exact when the signal is real. The fractional variance of the modified periodogram when the input signal is real, Gaussian white noise and the rectangular window is employed, has been shown to be [2]:

$$\mathrm{Fracvar}[\tilde{G}(\omega)] = 1 + \frac{\sin^2 K\omega}{K^2 \sin^2 \omega} \tag{2.28}$$

In this case, the fractional variance is a function of both K and ω. It equals 2 for $\omega = 0$ and $\omega = \pm\pi$, but it decays rapidly to 1 away from these points when K is large. The simplicity of eq. (2.27) is due to the fact that $\langle \tilde{X}^2(\omega) \rangle = 0$ when the signal is complex Gaussian.

For general real, zero mean Gaussian signals, (2.27) can be shown to have asymptotic validity when $K \to \infty$. Exceptions are the points $\omega = 0$ and $\omega = \pi$, where the fractional variance converges to 2 [4]. If one thinks of the periodogram as a smoothed version of a noisy, unbiased estimate of the periodogram, the increased variance for real signals can be given a intuitive explanation: Mathematically, such a smoothing may be expressed as a convolution integral similar to (2.15), where $G(\omega)$ is replaced by the noisy estimate. For $\omega = 0$ or $\omega = \pi$, only half the main lobe of the spectral window $W_s(\omega)$ will contribute to the smoothing, since the raw estimate must be a symmetric function in ω when the signal is real. With ω substantially away from these points, the entire main lobe covers independent parts of the raw estimate, and the efficiency of the hypothetical smoothing doubles.

The increased variance for real signal inputs at frequencies away from $\omega = 0$, π is due to 'variance leakage' from these points, caused by the side lobes of the spectral window [4, p. 464]. This is confirmed by (2.28), where no increase in variance can be found for $\omega = 2\pi n/K$, $n = 1, 2, --, K-1$. These frequencies are the zeros in the frequency response of the rectangular window, and they are, therefore, not affected by increased variance for $\omega = 0$ or $\omega = \pi$.

2.2.3 Averaging modified periodograms

A commonly used method for reducing the variance of the modified periodograms is to form a weighted average of periodograms from different segments, possibly overlapping, of the signal [7][56]. In this report, the averaged modified periodogram is defined as

$$\tilde{G}_M(k + \frac{M+1}{2} q,\omega;K) = \sum_{n=1}^{M} b(n)\tilde{G}(k+nq,\omega;K) \tag{2.29}$$

where $(K-q)$ samples overlap between adjacent signal segments has been assumed. $\{b(n)\}$ are the coefficients of the averaging Finite Impulse Response (FIR) filter. The requirement

$$\sum_{n=1}^{M} b(n) = 1 \tag{2.30}$$

must be satisfied for the expected value of the averaged periodogram to equal that of the modified periodogram. The fractional variance σ_M^2 of the averaged periodogram at a fixed frequency can be calculated from direct analogy with a similar problem discussed in [11]:

$$\sigma_M^2(\omega) = \sum_{m=-(M-1)}^{M-1} \tilde{b}(m)\xi(mq,\omega) \tag{2.31}$$

where

$$\xi(mq,\omega) = \langle\tilde{G}(\omega)\rangle^{-2}\mathrm{Cov}(\tilde{G}(k,\omega),\tilde{G}(k+mq,\omega)) \tag{2.32}$$

$$\tilde{b}(m) = \tilde{b}_s^{-1} \sum_{k=1}^{M-|m|} b(k)b(k+|m|) \tag{2.33}$$

$$\tilde{b}_s = [\sum_{k=1}^{M} b(k)]^2 \tag{2.34}$$

The constant $\tilde{b}_s$ is unity for a properly scaled averaging filter. The coefficients $\{\tilde{b}(m)\}$ are the convolution of the impulse response of the FIR filter with itself. The normalized covariance function

$\{\xi(mq,\omega)\}$ can be calculated using the technique that led to (2.24):

$$\langle\tilde{G}(k,\omega)\tilde{G}(k+mq,\omega)\rangle = \langle\tilde{G}(\omega)\rangle^2 + \frac{1}{K^2}\,|\langle\tilde{X}(k,\omega)\tilde{X}^*(k+mq,\omega)\rangle|^2 \qquad (2.35)$$

Proceeding similarly as for the solution of (2.11) yields the below expression for the time correlation of the windowed Fourier transform:

$$\langle\tilde{X}(k,\omega)\tilde{X}^*(k+mq,\omega)\rangle = \frac{K}{2\pi}\int_{-\pi}^{\pi} d\lambda\; W_s(\lambda)G(\omega-\lambda)e^{-jmq(\omega-\lambda)} \qquad (2.36)$$

Substitution in (2.32) then yields the normalized covariance function

$$\xi(mq,\omega) = \frac{\left|\int_{-\pi}^{\pi} d\lambda\; W_s(\lambda)G(\omega-\lambda)e^{jmq\lambda}\right|^2}{\left|\int_{-\pi}^{\pi} d\lambda\; W_s(\lambda)G(\omega-\lambda)\right|^2} \qquad (2.37)$$

For a given sampled power spectrum, the fractional variance can now be calculated exactly from (2.31) and (2.37). However, the above expression may be greatly simplified if some approximations are made. If a good window is used, the integrals in (2.37) will get far the most of their contributions from the main lobe of the window, i.e. for λ close to zero. If the main lobe is so narrow that the power spectrum varies little over its width, $G(\omega)$ can be put outside the integrals in (2.37). The equation then simplifies to

$$\xi(mq,\omega) = \frac{\left|\int_{-\pi}^{\pi} d\omega\; W_s(\omega)e^{jmq\omega}\right|^2}{\left|\int_{-\pi}^{\pi} d\omega\; W_s(\omega)\right|^2} = \frac{\left|\sum_{k=1}^{K-|mq|} w(k;K)w(k+|mq|;K)\right|^2}{\left|\sum_{k=1}^{K} w^2(k;K)\right|^2} \qquad (2.38)$$

The last transition follows by inverse Fourier transform. The covariance function $\{\xi(mq,\omega)\}$ becomes independent of ω, being simply the normalized squared correlation function of the time window. It is observed that in this approximation, the periodograms are uncorrelated for $|mq| > K$.

Moreover, it can be seen that $\tilde{X}(k,\omega;K)$ and $\tilde{X}(k+mq,\omega;K)$ are uncorrelated when $|mq| > K$. Being zero mean complex Gaussian variables, they are then independent. It follows that modified periodograms from nonoverlapping signal segments are not only uncorrelated: They are also <u>independent</u>.

Specializing to the case $b(m) = 1/M$ (pure averaging) yields (using eqs. (2.31), (2.33) and (2.38))

$$\sigma_M^2 = \frac{1}{M} \sum_{m=-M}^{M} (1 - |\frac{m}{M}|)\xi(mq) \tag{2.39}$$

The formulas (2.38), (2.39) are identical to the results of Welch, valid for real Gaussian signals, except that he had to make reservations near the points $\omega = 0$ and $\omega = \pi$ [7]. These were for the same reasons as previously discussed. Nuttall, because of his assumption of a continuous time signal, obtained an expression for the correlations $\{\xi(mq,\omega)\}$ similar to eq. (2.38), containing integrals instead of the summations [56]. For windows with rapidly decaying sidelobes, the results become nearly identical.

Unlike the raw periodogram, the averaged periodogram is a consistent estimator of the power spectrum when M increases and K and q are fixed. When M is large, its fractional variance equals c_v/M ($\xi(mq)$ is nonzero only for $|mq| < K$). The constant c_v depends on the window type and the degree of overlap. For nonoverlapping signal segments c_v is unity, while it increases with increasing degree of overlap. However, the overlap allows for using a larger M when the total data record length is fixed. The net result is then a reduction in variance, at the cost of an increased amount of computation.

It is of interest to quantify how the variance is affected by the degree of overlap between adjacent signal segments. If the fractional overlap $(K-q)/K$ is denoted r, and the available data record is L samples, one may average over a total number of sections

$$\begin{aligned} M &= 1 + (\frac{L}{K} - 1)\frac{1}{1-r} \\ &\simeq \frac{L}{K}\frac{1}{1-r} \quad \text{when } L/K \gg 1 \end{aligned} \tag{2.40}$$

For calculation of the fractional variance $\sigma_M^2(r)$, the expression

$$q = (1-r)K \qquad 0 \leq K < 1 \tag{2.41}$$

must be substituted in (2.38). Assuming L/K >> 1, the reduction in variance due to the overlap is

$$\frac{\sigma_\infty^2(r)}{\sigma_\infty^2(0)} = (1-r) \sum_{m=-r/(1-r)}^{r/(1-r)} \xi(mq) \tag{2.42}$$

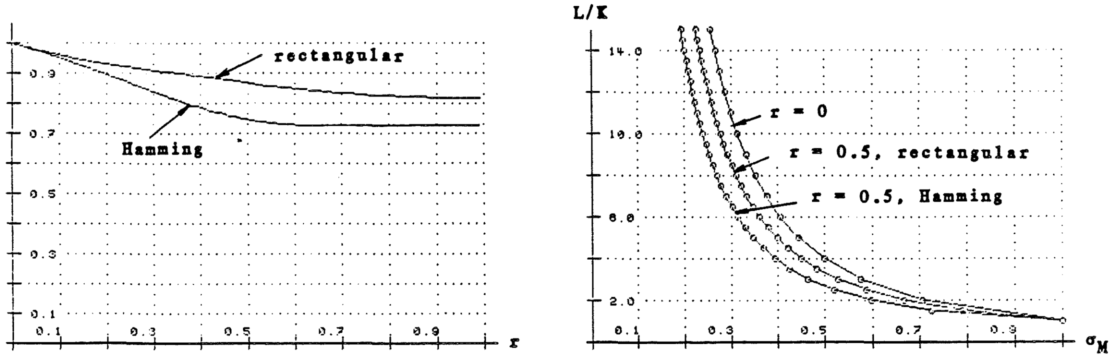

a) b)

Fig. 2.3 The effect of averaging modified periodograms from overlapping signal segments:
a) Reduction in fractional standard deviation caused by nonzero overlap. Valid when L >> K.
b) Required length of data record for a specified fractional standard deviation of the estimate.

The reduction in standard deviation as a function of r (the square root of (2.42)) is plotted in Fig. 2.3.a for the Hamming and the rectangular windows. It can be seen that there is a considerable yield in using overlapping segments. The reduction in standard deviation is larger for the Hamming window than for the rectangular (0.73 vs. 0.82 when r -> 1). However, increasing the overlap beyond a certain limit yields very little additional reduction in variance, while the computational burden increases dramatically. This limit is smallest for the Hamming window ($r \sim 0.6$ vs. $r \sim 0.85$). The larger reduction in variance for the Hamming window occurs since its noneven time weighting throws away much of the data near the endpoints of each signal segment. Unless overlap is employed, this information is not fully taken into account.

The above results can be given an intuitive explanation by regarding $\{\tilde{X}(k,\omega)\}$, ω fixed, as the output of a linear filter driven with white noise. The complex impulse response of the filter is $\{w(n;K)\exp(-jn\omega)\}$. The 6 dB bandwidth of the sequence $\{\tilde{X}(k,\omega)\}$ then is $\Delta f_a = k_w/K$, and hence it must be sampled at least with a rate larger than k_w/K ($\tilde{X}$ is complex) to preserve all information. This indicates that the fractional overlap should exceed $\sim (k_w-1)/k_w$, which is 0.17 for the rectangular and 0.45 for the Hamming window. This simple argument is reasonably accurate for the Hamming window, while Fig. 2.3.a indicates additional yield for a considerably larger degree of overlap when the rectangular window is employed. The reason for the discrepancy in the latter case is the large sidelobes of the rectangular window, which violates the assumtion of bandlimitness. The results are, however, qualitatively correct, in the sense that they indicate a more severe loss of information if overlap is not employed in the case of the Hamming window.

Note that the above results were derived under the assumption $L \gg K$ (strong averaging and steady state analysis). Nuttall has shown that when this assumption is violated, there exists in fact an optimum overlap between the signal segments. If the overlap is increased beyond this point, the variance increases slightly [56, p. 19]. The optimum overlap increases slowly with increasing L/K, being typically 65% for the cosine (Hanning) window. This phenomenon is a manifestation of the fact that it is not optimal to use an even weighting in the sum (2.29). The optimum weights can be found by solving the set of linear equations $\partial\sigma_M^2/\partial b(m) = 0$ for $\{b(m)\}$, using (2.31) and (2.33). The details have been carried out by Nuttall [56, p. 26], but it turns out that the yield of using a noneven weighting is small.

Another interesting question is how large the data record L should be chosen if the fractional variance of the spectrum estimate is to be smaller than a specified limit. The solution can be given graphically by combining (2.38)-(2.41), and plot σ_M vs. L/K. The result is shown in Fig. 2.3.b for $r = 0$ and $r = 0.5$. The rings denote possible points of operation (M is discrete). In agreement with Fig. 2.3.a, it is seen that for small σ_M, the necessary averaging time using the Hamming window with no overlap is nearly twice the time needed when using 50% overlap.

The expression (2.31) for the fractional variance of the spectrum estimate can be transformed to the frequency domain. Maximal overlap is assumed, i.e. $q = 1$. The frequency response of the averaging filter is then

$$B(\omega) = \sum_{m=1}^{M} b(m) e^{-jm\omega} \tag{2.43}$$

From the definition (2.33), it is straigthforward to show that the frequency response of the filter with the impulse response $\{\tilde{b}(m)\}$ satisfies

$$\tilde{B}(\omega) = \sum_{m=-M}^{M} \tilde{b} e^{-jm\omega} = |B(\omega)|^2 \tag{2.44}$$

Combining with (2.38) and inserting into (2.31) yields the following frequency domain expression for the fractional variance:

$$\sigma_M^2 = \frac{\sum_{m=-M}^{M} \tilde{b}(m) \int_{-\pi}^{\pi} d\lambda \int_{-\pi}^{\pi} d\sigma \; W_s(\lambda) W_s(\sigma) e^{jm(\lambda-\sigma)}}{B^2(0) \; \left|\int_{-\pi}^{\pi} d\lambda \; W_s(\lambda)\right|^2}$$

$$= \frac{\int_{-\pi}^{\pi} d\lambda \int_{-\pi}^{\pi} d\omega \; W_s(\lambda) W_s(\lambda-\omega) |B(\omega)|^2}{B^2(0) \; \left|\int_{-\pi}^{\pi} d\lambda \; W_s(\lambda)\right|^2} \tag{2.45}$$

If the filtering is strong $(Mq >> K)$, the bandwidth of $B(\omega)$ is much smaller than the bandwidth of the spectral window. The frequency response of the averaging filter can then be approximated with an ideal lowpass filter with DC gain $B(0)$, and cutoff frequency equal to the equivalent noise bandwidth $\Delta\omega_M/2$ of the averaging filter:

$$\Delta\omega_M = \frac{1}{B^2(0)} \int_{-\pi}^{\pi} d\omega \; |B(\omega)|^2 \tag{2.46}$$

The expression for the fractional variance then simplifies to ($\Delta\omega_M << \Delta\omega_a$)

$$\sigma_M^2 \simeq \Delta\omega_M \frac{\int_{-\pi}^{\pi} d\omega \; W_s^2(\omega)}{\left|\int_{-\pi}^{\pi} d\omega \; W_s(\omega)\right|^2} \tag{2.47}$$

Similarly, if the spectral window is approximated with the rectangular (boxcar) function

$$W_s(\omega) = \begin{cases} 1/\Delta\omega_a' & \Delta\omega_a'/2 < \omega < \Delta\omega_a'/2 \\ 0 & \text{elsewhere} \end{cases} \tag{2.48}$$

one obtains the following relation for the strong filtering case:

$$\sigma_M^2 \simeq \Delta\omega_M/\Delta\omega_a' = \Delta f_M/\Delta f_a' \tag{2.49}$$

Hence, under strong filtering the fractional variance of the averaged modified periodogram is equal to the ratio between the bandwidths of the averaging filter and the spectral window. The formula has general validity if the bandwidth of the spectral window is redefined as

$$\Delta\omega_a' = \frac{\left|\int_{\pi}^{\pi} d\omega \; W_s(\omega)\right|^2}{\int_{\pi}^{\pi} d\omega \; W_s^2(\omega)} \tag{2.50}$$

This quantity is denoted the statistical angular bandwidth of the window [56]. It is typically 40% larger than the 3 dB bandwidth of the window.

One important conclusion can be drawn from (2.44) and (2.50): The sidelobes of the spectral window have very small influence on the statistical bandwidth, due to the extremely fast rolloff of $W_s^2(\omega)$. If a signal record is spectrum analysed repeatedly using different windows, the variance of the estimate is solely given by the main lobe width of the window; it is hardly at all affected by the sidelobes. It follows that under strong filtering, the rectangular window has no resolutional advantages compared to a window with better sidelobe behaviour. This occurs since (2.49) implies that the transform length K can be chosen larger for the latter, for the same variance of the spectrum estimate (see Section 3.2.2).

The relation (2.49) can be simplified further if the filter (2.29) is a pure averager ($b(m) = 1/M$). The equivalent noise bandwidth of this filter is from (2.46)

$$\Delta\omega_M = \frac{1}{M^2} \int_{-\pi}^{\pi} d\omega \sum_{m=1}^{M} \sum_{m=1}^{M} e^{-jm\omega} e^{jn\omega} = \frac{2\pi}{M} \tag{2.51}$$

Substitution into (2.49) then yields the result $M\sigma_M^2 \Delta f_a' = 1$, which holds for unity sampling rate. For an arbitrary sampling rate with $MT_s \simeq LT_s = T$ (strong filtering implies $M = L - K + 1 \simeq L$ when $q = 1$), one obtains

$$\sigma^2 \Delta f_a' T \simeq 1 \tag{2.52}$$

stating that <u>under strong averaging the product of fractional variance, spectral resolution and total data collecting time is unity</u>. A reduction of one of these variables implies an increase in one or both of the others. The above relation was originally derived by Nuttall, using two somewhat different procedures [53], [56, eq. (22)]. He also pointed out that the result was identical to what Blackman and Tukey showed to be valid for the smoothed periodogram estimator. Therefore, under strong filtering, averaging periodograms of a partitioned signal sequence is equivalent to smoothing the raw periodogram from the entire sequence, provided the spectral windows are the same.

Both (2.49) and (2.52) were derived under the assumption of maximum overlap ($q = 1$). Fig. 2.3.a indicates that the relations will be good approximations when the fractional overlap exceeds ~ 60% for the Hamming and ~ 85% for the rectangular window.

<u>2.3 First order probability distributions of the averaged and the log averaged periodogram</u>

Additional insight into the performance of the averaged periodogram spectrum estimator is gained from knowledge of the its probability density for a fixed frequency. This is derived in the following.

2.3.1 The sub-periodograms

The modified periodogram can be split into two components. This follows from the definition (2.9), that can be rewritten in the form

$$\tilde{G}(\omega) = \tilde{G}_r(\omega) + \tilde{G}_i(\omega) \tag{2.53}$$

where

$$\tilde{G}_r(\omega) = \frac{1}{K} \mathrm{Re}^2[\tilde{X}(\omega)] \tag{2.54}$$

$$\tilde{G}_i(\omega) = \frac{1}{K} \mathrm{Im}^2[\tilde{X}(\omega)] \tag{2.55}$$

The 'sub-periodograms' $\tilde{G}_r$ and $\tilde{G}_i$ are computed from the real and the imaginary part of the Fourier transform $\tilde{X}$. The expected value of $\tilde{G}_r(\omega)$ can be calculated as follows:

$$\begin{aligned} \langle \tilde{G}_r(\omega) \rangle &= \frac{1}{4K} \langle |\tilde{X}(\omega) + \tilde{X}^*(\omega)|^2 \rangle = \frac{1}{2K} \langle \tilde{X}(\omega)\tilde{X}^*(\omega) \rangle \\ &= \frac{1}{2} \langle \tilde{G}(\omega) \rangle \end{aligned} \tag{2.56}$$

where (2.22) and (2.9) have been used. It follows immediately from (2.53) that

$$\langle 2\tilde{G}_r(\omega) \rangle = \langle 2\tilde{G}_i(\omega) \rangle = \langle \tilde{G}(\omega) \rangle \tag{2.57}$$

This equation suggests that $2\tilde{G}_r$ or $2\tilde{G}_i$ may be used as alternative 'raw' estimators of the power spectrum. This will be utilized in Section 2.4.

Similarly, the cross correlation between $\mathrm{Re}[\tilde{X}(\omega)]$ and $\mathrm{Im}[\tilde{X}(\omega)]$ is

$$\langle \mathrm{Re}[\tilde{X}(\omega)]\mathrm{Im}[\tilde{X}(\omega)] \rangle = \frac{1}{2} \mathrm{Im}[\langle \tilde{X}^2(\omega) \rangle] = 0 \tag{2.58}$$

Hence, the Gaussianess of the complex signal causes $\mathrm{Re}[\tilde{X}(\omega)]$ and $\mathrm{Im}[\tilde{X}(\omega)]$ to be uncorrelated. Now both these variables are linear combinations of zero mean, jointly Gaussian variables, and they are therefore also themselves zero mean Gaussian. It follows that for the class of complex Gaussian signals <u>$\mathrm{Re}[\tilde{X}(\omega)]$ and $\mathrm{Im}[\tilde{X}(\omega)]$ are statistically independent</u>. The normalized sub-periodograms $2\tilde{G}_r(\omega)/\langle \tilde{G}(\omega) \rangle$ and $2\tilde{G}_i(\omega)/\langle \tilde{G}(\omega) \rangle$ are then independent chi square distributed variables, each with one degree of freedom (χ_1^2).

Let the stochastic variable Z_η be chi square distributed with η degrees of freedom. It is well known that [4]:

$$\langle Z_\eta \rangle = \eta \tag{2.59}$$

$$\mathrm{Fracvar}(Z_\eta) = \frac{2}{\eta} \tag{2.60}$$

The fractional variance of the sub-periodograms therefore equals 2, i.e. twice the fractional variance of the modified periodogram itself.

2.3.2 The probability distribution of the averaged periodogram

The chi square distribution has the property that the sum of a number of independent chi square distributed variables itself becomes chi square with η_s degrees of freedom, where η_s is the sum of the individual degrees of freedom over the variables. It follows direcly from the previous paragraph that <u>the normalized modified periodogram $2\tilde{G}(\omega)/\langle\tilde{G}(\omega)\rangle$ is chi square distributed with two degrees of freedom</u>. For real processes, this result has asymptotic validity when $K \to \infty$ [1, p. 239].

It has earlier been shown that periodograms from nonoverlapping signal segments are independent. Consequently, when averaging M periodograms without overlap, the normalized variable $2M\tilde{G}_M(\omega)/\langle\tilde{G}(\omega)\rangle$ is chi square distributed with 2M degrees of freedom. From (2.60), the fractional variance of the averaged periodogram then is 1/M, which agrees with the result obtained in (2.39) with $r = 0$.

The question that now arises is how $\tilde{G}_M(\omega)$ is distributed when either a nonzero overlap and/or a weighted average is employed in (2.29). In these situations, one may still calculate the fractional variance of the estimate from (2.31)-(2.34) and (2.38). From analogy with the previous discussion, it then seems natural to approximate the distribution of $2M_e\tilde{G}_M(\omega)/\langle\tilde{G}(\omega)\rangle$ with a chi square distribution with $2M_e$ degrees of freedom, where $M_e \le M$ is given by

$$M_e = 1/\sigma_M^2 \tag{2.61}$$

Nuttall has shown that this is an excellent approximation to the true distribution of the estimate, regardless of window type, overlap, and the ratio L/K [57]. A similar approach was used in [1] to derive asymptotic expressions for the variance of the smoothed periodogram. In the following, M_e shall be referred to as the <u>efficient</u> number of terms in the averaging sum (2.29). It is the equivalent number of terms M one would have to choose to obtain the same fractional variance using pure averaging and nonoverlapping segments. From Fig. 2.3.a, one has for large M's and 50% overlap the relations $M_e \simeq 0.9\ M$ for the Hamming window, while $M_e \simeq 0.67\ M$ for the rectangular window.

The probability density for the normalized spectrum estimate $\tilde{G}_M(\omega)/\langle\tilde{G}(\omega)\rangle$ can be derived from a well known formula for transformation of probability densities [4, p. 86]:

$$p_Y(y) = p_Z(h^{-1}(y))\left|\frac{d}{dy}\ h^{-1}(y)\right| \tag{2.62}$$

where

$$Y = h(Z) \qquad \Leftrightarrow \qquad Z = h^{-1}(Y) \tag{2.63}$$

The formula is valid provided $h(\cdot)$ is strictly monotonical and its first derivative exists for all values of its argument. Assuming no overlap, it follows that the normalized variable

$$S_M = \frac{\tilde{G}_M(\omega)}{\langle\tilde{G}(\omega)\rangle} \tag{2.64}$$

has the probability distribution

$$p_{S_M}(s_M) = 2M\ p_{Z,2M}(2Ms_M) \tag{2.65}$$

where $p_{Z,\eta}(z)$ is the χ^2_η probability density [4]:

$$p_{Z,\eta}(z) = 2^{-\frac{\eta}{2}}\ \Gamma(\tfrac{\eta}{2})^{-1}\ z^{\frac{\eta}{2}-1}\ \exp(-\tfrac{z}{2}) \qquad z > 0 \tag{2.66}$$

$$\Gamma(\alpha) = \int_0^\infty dt\ t^{\alpha-1}e^{-t} \tag{2.67}$$

$\Gamma(\alpha)$ is the Gamma function. The resulting probability densities have been plotted in Fig. 2.4 for M = 0.5 (which is the density of the sub-periodograms), 1,2,5 and 10. The distributions are skewed, with large positive tails for the smaller M's. They narrow when M increases. For M = 10, the distribution approximates the shape of a Gaussian density. From the Central Limit Theorem it follows that when $M \to \infty$, the distribution will converge to a Gaussian density with unity mean and variance $1/M$.

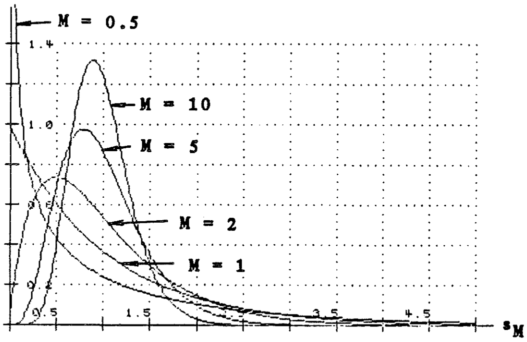

Fig. 2.4 Probability densities for $S_M = \tilde{G}_M/\langle\tilde{G}_M\rangle$, $r = 0$.

2.3.3 Probability distribution of the log averaged periodogram

In engineering applications one is often interested in a display of the power spectrum in a logarithmic scale. The probability distribution for the variable $\tilde{S}_M = 10\lg S_M$ can be derived from the probability density of S_M, using (2.62) and the relations

$$S_M = h^{-1}(\tilde{S}_M) = 10^{\frac{\tilde{S}_M}{10}} \tag{2.68}$$

$$\left|\frac{\partial}{\partial \tilde{S}_M} h^{-1}(\tilde{S}_M)\right| = [\ln 10/10]\ 10^{\frac{\tilde{S}_M}{10}} \tag{2.69}$$

The resulting probability densities are shown in Fig. 2.5.a for the same values of M as in Fig. 2.4. The distributions have large negative tails when M is small, but their modes are all close to 0 dB. When M increases, the distributions approach Gaussian shape faster than the corresponding distributions of S_M.

The means and the standard deviations of the distributions in Fig. 2.5.a have been calculated numerically for various values of M. The results

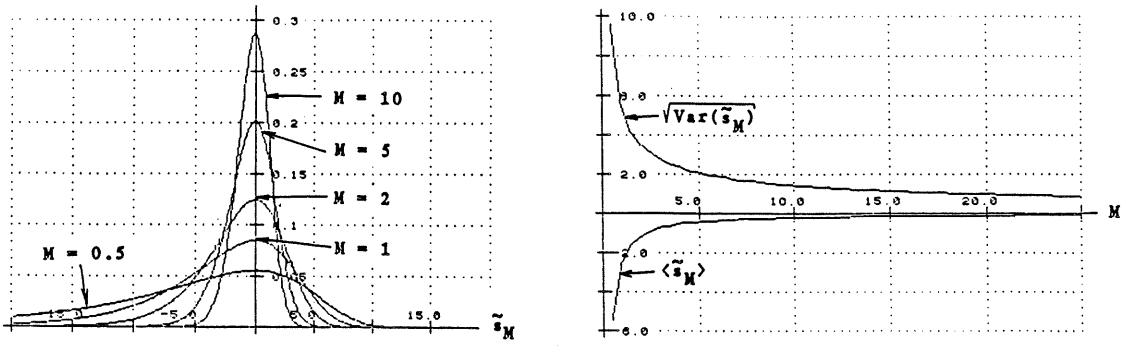

a) b)

Fig. 2.5 a) Probability densities for $\tilde{S}_M = 10 \lg \tilde{G}_M/\langle \tilde{G}_M \rangle$, $r = 0$.
b) Means and standard deviations of the distributions.

are shown in Fig. 2.5.b. Since, from (2.64),

$$\langle 10\lg \tilde{G}_M(\omega) \rangle = \langle \tilde{S}_M \rangle + 10\lg \langle \tilde{G}_M(\omega) \rangle \tag{2.70}$$

and $\langle \tilde{S}_M \rangle$ is nonzero (-2.5 dB for $M = 1$), it follows that $10\lg \tilde{G}_M(\omega)$ is a biased estimator of the dB spectrum. The bias is small for $M > 5$. Since it is independent of the mean, it can be corrected for, even if the exact shape of the spectrum is unknown.

Similarly, the variance of the dB spectrum estimate satisfies the relation

$$Var[10\lg \tilde{G}_M(\omega)] = Var(\tilde{S}_M) \tag{2.71}$$

Therefore, also the variance of the dB-spectrum estimate is independent of the mean. The standard deviation of $\tilde{S}_M$ is approx. 5.6 dB for $M = 1$ (the raw periodogram), but decreases rapidly with increasing M.

2.4 Averaging compressed periodograms

Computing the averaged periodogram from a number of individual 'raw' periodograms is a simple task in a computer possessing floating point arithmetic. High speed spectrum analysers often have to use dedicated integer arithmetic hardware, and then a large number of bits is required to represent linear version of the periodograms (16 bits yields 48 dB resolvable dynamic range). The bit requirement increases additionally during the accumulations of the averaging process. In this case, averaging of linear periodograms seems rather impractical - especially when the final result is to be presented in a compressed form, e.g. dB scale. One method of bypassing the problem is to interchange the order of averaging and compression, i.e. averaging individually compressed modified periodograms. This reduces the number of bits required in the averager. The cost of the reduction is an increase in variance compared to the initial approach. In the following, this increase shall be quantified for some specific forms of the compression function.

The Type 1 averager is defined as

$$\tilde{C}_M^1(k+\frac{M+1}{2}q,\omega;K) = \frac{1}{M}\sum_{m=1}^{M} f_c[\tilde{G}(k+mq,\omega;K)] \tag{2.72}$$

$f_c(\cdot)$ is a suitable compression function which reduces the dynamic range of the average. It shall be assumed that $q > K$, i.e the periodograms are computed from nonoverlapping signal sequences. This implies that they are independent, chi square distributed variables (see Section 2.3.3).

The modified periodogram is the sum of the sub-periodograms $\tilde{G}_r(\omega)$ and $\tilde{G}_i(\omega)$. An alternative way of averaging is to compress the sub-periodograms separately prior to summation. Hence, a Type 2 averager may be defined as

$$\tilde{C}_M^2(k+\frac{M+1}{2}q,\omega;K) = \frac{1}{M}\sum_{m=1}^{M} \{f_c[\tilde{G}_r(k+mq,\omega;K)] + f_c[\tilde{G}_i(k+mq,\omega;K)]\} \tag{2.73}$$

The reason for including this type of averager is that it leads to a cost effective implementation of a Chirp Z Transform spectrum analyser (Section 5.2.2).

The compression function $f_c(\cdot)$ should not be chosen arbitrarily. In order not to introduce additional bias, one must require the expected value of the averaged compressed periodograms $\tilde{C}_M^1$ and $\tilde{C}_M^2$ to have a known bias compared to the correspondingly compressed averaged linear periodogram. Any bias introduced by averaging compressed raw estimates can then be corrected for. It is difficult to continue the discussion in a general context, so we proceed with two specific forms of compression functions in the next sections.

2.4.1 Logaritmic compression

Initially a logaritmic compression function shall be studied:

$$f_c(\cdot) = \ln(\cdot) = \frac{\ln 10}{10}\,(10\lg(\cdot)) \tag{2.74}$$

From (2.60), the expectation value of the Type 1 averager using logarithmic compression can be expressed in terms of the expectation value of the variable $\tilde{S}_1$, eq. (2.68):

$$\langle \tilde{C}_M^1 \rangle = \langle \tilde{C}_1^1 \rangle = \frac{\ln 10}{10}\,\langle \tilde{S}_1 \rangle + \ln\langle \tilde{G} \rangle \tag{2.75}$$

The frequency and time arguments have been omitted for clarity. One effect of averaging the compressed periodogram is therefore a bias term that is independent of the mean of the modified periodogram. It can, if desired, be removed by subtraction. The variance of the Type 1 averaged estimate is

$$\mathrm{Var}(\tilde{C}_M^1) = \left[\frac{\ln 10}{10}\right]^2 \mathrm{Var}(\tilde{S}_1)/M \tag{2.76}$$

since the terms in the sum (2.72) are statistically independent when ω is fixed. In contrast, when using the normal order of averaging and compression, the variance of the resulting log averaged periodogram becomes from (2.74) and (2.71)

$$\mathrm{Var}(\ln \tilde{G}_M) = \left[\frac{\ln 10}{10}\right]^2 \mathrm{Var}(\tilde{S}_M) \tag{2.77}$$

To characterize the effect of the compression, the <u>variance performance index</u> of the Type 1 averager is defined as the ratio between the variances of the average of the individually compressed periodograms, and the compressed averaged periodogram, i.e.

$$r_{v1} = \frac{\mathrm{Var}(\tilde{C}_M^1)}{\mathrm{Var}(\ln \tilde{G}_M)} = \frac{\mathrm{Var}(\tilde{S}_1)}{M\,\mathrm{Var}(\tilde{S}_M)} \tag{2.78}$$

The scaling constant ln 10/10 disappeared through this normalization, showing that the performance index is independent of linear scaling of the compression function. Regardless of the shape of the compression function, one will always have $r_{v1} > 1$. Its size thus expresses the deterioration of estimator performance because of the interchanged order of compression and averaging.

As previously pointed out, the normalized sub-periodograms $\tilde{G}_r/\langle\tilde{G}\rangle$ and $\tilde{G}_i/\langle\tilde{G}\rangle$ are members of the S_M family defined in Section 2.3.3, with $M = 0.5$. Proceeding as above yields for the Type 2 averager

$$\langle\tilde{C}_M^2\rangle = \frac{\ln 10}{10} \langle\tilde{S}_{0.5}\rangle + \ln\langle\tilde{G}\rangle \tag{2.79}$$

$$\mathrm{Var}(\tilde{C}_M^2) = \left[\frac{\ln 10}{10}\right]^2 \mathrm{Var}(\tilde{S}_{0.5})/2M \tag{2.80}$$

The variance performance index for the Type 2 averager thus becomes

$$r_{v2} = \frac{\mathrm{Var}(\tilde{S}_{0.5})}{2M\ \mathrm{Var}(\tilde{S}_M)} \tag{2.81}$$

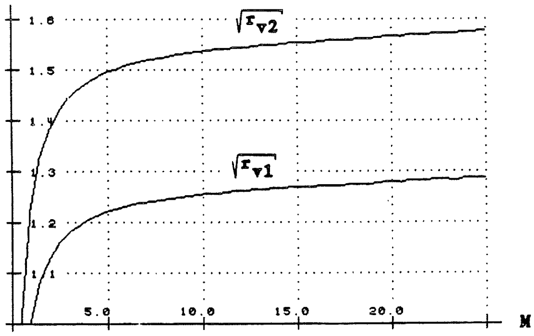

Fig. 2.6 Performance indices for logarithmic compression.

The square root of the indices r_{v1} and r_{v2} are plotted as a function of M in Fig. 2.6. The Type 1 averager is the least sensitive to an interchanged order of compression and averaging. When M is large, its increase in standard deviation levels off at approximately 28%, while it is nearly 57% for the Type 2 averager.

In a typical application, the compression will be incorporated as shown in Fig. 2.7. The periodograms (or sub-periodograms) are passed through a compression, prior to a B bit linear quantizer. Referred to the

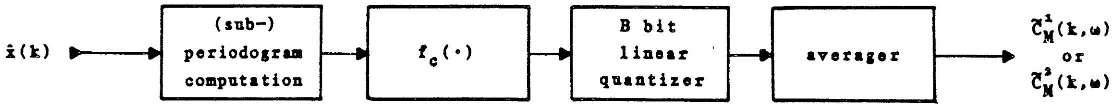

Fig. 2.7 Block diagram of quantization and averaging.

input of the compression function, the quantizer covers a total dynamic range

$$D_{max} = 10\lg \frac{G_{max}}{G_{min}} = 2^B \Delta_q \tag{2.82}$$

where G_{max}, G_{min} are the saturation limits of the quantizer and Δ_q is the dB distance between two adjacent quantization levels. The question that now arises is how large Δ_q can be chosen, without degrading the averaged variables $\tilde{C}^1_M$ and $\tilde{C}^2_M$. Intuitively, one should require the quantization to be so dense that the expected stochastic variations of each spectral component causes it to traverse several quantization levels. This can be ensured, for example, by selecting Δ_q to be less than half the standard deviation of the input data to the quantizer. This yields the numerical results (from Fig. 2.5.b)

$$\Delta_{q1} < \frac{1}{2} \sqrt{Var(\tilde{S}_1)} = 2.8 \text{ dB} \tag{2.83}$$

$$\Delta_{q2} < \frac{1}{2} \sqrt{Var(\tilde{S}_{0.5})} = 4.9 \text{ dB} \tag{2.84}$$

It is possible to analyse the exact implications of this assumption, since the probability density of the log periodogram is known. This work has, however, not been carried out. – Note that when logarithmic compression is employed, the variances of the compressed raw estimates are independent of their means. This implies that also the quantization effects are mean independent.

The useful dynamic range of the averaged estimates is less than $2^B\Delta_q$, since variance peaks or troughs of the input to the quantizer should not be allowed to cause severe saturation. The extremes of the useful dynamic range may be defined as the values $\langle\tilde{G}\rangle_{max}$, $\langle\tilde{G}\rangle_{min}$ that has a fixed probability, say 10%, of causing upper resp. lower saturation of the quantizer. Since $2\tilde{G}/\langle\tilde{G}\rangle$ is chi square distributed with 2 degrees of freedom, it follows that for the Type 1 averager

$$\langle\tilde{G}\rangle_{max1} = \frac{2G_{max}}{Z_{0.1,2}} \tag{2.85}$$

$$\langle\tilde{G}\rangle_{min1} = \frac{2G_{min}}{Z_{0.9,2}} \tag{2.86}$$

where $Z_{\alpha,\eta}$ is the α quantile in the chi square distribution with η degrees of freedom. The resulting 'full quality' dynamic range for the Type 1 averager then becomes

$$\begin{aligned} D_1 &= 10\lg \frac{\langle\tilde{G}\rangle_{max}}{\langle\tilde{G}\rangle_{min}} = 2^B\Delta_q - 10\lg \frac{Z_{0.1,2}}{Z_{0.9,2}} \\ &= 2.8\ 2^B - 13.4\ [dB] \end{aligned} \tag{2.87}$$

where (2.83) has been inserted. Repeating the procedure for the Type 2 averager yields similarly

$$\begin{aligned} D_2 &= 2^B\Delta_q - 10\lg \frac{Z_{0.1,1}}{Z_{0.9,1}} \\ &= 4.9\ 2^B - 22.3\ [dB] \end{aligned} \tag{2.88}$$

Selecting 4 bit quantization hence yields 31 dB dynamic range for the Type 1 averager and 56 dB for the Type 2 version. Increasing B to 5 yields D_1 = 76 dB, D_2 = 134 dB. It is apparent that the use of logarithmic compression prior to quantization is extremely bit-efficient, although it should be admitted that the exact implications of the chosen quantization have not been investigated in detail.

2.4.2 Power function compression

The cost of the bit reduction in the previous section was increased variance, caused by the interchanged order of averaging and compression. This can sometimes be compensated for by increasing the averaging time, but normally a large variance increase cannot be tolerated. Averaging compressed periodograms, where the compression function is less compressive than the logarithm, may then give a lower increase in variance; still the bit requirements may be reduced to an acceptable level. An interesting family of compression functions in this respect are the power functions:

$$f_c(\cdot) = (\cdot)^a \qquad 0 < a \leq 1 \tag{2.89}$$

These functions have the factorization property

$$f_c(\tilde{G}) = f_c(\langle\tilde{G}\rangle) f_c(\tilde{G}/\langle\tilde{G}\rangle) \tag{2.90}$$

It follows that $\langle f_c(\tilde{G})\rangle$ is proportional to $f_c(\langle\tilde{G}\rangle)$, with a constant of proportionality which does not depend on the mean $\langle\tilde{G}\rangle$. Power function compression therefore leads to a mean independent multiplicative bias.

From (2.72) and (2.90) one obtains for the Type 1 averager

$$\langle\tilde{C}_M^1\rangle = \langle\tilde{G}\rangle^a \langle S_1^a\rangle \tag{2.91}$$

$$\mathrm{Var}(\tilde{C}_M^1) = \langle\tilde{G}\rangle^{2a}[\langle S_1^{2a}\rangle - \langle S_1^a\rangle^2]/M \tag{2.92}$$

where the probability distributions of S_M were given in (2.64)-(2.67). Similarly, for the Type 2 averager:

$$\langle\tilde{C}_M^2\rangle = \langle\tilde{G}\rangle^a \langle S_{0.5}^a\rangle \tag{2.93}$$

$$\mathrm{Var}(\tilde{C}_M^2) = \langle\tilde{G}\rangle^{2a}[\langle S_{0.5}^{2a}\rangle - \langle S_{0.5}^a\rangle^2]/2M \tag{2.94}$$

The variance performance indices for the case of power function compression are defined as the ratio between the fractional variances of the types 1 or 2 averagers, and the fractional variance of the correspondingly compressed averaged periodogram. The indices therefore become independent of linear scaling also in this case. The mean and variance of the reference variable follow from analogy with the above equations:

$$\langle\tilde{G}_M^a\rangle = \langle\tilde{G}\rangle^a \langle S_M^a\rangle \tag{2.95}$$

$$\mathrm{Var}(\tilde{G}_M^a) = \langle\tilde{G}\rangle^{2a}[\langle S_M^{2a}\rangle - \langle S_M^a\rangle^2] \tag{2.96}$$

The performance indices in the case of power function compression become

$$r_{v1} = \frac{\text{Fracvar}(S_1^a)}{M\ \text{Fracvar}(S_M^a)} \tag{2.97}$$

$$r_{v2} = \frac{\text{Fracvar}(S_{0.5}^a)}{2M\ \text{Fracvar}(S_M^a)} \tag{2.98}$$

Expressions for the mean $\langle S_M^a \rangle$ can be obtained from the probability density of S_M, eqs. (2.65)-(2.67). Tedious, but straightforward, manipulations yield the simple result

$$\langle S_M^a \rangle = \frac{\Gamma(M+a)}{M^a\ \Gamma(M)} \tag{2.99}$$

which leads to the following solution for the fractional variance of the stochastic variable S_M^a:

$$\text{Fracvar}(S_M^a) = \frac{\Gamma(m+2a)\ \Gamma(m)}{M^a \Gamma(M)} \tag{2.100}$$

Substitution into (2.97) and (2.98) then gives the performance indices. The Gamma function can be calculated by numerical integration of (2.67). The square root of the resulting variance performance indices has been calculated for the compression powers $a = 0.5$ and $a = 0.25$. The results are shown in Fig. 2.8, which indicates that:

i) Averaging the 'amplitude periodogram' $\sqrt{\tilde{G}}$ gives only slightly higher fractional variance than taking the square root $\sqrt{\tilde{G}_M}$ of the averaged periodogram. The increase in fractional standard deviation levels off at approx. 4.5 % for $M > 10$.

ii) The Type 2 averager with $a = 0.5$ corresponds from (2.53)-(2.55) to averaging the absolute values of the real and imaginary part of $\tilde{X}$:

$$\sqrt{2\tilde{G}_r} + \sqrt{2\tilde{G}_i} \sim |\text{Re}[\tilde{X}]| + |\text{Im}[\tilde{X}]|$$

From Fig. 2.8, this gives less than 7% increase in fractional standard deviation compared to the reference $\sqrt{\tilde{G}_M}$. However, the increase relative to the Type 1 averager, that calculates the more complex expression

$$\sqrt{\tilde{G}} \sim \sqrt{\text{Re}^2[\tilde{X}] + \text{Im}^2[\tilde{X}]},$$

is merely 2.2%. In practice, it may be far simpler to compute a sum of absolute values than a full squaring/adding/square root operation (the so-called hypotenuse function). Fig 2.8 indicates that the additional variance introduced by this simplification is very small.

iii) Decreasing the compression power from 0.5 to 0.25 results in a significant deterioration. Again, the Type 2 averager is the most sensitive to compression. The performance indices are still much lower than when logarithmic compression was used ($\sqrt{r_{v1}}$: 1.12 vs. 1.28, $\sqrt{r_{v2}}$: 1.19 vs. 1.57).

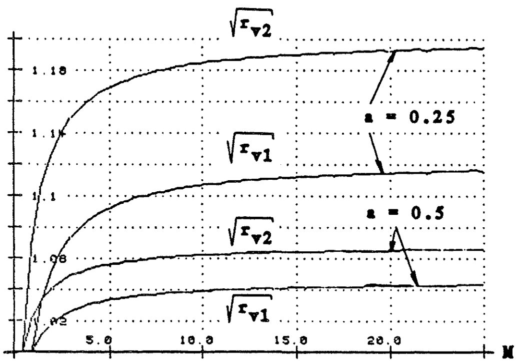

Fig. 2.8 Performance indices for power function compression.

A question that still remains unanswered is how large dynamic range one will obtain in the averaged compressed periodogram for a given number B bit quantization of the compressed 'raw' periodograms. We assume the linear quantization levels $n/2^B$, $n = 1, --, 2^B$. Referred to the input of the compression function, this corresponds to a maximum resolvable dynamic range

$$\begin{aligned} D_{max} &= 10 \lg 2^{\frac{B}{a}} \\ &\simeq 3 \frac{B}{a} \quad [\mathrm{dB}] \end{aligned} \tag{2.101}$$

Again, the full quality dynamic range is considerably less. As in the case of logarithmic compression, the high end is limited by saturation of the quantizer. The low end, however, now is limited by quantization noise. This occurs since the variance of the input variables to the quantizer decreases with decreasing mean, whereas the quantization steps are constant, $\Delta_q = 2^{-B}$. An estimate of the low end of the dynamic range can be found by relating Δ_q to the variance of the input data. Combining (2.92),(2.94) and (2.99) yields

$$\mathrm{Var}(\tilde{G}^a) = \langle\tilde{G}\rangle^{2a}[\Gamma(1+2a) - \Gamma^2(1+a)] \tag{2.102}$$

$$\mathrm{Var}((2\tilde{G}_r)^a) = \frac{1}{\pi} \langle 2\tilde{G}\rangle^{2a}[\sqrt{\pi}\, \Gamma(2a+0.5) - \Gamma^2(a+0.5)) \tag{2.103}$$

It has been used that $\Gamma(0.5) = \sqrt{\pi}$ and $\Gamma(1) \doteq 1$. In the previous section, the quantization steps were required to be less than half the standard deviation of the input data to the quantizer. In this case, this is equivalent to to requiring $\mathrm{Var}(\cdot) > 2^{-2B+2}$. Combining with the above equations then leads to the following lower limits:

$$\langle\tilde{G}\rangle_{min1} = 2^{-\frac{B-1}{a}} [\Gamma(2a+1) - \Gamma^2(a+1)]^{-\frac{1}{2a}} \tag{2.104}$$

$$\langle\tilde{G}\rangle_{min2} = 2^{-1-\frac{B-1}{a}} \frac{1}{\pi} [\sqrt{\pi}\, \Gamma(2a+0.5) - \Gamma^2(a+0.5)]^{-\frac{1}{2a}} \tag{2.105}$$

The saturation limits are the same as in the previous section. For the Type 1 averager, it is given by (2.85) with $G_{max} = 1$:

$$\langle\tilde{G}\rangle_{max1} = \frac{2}{Z_{0.1,2}} = 0.740 \tag{2.106}$$

Similarly, for the Type 2 case:

$$\langle\tilde{G}\rangle_{max2} = \frac{1}{Z_{0.1,1}} = 0.370 \tag{2.107}$$

The resulting full quality dynamic range is the ratio between (2.106) and (2.104) for Type 1, and correspondingly, the ratio between (2.107) and (2.105) for the Type 2 averager. For actual values of the power a, this yields

$$D_1 = \begin{cases} 3B - 4.3 \text{ [dB]} & a=1 \\ 6B - 14 \text{ [dB]} & a=0.5 \\ 12B - 37 \text{ [dB]} & a=0.25 \end{cases} \tag{2.108}$$

$$D_2 = \begin{cases} 3B - 5.8 \text{ [dB]} & a=1 \\ 6B - 15 \text{ [dB]} & a=0.5 \\ 12B - 35 \text{ [dB]} & a=0.25 \end{cases} \tag{2.109}$$

Selecting 8 bit quantization and $a = 1$ (no compression) thus yields $D_1 = 20$ dB and $D_2 = 18$ dB. Reducing the power to $a = 0.5$, the full quality dynamic range increases to $D_1 = 34$ dB and $D_2 = 33$ dB. The number of bits thus can be reduced significantly by selecting $a < 1$.

It should be emphasized that D_1 and D_2 by no means are synonymous with the entire dynamic range represented in the averaged compressed periodogram. The above relations only indicate the range where saturation and quantization effects safely can be neglected. Also, the deterioration due to quantization noise probably is very moderate until the standard deviation approaches the quantization steps Δ_q. This limit is found by replacing B with B+1 in the expressions. Hence, if somewhat increased variance in the low end of the dynamic range can be tolerated, the useful dynamic range is larger than indicated by D_1 and D_2.

The expressions (2.108)-(2.109) show an interesting phenomenon: When the compression power is reduced, the incremental yield in dynamic range for each additional bit increases, but the subtractive term also increases. The underlying mechanism is that when the compression power decreases, the variance of the compressed variable reduces. This causes the lowest useful quantization step to increase. The last effect counteracts the increase in dynamic range due to heavier compression. Therefore, when B is fixed, both (2.104) and (2.105) possess minimas as a function of a, i.e. for a given number of bits there exist powers a_{opt1}, a_{opt2} which maximizes the full quality dynamic range of the estimate. These minima can be found by a numerical search, and the results are listed in Table 2.1. The minima for the Type 2 averager are seen to be considerably smaller than the minima for the Type 1. The reason is that the fractional variances of the subperiodograms are twice that of the periodogram itself. Consequently, the latter variable tolerates less compression than the prior for a reduction in standard deviation to the same value 2^{-B+1}.

B		4	5	6	7	8
a_{opt1}		.29	.14	.060	.033	.020
$\min_a \{\langle\tilde{G}(\omega)\rangle_{min1}\}$	[dB]	-13	-28	-60	-127	-258
$\max_a D_1$	[dB]	11	27	59	125	257
$\sqrt{r_{v1}}$	(large M)	1.10	1.17	1.24	1.26	1.28
a_{opt2}		.17	.081	.039	.026	.016
$\min_a \{\langle\tilde{G}(\omega)\rangle_{min2}\}$	[dB]	-19	-46	-102	-207	-400
$\max_a D_2$	[dB]	15	41	98	202	397
$\sqrt{r_{v2}}$	(large M)	1.27	1.40	1.48	1.51	1.54

Table 2.1 Attainable dynamic range using power function compression vs. number of bits quantization.

The maximum attainable dynamic range using the power function class of compression functions approximately doubles (in dB scale) for each additional bit above 6. This result is qualitatively the same as when using logarithmic compression, eqs. (2.87),(2.88). For quantization levels close to unity, the power functions (2.89) in fact nearly coincides with a logarithmic function. This can be realized by writing

$$10\lg(1 - \frac{m}{2^B})^{\frac{1}{a}} = \frac{1}{a}\, 10\lg(1 - \frac{m}{2^B}) \simeq -m \frac{10}{a\, 2^B \ln 10} \tag{2.110}$$

The above expression is the dB distance between adjacent quantization levels, seen from the input of the compression function. In this approximation it is constant, i.e. corresponding to logarithmic compression. The approximation is good for $m \ll 2^B$. When the compression power a is small, one must require the mean of the compressed periodogram to exceed a large number of the lowest quantization levels for the quantization noise to be small. The approximation then holds over the entire full quality dynamic range. Consequently, the effective compression becomes nearly logarithmic when the compression power is small.

The power a_{opt} is of little practical interest, being so small that the corresponding variance performance indices (also listed in Table 2.1) are comparable with the indices using logarithmic compression. By comparing Table 2.1 with the results from the previous section, it can be seen that power function compression requires approximately 2 more bits than logarithmic compression for the same dynamic range. The latter should therefore normally be preferred, if the overall increase of variance is acceptable.

2.4.3 Asymptotic expressions for the variance performance indices

Asymptotic expressions for the variance performance indices when M is large can be derived by linearizing the compression function. Using logarithmic compression, one may write

$$\begin{aligned}\tilde{S}_M &= 10\lg(\langle S_M\rangle(1 + \frac{S_M-\langle S_M\rangle}{\langle S_M\rangle}) \\ &\simeq 10\lg\langle S_M\rangle + \frac{10}{\ln 10}\,\frac{S_M-\langle S_M\rangle}{\langle S_M\rangle}\end{aligned} \tag{2.111}$$

The approximation is valid when $S_M \simeq \langle S_M\rangle$, i.e. when M is large. Using (2.50), the variance of $\tilde{S}_M$ becomes

$$\begin{aligned}\mathrm{Var}(\tilde{S}_M) &= \left[\frac{10}{\ln 10}\right]^2 \mathrm{Fracvar}(S_M) \\ &= \left[\frac{10}{\ln 10}\right]^2 \frac{1}{M}\end{aligned} \tag{2.112}$$

since $2M\tilde{G}_M/\langle \tilde{G}_M\rangle$ is chi square distributed with 2M degrees of freedom when the signal segments are nonoverlapping. Combining with (2.78) and (2.81) yields the following asymptotic performance indices:

$$r_{v1} \simeq \left[\frac{\ln 10}{10}\right]^2 \mathrm{Var}(\tilde{S}_1) = 1.65 = (1.29)^2 \tag{2.113}$$

$$r_{v2} \simeq \frac{1}{2}\left[\frac{\ln 10}{10}\right]^2 \mathrm{Var}(\tilde{S}_{0.5}) = 2.51 = (1.59)^2 \tag{2.114}$$

which agrees well with Fig. 2.6 (the numerical values have been calculated earlier, Fig. 2.5.b).

Similarly, using power function compression one has the approximation

$$S_M^a \simeq \langle S_M\rangle\left(1 + a\,\frac{S_M-\langle S_M\rangle}{\langle S_M\rangle}\right) \tag{2.115}$$

It follows from (2.65) - (2.67) that

$$\text{Fracvar}(S_M^a) \simeq a^2\ \text{Fracvar}(S_M) = \frac{a^2}{M} \tag{2.116}$$

Inserting this expression into (2.97) - (2.100) yields for large M:

$$r_{v1} \simeq \left(\frac{\Gamma(2a+1)}{\Gamma^2(a+1)} - 1\right)\frac{1}{a^2} \tag{2.117}$$

$$r_{v2} \simeq \left(\sqrt{\pi}\ \frac{\Gamma(2a+0.5)}{\Gamma^2(a+0.5)} - 1\right)\frac{1}{2a^2} \tag{2.118}$$

Selecting the compression power $a = 0.5$ leads to the numerical values

$$r_{v1} \simeq \frac{4}{\pi}\,(4-\pi) = 1.093 = (1.045)^2 \tag{2.119}$$

$$r_{v2} \simeq \pi - 2 = 1.142 = (1.068)^2 \tag{2.120}$$

which agrees with Fig. 2.8.

Finally, asymptotic performance indices when M is large and $a \to 0$ may be derived by expanding the Gamma function in series to the second order in the power a in (2.117) and (2.118). By setting

$$\Gamma(a+1) \simeq 1 + \dot{\Gamma}(1)a + \frac{1}{2}\,\ddot{\Gamma}(1)a^2 \tag{2.121}$$

$$\Gamma(a+0.5) \simeq \sqrt{\pi} + \dot{\Gamma}(0.5)a + \frac{1}{2}\,\ddot{\Gamma}(0.5)a^2 \tag{2.122}$$

one obtains the asymptotic expressions

$$\lim_{\substack{a \to 0\\ M \to \infty}} r_{v1} = \ddot{\Gamma}(1) - \dot{\Gamma}^2(1) \tag{2.123}$$

$$\lim_{\substack{a \to 0\\ M \to \infty}} r_{v2} = \frac{1}{2\pi}\left(\sqrt{\pi}\ \ddot{\Gamma}(0.5) - \dot{\Gamma}^2(0.5)\right) \tag{2.124}$$

The derivatives can be evaluated by differentiating (2.67):

$$\dot{\Gamma}(\alpha) = \int_0^\infty dt \ \ln t \ t^{\alpha-1} e^{-t} \tag{2.125}$$

$$\ddot{\Gamma}(\alpha) = \int_0^\infty dt \ \ln^2 t \ t^{\alpha-1} e^{-t} \tag{2.126}$$

By direct comparison with the probability distribution functions for S_M, eq. (2.65), the following relations are realized (the numerical values are calculated from numerical integration of (2.125) and (2.126)):

$$\dot{\Gamma}(1) = \langle \ln S_1 \rangle = -0.5772 \tag{2.127}$$

$$\ddot{\Gamma}(1) = \langle \ln^2 S_1 \rangle = 1.978 \tag{2.128}$$

$$\dot{\Gamma}(0.5) = \sqrt{\pi} \ \langle \ln(2S_{0.5}) \rangle = -3.480 \tag{2.129}$$

$$\ddot{\Gamma}(0.5) = \sqrt{\pi} \ \langle \ln^2(2S_{0.5}) \rangle = 15.57 \tag{2.130}$$

Inserting this into (2.123), (2.124) yields finally

$$\lim_{\substack{M \to \infty \\ a \to 0}} r_{v1} = \mathrm{Var}(\ln S_1) = \left[\frac{\ln 10}{10}\right]^2 \mathrm{Var}(\tilde{S}_1) \tag{2.131}$$

$$\lim_{\substack{M \to \infty \\ a \to 0}} r_{v2} = \frac{1}{2} \mathrm{Var}(\ln S_{0.5}) = \frac{1}{2} \left[\frac{\ln 10}{10}\right]^2 \mathrm{Var}(\tilde{S}_{0.5}) \tag{2.132}$$

which are identical to the asymptotic performance indices using logarithmic compression. Thus, when the compression power a is reduced towards zero, the performance indices become the same as when logarithmic compression is employed. This confirms the tendencies shown in Table 2.1 for small compression powers.

2.5 Rejecting white noise from the periodogram

In Doppler ultrasound blood velocity measurements, the signal is always contaminated with white noise. Frequently the signal to noise ratio is poor. The time varying periodogram is often displayed in sonagram format (Section 3.3). To get a clear sonagram outline of the Doppler spectrum, it may be advantageous to remove the noise part of the spectrum estimate prior to display. Since the spectrum of white noise is flat, it can be removed by thresholding. The efficiency of this noise reduction scheme is analysed in the following.

We assume a rectangular signal spectrum with spectral density s, in white noise with spectral density n, Fig. 2.9.a. The threshold device has the transfer function shown in Fig. 2.9.b:

$$f_t(g) = \begin{cases} g - g_o & g > g_o \\ 0 & \text{elsewhere} \end{cases} \tag{2.133}$$

By choosing $g_o = n$ and performing the thresholding operation $f_t(G(\omega))$, the true signal spectrum is recovered, Fig. 2.9.c. However, in a practical situation, only the estimate $\tilde{G}_M(\omega)$ is known, Fig. 2.9.d. This estimate may have a large variance, and one must select $g_o > n$ to obtain efficient noise suppression. The first question to be answered is where the threshold must be set for the noise estimate to be less than g_o with probability α_n. It is assumed that K is large, so that the averaged periodogram $\tilde{G}_M$ is essentially unbiased. From Section 2.3.2, the variable $2M_e \, \tilde{G}_M(\omega)/n$ is approximately distributed $\chi^2_{2M_e}$ in the noise parts of the frequency axis. Consequently, the threshold must satisfy

$$\frac{g_o}{n} > \frac{Z_{1-\alpha_n, 2M_e}}{2M_e} \tag{2.134}$$

where $Z_{\alpha,\eta}$ is the α quantile in the χ^2_η distribution. The threshold has been calculated numerically as a function of M_e, and it is plotted in Fig. 2.10.a for the probabilities $\alpha_n = 0.95$ and $\alpha_n = 0.99$. With no averaging ($M_e = 1$), g_o/n must be set to 4.8 dB for $\alpha_n = .95$, increasing to 6.6 dB for $\alpha_n = 0.99$. The threshold level decreases rapidly with increasing averaging.

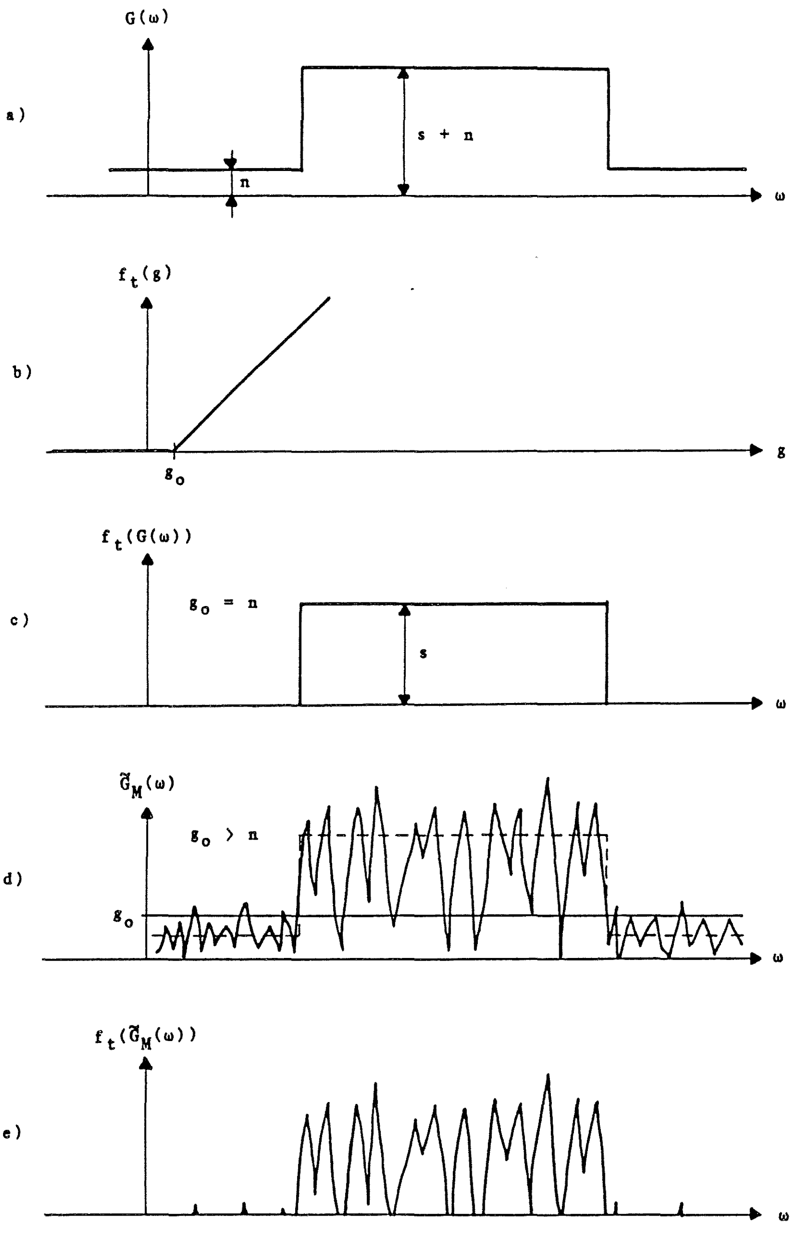

Fig. 2.9 Suppression of white noise by thresholding

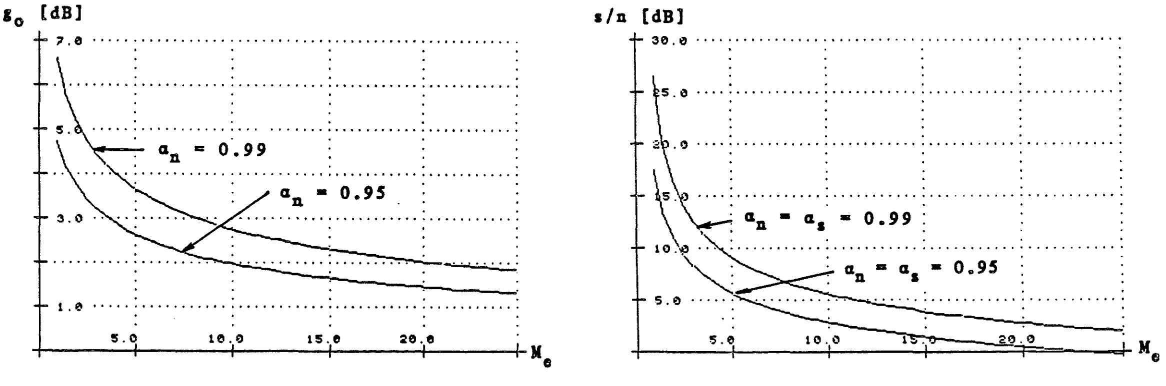

a) b)

Fig. 2.10 a) Reject threshold level versus M_e.
b) Critical signal to noise ratio for efficient rejection.

The thresholding also removes some of the frequency components in the signal part of the ω-axis, as illustrated in Fig. 2.9.e. The next question to be answered is how large the spectral signal to noise ratio s/n must be for any frequency component in the signal part of the ω-axis to exceed the threshold with probability α_s. Reasoning as above, one obtains

$$\frac{s+n}{g_o} > \frac{2M_e}{Z_{\alpha_s,2M_e}} \qquad (2.135)$$

Eliminating g_o from (2.134) and (2.135) finally yields

$$\frac{s}{n} > \frac{Z_{1-\alpha_n,2M_e}}{Z_{\alpha_s,2M_e}} - 1 \qquad (2.136)$$

This quantity has been calculated, and the result is plotted in Fig. 2.10.b for $\alpha_s = \alpha_n = 0.95$ and $\alpha_s = \alpha_n = 0.99$. The 'critical' spectral signal to noise ratio reduces strongly with increasing averaging, starting at 26.6 dB when $M_e = 1$ for the detection probability 0.99. The results in Fig. 2.10.b indicate that rejection of noise by thresholding is <u>not</u> efficient, unless either some averaging of periodograms is introduced, or the spectral signal to noise ratio is large. In the latter case, the yield of the thresholding is small anyway.

2.6 Computing the periodogram using the Discrete Fourier Transform (DFT)

2.6.1 The ordinary DFT

The DFT coefficients $\{F(n;N)\}$ of a complex sequence $\{\hat{x}(k)\}$, $k = 1,--,N$, is the Fourier transform of the sequence evaluated for $\omega = 2\pi n/N$, $n = 0,--,N-1$. They are given by

$$F(n;N) = \sum_{k=1}^{N} \hat{x}(k) e^{-j\frac{2\pi kn}{N}} \tag{2.137}$$

These coefficients can be calculated efficiently in a digital computer by means of an N-point Fast Fourier Transform (FFT) algorithm [3]. The most common algorithms are of the radix 2 type, which require N to be a power of 2.

The modified periodogram $\tilde{G}(\omega;K)$ can be computed on an N point grid using the FFT algorithm, provided $N \geq K$ [7]. This is easily recognized from (2.10) and (2.137), which yields

$$\begin{aligned} \tilde{X}(K/2,2\pi n/N;K) &= \sum_{k=1}^{K} w(k;K)\hat{x}(k) e^{-j\frac{2\pi kn}{N}} \\ &= \sum_{k=1}^{N} [w(k;K)\hat{x}(k)] e^{-j\frac{2\pi kn}{N}} \end{aligned} \tag{2.138}$$

The above expression is the DFT of the sequence $\{w(k;K)\hat{x}(k)]$, $k = 1--,N$, augmented with $N - K$ zeros. The change of the upper limit of the summation can be done since $w(k;K) = 0$ for $k > K$. The periodogram ordinates $\tilde{G}(K/2,2\pi n/N;K)$ can then be constructed by squaring and normalizing $\tilde{X}$, eq. (2.9). An estimate of the sampled power spectrum outside the interval $[0,2\pi(N-1)/N]$ is obtained by the periodic expansion

$$\tilde{G}(K/2,2\pi m + 2\pi n/N;K) = \tilde{G}(K/2,2\pi n/N;K) \tag{2.139}$$

This property shall be utilized in Chapter 3.

2.6.2 The sliding DFT

The difference between the sliding and the ordinary DFT is that the input data is advanced one sample each time a new spectral component is computed [16]. It is defined as

$$F_s(k \bmod N;N) = \sum_{m=k-N}^{k-1} \hat{x}(m)\, e^{-j\frac{2\pi mk}{N}} \qquad (2.140)$$

where (k mod N) is the remainder of the division k/N, $0 \le k \bmod N < N$. The sliding Discrete Fourier Transform destroys phase information when applied to a general waveform, but for periodogram analysis of stationary stochastic signals, it is applicable (the periodogram contains no phase information).

The sliding transform can be computed efficiently using the Chirp Z Transform [16]. The sliding transformer is then a single in/single out device, which uses the complex Doppler signal $\hat{x}(k)$ as an input, and responds with $F_s(k;N)$ on the output. It can be shown that such a device can also be used to compute the ordinary DFT of a signal sequence: Let the periodic expansion of the sequence be defined by

$$\hat{x}_p(k) = \hat{x}(k \bmod N) \qquad (2.141)$$

When $\{\hat{x}_p(k)\}$ is the input to the sliding transformer, its output will become periodic. In the time interval $k = 0,\text{--},N-1$, it is given by

$$\begin{aligned} F_s(k;N) &= \sum_{m=k}^{N} \hat{x}_p(m)\, e^{-j\frac{2\pi mk}{N}} + \sum_{m=N+1}^{k+N-1} \hat{x}_p(m)\, e^{-j\frac{2\pi mk}{N}} \\ &= \sum_{m=k}^{N} \hat{x}_p(m)\, e^{-j\frac{2\pi mk}{N}} + \sum_{m=1}^{k-1} \hat{x}_p(m)\, e^{-j\frac{2\pi mk}{N}} \qquad (2.142) \\ &= \sum_{m=1}^{N} \hat{x}_p(m)\, e^{-j\frac{2\pi mk}{N}} \qquad k = 0,\dots,N-1 \end{aligned}$$

which is recognized as the ordinary DFT of the N-point sequence $\{\hat{x}(k)\}$. Therefore, the DFT of an arbitrary waveform can be computed by feeding the waveform twice into the sliding transformer. Since the transformer has an N sample memory, its first $N - 1$ output samples must be discarded, while the next N samples are the desired DFT coefficients.

2.7 Summary of Chapter 2

The properties of the averaged modified periodogram spectrum estimator have been studied when applied to complex Gaussian signals. The main results are:

A. The 'raw' modified periodogram is a biased, high variance estimator of the power spectrum. The fractional variance of the estimate at a fixed frequency is unity, regardless of the transform length K and the window type. This simple result occurs only for complex Gaussian signals, but it has asymptotic validity when $K \to \infty$ also for real Gaussian signals. The magnitude of the bias can be controlled by selecting proper windowing of the data sequence when K is large.

B. The real and the imaginary part of the Fourier transform of the windowed signal sequence, $Re[\tilde{X}(\omega)]$ and $Im[\tilde{X}(\omega)]$, are statistically independent for any fixed ω.

C. Averaging M modified periodograms, constructed from different K-sample segments of the signal, reduces the fractional variance of the estimate to $1/M_e$, where $M_e \leq M$ is the efficient number of terms in the averaging sum. For nonoverlapping signal segments the periodograms are statistically independent, which ensures $M_e = M$. When the available signal record is limited, additional reduction in variance can be obtained by selecting some amount of overlap between adjacent segments. Increasing the overlap above a certain limit (~ 55% for the Hamming window) yields very little additional reduction in variance.

D. The product of fractional variance of the spectrum estimate, spectral resolution and the total data collecting time is unity, provided the ratio record length to segment length is large, and the overlap between adjacent signal segments is sufficiently large.

E. When averaging M periodograms from nonoverlapping signal segments, the variable $2M\tilde{G}_M(\omega)/\langle\tilde{G}_M(\omega)\rangle$ is chi square distributed with 2M degrees of freedom. When the segments are overlapping, the distribution of the variable $2M_e\tilde{G}_M(\omega)/\langle\tilde{G}_M(\omega)\rangle$ can be approximated with a chi square distribution with $2M_e$ degrees of freedom; $M_e \leq M$.

F. Averaging individually compressed modified periodograms allows for a large reduction of bits in a digital spectrum averager device. The compression introduces a known bias if proper compression characteristics are selected (e.g., logarithmic or power function compression). The variance of the average of individually compressed periodogram is higher than if the order of averaging and compression is interchanged, but the increase is moderate when the compression is weak. For example, averaging the square root of the modified periodogram gives less than 10% higher variance compared to taking the square root of the averaged linear periodogram; the bit requirements to the averager is reduced by nearly a factor 2 by this operation.

G. The amplitude periodogram is defined as

$$\sqrt{\tilde{G}(\omega)} \sim \sqrt{Re^2[\tilde{X}(\omega)] + Im^2[\tilde{X}(\omega)]}$$

The above expression can be replaced by the simpler

$$|Re[\tilde{X}(\omega)]| + |Im[\tilde{X}(\omega)]|$$

The expectation values of the two expressions are proportional when the mean $\langle\tilde{G}(\omega)\rangle$ varies. Averaging the latter expression yields a fractional variance of the point estimate which is only 4.5% higher than when averaging the amplitude periodogram $\sqrt{\tilde{G}(\omega)}$.

H. White noise can be rejected from the averaged modified periodogram by thresholding. The procedure is efficient even for low spectral signal to noise ratios (5-10 dB) if M_e is moderately large (> 5). However, the procedure is not efficient if averaging is not performed.

I. The modified periodogram can be computed efficiently by means of FFT or CZT techniques. An N point DFT may be used for calculating periodograms of different transform lengths $K \leq N$, simply by augmenting the sequence to be transformed with $N - K$ zeros.

3. THE PERIODOGRAM IN DOPPLER ULTRASOUND SIGNAL ANALYSIS

In this chapter, it will be focused on practical aspects of spectral analysis in Doppler ultrasound blood velocity measurements. Section 3.1 contains a short review of the properties of the Doppler signal, while limitations in the quality of the spectrum estimate arising from the rapid time variations of arterial velocity fields are analysed in Section 3.2. Other subjects covered are display of the spectrum estimate, and frequency aliasing in different types of Doppler instruments. Finally, Automatic Gain Control of the Doppler signal prior to the spectrum analysis is discussed.

3.1 Some properties of the Doppler signal in blood velocity measurements

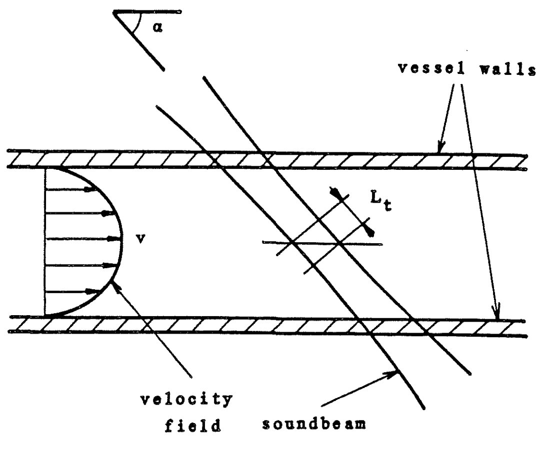

Fig. 3.1 Measurement of blood velocity by Doppler ultrasound.

A single red blood cell travelling through the sensitivity region (sample volume) of the Doppler instrument with velocity v, causes a burst of Doppler oscillations with the frequency

$$f_d = \frac{2v}{c_b} f_o \cos \alpha \qquad (3.1)$$

where f_o is the ultrasound carrier frequency, c_b is the speed of sound in blood (1560 m/s), and α is the angle between the sound beam and the velocity vector, Fig. 3.1. Fig. 3.2.a shows a typical Doppler return from a single scatterer. It has time duration T_t, the transit time of the scatterer across the sample volume,

$$T_t = \frac{L_t}{v \cos \alpha} = \frac{\Omega_t \lambda_o}{v \cos \alpha} \tag{3.2}$$

The transit length $L_t = \Omega_t \lambda_o$ is the projection of the velocity path into the soundbeam direction. Ω_t is a measure of the transit length in terms of wavelengths λ_o of the carrier frequency. The power spectrum of this Doppler burst is a spectral line with center frequency $\omega_d = 2\pi f_d$ and an angular bandwidth

$$\Delta\omega_t = k_t \frac{2\pi}{T_t} = k_t \frac{\omega_d}{2\Omega_t} \tag{3.3}$$

using (3.1) and (3.2), Fig. 3.2.b. The shape factor k_t depends on the envelope of the Doppler burst (compare with (2.18)). The fractional bandwith $\Delta\omega_t/\omega_d$ is independent of the center frequency ω_d. In PW Doppler measurements, the transit length is bounded by the duration of the emitted soundburst. The maximum fractional transit length Ω_t (ocurring when $\alpha = 0$) typically ranges from 2 - 10, depending on the resolution of the system.

In most measurement situations, scatterers with different velocities are present in the sample volume at the same time. It has been shown that the power spectrum of the resulting Doppler signal via the Doppler equation (3.1) corresponds to a blurred (smoothed) version of the weightened velocity distribution in the sample volume [5]. The weighting function is the soundbeam intensity across the sample volume, while the major contribution to the blurring is a convolution between the velocity distribution and a transit time kernel with frequency dependent spectral width given by (3.3).

When it comes to spectrum analysis, it is an important observation that the Doppler signal in ultrasound blood velocity measurements always has a nonzero bandwidth. It follows from the above discussion that in the case of a uniform velocity distribution, it is rarely less than 5 - 10% of its center frequency. In the presence of noise, this bandwidth limits the accuracy by which one can measure e.g. the maximum blood velocity in the sample volume.

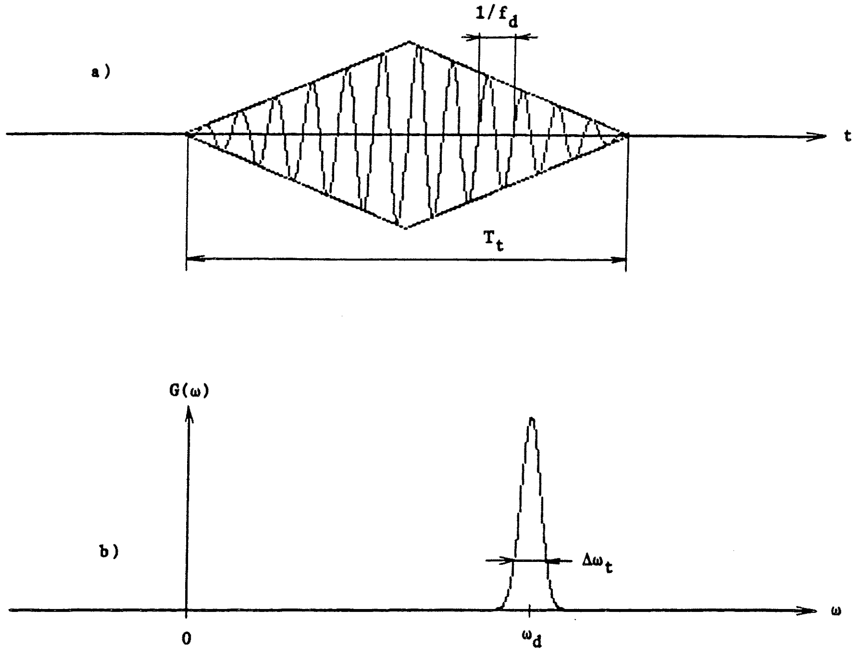

Fig. 3.2 a) Doppler burst from a single scatterer.
b) Power spectrum of Doppler burst.

3.2 Short time spectrum analysis of nonstationary Doppler signals

While the theory in Chapter 2 was derived assuming stationary Doppler signals, applications in blood velocity measurements involve measurements on time varying velocity fields in the human arteries and the heart. The Doppler signal then becomes nonstationary (evolutionary), but because of its Gaussianness it is still completely characterized by its autocorrelation function. This now, however, becomes a function of both time and lag, i.e. $R_{\hat{x}\hat{x}} = R_{\hat{x}\hat{x}}(t,t+\tau)$. Although the velocity field is pulsatile, the temporal volume flow in the vessels has lowpass time variation, with small components above 10-15 Hz [34]. Therefore, in the absence of turbulence, the velocity field changes little if it is observed for a sufficiently short time T. For typical arteries, T should not be much larger than 10 ms. Within this time frame, the Doppler signal may be assumed to be stationary. This quasistationarity approach implies that, when frequency broadening effects are negligible (see [23] for a detailed discussion), the expected value of a periodogram computed from a 10 ms signal record corresponds to the instantaneous velocity distribution in the sample volume, convolved with the spectral window $W_s(\omega;K)$, eq. (2.15). The velocity field may change significantly during the data collection if T is increased much above 10 ms. This would cause additional broadening of the shorttime spectrum during the phases of blood flow when the acceleration is strong. The consequences of the limited data collecting time are discussed below.

3.2.1 Resolution

The maximum frequency resolution one can obtain in periodogram spectrum analysis with data collecting time limited to T = 10 ms is

$$\Delta f_a = \Delta\omega_a/2\pi = k_w/T = 120 \text{ Hz} \tag{3.4}$$

where rectangular windowing has been assumed ($k_w = 1.21$), eq. (2.18). For a given ultrasound carrier frequency, the corresponding maximal velocity resolution is ($\cos\alpha = 1$)

$$\Delta v_a = \frac{c_b}{2f_o}\Delta f_a = \frac{9.4}{f_o\ [\text{Mhz}]}\ \text{cm/s} \tag{3.5}$$

However, resolution and variance are inversely related when the data record is limited, and one should seek to reduce the resolution as much as possible to increase the stability of the spectrum estimate. According to the previous section, the minimum bandwidth of the Doppler spectrum is limited by the transit time effect. In a case with plug flow in the sample volume, the bandwidth of the spectrum estimate is roughly the largest of the pair $(\Delta\omega_a, \Delta\omega_t)$, eqs. (2.18), (3.3). These equations can be combined to form the equivalent requirements [34]

$$\Delta\omega_a < \Delta\omega_t \quad \Longleftrightarrow \quad K > 2\Omega_t \frac{k_w}{k_t}\frac{f_s}{f_d} \tag{3.6}$$

When the shape factors k_w and k_t are equal, the above equation corresponds to requiring the data collecting time KT_s to each 'raw' periodogram to be larger than the transit time of the scatterers. It follows from (3.4) that for a typical Doppler signal with fractional bandwidth 10%, the above condition cannot be satisfied unless the Doppler shift exceeds ~ 1 kHz. Consequently, a low variance averaged periodogram with resolution equal to the transit time bandwidth of the signal cannot be obtained from a 10 ms signal segment, unless the Doppler frequency is several kHz.

The situation is somewhat more complex when the blood velocity is time varying, and there are velocity gradients in the sample volume. Then the frequency f_d that applies in the above formula is the Doppler shift that have the longest correlation time, i.e. that corresponding to the temporal and spatial minimum velocity. However, the minimum velocity is a parameter which normally is of little interest in clinical applications. In contrast, one most often wants to estimate the temporal peak, spatial maximum velocity in the sample volume. The resolution may then be reduced until it approaches the transit time bandwidth at f_p, the temporal peak Doppler frequency. If the sampling frequency of the spectrum analyser is variable, the ratio f_s/f_p may be reduced until aliasing occurs. For a unidirectional velocity field its minimum value is unity. Now Ω_t typically ranges from 2-10. Eq. (3.6) then indicates that a fairly small K is sufficient when estimation of the peak Doppler shift f_p is the important issue. - Priestly recommends that the resolution of the spectrum analyser should be chosen not less than half the bandwidth of the finest spectrum details that is to be reproduced [4, p. 520]. In the above situation, with $f_s/f_p = 1$, this leads to the requirement $K \geq 4\Omega_t$.

3.2.2 Variance

The fractional variance of the spectrum estimate has the functional dependency $\sigma_M^2 = f(L/K;r)$ (see Section 2.2.2). Using (2.18), the argument L/K can be rewritten to

$$\frac{L}{K} = \frac{T}{k_w} \Delta f_a \tag{3.7}$$

where $T = LT_s$. Eqs. (3.5) and (3.7) then yield

$$\frac{L}{K} = \frac{2Tf_o}{c_b k_w} \Delta v_a \tag{3.8}$$

Fig. 2.3.b is replotted in Fig. 3.3 for the case 50% overlap, but now with velocity resolution Δv_a as the dependent parameter. The figure shows the fractional standard deviation vs. velocity resolution. The

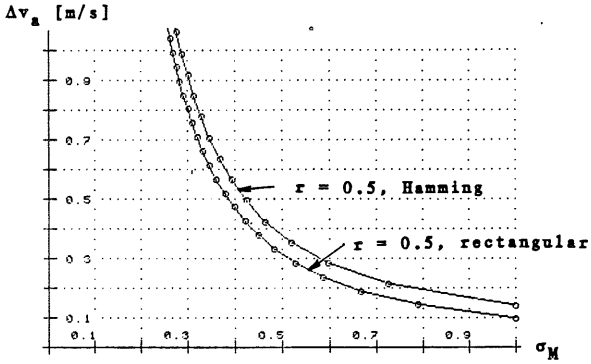

Fig. 3.3 Velocity resolution vs. fractional standard deviation of spectrum estimate (f_o = 1 MHz and T = 10 ms).

y-axis is scaled in m/s, assuming f_o = 1 MHz and T = 10 ms. If f_o or T are increased, the scaling of the y-axis reduces proportionally. Its use is best illustrated by an example: When employing a pulsed Doppler instrument with $\Omega_t = 5$, the fractional transit time bandwidth is approximately 10%, eq. (3.3). If the peak blood velocity is 2 m/s, a resonable choice of the velocity resolution is $\Delta v_a \sim 0.1$ m/s. Using the Hamming window, f_o = 2 MHz and 10 ms record length, the resulting fractional standard deviation of the estimate becomes approximately 0.7, from Fig. 3.3. Increasing the ultrasound carrier frequency to 5 MHz leads to a decrease in the standard deviation to 0.38. This clearly indicates that if one simultaneously wants good velocity resolution and low variance, the highest possible ultrasound carrier frequency should be employed. The underlying mechanism is that the Doppler shift, and thereby the signal bandwidth, increases with increasing carrier frequency.

In Fig. 3.3 it is also apparent that the relative difference in resolution when using the Hamming and the rectangular window, decreases rapidly when σ_M reduces. The reason is that to obtain a given $\sigma_M << 1$ (strong filtering) using the rectangular window, one needs a larger M than when the Hamming window is used. Since the length of the data record is fixed, this implies that the individual segment length K must be chosen smaller in the case of the rectangular window. Fig. 3.3 is merely a manifestation of what has previously been stated in (2.49). In fact, the two curves in Fig. 3.3 would have overlapped for small σ_M if the bandwidth definition $\Delta\omega_a'$ had been used to determine the constant k_w in (3.8), and the overlap had been increased to ~ 60% for the Hamming and ~ 85% for the rectangular window. This follows from (2.52) and Fig. 2.3.a.

3.3 Display of the spectrum

In clinical applications of Doppler ultrasound, the periodogram is computed in real time on a time-frequency grid, most often using DFT techniques. The available information is then contained in a matrix

$$\{G_s(m,n)\} = \{\tilde{G}_M(m(1-r)K, n\omega_s/N; K\} \qquad \begin{array}{l} n = -(N/2)+1,\dots,N/2 \\ m = 0,1,2,\dots \end{array} \qquad (3.9)$$

In the above partition of the frequency axis, the periodogram covers a symmetric frequency range from $-\omega_s/2$ to $\omega_s/2$. Use of asymmetric ranges will be discussed later. The matrix $\{G_s(m,n)\}$ sometimes is displayed as a 3 dimensional 'hidden line' plot [24][25], shown in Fig. 3.4.a (dB scale). On this occation, the Doppler signal was measured on the common carotid artery using pulsed Doppler with f_o = 5 MHz, Ω_t ~ 6, and a broad sound beam covering the entire artery cross section. The display shows raw periodograms, computed using the Hamming window with N = K = 128 and f_s = 8 kHz.

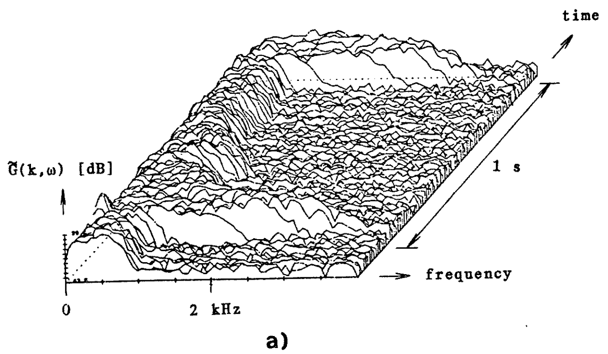

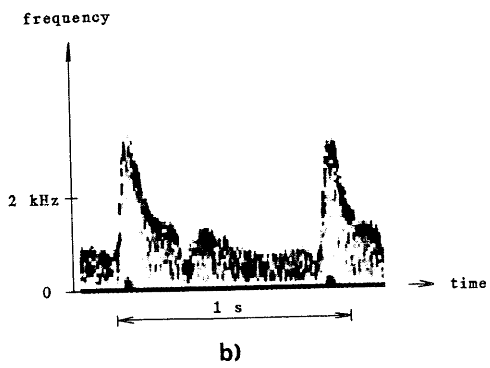

Fig. 3.4 Display of the spectrum estimate:
a) Hidden line format (dB plot).
b) Sonagram.

A more common display format is the sonagram (sonogram, spectragram, spectral display), shown in Fig. 3.4.b for the same signal. The paper darkening at the coordinate (m,n) is related to $G_s(m,n)$ by a monotonical grayscale transfer function (square root in the figure). The sonagram format is widely used because it is relatively easy to display and interprete, even though the hidden line display may provide more quantitative information about details of the spectral density. The strong, low frequency darkening of the sonagram during the upstroke of the velocity waveform is caused by remnants of wall motion signals. These artifacts can also be seen in Fig. 3.4.a.

All sonagrams presented in this report are made using the DAISY real time spectrum analyser (Vingmed A/S) [12]. DAISY is based on a Hamming windowed sliding DFT (see Section 4.1.2), with the parameters $N = K = 64$. No averaging is employed. The sampling frequency is continuously variable in the range 2-40 kHz, or it may be synchronized with the PRF of a pulsed Doppler instrument. The sonagrams prints are made using a fiber optic stripchart recorder.

For a given type of spectrum analyser several aspects determine the visual quality of the sonagram;

i) grayscale transfer function;
ii) pixel size of the picture presented;
iii) degree of background noise.

i) The transfer function from power spectral density to grayscale should be chosen compressive, as a linear transfer yields uneven, almost unreadable sonagrams, due to the large variance of the spectrum estimate. A compressive transfer function (e.g. square root) both enables display of a higher dynamic range in spectral density, and stabilizes the effect of the variance. However, the compression enhances weak frequency components, and it is important to realize that the apparent velocity distributions from the sonagram are broader than the real ones. The effect of varying the grayscale transfer function has been demonstrated by others [13, p. 48]. - A heavy compression is desirable when the spectral density near the maximum Doppler frequency (the sonagram envelope) is much smaller than that of the lower frequencies. This is commonly the case when using CW Doppler for measurements on flow jets in heart lesions [13]. A large dynamic range in the spectral display may then be necessary to visualize the envelope of the sonagram.

The choice of grayscale transfer function depends in practice also on the bandwidth of the Doppler spectrum relative to the sampling frequency of the spectrum analyser. This is due to the fact that a broad band signal yields a smaller spectral density than a narrowband signal of the same power. Experiences with DAISY indicate that good spectral displays can be obtained in most situations if the spectral dynamic range coded into 16 shades of gray can be varied in the range 25 to 40 dB.

ii) The quality of the sonagram depends to some extent on the pixel size in the display. Generally spoken, a spectral display consisting of small pixels tends to look better than one with more coarse quantizing. The number of pixels in the frequency direction (vertically) normally equals N, i.e. equal to the number of signal samples in the DFT. When N is small (DAISY: N = 64) an improved display is obtained by linear interpolation to 2N or more frequency points. This is shown by an experiment performed with DAISY in Fig. 3.5. The improvement when 128 frequency bins are displayed (lower part of the figure) is both due to smaller pixel size and the inherent smoothing effect of the interpolation.

Unless horizontal interpolation is done, the pixel size in the time direction becomes equal to the processing time of the spectrum analyser. In Fig. 3.5, this time is $64/f_s$ (3.8 ms for f_s = 17 kHz, 10 ms for f_s = 6.5 kHz). Even if DAISY does not average adjacent periodograms, an apparent reduction of variance results when the Doppler signal is oversamled (f_d/f_s small). The frequency resolution then degrades, and since the processing time decreases, the pixelsize in the time direction also decreases. If the sonagram is held at some distance from the eye, the individual spectrum estimates can no longer be resolved, and the sonagram appears to be smoothed. This effect is clearly present in Fig. 3.5.

iii) It may be desirable to remove the backgrond noise from the sonagram to get a cleaner outline of the Doppler frequencies. This can be done employing the thresholding technique discussed in Section 2.5. However, bearing the earlier results in mind, efficient rejection of a white noise spectrum cannot be done without deterioration of the Doppler spectrum, unless either the spectral signal to noise ratio is large, or the variance of the periodogram is small. Improved capability of

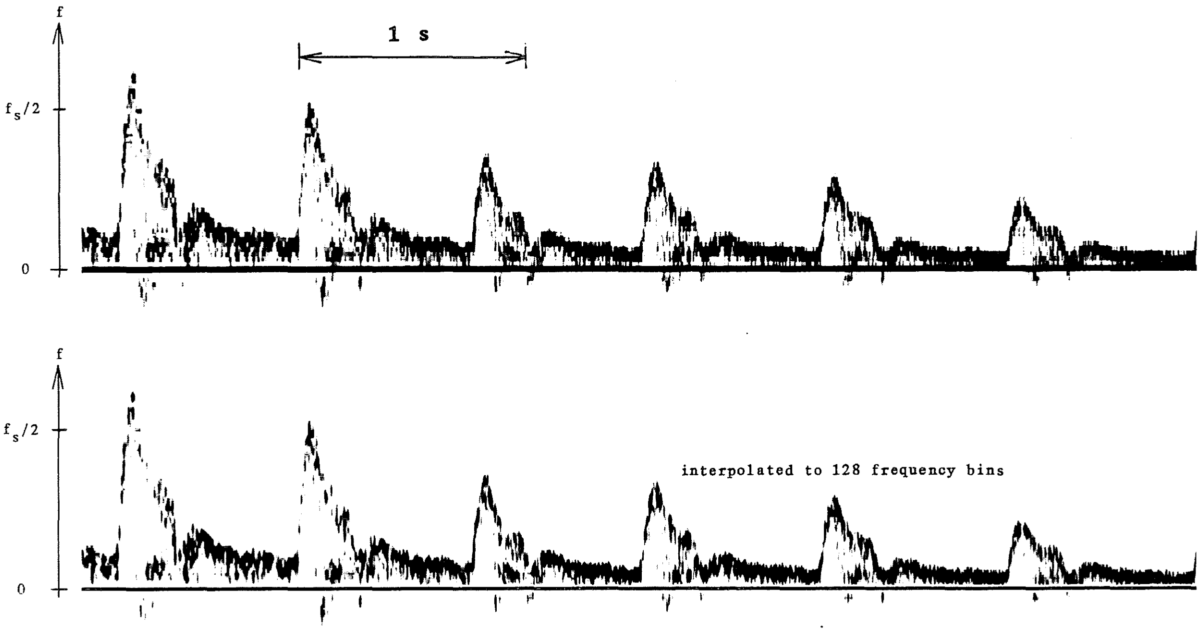

Fig. 3.5 N = 64 sliding DFT spectrum analysis (upper part) interpolated to 128 pixels vertically (lower part). The sampling frequency increases continuously from 6.5 kHz to 17 kHz during the record.

noise reduction therefore results from the use of the averaged periodogram estimator when compared against the commonly used 'raw' periodogram .

3.4 Discrete time spectrum analysis and frequency aliasing in different types of Doppler instruments.

Proper bandlimiting is required to avoid aliasing errors in sampled data signal processing. In CW Doppler this a not a problem. However, it is an inherent part of the pulsed Doppler principle that bandlimiting cannot be performed. Frequency aliasing therefore often occurs, usually caused by pathologically high blood velocities at large ranges (~ 5-15 cm). It is of great clinical importance to quantify these velocities. So far, aliasing has been the major problem with pulsed Doppler techniques applied in cardiology. Aliasing has also caused considerably confusion and misinterpretations in the applications part of the Doppler literature [13].

The common approach to pulsed Doppler signal processing is to smooth the received signal samples prior to performing the spectrum analysis. When the Nyquist limit is exceeded, the smoothed signal becomes an aliased version of the Doppler signal that corresponds to the velocity distribution. For that reason, it has until recently been taken for granted that the frequency limit of a pulsed Doppler system is the Nyquist limit $f_s/2$, where f_s is the pulse repetition frequency of the instrument. This is not the case. Several investigators have reported tracking methods for quantitation of mean Doppler frequencies exceeding the Nyquist limit [15][35][36]. This is possible since the sampling limitations for complex signals apply to the signal bandwidth, rather than its center frequency, eq. (2.8). Resolving these aliasing errors is almost trivial when complex spectrum analysis is applied, especially if the highpass filters of the Doppler instrument are implemented in discrete time. This is demonstrated in the following subsections. For the sake of completeness, also sampled data spectrum analysis of the signals from a CW Doppler instrument is discussed.

3.4.1 CW Doppler

In CW Doppler, the signal is a continuous time process, which is contaminated with wideband noise. A power spectrum is shown schematically in Fig. 3.6.a. The notch in the spectrum for $|\omega| < \omega_{hp}$ is caused by an efficient highpass filter in the CW Doppler instrument. It is inserted to remove strong, low frequency Doppler shifts from tissue. Thereby, unfortunately, also low Doppler frequencies from blood are removed.

Aliasing errors are avoided if the signal is properly bandlimited prior to the sampling for spectrum analysis. The simplest way of bandlimiting a complex process is to lowpass filter its quadrature components using identical analog lowpass filters, Fig. 3.7.a. This approach leads to a symmetric frequency response of the bandlimiting (anti aliasing) filter, Fig. 3.7.b. Hence, to satisfy (2.8), its cutoff frequency

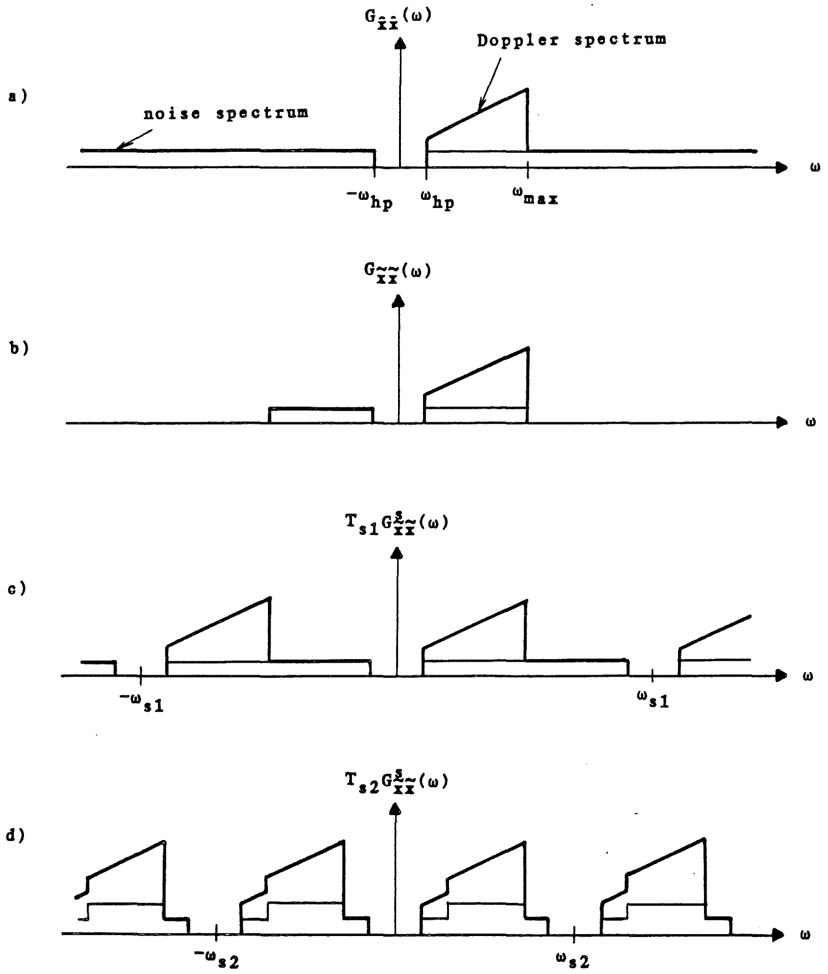

Fig. 3.6 Bandlimiting of CW Doppler signal:
a) spectrum of received signal.
b) spectrum of bandlimited signal.
c) sampled power spectrum, $\omega_{s1} = 2\omega_{max}$.
d) sampled power spectrum, $\omega_{s2} = 1.4\omega_{max}$.

$f_c = \omega_c/2\pi$ must be chosen less or equal to the Nyquist frequency $f_s/2$. The cutoff frequency also must exceed f_{max}, the magnitude of the maximum Doppler shift present. Selecting $2\omega_{s1} = \omega_c = \omega_{max}$ leads to the situation shown in Fig. 3.6.b and c. There is no ambiguity in the sampled power spectrum, since the bandlimited signal $\tilde{x}(t)$ has no frequency components in the frequency intervals $|\omega| > \omega_s/2$.

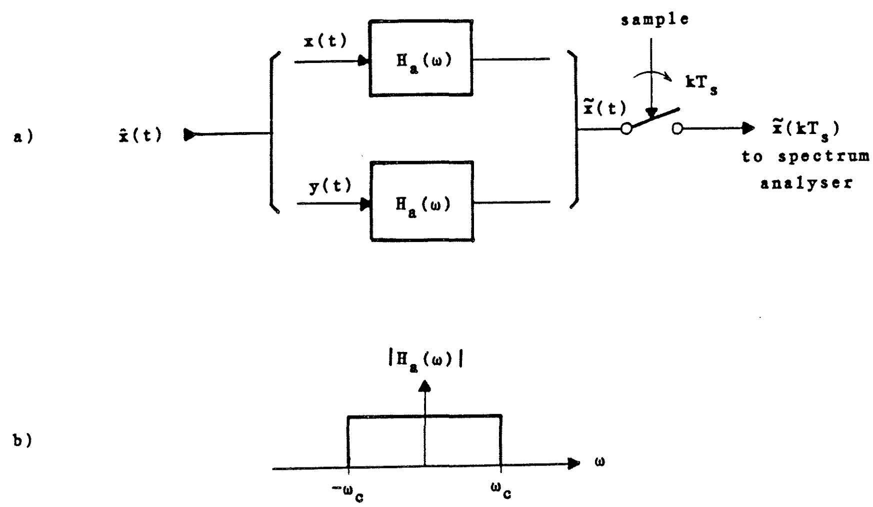

Fig. 3.7 a) Bandlimiting of complex process by lowpass filtering of its quadrature components.
b) Frequency response of ideal bandlimiting filter.

The above procedure may not be fully satisfactory if the number of frequency bins N of the spectrum analyser is small, and Doppler shifts of mainly one sign are present ($N = K$ assumed). In this case, only half the period of the sampled power spectrum contains Doppler information, Fig. 3.6.c. The resolution can be increased by reducing the sampling frequency to a value f_{s2} which only slightly exceeds f_{max}. This reduction causes the Doppler spectrum to spread out over a larger fraction of the sampled power spectrum, which improves resolution when N is fixed, Fig. 3.6.d. However, due to aliasing of the noise spectrum, the spectral signal to noise ratio degrades with 3 dB. The figure also shows that an asymmetric display range, e.g. $[0,\omega_{s2})$, is required to restore the true spectrum shape if only one frequency period of the sampled power spectrum is displayed. The symmetric display range specified in (3.10) leads to foldover (aliasing) errors when the Nyquist frequency is exceeded.

One frequency period of the sampled power spectrum covers a frequency window of width f_s. The above example illustrates that for sonagram display, the user should have freedom to select the partition of this window into positive and negative frequencies. More precisely, the sonagram data matrix (3.10) should be calculated on the frequency grid

$$G_s(m,n) = \tilde{G}_M(m(1-r)K, n\omega_s/N; K) \quad n = N - N_{max}-1,..,0,..,N_{max} \qquad (3.11)$$

where allowed values for N_{max} are 0,...,N-1. A proper N_{max} in a given situation is a value which gives no aliasing of the velocity waveform. Aliasing is easily identified from the sonagram, as illustrated in Fig. 3.8. In the left part of the figure the display range is symmetric (N_{max} = N/2). In the systole, the maximum Doppler frequency exceeds the Nyquist limit, and foldover occurs. In the right part, N_{max} is increased to to N-1 (the lowering of the baseline to the bottom of the display), and the true waveform is fully restored.

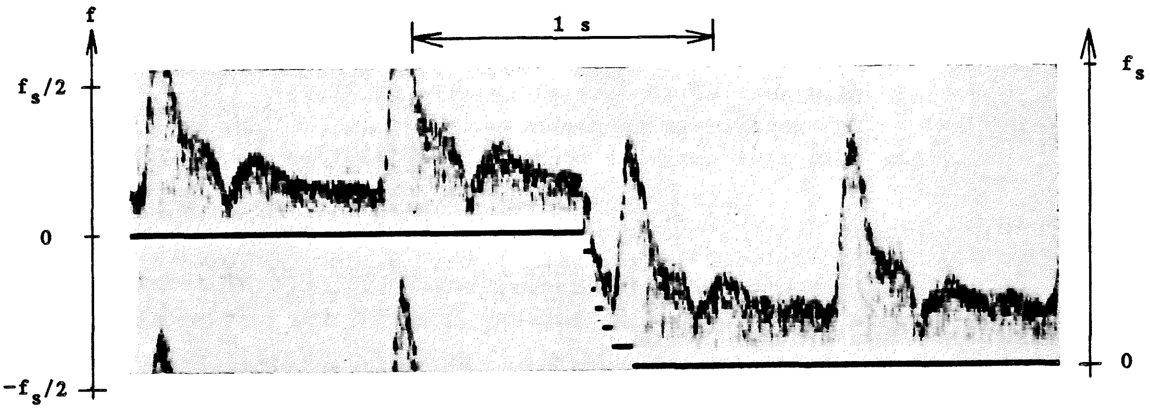

Fig. 3.8 Restoring of aliased waveform by shift of baseline.

In a situation with offset baseline, the anti aliasing filter should ideally have an asymmetric frequency response,

$$H_a(\omega) = \begin{cases} 1 & \omega \in [(N-N_{max})\omega_s/N, N_{max}\omega_s/N] \\ 0 & \text{elsewhere} \end{cases} \qquad (3.12)$$

This allows for maximum frequency resolution with no aliasing of the noise spectrum. Unfortunately, this type of analog filtering requires relatively complex electronic circuitry. A simpler approach is to use ordinary lowpass filters with symmetric frequency responses for band-limiting, and make the cutoff frequency vary with both sampling frequency and the baseline position in the display, i.e.

$$\omega_c = k_c(N_{max})\omega_s \tag{3.13}$$

where $k_c = 0.5$ if $N_{max} = N/2$ and $k_c = 1.0$ else. Even with a continuously variable sampling frequency, this kind of filtering is relatively simple to implement, using switched capacitor filters [37]. This type of solution allows for both optimum noise performance, with the baseline in the middle of the sonagram, and possibility for enhanced frequency resolution using offset baseline. The signal to noise ratio, however, deteriorates with 3 dB in the latter case.

3.4.2 PW Doppler with discrete time highpass filtering

A simple block diagram of the signal acquisition in a pulsed Doppler instrument with discrete time signal processing is shown in Fig. 3.9.a. The continuous time process $\hat{x}(t)$ now represents the Doppler signal one would have measured if able to selectively observe the chosen sample volume in continuous time, without interference from surrounding blood. The noise bandwidth of the signal at the input of the sampler (the range gate) is determined by the overall bandwidth of the transducer/receiver system. It is on the order of $1/T_p$ in a well designed system, where T_p is the time duration of the emitted soundburst [15]. Typically, this bandwidth is $10 - 100\ f_s$, where f_s denotes the pulse repetition frequency (PRF) of the instrument. Pulsed operation implies risk for both range and frequency ambiguity. A necessary condition to avoid range ambiguity is

$$f_s \leq \frac{c_t}{2d} \tag{3.14}$$

where d is the distance between the transducer and the range cell and c_t is the speed of sound in tissue (1540 m/s). Equality is reached if the emission of a soundburst follows immediately after sampling the echo from the previous burst ('optimal PRF'). Whether or not the condition (3.14) is sufficient, depends on how much the Doppler signal from the ambiguous sample volume(s) is attenuated.

After the range gating, the signal is passed through a discrete time

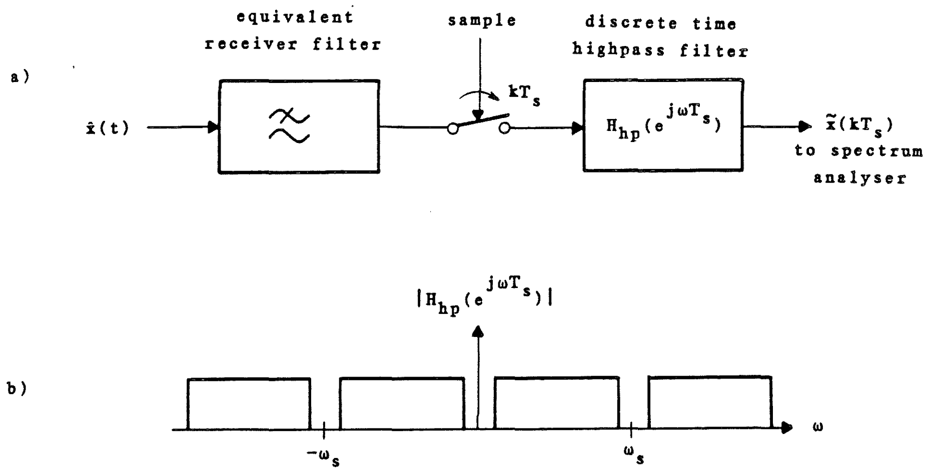

Fig. 3.9 Block diagram for signal acquisition in PW Doppler instruments with discrete time highpass filtering.

highpass filter, which serves the same purpose as in CW Doppler. The frequency response of the filter is periodic with period ω_s, Fig. 3.9.b. It therefore also attenuates Doppler frequencies in the vicinity of $\pm\, m\omega_s$, m = 1,2,--. The output from the highpass filter is the signal available for spectrum analysis. The use of this type of Doppler instrument thus leads to a sampled data signal processing chain, with sampling frequency equal to the PRF.

An ambiguity in Doppler frequency results from the lack of an anti aliasing filter prior to the sampler in the PW instrument. A signal $\hat{x}(t)$ with the power spectrum $G_{\hat{x}\hat{x}}(\omega)$ cannot be discerned from other signals with the spectra $G_{\hat{x}\hat{x}}(\omega \pm m\omega_s)$, m = 1,2,--, since they all yield identical sampled power spectra, eq. (2.7). However, the arterial velocity has a continuous time variation and, provided (2.8) is not violated, this allows for quantification of Doppler frequencies even exceeding the sampling frequency. Apparently, moderate aliasing can be corrected for using the baseline shift technique earlier demonstrated in Fig. 3.8. Correction of more severe aliasing can be done using the display format shown in Fig. 3.10. The figure shows a sonagram of a time varying sampled shorttime spectrum $\langle\tilde{G}(k,\omega;K)\rangle$, displayed in the extended frequency range $(-f_s, 2f_s)$. In principle, each of the three partial spectra shown could represent possible Doppler spectra. Now frequency aliasing can safely be excluded in the diastole, where the blood velocity is low. This implies that the mid partial spectrum correspondsto the true Doppler spectrum. Thus, the frequency ambiguity due to aliasing may be resolved, simply by displaying the sampled power spectrum over a frequency range corresponding to the true velocity variations (see also the discussion following eq. (2.8)). The common display format (with frequency span f_s) would have led to foldover errors in this case, regardless of the choice of baseline position.

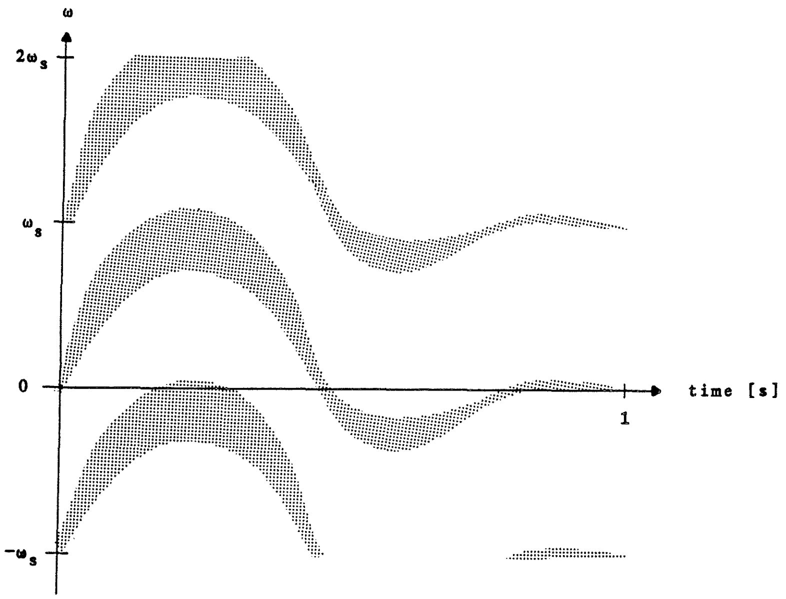

Fig. 3.10 Restoring of aliased waveform by displaying the sampled power spectrum over a range larger than ω_s.

The feasability of the above 'multi-period' sonagram display format is verified by the experiment shown in Fig. 3.11. In the left part of the sonagram a pulsed Doppler instrument operated at 10.1 kHz PRF, while the peak maximum Doppler frequency can be identified at ~ 19 kHz. This is confirmed in the right part of the sonagram, where the PRF was increased to 21.2 kHz (note the difference in scaling). Although the upper and lower parts of the sonagram are entirely identical, the extended display format strongly helps in identifying the peak frequency when the lowest PRF is employed. The notches in the frequency response for frequencies close to $\pm m\omega_s$ are also clearly visible in Fig. 3.11.

The highpass filter cutoff frequency was set to 300 Hz in the experiment.

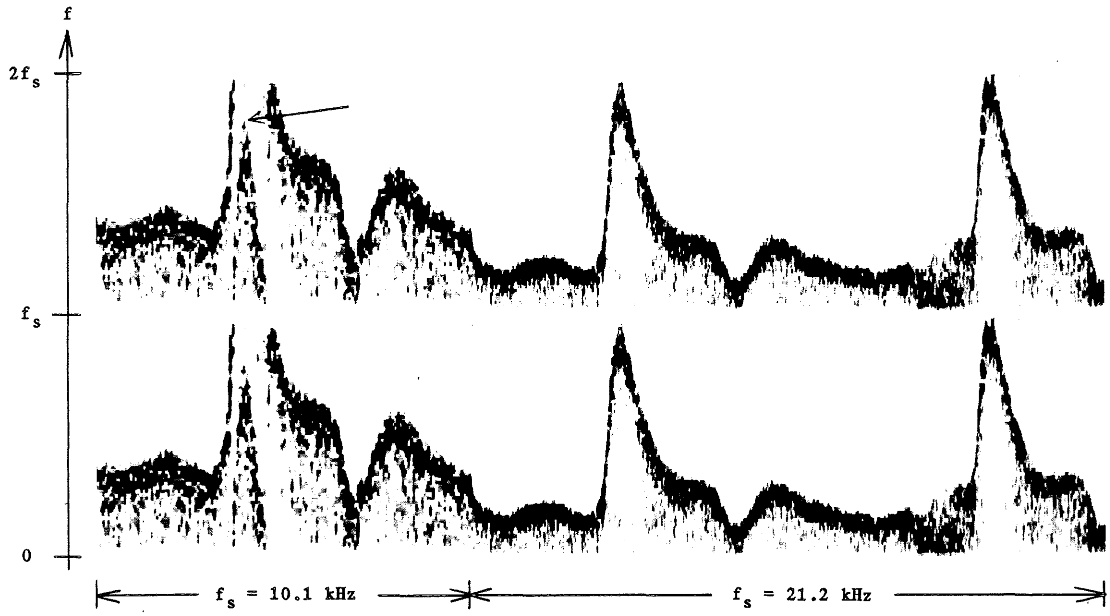

Fig. 3.11 Experimental restoring of waveform with severe aliasing (f_o = 10 MHz).

In principle, frequency shifts of sizes several times the PRF may be quantified, simply by adding more frequency periods of the sampled spectrum to the display in Fig. 3.11. The limiting factor is the bandwidth of the signal. If it exceeds the PRF, the partial spectra will overlap, and the peak frequency may be difficult to identify. In the above example a peak frequency equal to nearly 4 times the Nyquist frequency was measured, even if Fig. 3.11 reveals that the signal bandwidth in fact did exceed f_s. The peak frequency can still be identified, since the spectral density at the peak is much larger than the spectral density of the overlapping partial spectrum. However, the shown example is not always representative: In the experiment aliasing was provoked by deliberately chosing a high ultrasound frequency (10 MHz), and a very low PRF, while measuring on a constricted, but otherwise normal carotid artery. In contrast, the most severe aliasing problems occur in heart lesions in 7 - 15 cm depth, which necessitates a low PRF. Large velocity gradients in the sample volume then often cause the Doppler spectrum to extend from zero to the maximum frequency, i.e. the bandwidth of the Doppler signal is equal to its maximum frequency. In these situations, the spectral density may even decrease with frequency. In total, these effects may cause great difficulties in identifying frequencies larger than the sampling frequency, even when using the display format in Fig. 3.11. Still, this is a factor 2 improvement compared to what until recently was considered to be the frequency limit of a pulsed Doppler instrument.

Hoeks has proposed an algorithm for automatic anti aliasing correction in PW Doppler systems with discrete time signal processing [15]. It is based on the use of a discrete time instantaneous frequency estimator. The underlying principle is to track the center frequency of the Doppler spectrum as a function of time. Thereby incremental changes in mean frequency can be detected without ambiguity, even if the absolute value of the mean frequency is larger than f_s. However, the method breaks down when the bandwidth of the Doppler spectrum exceeds $\sim f_s/2$, whereas the spectral method in Fig. 3.11 at least works up to a bandwidth f_s. The spectral method of quantifying Doppler shifts above the Nyquist frequency has an additional important advantage compared to Hoek's approach: It is immediately apparent from the spectral display when the signal bandwidth exceeds f_s, so one always knows for sure when the aliasing cannot be resolved. This is not the case using tracking tecniques; breakdown of the algorithm then leads to erroneous mean frequency estimates, without a clear indication of the error. Misinterpretation of the results then seems likely.

The synchronous operation of the PW Doppler and the spectrum analyser has additional implications. Since the total data collecting time T is fixed, both the resolution and the variance of the averaged periodogram become functions of $KT_s = K/f_s$. The sampling frequency now is determined from the the Doppler range setting. Consequently, also the number of data samples K to be Fourier transformed should be made variable. Unless this is the case, both resolution and variance will change with the range setting of the Doppler instrument. When optimal PRF is employed, the total number of signal samples L available for spectrum analysis becomes

$$L \leq \frac{c_t T}{2d}$$

$$= \frac{770}{d\ [\text{cm}]} \qquad \text{when } T = 10\text{ms}. \tag{3.15}$$

Thus, the available data record per spectrum estimate varies between the limits ~ 50 ($d = 15$ cm) and ~ 400 ($d = 2$ cm).

3.4.3 PW Doppler with continuous time filtering

In cardiac applications of Doppler ultrasound, the power ratio between unwanted signals from tissue and the signal from blood may be extremely unfavorable (80–100 dB). Due to the limited dynamic range of high speed A/D converters presently available, PW Doppler instruments for cardiac applications exclusively employ analog highpass filtering for the rejection of wall motion signals. In the previous section it was shown that in pulsed Doppler systems with discrete time signal processing it is possible to resolve frequency shifts of magnitude equal to or greater than the PRF, provided the total signal bandwidth does not exceed the PRF. This holds also for systems with analog filtering, although some additional constraints are superimposed. These are analysed in the following.

A conceptual block diagram of an instrument of this type is shown in Fig. 3.12.a. The output from the sampler (the Doppler range gate) now is the impulse train $\{\hat{x}(kT_s)\delta(t-kT_s)\}$, which is highpass filtered and smoothed by an analog bandpass filter with symmetric frequency response $H(\omega)$. A possible choice of frequency response is given in Fig. 3.12.b. The lower cutoff frequency of the filter is ω_{hp}, while the upper cutoff ω_{lp} is slightly below the Nyquist frequency. It follows from the sampling theorem that the output signal $\tilde{x}(t)$ from the bandpass filter is a perfect reconstruction of the continuous time Doppler signal $\hat{x}(t)$, if the power spectrum $G_{\hat{x}\hat{x}}(\omega)$ is nonzero only on the intervals $\omega_{hp} < |\omega| < \omega_{lp}$. The situation then fully corresponds to the case of the CW Doppler with respect to choice of sampling frequency of the spectrum analyser, anti aliasing filtering etc. However, if $G_{\hat{x}\hat{x}}(\omega)$ has frequency components exceeding the Nyquist frequency, the smoothing filter causes $\tilde{x}(t)$ to become an aliased version of $\hat{x}(t)$, even when

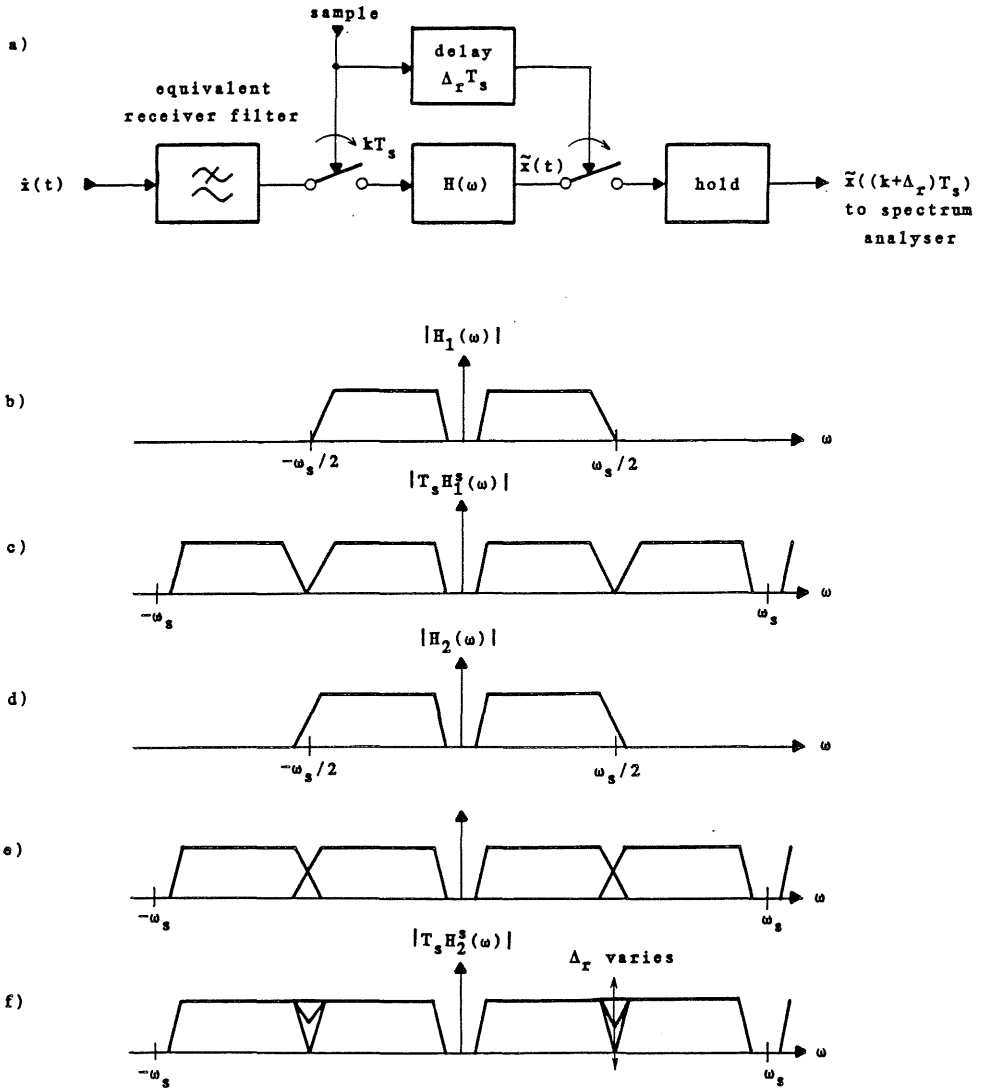

Fig. 3.12 Block diagram of PW Doppler instrument with analog filtering.

the total signal bandwidth is less than ω_s. For example, a spectral component with the positive frequency $\omega_s/2 + \varepsilon$, $0 < \varepsilon < \omega_s/2$, is mapped to the negative frequency $-\omega_s/2 + \varepsilon$ in $\tilde{x}(t)$ (this can be realized by combining Fig. 3.12.b and Fig. 2.1.b).

If the upper edge of the bandpass filter in Fig. 3.12.b could be made with an infinitely sharp cutoff at the Nyquist frequency, the sampled power spectrum $\tilde{G}^{s}_{\hat{x}\hat{x}}(\omega)$ could have been restored without error, simply by sampling $\tilde{x}(t)$ synchronously with the Doppler range gating. The net effect of the analog bandpass filter and the sampling then would be discrete time highpass filtering, equivalent to the situation in Fig. 3.9.a. Problems are introduced when the smoothing filter has a cutoff edge with finite steepness. This is realized by analysing the situation in Fig. 3.12.a somewhat closer. A delay $\Delta_r T_s$, $0 < \Delta_r < 1$, has been inserted between the samplers in the pulsed Doppler and the spectrum analyser. This delay can be modeled as a time advance with transfer function $\exp(j\omega\Delta_r T_s)$, preceding a sampler running synchronously with the PW Doppler sampler [2, p. 118]. The transfer function between the discrete time sequences $\{\hat{x}(kT_s)\}$ and $\{\tilde{x}((k+\Delta_r)T_s)\}$ is then given by [2, p. 86]

$$H^{s}(\omega) = \frac{1}{T_s}\sum_{n=-\infty}^{\infty} \tilde{H}(\omega - n\omega_s) \tag{3.16}$$

where $\tilde{H}(\omega)$ is the overall transfer function of the smoothing filter and the sample delay:

$$\tilde{H}(\omega) = H(\omega)e^{j\omega\Delta_r T_s} \tag{3.17}$$

The sampled transfer function resulting from the filter design in Fig. 3.12.b is shown in Fig. 3.12.c. The slow rolloff of the smoothing lowpass filter causes a notch at the Nyquist frequency. This is highly undesired, and to have it removed, the cutoff frequency of the lowpass filter must increased somewhat, Fig. 3.12.d. The edges of the lowpass filter now overlap in the sampled transfer function, and, bearing (2.7) in mind, it is tempting to claim that the notch is removed, Fig. 3.12.e. This is, however, not necessarily true. The relation (2.7) holds for stationary signals only. Although $\hat{x}(t)$ is stationary, the signal $\tilde{x}(t)$ is an imperfect reconstruction. It can be shown that $\tilde{x}(t)$ becomes nonstationary if $G_{\hat{x}\hat{x}}(\omega)$ has nonzero components in the regions where the filter edges overlap (stated without proof). Therefore, (2.7) does not hold when applied to the smoothed signal.

The overall discrete time transfer function $H^{s}(\omega)$ may be calculated from (3.16). Since it is periodic, it needs only to be calculated on the interval $0 < \omega < \omega_s$. If the lowpass filtering is efficient, only two terms will contribute significantly to the sum (3.17) in this region,

$$T_s H^s(\omega) = \tilde{H}(\omega) + \tilde{H}(\omega-\omega_s) \tag{3.18}$$

Splitting into amplitude and phase one may write

$$\tilde{H}(\omega) = |\tilde{H}(\omega)| \; e^{j\tilde{\gamma}(\omega)} = |H(\omega)| \; e^{j\tilde{\gamma}(\omega)} \tag{3.19}$$

The following relation holds when the quadrature components are filtered with real impulse response filters:

$$\tilde{H}(-\omega) = \tilde{H}^*(\omega) \tag{3.20}$$

The sampled transfer function may thus be written

$$T_s H^s(\omega) = |H(\omega)| e^{j\tilde{\gamma}(\omega)} + |H(\omega-\omega_s)| e^{-j\tilde{\gamma}(\omega_s-\omega)} \tag{3.21}$$

At the Nyquist frequency, the transfer function becomes real valued:

$$T_s H^s(\omega_s/2) = 2 \; |H(\omega_s/2)| \; \cos \tilde{\gamma}(\omega_s/2) \tag{3.22}$$

It follows that <u>the magnitude of the sampled frequency response at the Nyquist frequency is highly dependent on the overall phase angle of the analog filter</u>. This can in turn be written $\tilde{\gamma}(\omega) = \gamma(\omega) + \omega\Delta_r T_s$, where $\gamma(\omega)$ is the phase of the smoothing filter, and $\omega\Delta_r T_s$ originates from the delay between the samplers. Inserting into (3.22) yields

$$T_s H^s(\omega_s/2) = 2|H(\omega_s/2)| \; \cos(\pi\Delta_r + \gamma \; (\omega_s/2)) \tag{3.23}$$

Hence, when the fractional sampling delay Δ_r varies, the sampled data transfer function varies between the extremes 0 and $2|H(\omega_s/2)|$ at the Nyquist frequency, Fig. 3.12.f. Increasing the upper cutoff frequency of the smoothing filter to allow for signal transmission at the Nyquist frequency is therefore a necessary, but not a sufficient condition for removing the notch near $\omega_s/2$: <u>The delay between the samplers in the pulsed Doppler and the spectrum analyser must also be set properly, to avoid an accidental notch in the frequency response</u>. This is a nontrivial practical problem, since it is desirable to vary the lower and the upper cutoff frequencies of the bandpass filter independently in a measurement situation. Changing either of these may change $\tilde{\gamma}(\omega_s/2)$, with the risk of generating a notch at the Nyquist frequency.

The plot in Fig. 3.12.f is an oversimplification, only meant as an illustration of the problem: Practical filters often have strong phase variations in the vicinity of the cutoff frequency. Unless the smoothing filter is carefully designed, the sampling delay that maximizes the signal transmission at the Nyquist frequency may cause strong ripple elsewhere in the passband. The problem of designing the smoothing lowpass filter for a pulsed Doppler instrument is discussed in detail in Appendix I for the case of all-pole filters.

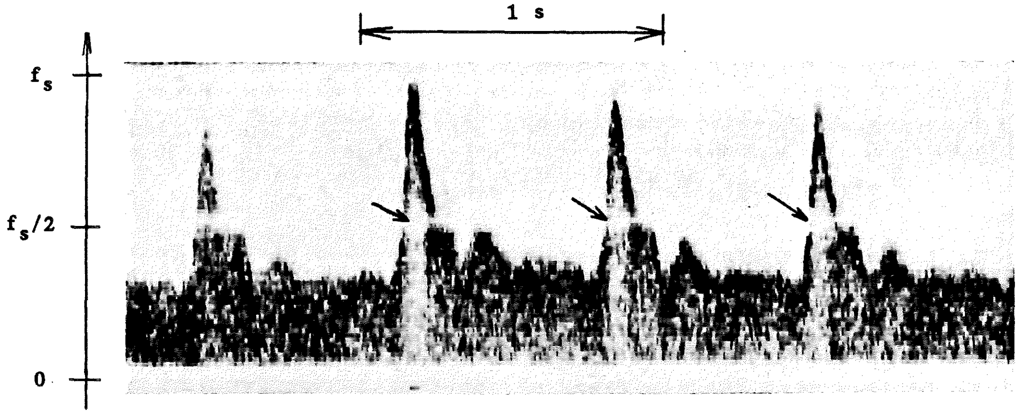

Fig. 3.13 Sonagram recorded with unfavorable sampling delay Δ_r. Note the white band at the Nyquist frequency (f_0 = 10 MHz, f_s = 20 kHz).

The effect on the sonagram of an unfavorable fractional sampling delay is shown in Fig. 3.13. The notch at the Nyquist frequency is apparent, although it is not very disturbing on this occation. Changing Δ_r with 0.5 would have removed the notch entirely. This was done in Fig. 3.11, which was recorded using the same setup as Fig. 3.13.

Synchronized complex spectrum analysis/sampling delay positioning and baseline shift to correct for aliasing has previously been implemented in DAISY. The increased velocity limit is of great importance in clinical measurements [13].

3.5 Automatic Gain Control of the Doppler signal

3.5.1 Implications of Automatic Gain Control

Experiences with DAISY indicate that it is advantageous to precede the spectrum analyser with an Automatic Gain Control (AGC) of the Doppler signal. This has also been suggested by Rittgers et al. [33]. The advantages with automatic gain control are:

i) The spectrum analyser automatically adapts itself to changing input signal levels. This minimizes the needs for controls, and prevents misadjustments.

ii) In some situations the signal power varies much during the heart cycle. A typical example is in combined mitral stenosis and mitral regurgitation, where the signal power in the diastole (stenosis) typically is much larger than the signal power in the systole (regurgitation). A fast AGC then enables full quality display of both the systolic and the diastolic frequency components.

iii) Wall motion signals, especially valve 'clicks' in heart measurements, are prevented from temporarily saturating the spectrum analyser, and thereby causing artifacts in the sonagram.

iv) Reduced dynamic range requirements for the spectrum analyser.

One drawback with an AGC is that the sonagram intensities at different time instants no longer are related to global differences in backscattered signal power. Another disadvantage occurs in situations where the Doppler signal power goes to zero during parts of the heart cycle, e.g. measurements on the ascending aorta in adults. When the signal power reduces, the AGC will amplify the background noise, which causes a strong, disturbing darkening of the sonagram over the entire frequency range.

Both the above problems can be solved by selecting the maximum gain of the AGC circuit manually, while the limiting function of the AGC is retained at a constant level. The noise floor of the sonagram is then set manually, while the limiting still prevents overload of the spectrum analyser due to valve clicks, etc. The problem of a fluctuating noise floor can also be eliminated using adaptive thresholding, where the reject level adjusts itself dynamically, according to the gain variations of the AGC.

The suggested approach to automatic gain control of the Doppler signal is somewhat different than the approach of Rittgers et al. They employed an AGC which only updated its gain once per heartbeat. However, they were using the spectrum analyser solely in measurements on peripheral vessels, where wall motion signals hardly represent problems. The situation in measurements on the heart is quite different, and for reasons earlier given, a fast AGC is preferable.

3.5.2 Analysis of an AGC scheme

A block diagram of a useful AGC structure for the complex Doppler signal is shown in Fig. 3.14. The structure is similar to a scheme given in [23], and it has also been included in DAISY. AGC is obtained by comparing the average output signal amplitude of one of the quadrature components with a reference voltage u_r. The error signal is integrated with time constant T_i. The output $u_i(t)$ from the integrator is modified by the nonlinear function $\alpha \exp[\beta(\cdot)]$, where α, β are constants, before being multiplied with the input signal. The nonlinear block ensures that the dynamic properties of the AGC become independent of the average input level of the Doppler signal.

In the following, a simplified analysis of the dynamics of this scheme is given. The input signal to the AGC is assumed to be a sinewave, with a step discontinuity in amplitude, i.e.

$$x(t) = \begin{cases} u_o \sin \omega_d t & t < 0 \\ k u_o \sin \omega_d t & t \geq 0 \end{cases} \tag{3.26}$$

where $k, u_o > 0$. The AGC is assumed to be in steady state for $t < 0$. The output signal amplitude is then $\pi u_r/2$, since the time average of a rectified sinewave is $2/\pi$ times its amplitude. It is also assumed that the signal frequency ω_d is so high that the oscillatory components of the gain with frequency $2m\omega_d$, m integer (frequency doubling because of the rectifier), are negligible. Under these assumptions, the AGC will slowly modulate the envelope of the output sinewave, and its output can be written

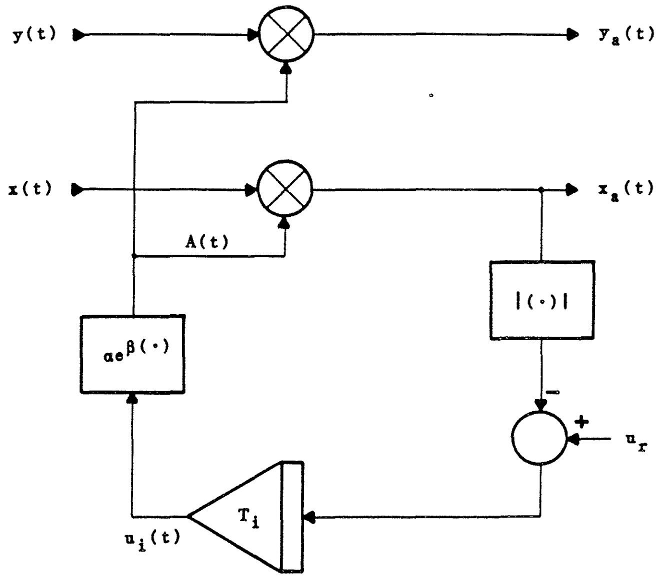

Fig. 3.14 AGC block schematics.

$$x_a(t) = \begin{cases} \frac{\pi}{2}\, u_r \sin \omega_d t & t < 0 \\ \frac{\pi}{2}\, u(t) \sin \omega_d t & t \geq 0 \end{cases} \tag{3.27}$$

with the continuity condition

$$\lim_{t \to 0_+} u(t) = k u_r \tag{3.28}$$

The loop equations for the AGC can be written out directly from Fig. 3.14:

$$A(t) = \alpha\, e^{\beta u_i(t)} \tag{3.29}$$

$$u_i(t) - u_i(0) = \frac{1}{T_i} \int_0^t dt\, \left(u_r - \frac{\pi}{2}\, u(t) |\sin \omega_d t|\right) \tag{3.30}$$

(3.30)

$$\simeq \frac{1}{T_i} \int_0^t dt\, (u_r - u(t))$$

$$x_a(t) = A(t) x(t) \tag{3.31}$$

The above equations can be combined into one single integral equation. Differentiating this with respect to time leads to the simple differential equation

$$\frac{du}{(u-u_r)u} = -\frac{\beta}{T_i}\,dt \tag{3.32}$$

which can be solved by integration. The resulting output envelope becomes

$$\frac{u(t)}{u_r} = \frac{1}{1 - \frac{k-1}{k}\exp(-\frac{t}{T_A})} \tag{3.33}$$

where the time constant T_A is

$$T_A = \frac{T_i}{\beta u_r} \tag{3.34}$$

The response time of the circuit is independent of the initial input level u_o and the gain parameter α, while it is affected both by the reference level u_r and β. The 'attack' response of the AGC is approximately ($k >> 1$)

$$\frac{u_a(t)}{u_r} \simeq \frac{1}{1 - \exp(-\frac{t}{T_A})} \tag{3.35}$$

The attack recovery time T_a for the output envelope to return within 3 dB of the reference level is

$$T_a \simeq -\ln(1 - \frac{1}{\sqrt{2}})T_A = 1.23\ T_A \tag{3.36}$$

The approximation is good when $k > 5$ (14 dB). Correspondingly, the decay response becomes ($k << 1$)

$$\frac{u_d(t)}{u_r} \simeq \frac{k}{k + \exp(-\frac{t}{T_A})} \tag{3.37}$$

with a 3 dB decay recovery time

$$\begin{aligned} T_d &\simeq -[\ln k + \ln(\sqrt{2}-1)]T_A \\ &= (0.88 - 0.115\ k\ [dB])T_A \end{aligned} \tag{3.38}$$

The decay recovery time increases logarithmically when k decreases. It is therefore proportional to the dB decrease in k. A 20 dB decrease gives a recovery time 3.18 T_A, which is 2.5 times larger than the corresponding attack recovery time. This may be an advantage, as one generally wants a very fast attack to prevent overload from valve clicks. However, the AGC must not be so fast that it introduces distortion of normal Doppler frequencies (f_d > 100 Hz). Experiences with 'DAISY' indicate that a good compromise is $T_A \sim 20$ ms.

Fig. 3.15 shows dB plots of the time response of u(t) for some selected values of k. The increased decay recovery times for small k's is apparent, while the attack recovery time varies little when k increases from 6 dB to 20 dB.

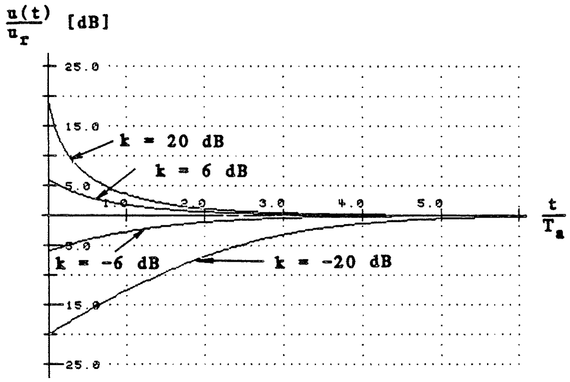

Fig. 3.15 Step response of AGC circuit in fig. 3.14.

The last subject to be discussed is the setting of the reference level u_r. The signal is Gaussian, and the following well known relation holds:

$$u_r = \langle|x(t)|\rangle = \sqrt{\frac{2}{\pi} R_{xx}(0)} \tag{3.39}$$

This also follows from (2.99) with M = a = 0.5. Assume that the spectrum analyser saturates at the input levels $\pm u_s$. Allowing for 1% probabilty of saturation then is equivalent to requiring that

$$R_{xx}(0) = \left[\frac{u_s}{n_{0.005}}\right]^2 \tag{3.40}$$

where $n_{0.005}$ is the 0.005 quantile in the Gaussian (0,1) distribution. Combining the above equations yields

$$u_r = \sqrt{\frac{2}{\pi}} \frac{u_s}{n_{0.005}} = 0.310\ u_s \tag{3.41}$$

In practice, a somewhat smaller reference may be preferred. This provides some overload margin during abrupt increases in signal power (e.g. wall motion signals).

3.6 Summary of Chapter 3

Some aspects of spectral analysis of Doppler signals from blood has been discussed. The main points are:

A. Because of the transit time effect, the Doppler signal always has a minimum fractional bandwidth. This limits the velocity resolution one can obtain, and little is gained by selecting the resolution of the spectrum analyser much higher than this bandwidth.

B. The pulsatility of arterial blood velocities limits the data collecting time for spectral analysis to approximately 10 ms. This implies that low variance spectrum analysis with resolution equal to typical transit time bandwidths cannot be obtained with Fourier transform tecniques, unless the Doppler shift exceeds several kHz.

C. For optimum sonagram quality in different situations, the grayscale transfer function should be made with a variable compression. Spectral components from white noise in the Doppler signal can be rejected from the display by thresholding the averaged periodogram.

D. Complex spectral analysis can quantify frequencies above the Nyquist frequency $f_s/2$. This is easy to obtain also for traditional pulsed Doppler systems with smoothing lowpass filters, if the sampler in the spectrum analyser runs synchronously with the Doppler PRF. One can identify peak velocities of pulsatile velocity waveforms up to a limit where the signal bandwidth exceeds the PRF. Identification of Doppler shifts of magnitude less than the PRF can be done by a simple baseline shift in the sonagram display. Frequencies exceeding the PRF require the display of two or more frequency periods of the sampled power spectrum to be resolved.

E. In the mode of operation described in point D, the maximum system sampling frequency is limited by the range setting of the pulsed Doppler instrument. A variance/resolution tradeoff may then be performed by varying the effective window length of the spectrum analyser.

F. Synchronous operation of a sampled data spectrum analyser and a PW Doppler with nonideal smoothing filters may lead to a notch in the overall frequency response at the Nyquist frequency. The notch can be removed by introducing a proper phase delay between the Doppler range gate and the sampler for spectrum analysis.

G. It is advantageous to precede the spectrum analyser with an automatic gain control/limiter. This reduces the dynamic range requirements to the spectrum analyser. Transient saturation of the spectrum analyser caused by strong, low frequency signals from tissue can be prevented if the AGC is fast.

4. EVALUATION OF TWO CONCEPTS FOR REAL TIME SPECTRAL ANALYSIS

In this chapter, two different approaches for the real time computation of periodograms are evaluated. The first is based on the sliding DFT, which allows for a simple analog hardwired solution, using the Chirp Z Transform (CZT) algorithm. The second concept is based on the ordinary Discrete Fourier Transform.

4.1 Sliding DFT spectral analysis

4.1.1 The Chirp Z Transform

The CZT is an algorithm which can be used for computing the z transform of a sequence on spiral contours with focus $z = 0$ in the z-plane [3]. The unit circle is a limiting case of such a spiral contour, and the CZT may therefore be used for computing the DFT of a signal sequence. The sliding DFT, eq. (2.140), can be converted to the CZT format by successive use of the substitutions

$$\begin{aligned} -2mk &= (m-k)^2 - k^2 - m^2 \\ m &= k - n \end{aligned} \tag{4.1}$$

yielding

$$\begin{aligned} F_s(k;N) &= \tilde{X}(k,2\pi(k \bmod N)/N;N) \\ &= \sum_{n=1}^{N} w(N-n;N)\hat{x}(k-n)e^{-j\frac{\pi(k-n)^2}{N}} e^{-j\frac{\pi k^2}{N}} e^{j\frac{\pi n^2}{N}} \\ &= e^{-j\frac{\pi k^2}{N}} \sum_{n=1}^{N} (w(n;N)e^{j\frac{\pi n^2}{N}})(\hat{x}(k-n)e^{-j\frac{\pi(k-n)^2}{N}}) \\ &= e^{-j\frac{\pi k^2}{N}} \sum_{n=1}^{N} h(n)\hat{x}_c(k-n) \end{aligned} \tag{4.2}$$

where

$$h(n) = w(n;N)e^{j\frac{\pi n^2}{N}} \quad n = 1, \ldots, N \tag{4.3}$$

$$\hat{x}_c(k) = \hat{x}(k)c(k) \tag{4.4}$$

$$c(k) = e^{-j\frac{\pi k^2}{N}} = e^{-j\frac{\pi(k \bmod N)^2}{N}} \tag{4.5}$$

Windowing has been included to add generality. The derivation assumes that the window has the usual even symmetry, i.e. $w(n;N) = w(N-n;N)$. Eq. (4.2) expresses that the windowed sliding DFT can be computed by means of two complex multipliers and a linear FIR chirp filter with complex coefficients, as illustrated in Fig. 4.1. The signal is premultiplied with a periodic, linear downchirp prior to entering the FIR-convolver. Finally, a postmultiplication with another linear downchirp yields the Fourier coefficients $F_s(k;N)$. The postmultiplication is unnecessary for periodogram computation, since multiplication with the chirp only represents a phase shift of each output sample from the convolver [16]. This phase shift will disappear in the squaring in (2.9). Windowing of the sliding transform is incorporated by windowing the complex FIR filter coefficients according to (4.3). The above procedure is also known as Bluestein's algorithm [17].

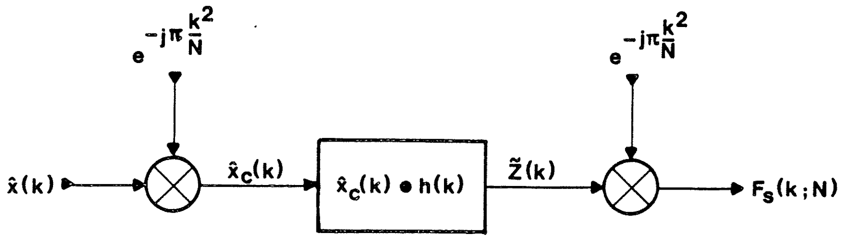

Fig. 4.1 Block diagram of the Chirp z Transform (complex variables). $\bullet$ denotes convolution.

The Chirp Z approach can basically be used in two ways to calculate the ordinary DFT:

i) Extending the length of the chirp convolver to 2N-1 coefficients, where last $N-1$ coefficients are the periodic extension of (4.3), i.e. $h(n+N) = h(n)$, $n = 1,\ldots,N-1$. The convolver is loaded with data during the first N cycles of an analysis. The next $N-1$ cycles the input to the convolver must be set to zero. The output from the extended convolver filter is valid from sample N to sample $2N-1$. This algorithm is known as the conventional CZT [16].

ii) The operation in i) can equally well be performed using an N sample filter in the sliding transform configuration (4.2) [14]. The convolver is loaded with the premultiplied signal during the first N samples, and then reloaded with the same input during the next N - 1 samples. This procedure yields the ordinary Fourier transform of the sequence (formally proved in Section 2.6.2).

Note that both the above procedures require rectangular windowing of the coefficients in the complex convolver. The desired windowing may instead be incorporated as an integral part of the premultiplication. The modified premultiplication waveform then becomes

$$c(k) = \begin{cases} w(k;K)e^{-j\frac{\pi k^2}{N}} & k = 1,\dots,K \\ 0 & k = K+1,\dots,N \end{cases} \tag{4.6}$$

$$c(k+N) = c(k)$$

Both the above procedures require the signal to be available from a buffer memory to become practical in real time spectral analysis. Otherwise, procedure i) will discard half of the available data due to the blanking on the input. Repetition of the input signal (procedure ii)) is not feasible at all without a memory.

4.1.2 Analog computation of the sliding DFT

The Chirp Z Transform allows for relatively simple, high speed computation of the sliding DFT using analog shift registers for the convolution part of the transform. Suitable chirp filters for sliding transform computation are commercially available for N = 512 (CCD - Charge Coupled Device type), and N = 64 (BBD - Bucket Brigade Device type) [18][19]. Application in spectrum analysis was first reported by Brodersen [16], while several investigators later have used these devices for real time processing of Doppler signals [12][20][21]. Also Surface Acoustic Wave (SAW) devices have been used in chirp configuration for analysis with extremely high processing rates [22].

If (4.2) is written out in terms of real and imaginary parts, the block

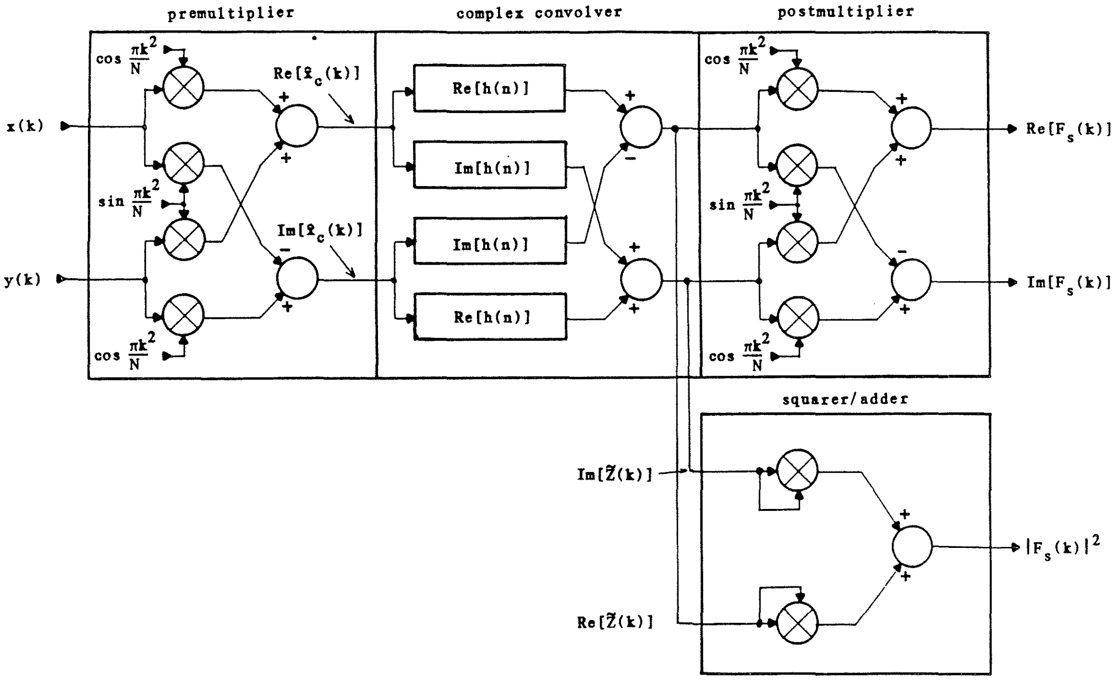

Fig. 4.2 Block diagram of the Chirp Z Transform (real variables).

diagram in Fig. 4.2 can be drawn. The bulk part of the processing in the Chirp Z Transform is performed by the four chirp filters in the complex convolver. The filters are denoted with their impulse responses in the drawing. These are (from eq. (4.3))

$$\begin{aligned} Re[h(n)] &= w(n;N)\cos \frac{\pi n^2}{N} \\ Im[h(n)] &= w(n;N)\sin \frac{\pi n^2}{N} \end{aligned} \qquad n = 1,\ldots,N \qquad (4.7)$$

For periodogram computation, the post multiplication block can be substituted with the squaring/adding block in the lower right part of Fig. 4.2.

Some selected data of chirp filters currently available are listed in Table 4.1 [18][19]. Both dynamic range and coefficient accuracy are comparable to 10 bit digital systems. The processing capacity of the chips is very large: At the maximum sampling frequency, a 512 points complex sliding transform is computed in 256 µs, while a 64 points sliding transform takes only 64 µs. An ordinary DFT computation requires twice this time. Table 4.1 also shows that the sampling

Type	N	coef. error	dyn. range	max f_s	min f_s	comments
R5602	64	± 0.5 %	60 dB	1 MHz	1 kHz	single filter
R5601	512	9 bit	60 dB	2 MHz	4 kHz	quad filters

Table 4.1 Specifications for available chirp filters.

frequency of the chirp filters must exceed a certain limit (1 or 4 kHz) for the filters to function according to the specifications. The 512 sample device (R5601) contains the entire convolver block in Fig. 4.2 on one chip, while the 64 sample device (R5602) is a single chirp filter. A 64 points sliding transformer therefore requires four chirp chips and two analog summation amplifiers for the complex convolution. The premultiplication part of the transform can be implemented using multiplying D/A converters (MDAC's) for multiplication of the analog input signals with digital versions of the variables $\cos \pi k^2/N$ and $\sin \pi k^2/N$ [16].

A practical real time spectrum analyser based on the sliding CZT may be organized as shown in Fig. 4.3. A digital moving averager is included to reduce the variance of the spectrum estimate. An output buffer memory may also be desirable, to simplify the interface between the spectrum analyser and the display device (fibre optic recorder or video display). It also facilitates change of the readout format of the sonagram, for example baseline shifting for aliasing correction.

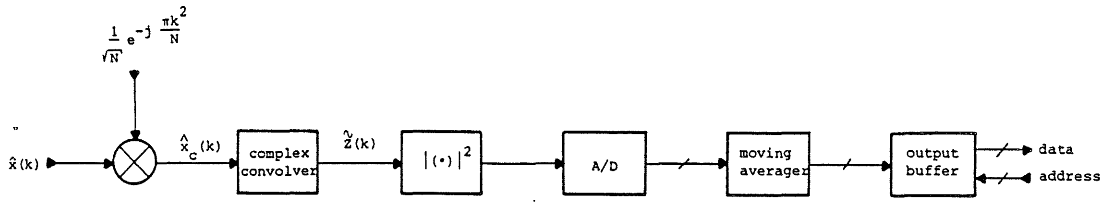

Fig. 4.3 Sliding DFT Chirp Z Transform spectrum analyser.

The main features of the structure shown in Fig. 4.3 are speed and simplicity, since the sliding transformer requires relatively modest amounts of electronics to be implemented. The maximum sampling frequency of the 512 sample filters is 2 MHz, while it is 1 MHz for the 64 sample version. In our applications, the maximum signal sampling rate is 40-50 kHz. The signal processing capacity of the devices is therefore poorly utilized in the shown configuration.

Unfortunately, the sliding transform spectrum analyser has limitations:

i) One must always have $K = N$, since augmenting with zeros is not possible using the sliding transform. When the Doppler signal is available as a continuous time signal, this may be tolerable: The resolution/variance is a function of the ratio L/K, which may be varied solely by changing the sampling frequency of the spectrum analyser (compare with Fig. 3.5). However, measurements of frequencies above the Nyquist frequency in pulsed Doppler systems require the spectrum analyser to run synchronously with the Doppler PRF. The 512 point convolver is then unsuited , since it leads to prohibitive data collecting times ($T = 100$ ms for measurements at 15 cm depth, compare with eq. (3.15)). The 64 sample solution is more suitable in this respect. The inability of selecting $K < N$ is still a drawback, since it causes the variance and resolution to vary with the PRF (and thereby, the range setting) of the pulsed Doppler instrument.

ii) There is no simple way of performing transforms of overlapping signal segments. A Hamming windowed averaged sliding periodogram analyser therefore yields approximately twice the variance of a comparable nonsliding analyser employing 50% overlap. In Doppler blood velocity measurements, with limited data collecting time, this is a severe drawback.

iii) The computation time of the sliding transform spectrum analyser varies with its sampling frequency. If the goal is to keep the total data collecting time to one averaged periodogram constant, the number of terms M to be summed in the moving averager must be a function of the sampling frequency. This complicates the design of the averager.

All sonagrams in this report are made with a spectrum analyser of the type in Fig. 4.3, using the Hamming windowed N = 64 chirp filter devices for the complex convolver. No spectrum averager was available, so the theoretically predicted improvements using averaging have not been verified experimentally. The deficiency pointed out under i) can be clearly noticed in Fig. 3.11; the sonagram has a much more uneven appearance when the PRF is low.

4.2 Ordinary DFT spectral analysis

A block diagram for a real time spectrum analyser based on an N point ordinary DFT processor is shown in Fig. 4.4.a. The complex Doppler signal is still assumed to be available in analog form, and it is A/D converted before dumped into an input buffer memory. The DFT processor reads data from this buffer, weighted by a K-point window ($K \leq N$). The resolution of the spectrum analyser can be varied by changing K or the window type. The number of output frequency bins N remains constant under these parameter changes. The magnitude square of the DFT coefficients are written into an averager/output buffer serving the same purpose as in Fig. 4.3.

A possible input buffer organization is shown in Fig. 4.4.b [14]. The buffer is separated into two different parts, operating in a ping-pong manner: While the DFT processor is reading the K samples from one part, the other is filled with data, and vice versa. The scheme is simple, but it has the same deficiencies, both with respect to lacking overlap between transforms and variable processing rate, as the sliding periodogram analyser previously discussed.

A more flexible input buffer is shown in Fig. 4.4.c. This buffer is organized as a sliding ring with a sufficient number of words (> K) to prevent overflow. New data is written into the word which the address pointer WP directs at. Immediately prior to each write cycle, this

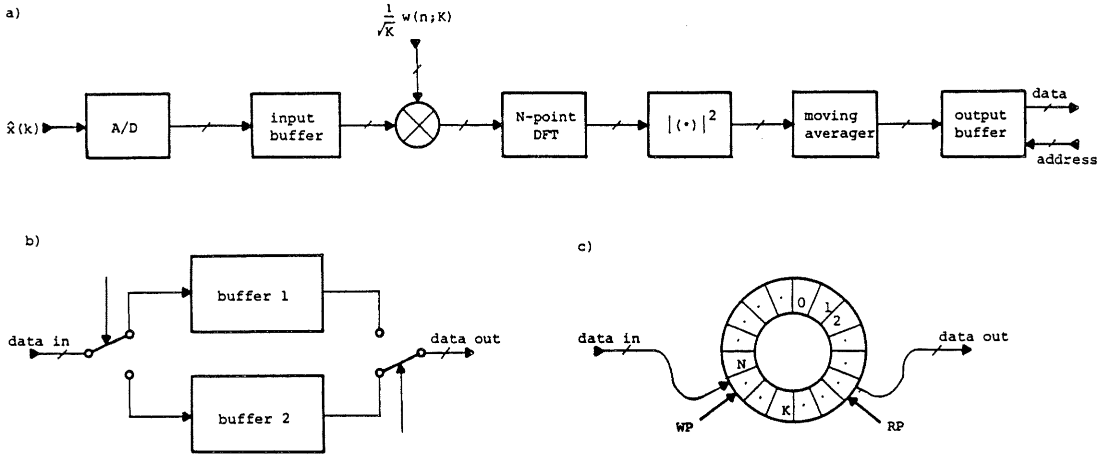

Fig. 4.4 Ordinary DFT spectrum analyser.
a) Block diagram.
b) Ping-pong input buffer.
c) Sliding ring input buffer.

pointer is incremented (WP:=WP+1). When a new periodogram is to be computed, the read address pointer RP is initialized to RP = WP-K. After reading the contents of cell RP, the read pointer is incremented, a new readout then follows, and so forth. This has the effect of reading out the K most recent signal samples from the ring buffer. It may be advantageous to read the buffer contents out in the opposite direction of the reading in, initializing the read pointer to RP = WP. A time reversal has no effect on the periodogram, if simultaneously the real and imaginary parts of the signals are interchanged on the input to the spectrum analyser. This is realized by writing

$$y(t) + jx(t) = j\hat{x}^*(t) \tag{4.8}$$

$$|F\{j\hat{x}^*(-t)\}|^2 = |jF^*\{\hat{x}(t)\}|^2 = |F\{\hat{x}(t)\}|^2 \tag{4.9}$$

where $F\{\cdot\}$ denotes Fourier transform. Reading out in reverse time may possibly simplify the addressing circuitry of the buffer when K is variable.

The sliding ring organization is similar to buffers previously used in time compression spectrum analysers [24]. It has the advantage of allowing for a variable degree of overlap between adjacent transforms, provided the DFT processor is sufficiently fast. In contrast to the ping-pong organization, it never requires a fast DFT processor to run idle. It therefore allows for a constant periodogram output rate, regardless of the signal sampling frequency, which is an advantage from a display point of view. Assuming 100% duty cycle for the DFT processor, the fractional overlap between two adjacent signal segments is

$$r \simeq 1 - \frac{T_c}{KT_s} \tag{4.10}$$

where T_c is the computing time for one DFT. Consequently, the necessary buffer size W_b is (complex words)

$$W_b > K + \frac{T_c}{T_s} \tag{4.11}$$

The speed requirement for the DFT processor can be found from (4.10). Requiring 50% overlap or more $(r \leq 0.5)$ for all combinations of K and f_s implies that

$$T_c \leq 0.5\ (KT_s)_{min} \tag{4.12}$$

Selecting $(f_s)_{max} = 40$ kHz and $K_{min} = 64$ (a smaller K is hardly actual at this high sampling rate) requires the DFT computing time to be less than 0.8 ms.

It is convenient to select the number of terms M in the spectrum averager to be constant, regardless of the sampling frequency. The data collection time to one averaged periodogram then becomes

$$T = KT_s + (M-1)T_c \tag{4.13}$$

Averaging for 10 ms is obtained by selecting $M = 12$ when $T_c = 0.8$ ms. Even if M is constant, the efficient number of terms in the average varies continuously with KT_s. In the case of Hamming windowing, the fractional variance of the estimate is relatively insensitive to an increase of the overlap above 50 - 60% (Fig. 2.3.a). This implies that the fractional variance of the spectrum estimate resulting from the above scheme can be found approximately from Fig. 2.3.b, setting

$$\frac{L}{K} = \frac{T}{KT_s} = 1 + \frac{(M-1)T_c}{KT_s} \tag{4.14}$$

where also non-integer values of L/K are allowed. The above scheme thus provides every possibility for trading off resolution for a reduction in variance, either by reducing K, or by increasing the sample rate.

4.3 Summary of Chapter 4

A high speed, sliding DFT spectrum analyser can be implemented with relatively modest amounts of hardware using the Chirp Z transform, especially if spectrum averaging is not required. However, it lacks the possibility of employing variable transform length, which is a severe drawback when used with a pulsed Doppler instrument. When spectrum averaging is included, the sliding transform analyser yields an averaged periodogram with unnecessary high variance, since it is incapable of computing DFT's from overlapping signal segments.

In contrast, the ordinary DFT analyser with a sliding ring input buffer yields a solution with maximal flexibility, provided the DFT processor is sufficiently fast (computing time preferably less than 1 ms). It offers equal or superior performance to the sliding transform analyser in every respect.

5 SYSTEM ARCHITECTURE FOR A HARDWIRED REAL TIME SPECTRUM ANALYSER

Based on requirements stated in the previous chapters, the system architecture of a flexible real time spectrum analyser for analysis of Doppler signals from blood shall now be discussed. It is based on the ordinary DFT/sliding ring input buffer structure described in Section 4.2 (Fig. 4.4.a and c). It has been chosen to compute a 64 point DFT by feeding the signal sequence to be transformed twice through a sliding Chirp Z transformer. This method has earlier been discussed in Sections 2.6.2 and 4.1.1. The solution is partly analog, allowing for a minimum computation time ~ 128 μs. The high speed makes the concept highly appealing also for multigated Doppler instruments. The spectrum analyser may then be shared between the signals from different range gates, allowing for spectrum analysis of 16 independent signals every ~ 2 ms. The details of the solution given in this chapter concern samples from one signal only (Doppler signal assumed to be analog), but the extensions to a multigated instrument are straightforward. The changes required are mainly in the organization of the input and output buffers, and some additional memory in the spectrum averager and the AGC.

Recent advances in VLSI technology has resulted in commercially available single chip digital signal processors [54][55]. These are well suited for real time FFT computations. A solution based on two signal processors of the type TMS 32010 has been presented [58], computing a 64 point spectrum in 1.5 ms. The digital signal processors are good alternatives to the quasi analog approach here proposed for single range PW or CW instrument applications. For use in multigated Dopplers, it is still hard to compete with the speed and compactness of the CZT solution.

In the following, detailed hardware solutions will be presented only where the design is nontrivial.

5.1 Doppler signal preprocessing

A block diagram for preprocessing of the analog Doppler signal prior to the spectrum analysis is shown in Fig. 5.1. It comprises of anti aliasing filters, sample and hold, a multiplexed AGC and A/D converter, and finally an input buffer memory. Some control signals are also indicated. The diagram is discussed in detail in the next sections.

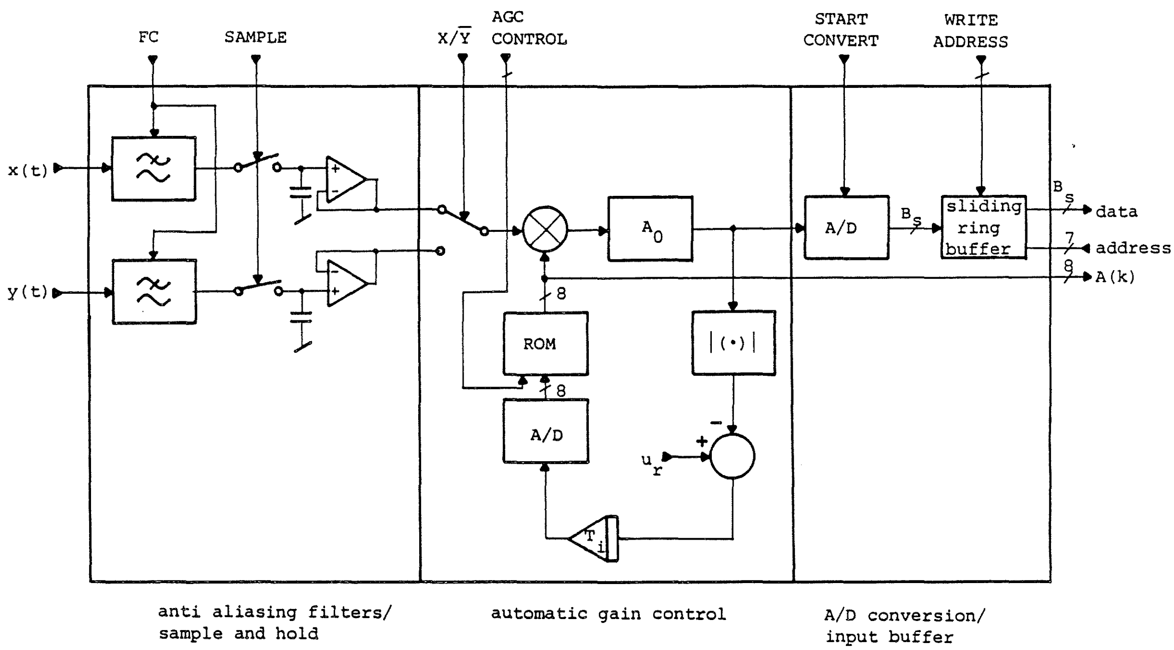

Fig. 5.1 Doppler signal preprocessing.

5.1.1 Anti aliasing filters/sample and hold

The cutoff frequency f_c of the anti aliasing filters should vary proportionally to the sampling frequency of the spectrum analyser. For maximum flexibility, the sampling should at choice either be free running at any selected frequency in the range 4-40 kHz, or, for measurements of frequencies above the Nyquist limit in pulsed Doppler, run synchronized with the range gating. In the latter case, the control logic must also provide the correct phase delay between the Doppler range gate and the spectrum analyser sampler.

The cutoff frequency of the anti aliasing filters should be set according to the following rules:

i) Freerunning sampling, symmetrical spectral display: $f_c = f_s/2$

ii) Freerunning sampling, asymmetrical spectral display: $f_c = f_s$

iii) Synchronized sampling: $f_c = \infty$

Cases i) and ii) were earlier discussed in Section 3.4.1. In case iii) there is no need for anti aliasing filtering; the pulsed Doppler instrument contains smoothing filters with cutoff at the Nyquist frequency.

The above requirements can be met using switched capacitor filters. These are monolithic, sampled data filters with cutoff frequencies proportional to an external clock frequency. The control logic must supply the filters with clock frequencies according to the above rules. One of the commercial devices is particularly suitable for the purpose, since it contains two independent 2-pole filters on one chip [37]. The monolithic design guarantees close matching between the two filters in one device, and thus, equal filtering of the real and imaginary part of the Doppler signal. A suitable filter characteristic is 4-pole Chebychef with ~ 1 dB passband ripple. This yields reasonably steep edges with moderate circuit complexity. Although Chebychef filters in general introduces some phase distortion of the signal, it can be neglected; the spectrum of the Doppler signal is the only concern.

Fig. 5.2 shows a control system for automatic selection of the fractional sampling delay Δ_r when the spectrum analyser runs in synchronism with a pulsed Doppler instrument (compare with Fig. 3.12.a). The system is controlled by a microprocessor. A test signal with frequency $f_s/2$ is injected on the input of the Doppler range gate each time the PRF or the highpass filter setting of the Doppler instrument is changed, controlled by the signal MEASURE/$\overline{\text{TEST}}$. At the output of the smoothing filter, this appears as a sinewave (the choice of a near 90^o phaselag in the drawing was arbitrary). The synchronism between the test signal and the second sample and hold causes its output to be a squarewave with amplitude depending strongly on Δ_r (lower part of Fig. 5.3). The microprocessor adjusts the fractional delay Δ_r between the two samplers, while measuring the amplitude of the squarewave. It then selects the value which yields the highest amplitude. This corresponds to the phase angle $\tilde{\gamma}(\omega_s/2) = m\pi$, m integer, in eq. (3.22). The test signal can then be switched off, returning to normal measurement mode. The whole procedure should take no more than a few milliseconds, with minimal disturbance for the system operator.

5.1.2 Automatic Gain Control

The AGC circuit in Fig. 5.1 is basically the scheme described in

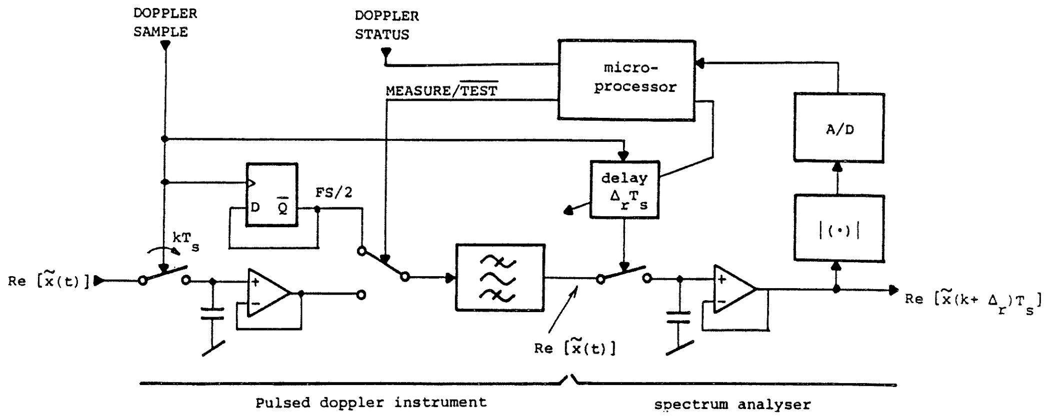

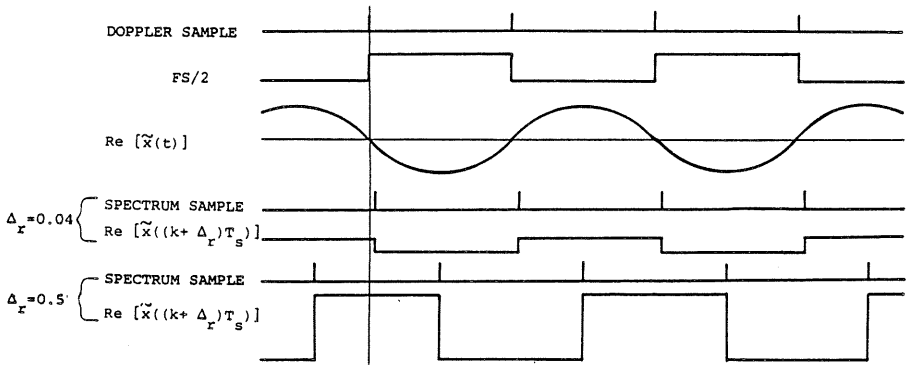

Fig. 5.2 **Control system for automatic selection of proper sampling delay Δ_r. The lower part of the figure shows typical signals under operation of the system.**

Section 3.5.2. The variable gain element is a multiplying D/A converter, which is multiplexed between the real and the in quadrature signal channels. This ensures identical treatment of both channels [38]. The output from the AGC integrator is A/D converted each time the Doppler signal is sampled. The discrete time implementation causes no instability problems; the sampling time T_s is at least 2 decades smaller than the AGC time constant. The 8 bit output from the A/D converter is modified through a ROM lookup table before entering the MDAC. The contents of this table is the function $\alpha \exp[\beta(\cdot)]$, eq. (3.29). Several different ROM programs may be included to allow for programmable variation of AGC parameters, e.g. maximum gain, or the AGC time constant.

The gain of the AGC block is a discrete variable of the form $A = nA_0/256$, $n = 0,\ldots,255$. The minimum value for n should be restricted to approx. 5; otherwise the relative gain change between successive n's becomes very large. The maximum AGC range then becomes 255/5, or 34 dB, which is more than adequate. Alternatively, a logarithmic multiplying D/A converter may be used as a gain control element. This would allow for a larger AGC range, but the devices are considerably more costly than ordinary MDAC's.

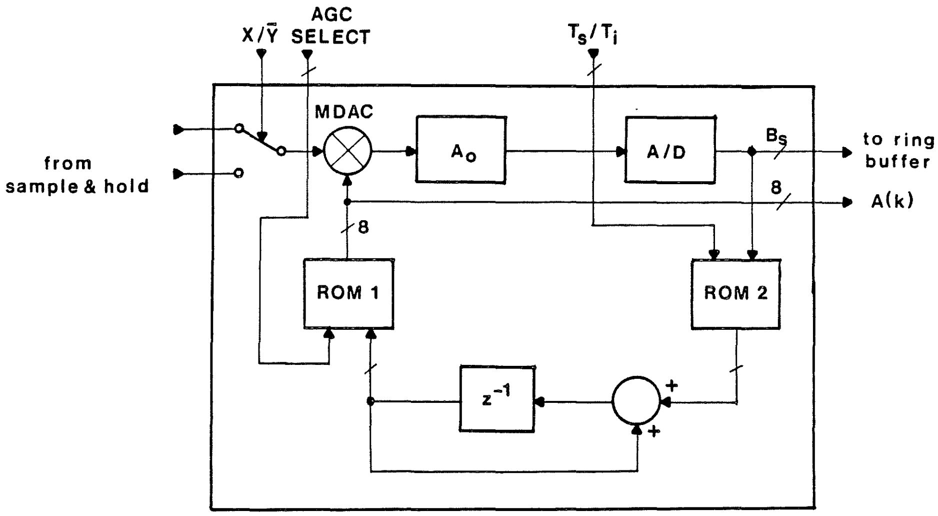

Fig. 5.3 All digital AGC loop.

An alternative, all digital implementation of the AGC feedback loop is obtained by moving the input to the rectifying block in Fig. 5.1 behind the A/D converter, as shown in Fig. 5.3. The integrator now is implemented in discrete time (z^{-1} symbolizes one sample delay). The ROM 2 contains the lookup table $T_s(u_r - |(\cdot)|)/T_i$. This solution obsoletes the A/D conversion within the feedback loop, but in order to maintain a constant AGC time constant, it requires a sampling frequency dependent scaling factor T_s/T_i in the loop. However, since the loop is all digital, it can easily be multiplexed between a number of independent Doppler signals. The solution is therefore appealing in multigated systems. The approach in Fig. 5.1 is less suited in this respect, requiring a number of independent analog integrators.

5.1.3 Signal A/D conversion

The quantization noise of the signal A/D conversion may be a limiting factor for the dynamic range of the spectrum analyser. A B_s-bit A/D conversion of a real signal yields the quantization noise power [2]

$$N_q = \frac{2^{-2B_s}}{3} u_s^2 \tag{5.1}$$

where the saturation levels of the A/D converter are $\pm u_s$. The maximum input signal power S_{max} of the real signal is limited by the saturation of the A/D converter. Assume that the reference level of the AGC is set according to (3.41). The signal to noise ratio for each of the quadrature components becomes, using eqs. (3.40) and (5.1)

$$\begin{aligned}(\frac{S}{N_q})_{max} &= \frac{3}{n_{0.005}^2} 2^{-2B_s} \\ &\simeq 6B_s - 3 \text{ [dB]}\end{aligned} \tag{5.2}$$

For a complex Gaussian signal, the quantization noise in the real and the in quadrature signal channels may be assumed to be independent. The total quantization noise power for the complex signal thus becomes $2N_q$. Since the class of complex Gaussian signals satisfies the relation $R_{\hat{x}\hat{x}}(0) = 2R_{xx}(0) = 2R_{yy}(0)$ (follows from the definition (2.1) using (2.2)-(2.4)), the relation (5.2) holds also for a complex Gaussian signal. Selecting $B_s = 8$ bits thus at best yields 45 dB signal to quantization noise ratio, assuming a perfectly scaled input signal to the A/D converter.

Using standard ultrasound emission levels (average acoustic power < 100 mW/cm^2 at the transducer's face), the power ratio between the Doppler signal and the transducer's thermal noise rarely exceeds 30-40 dB. When low frequency ultrasound (1-2 MHz) is employed to measure high velocities in deep central vessels (or in the heart), much lower signal to noise ratios often occur (< 10dB), especially in old patients. Occasionally, signal to noise ratios up to 50 dB may be obtained, measuring with high frequency ultrasound (5-10 MHz) on the larger peripheral vessels (carotid or femoral arteries) in young, healthy persons. In this context it seems justified that using 8 bit signal quantization hardly represents a severe limitation - especially if the A/D converter is preceded a fast AGC/limiter.

5.1.4 Doppler signal input buffer

The design of the sliding ring input buffer can be done directly from its description in Section 4.2. We have earlier selected the parameters $K_{max} = N = 64$ and $(f_s)_{max} = 40$ kHz. If the computing time requirement $T_c = 0.8$ ms is adopted from Section 4.2, the minimum buffer size becomes 96 complex 8 bit words.

Since the DFT is computed by a sliding CZT processor, the contents of the buffer memory must be replayed twice during the analysis, possibly in reverse time. The output from the CZT is valid during the second replay.

5.2 The sliding DFT computer

The sliding DFT computer is based on the simplified CZT block schematics (postmultiplication part of CZT omitted) shown in Fig. 4.2. It comprises of two separate parts: The premultiplier and the complex convolver.

5.2.1 The premultiplier

A straigthforward hardware scheme for computing the premultiplying part of the Chirp Z Transform is shown in Fig. 5.4. Since a digital input buffer is employed, the data inputs {x(k)}, {y(k)} to the premultiplier are digital. The outputs to the complex convolver are analog. Initially, rectangular windowing of the premultiplier shall be assumed. The calculations to be performed then are (from (4.4) and (2.2))

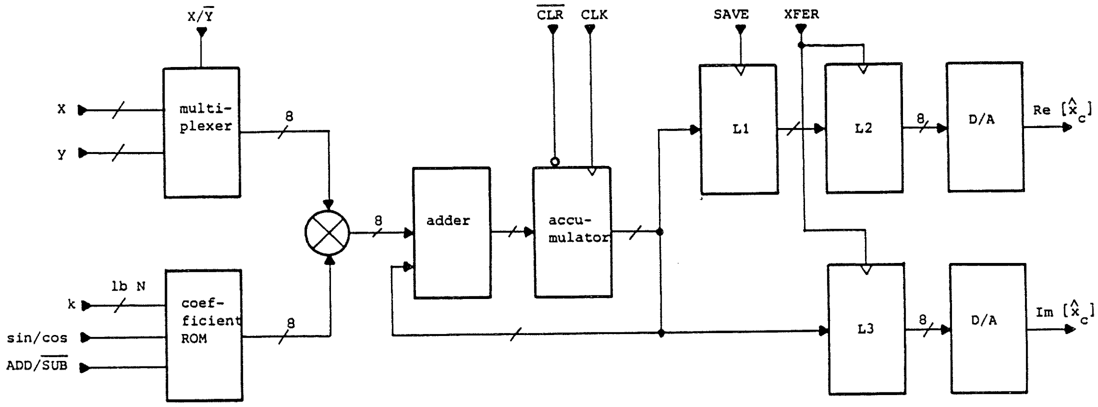

Fig. 5.4 Digital premultiplier.

$$\mathrm{Re}[\hat{x}_c(k)] = x(k)\cos\frac{\pi k^2}{N} + y(k)\sin\frac{\pi k^2}{N} \tag{5.3}$$

$$\mathrm{Im}[\hat{x}_c(k)] = y(k)\cos\frac{\pi k^2}{N} - x(k)\sin\frac{\pi k^2}{N} \tag{5.4}$$

The structure of this operation is identical with the well known FFT 'butterfly'. The solution in Fig. 5.4 stores the sine and cosine coefficients in a ROM in both normal and sign inverted versions. Then both the above sums of products can be computed sequentially, using a single multiplier/adder/accumulator. The sequence starts with clearing of the accumulator. The product $x(k)\cos(\pi k^2/N)$ is then computed and stored in the accumulator. The next clock period the partial product $y(k)\sin(\pi k^2/N)$ is formed and added to the first partial product. The accumulator now contains $\mathrm{Re}[\hat{x}_c(k)]$, which is transferred to an intermediate storage latch L_1 by means of the control signal SAVE. During the next cycles $\mathrm{Im}[\hat{x}_c(k)]$ is computed in a similar way. Then, both $\mathrm{Re}[\hat{x}_c(k)]$ and $\mathrm{Im}[\hat{x}_c(k)]$ are transferred synchronously to the output latches L2, L3, using the control signal XFER, and finally D/A converted. Necessary control signals must be provided from a simple sequencer circuit.

The multiplier/adder/accumulator function is available as single chip devices. Unfortunately, these are relatively expensive, and it shall be shown in the following that the multiplier can be replaced with inexpensive ROM's in an elegant way, without deterioration of performance. This is possible since it turns out that the set

$$\{|\sin\frac{\pi k^2}{N}| \cup |\cos\frac{\pi k^2}{N}|\} \quad k = 0,1,..,N-1 \tag{5.5}$$

contains only a small number of different elements. The set can alternatively be written

$$\{|Re[e^{j\frac{\pi k^2}{N}}]| \cup |Im[e^{j\frac{\pi k^2}{N}}]|\}$$

$$= \{Re\ [e^{j\frac{\pi}{N}(k^2 \bmod \frac{N}{2})}] \cup Im\ [e^{j\frac{\pi}{N}(k^2 \bmod \frac{N}{2})}]\} \tag{5.6}$$

$$= \{\sin[\tfrac{\pi}{N}(\tfrac{N}{2} - (k^2 \bmod \tfrac{N}{2}))] \cup \sin[\tfrac{\pi}{N}(k^2 \bmod \tfrac{N}{2})]\}$$

when N is even. The last transition follows by expressing the cosine function in the first quadrant in terms of the sine function. An integer set E may now be defined as

$$E = \{e(n)\}_{n=0}^{N_e-1} = \{(\tfrac{N}{2} - (k^2 \bmod \tfrac{N}{2})) \cup (k^2 \bmod \tfrac{N}{2})\}_{k=0}^{N\ -1} \tag{5.7}$$

The set E contains $N_e \leq N$ different integers, which are assumed to be numbered in terms of increasing magnitude. The set (5.5) can therefore be written

$$\{|\sin \tfrac{\pi k^2}{N}| \cup |\cos \tfrac{\pi k^2}{N}|\}_{k=0}^{N-1} = \{\sin(\tfrac{\pi}{N}e(n))\}_{n=0}^{N_e-1} \tag{5.8}$$

An examination of the set E for the case when N is a power of 2, $N = 2^b$, b integer, shows that $N_e \ll N$. Some values of N_e are listed in Table 5.1. N_e satisfies the empirical recursive relation

$$N_e(b+1) = 2[N_e(b)-1] - \tfrac{1}{2}[1 + (-1)^{b+1}] \tag{5.9}$$

starting with $N_e(2) = 3$ (the relation has not been checked for b larger than 9 (corresponds to N = 512), and no attempt has been made to prove it for a general integer power). Actual values for the available chirp filters are N = 64 which gives $N_e = 13$, and N = 512 which gives $N_e = 88$.

b	2	3	4	5	6	7	8	9
N	4	8	16	32	64	128	256	512
N_e	3	4	5	8	13	24	45	88

Table 5.1 Number of elements in the set E.

According to (5.8) one may now write

$$\sin \frac{\pi k^2}{N} = \mathrm{sgn}(\sin \frac{\pi k^2}{N}) \sin[\frac{\pi}{N} e(m_s(k))] \tag{5.10}$$

$$\cos \frac{\pi k^2}{N} = \mathrm{sgn}(\cos \frac{\pi k^2}{N}) \sin[\frac{\pi}{N} e(m_c(k))] \tag{5.11}$$

where $\mathrm{sgn}(\cdot)$ is the signum function. The functions $\{m_s(k)\}$, $\{m_c(k)\}$ map the argument k into the proper element e of the set E. Once the set E has been established by examination of (5.7), construction of $m_s(k)$ and $m_c(k)$ can be done by inspection of (5.10).

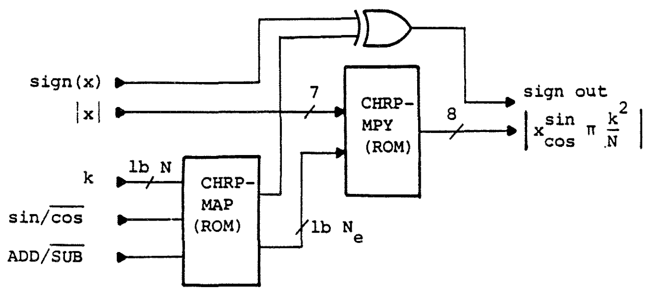

Fig. 5.5 ROM-multiplication using mapping.

The above equations suggest the use of the multiplier structure shown in Fig. 5.5. The CHRP-MAP table contains the functions $\{m_s(k)\}$ and $\{m_c(k)\}$, which are selected by the control line sin/$\overline{\text{cos}}$. Together with $|x(k)|$ and $|(y(k)|$, its output addresses the CHRP-MPY ROM, (magnitude/sign digital number representation is assumed). The CHRP-MPY ROM is a lookup table containing rounded products

$\{|(\cdot)|\sin(\pi e(n)/N)\}$, $n = 0,..,N_e-1$. The sign of the product is calculated by separate processing. An 8 bit wide ROM thus provides 9 bit product accuracy. With $N = 64$ and 8 bit signal quantization, the size of the multiplier ROM becomes $2^{7+\mathrm{lb}N_e} = 2^{11}$ byte, or 2048 byte, which is fairly modest. The concept is therefore both economical and appealing.

The reason for not including the windowing part of the premultiplication directly in (5.3)-(5.4) as initially suggested in Fig. 4.4 is now obvious: The windowed chirps have in general a much larger value set than the non-windowed. This would have made the proposed mapping technique less efficient. Instead, the window multiplication may be carried out in cascade with the chirp multiplication. Windowing may also be performed using ROM multiplication and mapping technique, writing

$$w(k;K) = e_w(m_w(k;K)) \qquad k = 0,1,..,N \tag{5.12}$$

where $m_w(k)$ is a mapping function, similar to $m_s(k)$ and $m_c(k)$, and $\{e_w(n)\}$ is a value set with a small number of elements. Due to the even symmetry of the window, a value set with 32 elements can give an exact representation of any window of length $K < 64$. However, it has earlier been pointed out that it is desirable to vary the transform length by employing windows of different lengths, and augment with zeros. This can be obtained, simply by changing the mapping function, but some roundoff errors are inevitable if a number of different windows must share a common 32 valued set $\{e_w(n)\}$. Still, a proper selection of this set and the corresponding mapping functions allows for the use of a number of quantized windows of widely different lengths, all with acceptable sidelobe levels. This is elaborated further in Appendix II.

A simplified block diagram for an 8 bit $N = 64$ windowed premultiplier based on the above ideas is shown in Fig. 5.6. The control sequencer is omitted. The number representation of the data $\{x(k)\}$, $\{y(k)\}$ from the input buffer memory is offset binary (OB). In contrast to Fig. 5.5, the CHIRP-MPY ROM now supplies full signed products in an 8 bit 2-complement (2C) format to the adder/accumulator. In addition to the multiplication with the window, the WNDW-MPY ROM also converts the data back to the the offset binary format required by the D/A converters. The scheme allows for choice between 16 different window types

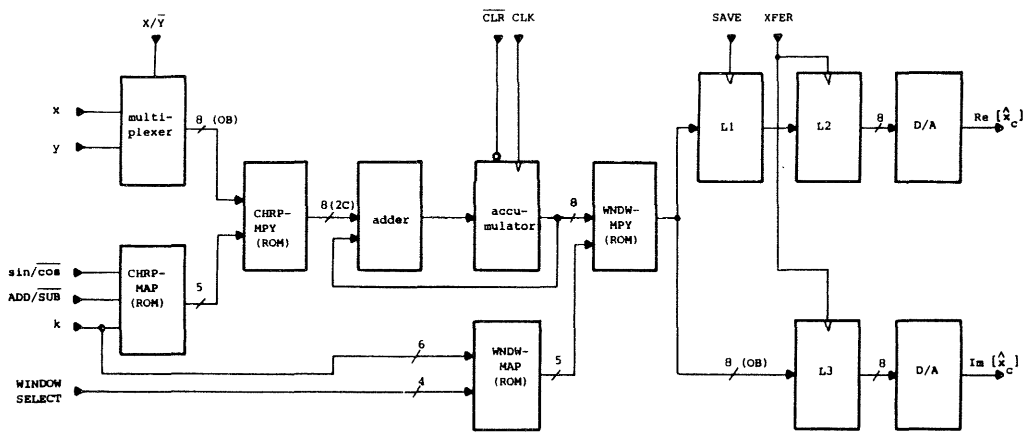

Fig. 5.6 Digital premultiplier including windowing.

and/or K's by changing the window mapping function $\{m_w(k;K)\}$. Use of 200 ns 8k x 8 bit EPROM's for the CHIRP-MPY and WNDW-ROM's and 2 additional registers to allow for pipelining, leads to a design where a full complex premultiplication/windowing takes only 1 µs. This fits the maximum sampling frequency of the 64 sample chirp filters used in the complex convolver. The minimum computing time for the DFT thus becomes 128 µs.

5.2.2 The complex convolver

The convolver is a fully analog computation circuit which in principle can be designed directly from the block diagram in Fig. 4.2. It then requires 4 independent 64 point chirp filters, rectangular windowed, and 2 adder/subtractor circuits.

A reduction of convolver complexity with a factor 2 is possible, at the cost of a corresponding increase in computing time. This can be obtained by computing the sub-periodograms $\tilde{G}_r$ and $\tilde{G}_i$ sequentially in time, rather than using the parallell organization indicated in Fig. 4.2. The averaged periodogram is then formed by adding 2M sub-periodograms, possibly compressed (eq. (2.73)), rather than using the M term version eq. (2.72). In the following, it is shown how this type of operation can be obtained.

By comparing (4.2), (2.142) and (2.10), the output of the complex convolver can be written

$$\begin{aligned}\tilde{Z}(k) &= \sum_{n=1}^{N} e^{-j\frac{\pi n^2}{N}} (\hat{x}_c(k-n))_p \\ &= \tilde{X}(K/2, 2\pi k/N; K)\, e^{j\frac{\pi k^2}{N}}\end{aligned} \tag{5.13}$$

where

$$\hat{x}_c(k) = w(k;K)\hat{x}(k)e^{-j\frac{\pi k^2}{N}} \tag{5.14}$$

The set $\{(\hat{x}_c(k))_p\}$ is the periodic extension of the N-sample sequence $\{\hat{x}_c(k)\}$. We also define

$$\tilde{Z}_r(k) = \mathrm{Re}[\tilde{Z}(k)] \tag{5.15}$$

$$\tilde{Z}_i(k) = \mathrm{Im}[\tilde{Z}(k)] \tag{5.16}$$

It has earlier been shown that $\mathrm{Re}[\tilde{X}(k)]$ and $\mathrm{Im}[\tilde{X}(k)]$ are identically distributed, statistically independent zero mean Gaussian variables. From (5.13), the same holds also for $\tilde{Z}_r(k)$ and $\tilde{Z}_i(k)$ (orthogonal transformation). The following definition of the sub-periodograms is then statistically equivalent to (2.53)-(2.55):

$$\tilde{G}_r(K/2, 2\pi k/N; K) = \frac{1}{K}\tilde{Z}_r^2(k) \tag{5.17}$$

$$\tilde{G}_i(K/2, 2\pi k/N; K) = \frac{1}{K}\tilde{Z}_i^2(k) \tag{5.18}$$

Writing out (5.13) leads to the following results (compare with Fig. 4.2):

$$\begin{aligned}\tilde{Z}_r(k) &= (\mathrm{Re}[\hat{x}_c(k)] \circledast \mathrm{Re}[h(k)]) - (\mathrm{Im}[\hat{x}_c(k)] \circledast \mathrm{Im}[h(k)]) \\ &= (\mathrm{Re}[\hat{x}_c(k)] \circledast \mathrm{Re}[h(k)]) + (-\mathrm{Im}[\hat{x}_c(k)] \circledast \mathrm{Im}[h(k)])\end{aligned} \tag{5.19}$$

$$\tilde{Z}_i(k) = (\mathrm{Im}[\hat{x}_c(k)] \circledast \mathrm{Re}[h(k)]) + (\mathrm{Re}[\hat{x}_c(k)] \circledast \mathrm{Im}[h(k)]) \tag{5.20}$$

where $\circledast$ denotes convolution. This suggests the use of the 'residual' convolver configuration shown in Fig. 5.7, both for the computation of $\{\tilde{Z}_r(k)\}$ and $\{\tilde{Z}_i(k)\}$. A slight modification of the premultiplier then is necessary, since computation of $\{\tilde{Z}_r(k)\}$ using (5.19) requires its output to be

$$-\mathrm{Im}[\hat{x}_c(k)] + j\mathrm{Re}[\hat{x}_c(k)] = j\hat{x}_c(k) \tag{5.21}$$

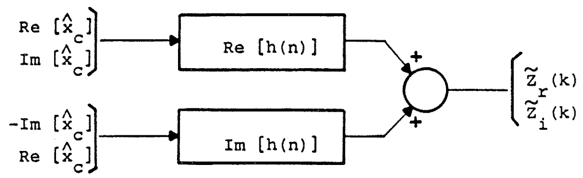

Fig. 5.7 Simplified convolver for serial computation of $\tilde{Z}_r(k)$ and $\tilde{Z}_i(k)$.

Hence, both $\{\tilde{Z}_r(k)\}$ and $\{\tilde{Z}_i(k)\}$ can be computed by replaying the windowed N-sample signal sequence to be transformed 4 times from the input buffer; the first 2 times the ordinary premultiplier program (4.6) is used, yielding a valid $\{\tilde{Z}_i(k)\}$ on the output of the convolver during samples N to 2N - 1. The next 2 replays the modified premultiplier equation (5.21) is computed, leading to $\{\tilde{Z}_r(k)\}$ during samples 3N to 4 N - 1. The time for computing the full DFT thus increases from 2N to 4N cycles. For N = 64, this gives a minimum computing time 256 µs, which still is approximately 3 times faster than the requirement stated for single range PW or CW Doppler instruments. The increased computing time is less tolerable in a multigated PW Doppler instrument, where the spectrum analyser is multiplexed between a large number of independent signals. On the other hand, this type of instrument tends to use PRF's in the range 5 - 15 kHz, depending on the application. The computing time requirement $T_c = 0.8$ µs for the signal from each range gate can therefore be relaxed considerably in this situation (it was set assuming 40 kHz sampling rate).

5.3 DFT Postprocessing

A flexible structure for processing the analog outputs from the convolver to a final moving averaged compressed periodogram is shown in Fig. 5.8. It comprises of some analog processing, spectrum A/D conversion, a moving averager, cancelling of white noise, a variable spectrum compression for sonagram display, and finally an interpolator circuit and an output buffer. Some brief comments shall be made on each block.

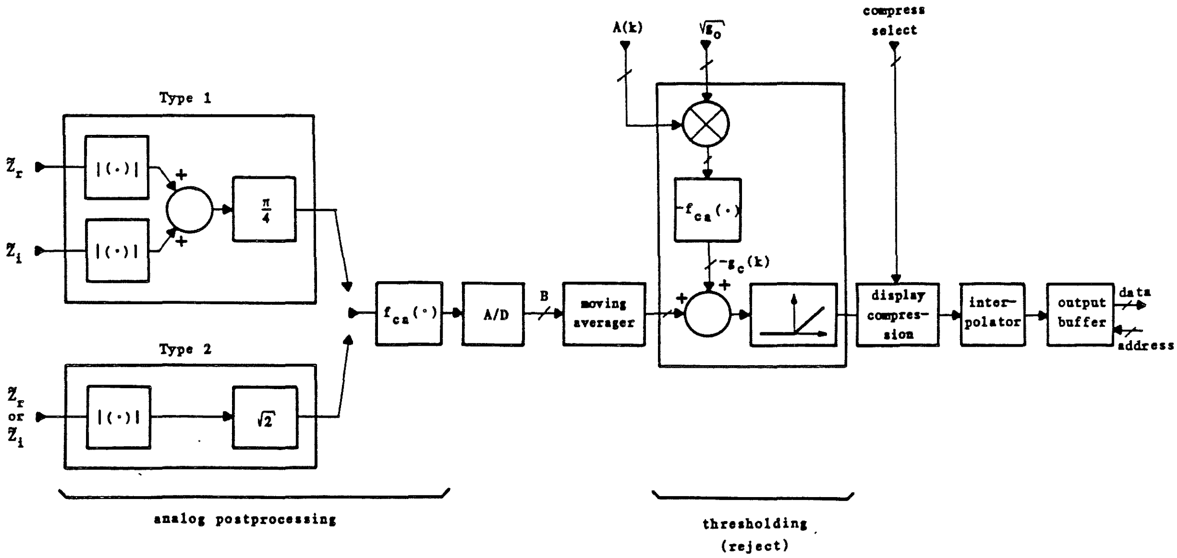

Fig. 5.8 DFT postprocessing.

5.3.1 Analog postprocessing

The purpose of this block is to combine the real and/or imaginary analog signal outputs from the complex convolver into a signal suited for A/D conversion. When the signal is quantized to 8 bit, the signal to quantization noise power ratio is maximum 45 dB (Section 5.3.1). If the signal is narrowband, the ratio between the spectral densities of the signal and the quantization noise ratio may be considerably higher. A narrowband signal will concentrate over an angular bandwidth $\Delta\omega_a \sim 2\pi/K$, while the quantization noise spreads out over the entire bandwidth 2π. The spectral signal to noise ratio may therefore be as much as 10 lgK dB's higher than the signal to noise power ratio. When $K = 64$ and 8 bit signal quantization is employed, this means that the A/D conversion of the convolver outputs should be able to handle a dynamic range in excess of 60 dB. Limitations of the BBD chirp filters may degrade this expected performance somewhat, but probably not very much. This assumption is based on earlier experiences with the same chirp filters, where a 60 dB output dynamic range was obtained (peak spectral density with maximum amplitude single frequency input, relative to peak intrinsic spectral noise level with signal input grounded) from an all analog sliding DFT spectrum analyser of the type shown in Fig. 4.3 ('DAISY', unpublished data).

Two alternative input paths from the convolver are shown in Fig. 5.8. The 'Type 1' path applies if the parallell solution (full 4-filter complex convolver) is chosen, while the 'Type 2' path applies for for serial computation of $\tilde{Z}_r(k)$ and $\tilde{Z}_i(k)$. Note that for the Type 1 alternative, it has been chosen to compute the expression $\pi(|\tilde{Z}_r|+|\tilde{Z}_i|)/4$ rather than the sum of squares $\tilde{Z}_r^2 + \tilde{Z}_i^2$. Apart from being simpler to implement, this approach easily allows for the necessary 60 dB dynamic range using analog circuitry. In contrast, the sum of squares would require 120 dB dynamic range on the output of an analog squaring device.

The output from the rectifiers are passed through an analog compression function $f_{ca}(\cdot)$ prior to A/D convertion for digital averaging. Averaging the output from the Type 2 path in Fig. 5.8 then corresponds exactly to the Type 2 averager, eq. (2.73), discussed in Section 2.4. The net compression is the combined effect of the rectification and the compression, i.e.

$$f_c(\cdot) = f_{ca}(\sqrt{(\cdot)}). \tag{5.22}$$

In the following, it shall be assumed that averaging the compressed sum of absolute values $f_{ca}(\pi(|\tilde{Z}_r| + |\tilde{Z}_i|)/4K)$ is approximately equivalent to averaging $f_c(\tilde{G}) = f_{ca}(\sqrt{(\tilde{Z}_r^2 + \tilde{Z}_i^2)/K})$., i.e. the correspondingly compressed amplitude periodogram. This is justified by the following facts:

i) The approximation

$$\pi(|\tilde{Z}_r| + |\tilde{Z}_i|)/4 \simeq \sqrt{\tilde{Z}_r^2 + \tilde{Z}_i^2}$$

has a bounded peak error. The peak fractional error is -21%, occurring when one of the variables $\tilde{Z}_r$, $\tilde{Z}_i$ is zero.

ii) The below relations hold:

$$\sqrt{\frac{\pi}{2}}\,\langle\sqrt{2\tilde{G}_r}\rangle = \frac{2}{\sqrt{\pi}}\,\langle\sqrt{\tilde{G}}\,\rangle = \sqrt{\langle\tilde{G}\rangle} \tag{5.23}$$

This follows directly from (2.99), first with M = a = 0.5, and then with M = 1, a = 0.5. This is equivalent to

$$\frac{\pi}{4}\,\langle|\tilde{Z}_r| + |\tilde{Z}_i|\rangle = \langle\sqrt{\tilde{Z}_r^2 + \tilde{Z}_i^2}\,\rangle \tag{5.24}$$

ii) The fractional variance of the variable $|\bar{Z}_r| + |\bar{Z}_i|$ is only 4.5% higher than the fractional variance of the variable $\sqrt{\bar{Z}_r^2 + \bar{Z}_i^2}$, see Section 2.4.3.

In total, this indicates that the probability distributionsof the two variables are fairly similar. It therefore seems justified that the analysis of the Type 1 averager, eq. (2.72), is reasonably accurate also for the simplified Type 1 structure in Fig. 5.8.

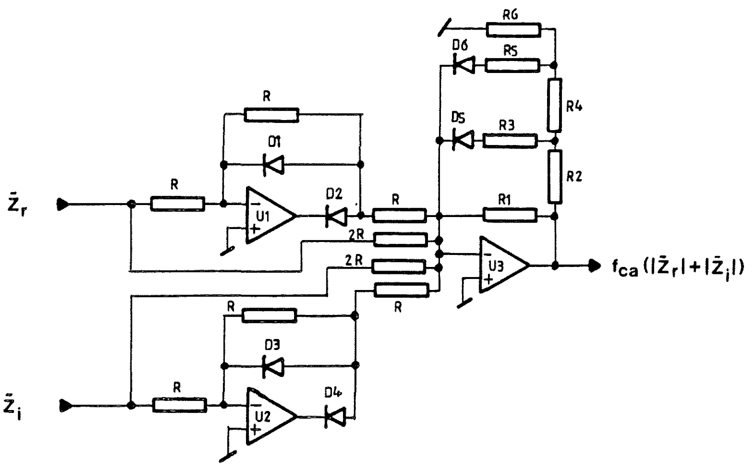

Fig. 5.9 Analog postprocessor for the Type 2 convolver.

A simple hardware solution to the analog preprocessor circuit for the Type 1 situation is shown in Fig. 5.9. It consists of two 'ideal' rectifiers U1, U2 and analog compression in the amplifier U3. The compression occurs since the feedback across the amplifier increases with increasing output level. The circuit can be taylored to approximate different choices of $f_{ca}(\cdot)$ by varying the resistors $R_1 - R_6$.

5.3.2 A/D conversion of the convolver outputs/spectrum averager

A number of tradeoffs must be evaluated before this block is designed. Two different approaches seem practical:

i) Select a relatively moderate compression of the form $f_c(\cdot) = (\cdot)^a$, or, equivalently, $f_{ca}(\cdot) = (\cdot)^{2a}$. This approach ensures a low variance increase from the compression, at the cost of requiring a relatively large number of bits B in the spectrum A/D conversion to allow for succicient dynamic range. Selecting $B = 8$ and $a = 0.4$ then yields a maximum resolvable dynamic range $D_{max} = 60$ dB, eq. (2.101), while the 'full quality' dynamic range is $D_1 = 41$ dB, eqs. (2.104), (2.106). The asymptotic variance performance index for the Type 1 solution is $r_{v1} = 1.14$ when $a = 0.4$. The corresponding numbers for the Type 2 implementation are $D_2 = 41$ dB and $r_{v2} = 1.23$. Increasing the number of bits above 8 should be avoided, since it implies a strong increase in the amount of hardware required.

ii) For the parallell solution it may be actual to select logarithmic compression and use only 4-5 bits quantization. For the serial type solution this is far less acceptable, since its variance performance index increases strongly in doing this ($r_{v2} = 2.51$ for large M). The low number of bits permits the use of a simple 8 bit recursive averager of the form

$$\tilde{C}_M^1((m+1)q,2\pi k/N,;k) = \beta\tilde{C}_M^1(mq,2\pi k/N;k) + (1-\beta)f_c(\tilde{G}((m+1)q,2\pi k/N;K)) \quad (5.24)$$

where

$$\beta = e^{-\frac{2}{M}} \simeq 1 - \frac{2}{M} \qquad \text{for } M > 5 \quad (5.25)$$

This averager is a first order discrete time lowpass filter with noise reduction capability similar to that of the ordinary averager (2.72) (compare with eqs. (2.45),(2.46)). When the input variable to the recursive averager is quantized to 4-5 bits, a simple and fast hardware solution can be designed, using 8 bit accumulation and a ROM lookup table for the multiplication with the constant β. This allows for averaging $M \sim 8$-16 terms without overflow problems. This solution may be preferred in multigated instruments, where high speed is essential.

The impulse response of the recursive averager has an infinite tail. It decays exponentially, with a 63% decrease per $MT_c/2$ time units (~ 5 ms). This infinte time duration makes the recursive averager unsuited for averaging weakly compressed periodograms. With power function compression, the decay rate of the impulse response becomes $(-8.68/a)$ dB per MT_c time units (referred to a noncompressed spectrum). If the recursive averager is employed on linear periodograms ($a = 1$), this means that a spectral line needs $\sim 5\ MT_c$, or 50 ms, to decay 40 dB. The recursive averager is therefore not useful, unless strong compression of the output from the convolver is employed.

The choice between solutions i) and ii) must be made on a cost/benefit base. Solution i) yields the lowest variance, but requires a somewhat more complex averager than solution ii).

5.3.3 Rejecting white noise

It has earlier been shown that white noise can be removed from the sonogram by thresholding the averaged periodogram. Apparently, the same effect can be obtained by thresholding the averaged compressed periodogram, provided the threshold level is adjusted according to the compression. If the spectrum analyser includes an AGC prior to the signal A/D conversion, the threshold should be made time varying, since the varying gain causes the estimated spectral intensity of the white noise to fluctuate. In the following, the gain variations of the AGC are assumed to be slow compared to the averaging time $MT_c \sim 10$ ms.

In clinical measurements, the reject threshold will be operator adjusted, with setpoint such that the noise floor just disappears from the sonagram. If the desired threshold on the linear periodogram is g_o, Fig. 2.9.b, the corresponding threshold level on the compressed periodogram becomes

$$g_c(k) = f_c(A^2(k)g_o) = f_{ca}(A(k)\sqrt{g_o}) \tag{5.26}$$

which is the basis for the solution indicated in Fig. 5.8. Thresholding is obtained by adding $-g_c(k)$ to the output from the spectrum averager. This yields directly the desired output when the result is positive. If the result is negative, the output is set to zero. The function $-f_{ca}(A_s(k)\ g_o)$ can be calculated in advance and stored in a single ROM lookup table, with progammable choice of threshold g_o.

5.3.4 Compression for sonagram display

According to the discussion in Section 3.3, several different compression characteristics should be included to ensure a good display in different situations. In Fig. 5.8 this is taken care of by passing the output from the reject function block through an additional ROM lookup table. If the desired compression of the linear periodogram is $f_{cd}(\cdot)$, the look up table should contain the composite function $f_{cd}[(f_{ca}^{-1}(\cdot))^2]$. This corrects for the initial analog compression of the convolver output.

5.3.5 Interpolator and output buffer

It has earlier been pointed out that $N = 64$ is somewhat too few frequency bins for generating a high quality sonagram display. Therefore Fig. 5.8 contains an interpolator that increases the number of frequency bins to 128 prior to display. This can be done by adding the spectrum estimate to itself, delayed 1/2 spectral line, as indicated in the upper part of Fig. 5.10. A hardware circuit that performs this operation is shown in the lower part. The two latches L1 and L2 are clocked on opposite edges of the control signal LSBI. The contents of the latches then alternates between being the same, or originating from adjacent (noninterpolated) spectral lines.

Finally the output from the interpolator is written into an output buffer memory, where it is available for sonagram display or further processing, for example microcomputer assisted calculation of mean or maximum frequency of the spectrum.

5.4 Concluding remarks

The suggested hardware solution allows for great flexibility in clinical use. Both sampling frequency and transform length can be varied to select the optimum variance/resolution tradeoff in a given situation. If desired, the CZT part of the system can be substituted with a digital FFT processor. The high speed of the BBD devices makes the proposed concept appealing also for multigated systems. Where alternative solutions have been suggested, for example parallell vs. serial computation of Z_r and Z_i in Section 5.2.2, the final choice should be made on a cost/benefit basis.

For some applications the $N = 512$ chirp filters discussed in Section 4.1.2 may represent an interesting alternative. The minimum computing

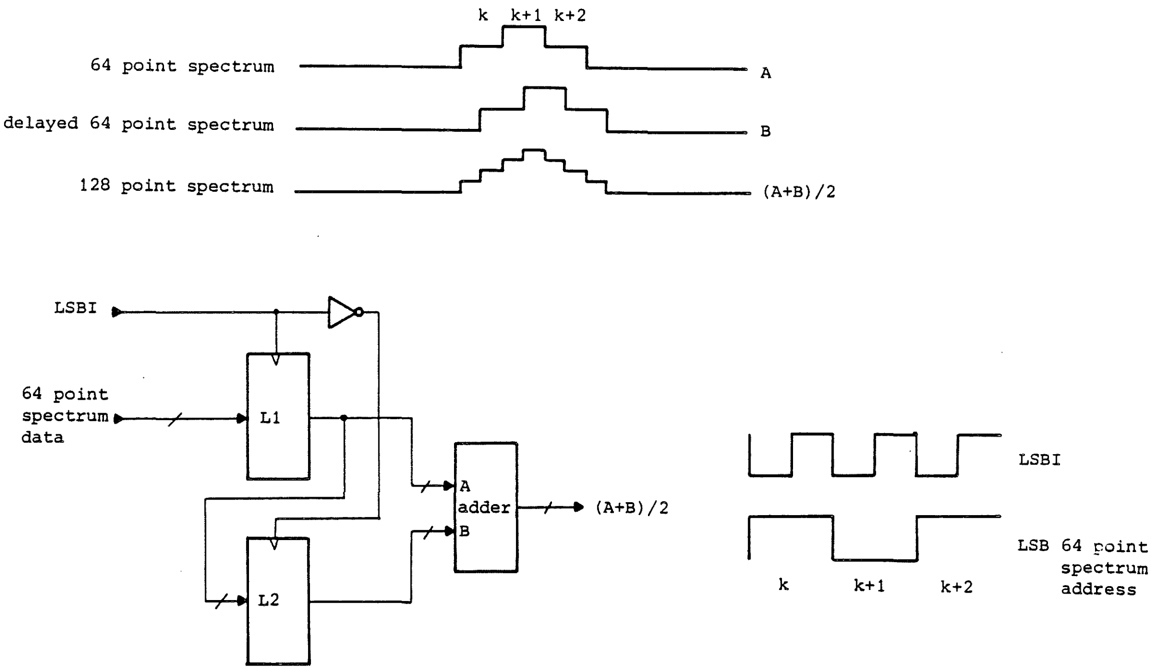

Fig.5.10 64 points to 128 points interpolator for spectrum display.

time for one periodogram using these devices is 512 μs, which is more than adequate for single range systems. However, this speed requires a 0.5 μs cycle time also in the premultiplier, which cannot be obtained with the hardware outlined, unless some parallellism is included. Obviously, the interpolator circuit is not needed if a 512 point transform is computed.

Apart from a different way of computing the DFT, there are some important differences between the proposed design and most Doppler signal spectrum analysers previously reported. The primary difference is our direct use of complex spectrum analysis, whereas other investigators (except [12][50]) first converted the complex Doppler signal to a real bandpass signal by the heterodyning operation $\mathrm{Re}[\tilde{x}(t)\exp j2\pi f_p t]$, and then analysed the heterodyned signal using real signal spectrum analysis. Typically, f_p has been chosen as 0.15 PRF in pulsed Doppler applications [26]. Apart from being unnecessary complicated and not fully utilizing the complex FFT algorithm, this approach does not easily allow for the the simple 'unwrapping' of aliased PW spectra demonstrated in Fig. 3.8.

Another difference from previous works is the use of time compression to take full advantage of the large processing capacity of the chirp filters. Although experimental evidence for improved performance has not been given, it seems justified that spectrum averaging will greatly improve e.g. registrations of the high frequency/low signal to noise ratio Doppler shifts occuring in valve incompetencies in the heart. In this situation, it is likely that improved reject of noise due to averaging will become especially important.

A hardware spectrum analyser based on the principles from Chapter 5 is presently being designed. The results will be presented elsewhere.

ACKNOWLEDGEMENT

This work has been supported by grants from the Norwegian Institute of Technology, Trondheim.

APPENDIX I

Smoothing lowpass filters for pulsed Doppler instruments.

Fig. I.1 is a model for the sampling (range gating) and the smoothing lowpass filter of a pulsed Doppler instrument with analog highpass filtering (compare with Fig. 3.12.a). The highpass filter itself is of no interest for the following discussion, and it has therefore been left out from the figure. The desired combined transfer function of the sample and hold element and the lowpass filter is an ideal lowpass filter, with cutoff at the Nyquist frequency. Then, from Shannon's sampling theorem, the filter output $\tilde{x}(t)$ becomes identical to the input signal $\hat{x}(t)$, provided its power spectrum satisfies $G_{\hat{x}\hat{x}}(\omega) = 0$ for $|\omega| > \omega_s/2$.

Ideal lowpass filters cannot be designed in practice. In this appendix, the consequences of deviations from the ideal shall be analysed. On this basis, 'optimal' all-pole lowpass transfer functions are derived.

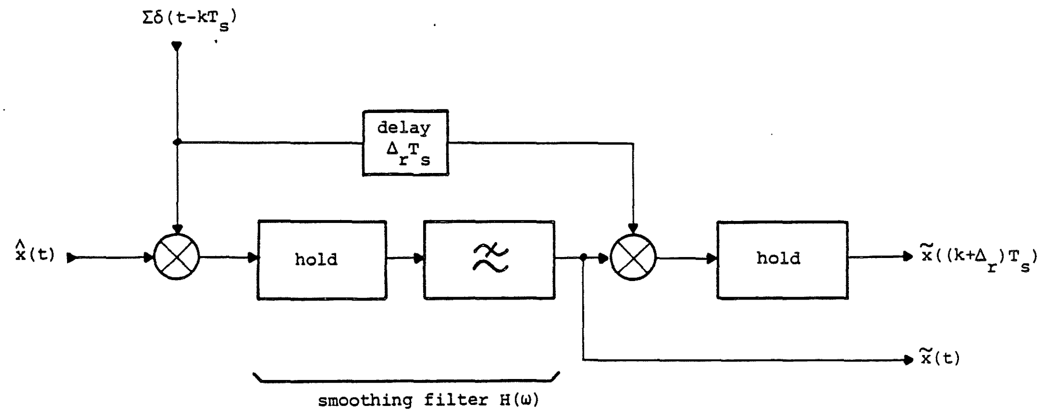

Fig. I.1 Range gating, smoothing and sampling for spectrum analysis in a PW Doppler instrument with analog filtering.

The choice of filter transfer function depends on how the signal is processed after the filtering. Some Doppler systems employ wideband analog signal processing, e.g. mean frequency estimation. In this case, the smoothed signal $\tilde{x}(t)$ is analysed over a bandwidth much larger than the sampling frequency. The filtering problem is then similar to that of smoothing the boxcar output from D/A-converters. An important difference, however, is that the spectral properties of the smoothed signal is the only concern; there is no requirement for phase linearity of the filter. Atkinson and Woodcock recently suggested the use of standard Butterworth filters for smoothing in this situation [24]. Systems with discrete time signal processing require that the smoothed signal is resampled at the Doppler PRF prior to the analysis. It was shown in Section 3.4.3 that a careful filter design and a proper sampling delay both are necessary to avoid excessive ripple in the sampled transfer function. It turns out that a filter design that is optimal for use with analog signal processing is not optimal in the case of discrete time analysis, and vice versa.

This appendix is organized as follows: In Section I.1 filters are designed that are optimal for analog mean frequency estimation. This is done on the basis of a set of design rules derived in the subsections I.1.1 and I.1.2. In Section I.2 filters suitable for discrete time signal processing are derived.

I.1 Smoothing filters for analog signal processing

Fig. I.2 shows the spectrum of the sampled signal $\{\hat{x}(T_s)\delta(t-kT_s)\}$, where $\delta(t)$ is a unity impulse at $t = 0$, together with frequency responses of both an ideal and a more practical smoothing filter. The frequency response of the filter should satisfy the following requirements;

i) resonably flat passband response, with cutoff frequency ω_c as close to the Nyquist frequency as possible;

ii) efficient suppression of higher order spectra;

iii) no more than 6-7 dB attenuation at the Nyquist frequency.

The phase response of the smoothing filter is unimportant. Requirement iii) is a necessary condition to avoid a severe notch in the sampled frequency response $|H^s(\omega)|$ at the Nyquist frequency, eq. (3.22). The requirements i) and ii) are conflicting, because a large passband ripple normally allows for a steeper transition region of the filter. Several questions now arise: How large passband ripple should be tolerated?

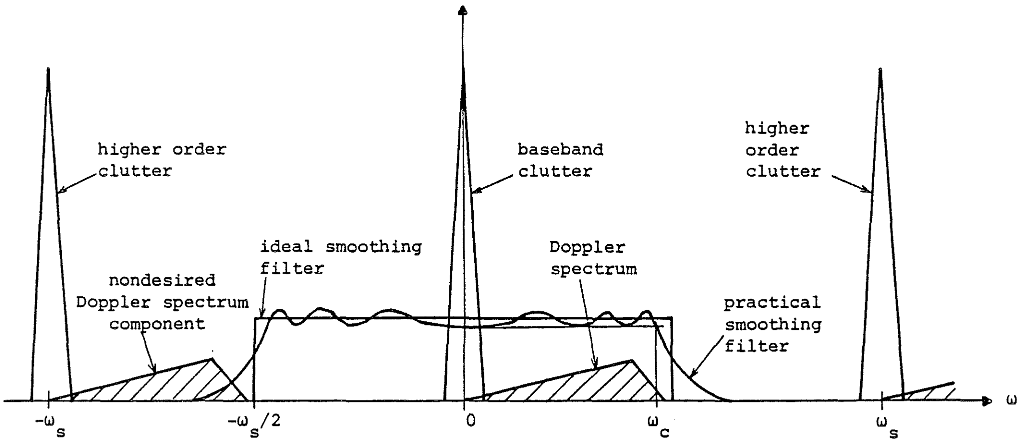

Fig. I.2. Spectrum of received signal samples and frequency responses of ideal and practical smoothing filters.

Where should the passband edge ω_c be placed when the lowpass filter has a finite cutoff rate? How large stopband attenuation is required? These questions are answered below.

I.1.1 Passband requirements

A relatively large passband ripple can be tolerated if the most important parameter of the Doppler spectrum is its maximum frequency, because even a significant amount of ripple does not much affect the edges of the spectrum. Excessive ripple may, however, cause the mean frequency $\tilde{\omega}$ of the reconstructed signal $\tilde{x}(t)$ to deviate much from the true mean frequency $\bar{\omega}$ of of the input signal $\hat{x}(t)$. Assume that a smoothing filter with equiripple passband characteristic is employed. Its frequency response can then be written

$$|H(\omega)| = \begin{cases} 1 + r_0 r(\omega) & |\omega| < \omega_c < \omega_s/2 \\ 0 & |\omega| > \omega_c \end{cases} \qquad (I.1)$$

For simplicity, an ideal stopband has been assumed. The ripple function $r(\omega)$ oscillates between the boundaries ± 1 in the passband, as shown in Fig. I.3. The fractional ripple amplitude r_0 is assumed to be small and positive, $0 < r_0 << 1$. In the following, the passband edge of $H(\omega)$ is defined to be the highest frequency ω_c which satisfies $r(\omega_c) = -1$ (see Fig. I.2).

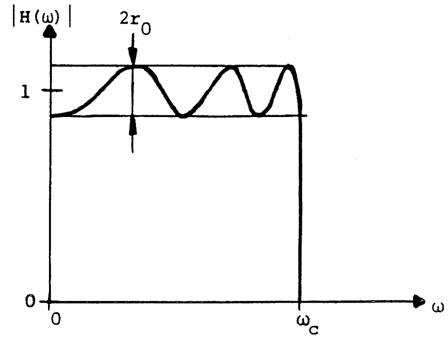

Fig. I.3 Equiripple filter transfer function with ideal stopband.

The mean Doppler frequency is (assuming $G_{\hat{x}\hat{x}}(\omega) = 0$ for $|\omega| > \omega_c$)

$$\bar{\omega} = \frac{\int_{-\omega_c}^{\omega_c} d\omega \; \omega G_{\hat{x}\hat{x}}(\omega)}{\int_{-\omega_c}^{\omega_c} d\omega \; G_{\hat{x}\hat{x}}(\omega)} \tag{I.2}$$

The mean frequency of the smoothed signal is

$$\tilde{\omega} = \frac{\int_{-\omega_c}^{\omega_c} d\omega \; \omega |H(\omega)|^2 G_{\hat{x}\hat{x}}(\omega)}{\int_{-\omega_c}^{\omega_c} d\omega \; |H(\omega)|^2 G_{\hat{x}\hat{x}}(\omega)} \tag{I.3}$$

Substituting (I.1) into (I.3) and expanding the resulting expression in series to the first order in r_0 then yields an approximate expression for the fractional mean frequency error caused by the ripple

$$\varepsilon_r = \frac{\tilde{\omega}-\bar{\omega}}{\bar{\omega}} \simeq 2r_o \frac{\int_{-\omega_c}^{\omega_c} d\omega \, \frac{\omega-\bar{\omega}}{\bar{\omega}} \, r(\omega) G_{\hat{x}\hat{x}}(\omega)}{\int_{-\omega_c}^{\omega_c} d\omega \, G_{\hat{x}\hat{x}}(\omega)} \tag{I.4}$$

Rewriting $G_{\hat{x}\hat{x}}(\omega)$ to $(\sqrt{G_{\hat{x}\hat{x}}(\omega)})^2$ and using the Schwarz inequality on the above expression, leads to the following bound for the absolute relative error:

$$\varepsilon_r^2 \leq 4r_o^2 \frac{\int_{-\omega_c}^{\omega_c} d\omega \left[\frac{\omega-\bar{\omega}}{\bar{\omega}}\right]^2 G_{\hat{x}\hat{x}}(\omega) \int_{-\omega_c}^{\omega_c} d\omega \, r^2(\omega) G_{\hat{x}\hat{x}}(\omega)}{\int_{-\omega_c}^{\omega_c} d\omega \, G_{\hat{x}\hat{x}}(\omega)}$$

$$= 4r_o^2 \, \frac{\bar{\omega}^2_{rms} - \bar{\omega}^2}{\bar{\omega}^2} \, \frac{\int_{-\omega_c}^{\omega_c} d\omega \, r^2(\omega) G_{\hat{x}\hat{x}}(\omega)}{\int_{-\omega_c}^{\omega_c} d\omega \, G_{\hat{x}\hat{x}}(\omega)} \tag{I.5}$$

$$\leq 4r_o^2 \, \frac{\bar{\omega}^2_{rms} - \bar{\omega}^2}{\bar{\omega}^2}$$

where

$$\bar{\omega}^2_{rms} = \frac{\int_{-\omega_c}^{\omega_c} d\omega \, \omega^2 G_{\hat{x}\hat{x}}(\omega)}{\int_{-\omega_c}^{\omega_c} d\omega \, G_{\hat{x}\hat{x}}(\omega)} \tag{I.6}$$

The last transition in (I.5) follows since, by definition, $r^2(\omega) < 1$ in the passband. The quantity $(\bar{\omega}^2_{rms}-\bar{\omega}^2)/\omega^2$ may be termed the fractional Mean Square bandwidth of the spectrum [29]. The magnitude of the error bound therefore increases with the bandwidth of the spectrum.

The significance of (I.5) can be illustrated using the following family of spectra :

$$G(\omega) = \begin{cases} \frac{4\pi}{p\omega_M}\left(1 - \frac{\omega}{\omega_M}\right)^{\frac{2}{p} - 1} & 0 \leq \omega < \omega_M \\ 0 & \text{elsewhere} \end{cases} \tag{I.7}$$

These spectra arise in Doppler measurements on a straight circular vessel with velocity profiles of the form

$$v(r) = v_o\left(1 - \left(\frac{r}{a}\right)^p\right) \qquad 0 \leq r \leq a \tag{I.8}$$

where v_o is the central velocity and a is the radius of the vessel [5]. In deriving (I.7) it has been assumed uniform insonification of the entire vessel crossection and the transit time effect has been neglected. The parameter p is a profile factor: A parabolic velocity profile is obtained with $p = 2$, while the profile gets increasingly blunter when p increases. The family (I.7) therefore contains representative Doppler spectra in situations where mean frequency estimation is interesting (flow measurements). The ratios $\omega_{rms}^2/\bar{\omega}^2$ for these spectras are [28]

$$\frac{\bar{\omega}_{rms}^2}{\bar{\omega}^2} = \frac{p+2}{p+1} \tag{I.9}$$

which leads to the following error bound:

$$\begin{aligned} |\varepsilon_r| &\leq \frac{2r_o}{\sqrt{p+1}}\sqrt{\int_0^{\omega_M} d\omega\; r^2(\omega)G(\omega)} \\ &\leq \sqrt{\frac{4}{p+1}}\; r_o \end{aligned} \tag{I.10}$$

Thus, the passband ripple gives a fractional mean frequency error which in the case of a parabolic velocity profile is less than 1.15 times the fractional ripple amplitude. The error reduces with increasing bluntness of the velocity profile; the somewhat flatter profile $p = 15$ yields $|\varepsilon_r| \leq 0.5\ r_o$. The fractional error reduces when the bandwidth of the spectrum extends over several periods of $r(\omega)$. This can be seen from eq. (I.4) ($r(\omega)$ has approximately zero mean in the passband). Consequently, for spectra with large bandwidths, the bound (I.5) is overpessimistic.

It seems justified to conclude that a small passband ripple amplitude, say $r_o = 0.02-0.05$, may be tolerated; it introduces very small errors in the mean frequency of the smoothed signal, regardless of the spectrum shape.

I.1.2 Stopband requirements and the selection of cutoff frequency.

In the stopband ($|\omega| > \omega_s/2$), the smoothing filter must suppress higher order spectras orginating from the sampling process. Since $H(\omega)$ has a finite rolloff rate, the stopband attenuation is smallest just above the Nyquist frequency. Fig. I.2 reveals that a desired frequency component at a positive frequency $\omega < \omega_s/2$ always is accompanied by an unwanted frequency component at the negative frequency frequency $\omega - \omega_s$. Apparently, insufficient attenuation of this component leads to problems in analog mean frequency estimation when $\tilde{x}(t)$ has frequency components close to the Nyquist frequency. The ratio between the amplitudes of the undesired and the desired frequency component is from Fig. I.2

$$k_s(\omega) = \frac{|H(\omega-\omega_s)|}{|H(\omega)|} = \frac{|H(\omega_s-\omega)|}{|H(\omega)|} \qquad 0 << \omega < \omega_s/2 \qquad \text{(I.12)}$$

If the input signal has the frequency ω, it is straightforward to show that the fractional mean frequency error caused by the second order frequency component is

$$\varepsilon_a(\omega) = \frac{\tilde{\omega} - \omega}{\omega} \simeq -k^2(\omega_1)\ \frac{\omega_s}{\omega} \qquad 0 << \omega < \omega_s/2\,,\ k<<1 \qquad \text{(I.13)}$$

It has been assumed that $|H(\omega)| \simeq 0$ for $|\omega| > \omega_s$. If $|H(\omega)|$ has a narrow transition region, the ratio $k_s(\omega)$ will abruptly start to increase when ω exceeds the passband limit ω_c, reaching unity at the Nyquist frequency. The system limit frequency due to insufficient filtering of the second order frequency component may be defined to be the point ω_a where the fractional mean frequency error $|\varepsilon_a|$ exceeds some predetermined limit. If maximum 5% fractional error with single frequency input is allowed, eq. (I.13) yields

$$k(\omega_a) \simeq \sqrt{\frac{0.05}{2}} = 0.16 \\ = -16 \text{ dB} \tag{I.14}$$

It has been assumed that $\omega_a \simeq \omega_s/2$. Hence, there are two different mechanisms that determine the maximum frequency limit of the conventional 'smoothing' pulsed Doppler systems with mean frequency estimators: The first is the passband attenuation itself, limiting the frequency response to $\omega_c < \omega_s/2$. Secondly, insufficient attenuation of higher order spectra causes large, aliasing-like mean frequency errors above ω_a. The effective system limit frequency is therefore approximately the least of the pair (ω_c, ω_a). For any given filter structure the variables ω_c and ω_a are dependent, in the sense that increasing one causes the other to decrease, and vice versa. It is therefore natural to choose a filter design that satisfies $\omega_c = \omega_a$.

Another important parameter of the smoothing filter is its attenuation at the sampling frequency. Strong, low frequency Doppler shifts from moving tissue is, due to the sampling, present at $\omega = \pm n\omega_s$, $n = 0,1,..,$ see Fig. I.2. In the baseband $(n = 0)$, they are suppressed by efficient highpass filters. The higher order components must be removed by the smoothing filter. It is therefore important that its attenuation in the vicinity of $\pm n\omega_s$, $n = 1,2,..$ is very large. In practice, this is a problem only for $n = 1$, i.e at the sampling frequency.

The following design criterions now seem reasonable: The passband edge should be forced as close to the Nyquist frequency as possible, while keeping the passband ripple at an acceptable level (< 5%). In addition, the constraint $\omega_c = \omega_a$ should be met. Since $|H(\omega_c)| \simeq 0$ dB when r_o is small, the last requirement is equivalent to (from eqs. (I.12) and (I.14))

$$|H(\omega_s - \omega_c)| = |H(\tfrac{1}{2}\,\omega_s + (\tfrac{1}{2}\,\omega_s - \omega_c))| \simeq -16 \text{ dB} \tag{I.15}$$

i.e. the passband cutoff frequency ω_c and the -16 dB point of $|H(\omega)|$ should be placed symmetrically around the Nyquist frequency. This may well be in conflict with the constraint $|H(\omega_s/2)| \geq -6$ dB initially stated. In the following, ω_c shall therefore be selected as a compromise between these requirements. The numerical value -16 dB in (I.15) is a direct result of selecting the maximum fractional error due to insufficient attenuation of second order frequency components to be 5%. If this limit had been reduced to 2%, the threshold would have moved down to -20 dB. Finally, the filter attenuation at the sampling frequency must be adequate to remove the higher order clutter from tissue.

I.1.3 Optimizing the frequency response.

Assume that the lowpass filter consists of N second order all-pole sections in cascade, i.e.

$$H_L(\omega) = \prod^{n=1,N} h_n(\omega) \tag{I.16}$$

$$h_n(\omega) = \frac{1}{1 - \alpha_n^2\omega^2 + j2\xi_n\alpha_n\omega} \tag{I.17}$$

The undamped angular resonance frequency of section n is

$$(\omega_o)_n = \frac{1}{\alpha_n} \tag{I.18}$$

The reason for selecting an all-pole design is its simplicity to implement, using standard active network designs. The transfer function of the sample and hold element is [2]

$$H_h(\omega) = \frac{\sin\frac{\omega}{2}}{\frac{\omega}{2}} e^{-j\frac{\omega}{2}} \tag{I.19}$$

where unity sampling frequency has been assumed. Fortunately, $H_h(\pm\omega_s) = 0$, which helps in attenuating the higher order clutter from tissue. The overall transfer function of the smoothing filter is (Fig. I.2)

$$H(\omega) = H_h(\omega)H_L(\omega) \tag{I.20}$$

The problem is to select the unknown parameters $\{\alpha_n, \xi_n\}$, such that $|H(\omega)|$ approximates 1 within a specified ripple tolerance r_o for

$\omega < \omega_c$, and approaches 0 for $\omega > \omega_s/2 = \pi$. This can be obtained using a modified version of a design method earlier derived by Steiglitz [30]. By means of the iterative method of Fletcher and Powell [31] the following quadratic 'deadband' criterion shall be minimized:

$$J_r = \sum_k e^2[c|H(\omega_k)|] + wc^2 \sum_m |H(\omega_m)|^2 \tag{I.21}$$

The sets $\{\omega_k\}$ and $\{\omega_m\}$ are dense grids in the passband $[0,\omega_c)$ and in the stopband $\omega > \pi$, respectively. The parameter c is an unknown gain, and w is a positive weighting coefficient for adjusting the relative contribution to J_r from the stopband. The error function $e[\cdot]$ is defined as

$$e[|x|] = \begin{cases} |x| - 1 - r_o & |x| > 1 + r_o \\ |x| - 1 + r_o & |x| < 1 - r_o \\ 0 & \text{elsewhere} \end{cases} \tag{I.22}$$

The idea of this criterion is to allow for a controllable passband ripple amplitude r_o, while maintaining as high stopband attenuation as possible. The basic difference from Steiglitz' original approach is that he used an ordinary least squares fit ($r_o = 0$) in the design of mixed poles/zeros digital filters.

The unknown $2N + 1$ parameters may be collected in a vector $\underline{Z}$:

$$\underline{Z}^T = \{z_n\}^T = \{\xi_1, \alpha_1, \xi_2, \alpha_2, \ldots \ldots, \xi_N, a_N, c\}^T \tag{I.23}$$

The minimization method of Fletcher and Powell requires the gradient $\partial J_r/\partial \underline{Z}$ to be known. This is simplified by observing that [30]

$$\frac{\partial(c|H(\omega)|)}{\partial z_n} = |H(\omega)|^{-1} \operatorname{Re}[H^*(\omega) \frac{\partial(cH(\omega))}{\partial z_n}] \quad n = 1,2,.,2N+1 \tag{I.24}$$

The gradient then becomes

$$\frac{\partial J_r}{\partial z_n} = 2 \sum_k e[c|H(\omega_k)|] \frac{\partial(c|H(\omega_k)|)}{\partial z_n} + 2wc \sum_m |H(\omega_m)| \frac{\partial(c|H(\omega_m)|)}{\partial z_n} \tag{I.25}$$

where from (I.16) - (I.20) and (I.24)

$$\frac{\partial(cH(\omega))}{\partial z_{2n-1}} = -2cH(\omega)\,\frac{j\alpha_n\omega}{1-\alpha_n^2\,\omega^2 + j2\xi_n\alpha_n\omega} \qquad n = 1,..N \tag{I.26}$$

$$\frac{\partial(cH(\omega))}{\partial z_{2n}} = -2cH(\omega)\,\frac{-\alpha_n\omega^2 + j\xi_n\omega}{1-\alpha_n^2\,\omega^2 + j2\xi_n\alpha_n\omega} \qquad n = 1,..N \tag{I.27}$$

$$\frac{\partial(cH(\omega))}{\partial z_{2N+1}} = H(\omega) \tag{I.27}$$

The optimization problem now is entirely specified. The choice of stopband grid is fairly uncritical, since all-pole filters decay monotonically in the stopband (the zeros in $H_h(\omega)$ are fixed, not affected by the optimization). In the computations the following grids were used:

$$\omega_m = 1.2\pi + \frac{0.8\pi}{19}(m-1) \qquad m = 1,2,..\,,20 \tag{I.29}$$

$$\omega_k = \frac{\omega_c}{1-e^{-2.5}}\left(1 - e^{-\frac{2.5(k-1)}{99}}\right) \qquad k = 1,2,..\,,100 \tag{I.30}$$

This has the effect of increasing the passband grid density with approximately 10 times in the vicinity of ω_c, compared to the low frequency region. This improves the convergence in the optimization, for reasons that will become clear later. - Steigliz used an even grid density in his work.

The minimization of J_r was performed by the FORTRAN subroutine DFMFP [32]. Initial values for the search were the parameters of a 2N order Chebychef lowpass filter with 2 dB passband ripple. The ripple amplitude r_o was set to 0.05, and the stopband weight w was 0.01. Initial value for the gain parameter c was $1 - r_o$. Repeated runs with somewhat different initial values were performed, to ensure that the global minimum of J_r was found. The cutoff frequency ω_c was adjusted manually until a good compromise between the requirements $|H(\pi)| = -6$ dB and $|H(2\pi-\omega_c)| \simeq -16$ dB was obtained.

I.1.4 Results

Plots of the resulting $|H(\omega)|$, $|H_L(\omega)|$ and the sampled frequency response $|H^s(\omega)|$, eq. (3.18), are shown in Fig. I.4. The left column shows a 4th order filter design (N = 2), while the right column shows corresponding plots for a 6th order filter (N = 3). The filter parameters are listed in Table I.1.

The outlined procedure yields filter designs with, for practical purposes, equiripple passband transfer functions. The resulting ripple is marginally larger than the specified value 0.05. Both the shown designs has 7 dB attenuation at the Nyquist frequency. By inspection of Fig. I.4.a it is found that $|H(\omega_s-\omega_c)| = 0.17$ for N = 2, and from Fig. I.4.b $|H(\omega_s-\omega_c)| = 0.16$ for N = 3. The fractional error $|\varepsilon_a(\omega_c)|$ in single frequency estimation then is 6.5% at the passband cutoff for the 4-pole, and 5.4% for the 6-pole design (the values for ω_c given in Table I.1 have been inserted in (I.13)). Thus, large mean frequency errors from passband attenuation and insufficient attenuatrion of higher order frequency components occur at nearly the same frequency.

The yield of increasing the filter order from 4 to 6 is twofold: The passband edge ω_c (and ω_a) increases from 0.89π to 0.945π, which is ~ 6% increase of the upper frequency limit of the system. Also, the rolloff rate of the filter increases, and a more efficient suppression of clutter components at the sampling frequency results (comparing Fig. I.4.c and d: approximately 19 dB improvement). Which filter order one should select in a given situation depends on the application: In PW Dopplers for measurements on peripheral vessels (5-10 MHz ultrasound frequency, high PRF's), the wall motion clutter is confined to a frequency range which is a small percentage of the sampling frequency. A 4th order filter then probably suffices. For central applications (1-2 MHz, low PRF's), the zeros in the sample and hold transfer function become less efficient, and the 6th order filter may be required.

The frequency response $|H_L(\omega)|$ of the lowpass filters alone (excluding the sample and hold) are shown in Fig. I.4.e and f. It approximates a x/sin x response in the passband, to compensate for the rolloff of the sample and hold.

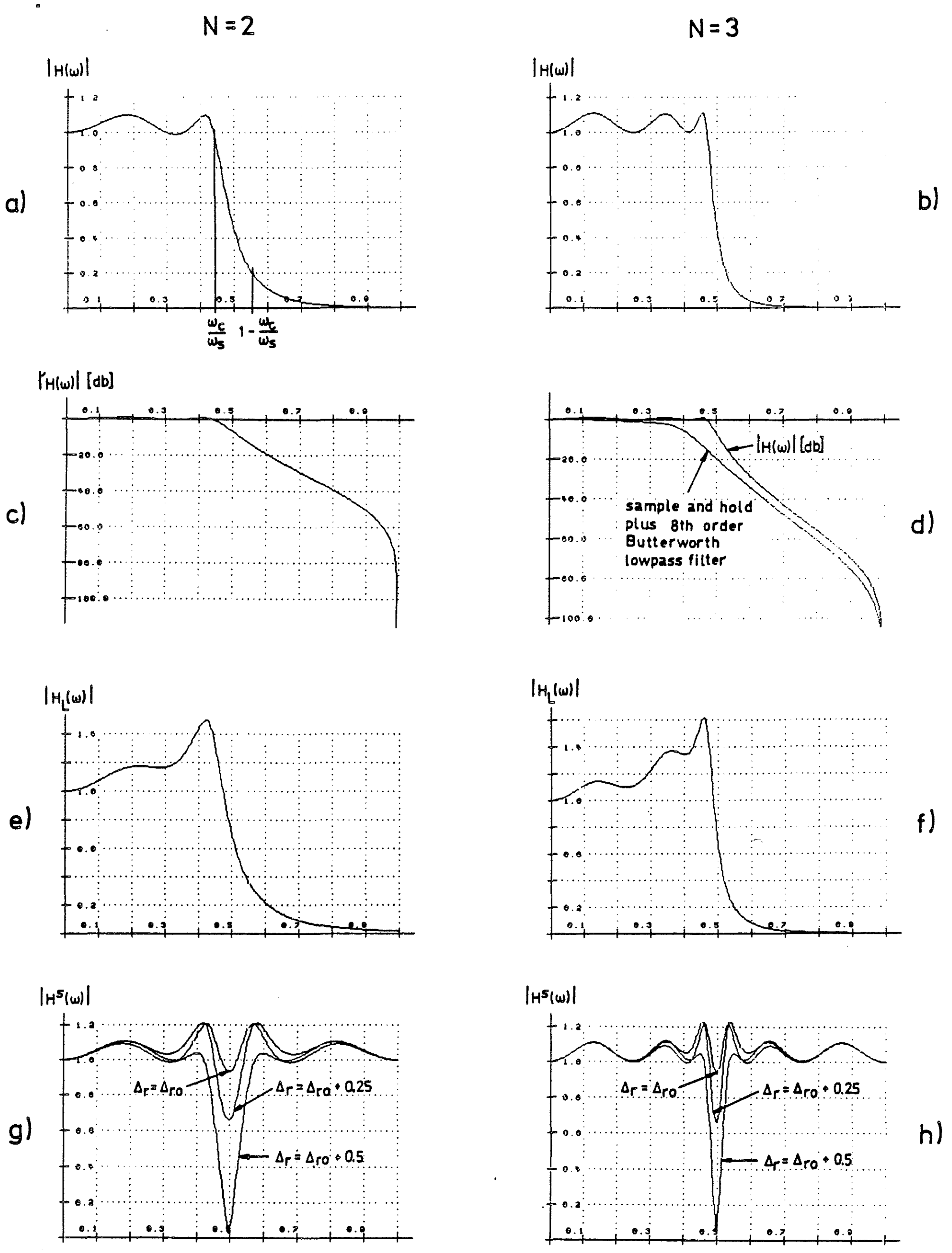

Fig. I.4 Frequency responses of optimal all-pole smoothing filters. The frequency axis are scaled relative to the sampling frequency.
Left column: 4 th order filters
Right column: 6 th order filters

The derived filters characteristics are fairly different from the design recommended by Atkinson and Woodcock [24]. They stated that a reasonable choice of $H_L(\omega)$ is an 8th order Butterworth filter, with corner frequency 600 Hz when f_s = 1500 Hz. In our scaling, this corresponds to a Butterworth corner at 0.8π. This response is plotted in Fig. I.4.d for comparison. It can be seen that the Butterworth filter is clearly inferior to the new design: The rolloff of the sample and hold causes passband attenuation already at $0.3\omega_s$. The attenuation in the vicinity of the sampling frequency is only 6 dB higher than for our 6-order design, in spite of the higher filter order and the lower corner frequency. The 20 dB attenuation at the Nyquist frequency also seems excessive.

The sampled frequency responses $|H^s(\omega)|$ are plotted in Fig. I.4.g and h for some selected values of the fractional sampling delay Δ_r. The sampling delay that maximizes the magnitude of the sampled frequency reponse at the Nyquist frequency is denoted Δ_{ro}. From (3.23) one obtains

$$\Delta_{ro} = - \frac{\gamma(\omega)}{\pi} \tag{I.31}$$

where $\gamma(\omega)$ is the overall phase angle of the smoothing filter:

$$H(\omega) = |H_h(\omega)| \; |H_L(\omega)| e^{j\gamma(\omega)} \tag{I.32}$$

The problem with notches in the sampled frequency response at the Nyquist frequency was illustrated schematically in Fig. 3.12.f, and it is also apparent from the shown plots. Selecting the delay $\Delta_r = \Delta_{ro} + 0.5$ generates a zero in $|H^s(\omega_s/2)|$. Changing Δ_r to Δ_{ro} removes the zero, but instead the passband ripple increases. Note that since the 6 pole filter has a fairly narrow transition region, the notch in its sampled frequency response becomes correspondingly narrow.

The reason for using a denser $\{\omega_k\}$ grid close to the cutoff frequency in the passband becomes clear when studying Fig. I.4.b. The ripple oscillates increasingly faster when ω increases from 0 to ω_c. Thus, the grid density should also increase, to ensure adequate sampling close to the passband edge. Besides, this has the desired effect of introducing a frequency dependent weighting of the passband error $e[\cdot]$. The increased grid density causes the effective weighting per frequency unit to increase near the band edge. In combination with the 'deadband' criterion and the increasing 'frequency' of the ripple, this weighting favours equiripple passband behaviour.

To save computing time, the first part of the optimization was run with a relatively coarse grid in the passband (40 points). When the search approached minimum of J_r, the grid density was increased to the 100 points specified in (I.30). The increased density did not increase the computing time very much, since $e[\cdot] = 0$ over most of the passband when J_r approaches minimum. The passband gradient computation could then be omitted in these points, because the multiplication with $e[\cdot]$ in (I.25) anyway results in zero contribution.

It can be concluded that the filter designs given provide nearly optimal properties in conventional 'smoothing' pulsed Doppler systems with analog filtering. They may also be used with discrete time signal processors, to allow for measurements of frequencies exceeding the Nyquist frequency. In this respect, the proposed designs have nonoptimal passband responses, with an increasing ripple near the Nyquist frequency.

N	r_o	ω_c	ξ_1	$(\omega_o)_1/\pi$	ξ_2	$(\omega_o)_2/\pi$	ξ_3	$(\omega_o)_3/\pi$
2	.05	.89	.6358	.5218	.1230	.8922	-	-
3	.05	.945	.6642	.3638	.2206	.7329	.05715	.9439

Table I.1 Parameters of smoothing filters optimal for mean frequency estimation

I.2 Smoothing filters for discrete time signal processing

When discrete time signal processing is employed (frequency estimation or spectral analysis), it is natural to optimize directly the sampled frequency response $|H^s(\omega)|$. This can be performed as a straightforward extension of the method employed in the previous section. The necessary equations are given in the following.

I.2.1 Optimization criterion

An appropriate criterion is

$$J_s = \sum_k e^2[c|H^s(\omega_k)|] + wc^2 \sum_m |H(\omega_m)|^2 \tag{I.33}$$

using the same definitions as in Section I.1.3, except that the passband edge is fixed at $\omega_c = \pi$. The sampled frequency response is from (3.18) and (3.19)

$$H^s(\omega) = H(\omega)^{j\Delta_r\omega} + H^*(2\pi-\omega)^{-j(2\pi-\omega)\Delta_r} \tag{I.34}$$

In the following, $\Delta_r = \Delta_{ro}$ shall always be selected. Substituting (I.31) into (I.34) and rearranging terms then yields

$$H^s(w) = A(\omega)\ [H(\omega)e^{-j\gamma(\pi)} + H^*(2\pi-\omega)e^{j\gamma(\pi)}] \qquad 0 < \omega < 2\pi \tag{I.35}$$

where

$$A(\omega) = e^{j\gamma(\pi)}\ e^{-j\frac{\gamma(\pi)}{\pi}\omega} \tag{I.36}$$

Since $|A(\omega)| = 1$, it does not affect the magnitude of the sampled frequency response. It can, therefore, be set to unity during the optimization. Proceeding as in Section I.1.3 then yields the following expressions for the gradient:

$$\frac{\partial J_s}{\partial z_n} = 2\sum_k e[c|H^s(\omega_k)|]\ |H^s(\omega_k)|^{-1}\ \mathrm{Re}[(H^s(\omega_k))^*\ \frac{\partial(cH^s(\omega_k))}{\partial z_n}]$$

$$n = 1,\ldots,2N+1 \tag{I.37}$$

$$+ 2wc\sum_m |H(\omega_m)|\frac{\partial(c|H(\omega_m)|)}{\partial z_n}$$

The stopband terms are the same as in the previous section. The passband terms become from eq. (I.35)

$$\frac{\partial(cH^s(\omega))}{\partial z_n} = \frac{\partial(cH(\omega))}{\partial z_n}\ e^{-j\gamma(\pi)} + \left[\frac{\partial(cH(2\pi-\omega))}{\partial z_n}\ e^{-j\gamma(\pi)}\right]^*$$

$$n = 1,\ldots,N \tag{I.39}$$

$$+j\ \frac{\partial\gamma(\pi)}{\partial z_n}\ [(cH(2\pi-\omega)e^{-j\gamma(\pi)})^* - cH(\omega)e^{-j\gamma(\pi)}]$$

$$\frac{\partial(cH^s(\omega))}{\partial z_{2N+1}} = H^s(\omega) \tag{I.39}$$

With exception of the phase terms, the expressions for the above terms have already been derived in the previous section. Eqs. (I.16), (I.17) and (I.19) yield

$$\gamma(\pi) = -\frac{\pi}{2} - \sum_{n=1}^{N} \arctan \frac{2\pi\xi_n a_n}{1 - (\pi a_n)^2} \tag{I.40}$$

The constant $\pi/2$ originates from the sample and hold response. It follows that

$$\frac{\partial\gamma(\pi)}{\partial z_{2n-1}} = 2\pi a_n \frac{1 - (\pi a_n)^2}{[1 - (\pi a_n)^2]^2 + (2\pi a_n \xi_n)^2} \tag{I.41}$$

$$n = 1,..,N$$

$$\frac{\partial\gamma(\pi)}{\partial z_{2n}} = 2\pi\xi_n \frac{1 + (\pi a_n)^2}{[1 - (\pi a_n)^2]^2 + (2\pi a_n \xi_n)^2} \tag{I.42}$$

The optimization problem now is entirely specified. The results from the previous section are proper initial values for the iterations.

I.2.2 Results

The results are shown in Fig. I.5. The left column applies for the 4-pole and the right for the 6-pole filter. Filters with 5% (Fig. I.5.a and b) and 1% (c and d) fractional ripple amplitude have been designed. The sampled frequency response $|H^s(\omega)|$ is approximately equiripple in all cases.

The corresponding lowpass filter responses $|H(\omega)|$ are shown in Fig. I.5.e and f. The stopband responses of $|H(\omega)|$ are plotted in Fig. I.5.g (logarithmic scale). For the case of 5% ripple amplitude, these are similar to the results of the previous section. Reducing the ripple amplitude from 0.05 to 0.01 reduces the stopband attenuation with ~ 6 dB.

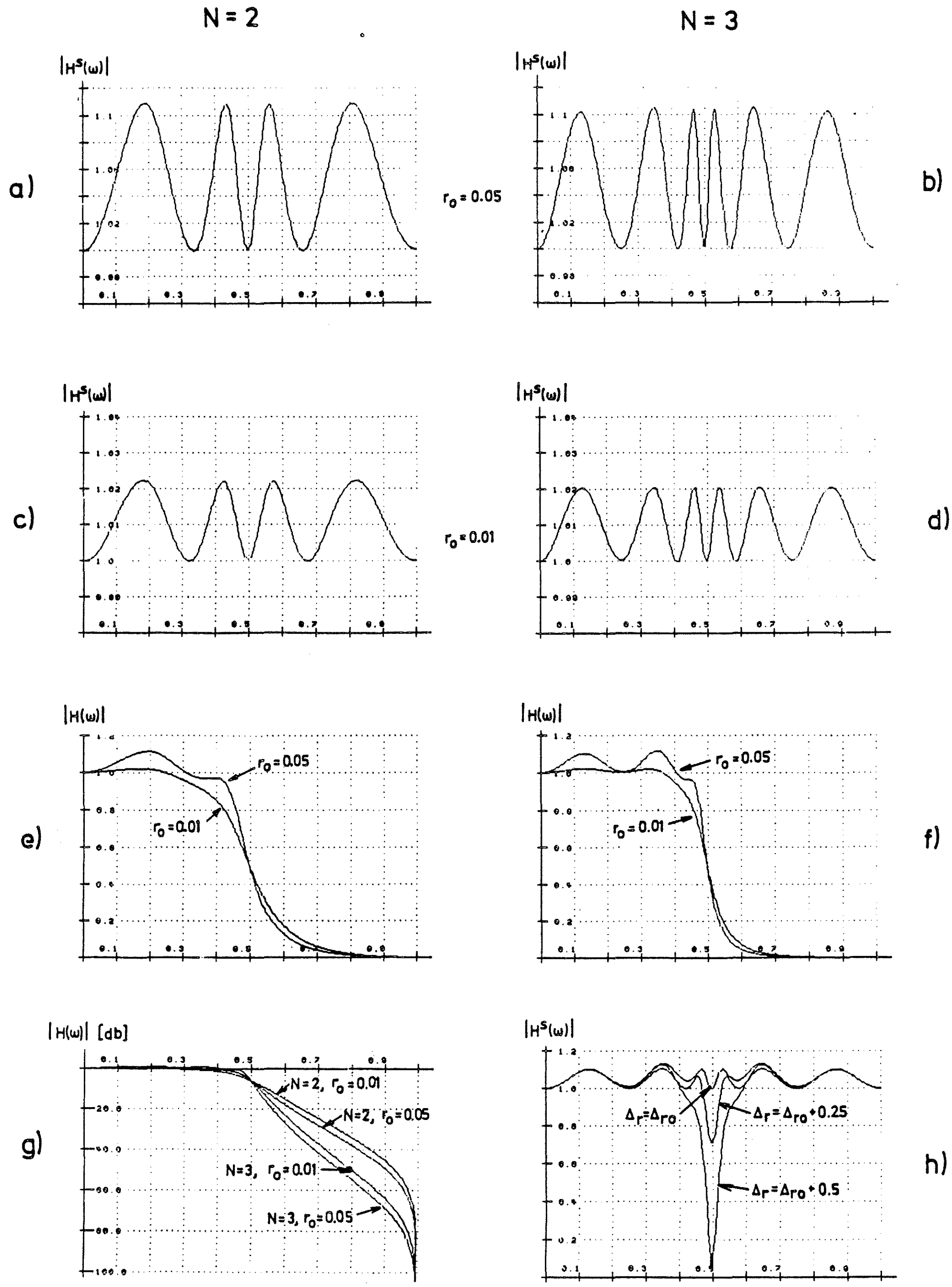

Fig. I.5 Frequency responses all-pole smoothing filters with optimal sampled frequency responses. The frequency axis are scaled relative to the sampling frequency.
Left column: 4 th order filters.
Right column: 6 th order filters.

Suppose that $H(\omega)$ is cascaded with an ideal analog highpass filter with cutoff frequency $\omega_{hp} < \omega_s/2$. The sampled frequency response of the combined system becomes from (3.16):

$$T_s |H^s_{hp}(\omega)| \simeq \begin{cases} |H(\omega_s+\omega) + H^*(\omega_s-\omega)| & 0 < |\omega| < \omega_{hp} \\ |H^s(\omega)| & \omega_{hp} < |\omega| < \omega_s - \omega_{hp} \end{cases} \quad \text{(I.43)}$$

Thus, the low frequency attenuation of the sampled frequency response is ultimately limited by the attenuation of $|H(\omega)|$ in the vicinity of the sampling frequency. This is the reason why a stopband penalty was included also in the criterion J_s, eq. (I.33).

The sensitivity of $|H^s(\omega)|$ to a change in the fractional delay Δ_r is illustrated in Fig. I.5.h ($N = 3$, $r_o = 0.05$). When Δ_r changes from Δ_{ro}, a notch appears at the Nyquist frequency, while the ripple increases also in some distance from the notch.

The optimal parameter values that corresponds to the plots in Fig. I.5 are listed in Table I.2.

N	r_o	ξ_1	$(\omega_o)_1/\pi$	ξ_2	$(\omega_o)_2/\pi$	ξ_3	$(\omega_o)_3/\pi$
2	.05	.6194	.5381	.1497	.9164	-	-
3	.05	.6712	.3717	.2177	.7429	.07131	.9561
2	.01	.7331	.6673	.2340	.9504	-	-
3	.01	.7985	.4715	.3128	.7759	.1170	.9681

Table I.2 Parameters of smoothing filters with optimal sampled frequency responses.

APPENDIX II

Windows of different lengths sharing a common value set

An important aspect of the spectrum analyser concept outlined in Chapter 5 was the ability of changing window length as a means to perform the resolution/variance tradeoff. When a 64 point DFT is employed, a sufficient range of variation for the window length K is ~ 24-64. If the different time windows are denoted $\{w(k;K)\}$, the use of the mapping/PROM multiplication technique suggested in Fig. 5.6 superimposes the requirement

$$w(k;K) \subseteq \{e_w(n)\}_{n=0}^{31} \qquad \begin{matrix} k = 0,\text{--},K-1 \\ K = 24,\text{--},64 \end{matrix} \tag{II.1}$$

i.e. all windows need to be described in terms of a common 32 point value set. When $K < 64$, the spectrum analyser demands $w(k;K) = 0$ for $k = K,\text{--},63$, such that zero has to be contained in the set.

Eq. (II.1) strongly limits the degrees of freedom one has in selecting different window types. Since many classical windows are described in terms of a rised cosine function, use of the below valueset seems reasonable:

$$e_w(n) = 0.5 - 0.5 \cos \frac{2\pi n}{64} \qquad n = 0,\text{--},31 \tag{II.2}$$

This allows for nearly exact representation of the following windows:

i) $K = 16,32,64$: Hanning window

$$w(k;K) = 0.5 - 0.5 \cos 2\pi\frac{k}{K} \qquad k = 0,1,..,\frac{K}{2}-1$$

$$w(K-k;K) = w(k,K) \tag{II.3}$$

$$w(K/2,K) = 1 \simeq 0.5 - 0.5 \cos 2\pi\frac{31}{64} = 0.9976$$

ii) $32 < K < 64$ Cosine tapered (Tukey) window

$$w(k,K) = \begin{cases} 0.5 - 0.5 \cos 2\pi\frac{k}{32} & k = 0,\text{--},15 \\ 1 \simeq 0.9976 & k = 16,\text{--},K\text{-}16 \end{cases}$$

$$w(K-k;K) = w(k) \qquad \text{(II.4)}$$

iii) $16 < K < 32$ Cosine tapered (Tukey) window

$$w(k;K) = \begin{cases} 0.5 - 0.5 \cos 2\pi\frac{k}{16} & k = 0,\text{--},7 \\ 1 \simeq 0.9976 & k = 8, \ldots, K\text{-}8 \end{cases} \qquad \text{(11.5)}$$

$$w(k;K) = w(k)$$

The only quantization error in the above expressions is the substitution of the window peak value 1 with the approximation 0.9976. In our context this error is of no practical importance, as it is anyway smaller than the resolution of an 8 bit system.

The frequency responses of the above windows for K = 24, 32, 44 and 64 are shown in the left column of Fig. II.1. The Hanning windows (Fig. II.1.c and g) have reasonably good frequency responses, whereas the first sidelobes of the Tukey windows (a and e) are rather high. In combination with the wide mainlobe, this makes the window in Fig. II.1.a unsuited for practical use.

The above windows are all characterized by a rapid rolloff of their sidelobes. By selecting a window with a slower rolloff, e.g. the Hamming window, the peak sidelobe levels may be reduced, while still satisfying (II.1). The Hamming window is defined as

$$w_h(k;K) = 0.54 - 0.46 \cos \frac{2\pi k}{K} \qquad k = 0,\text{--},K\text{-}1 \qquad \text{(II.6)}$$

Since $\{w_h(k;K)\}$ does not match the selected valueset (II.2), a quantized Hamming window may be defined as

$$w_{hq}(k;K) = \min_n |w_h(k;K) - e_w(n)| \qquad \text{(II.7)}$$

i.e. by rounding off to the nearest quantization level. The resulting

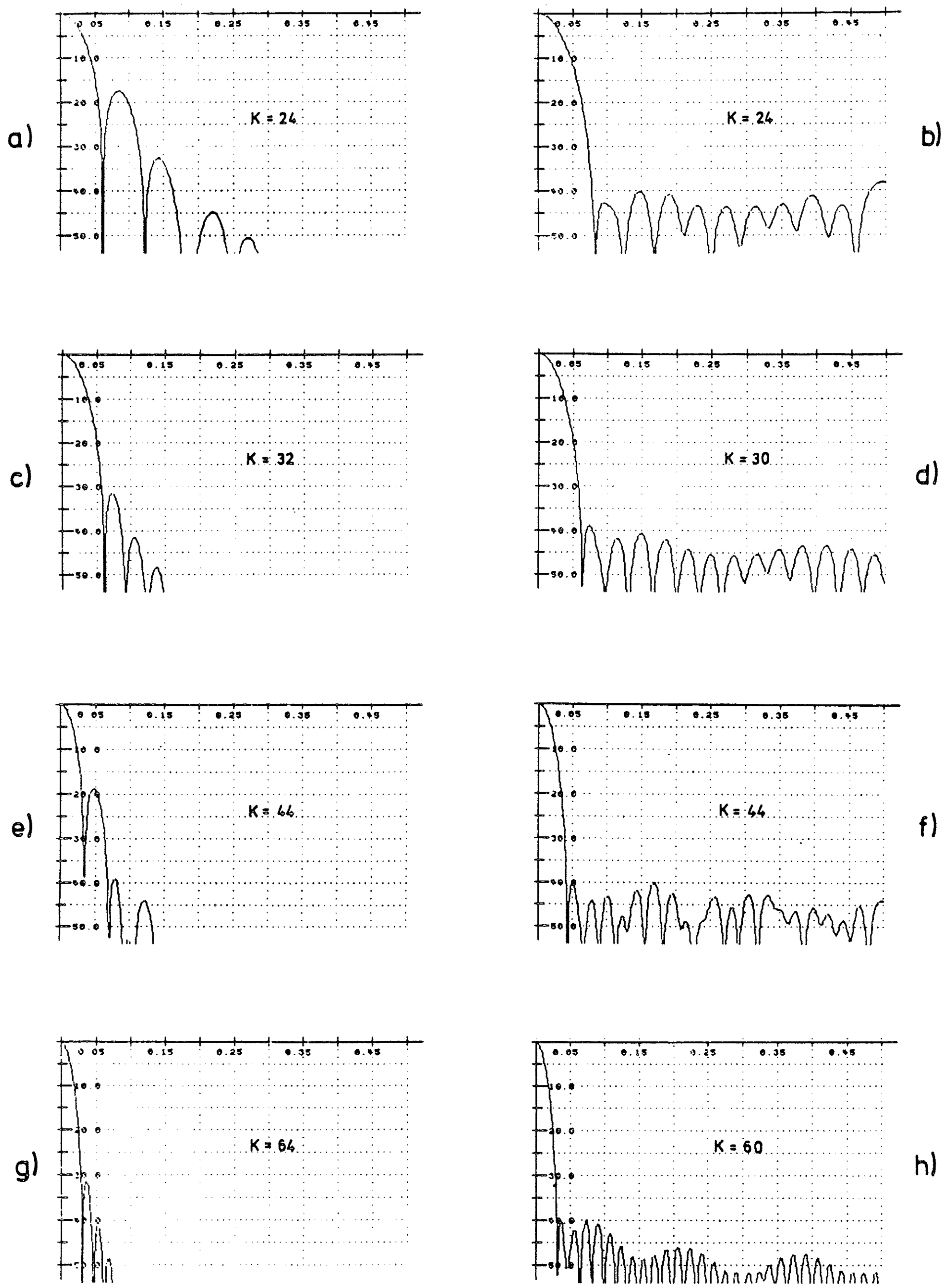

Fig. II.1 Frequency responses of time windows sharing a common 32-element valueset.
Left column: Hanning and Tukey windows.
Right column: Quantized Hamming windows.

frequency responses are shown in the right column of Fig. II.1. The sidelobes of the quantized Hamming windows are relatively even, with peak sidelobe levels at approximately -40 dB. This is adequate for the purpose. Note that 30 and 60 samples quantized windows have been selected rather than 32 and 64, the reason being that quantized versions of the latter windows showed somewhat larger spurious peaks in their sidelobes (approx. -36 dB).

The windows shown are probably not optimum choices in any respect under the constraint (II.1). It has, nevertheless, been demonstrated that windows of widely different lengths, sharing a common 32 point valueset, can be designed without excessive sidelobes.

REFERENCES

[1] G.M. Jenkins and D.G. Watts: 'Spectral Analysis and its applications', San Fransisco: Holden-Day 1968.

[2] S.A. Tretter: 'Introduction to Discrete Time Signal Processing', New York: John Wiley, 1976.

[3] L.R. Rabiner, B. Gold: 'Theory and application of Digital Signal Processing', New Jersey: Prentice Hall 1975.

[4] M.B. Priestly: 'Spectral analysis and Time Series', London: Academic press 1981.

[5] B.A.J. Angelsen: 'A theoretical study on the scattering of ultrasound from blood', IEEE Trans. Biomed. Eng., Vol. BME-27, pp. 61-67, Feb. 1980.

[6] F.J. Harris: 'On the use of windows for harmonic analysis with the Discrete Fourier transform', Proc. IEEE, Vol. 66, pp. 51-83, Jan. 1978.

[7] P.D. Welch: 'The use of fast Fourier transform for the estimation of power spectra: A method based on time averaging over short, modified periodograms', IEEE Trans. Audio Electroacoust., Vol. AU-15, pp. 70-73, June 1967.

[9] A.H. Nuttall: 'Some windows with very good sidelobe behaviour', IEEE Trans. Acoust., Speech, Signal Process., Vol. ASSP-28, pp. 334-335, June 1980.

[10] H.L. Van Trees: 'Detection, Estimation, and Modulation theory, Part III', New York: J. Wiley, 1971.

[11] K. Kristoffersen, B.A.J. Angelsen: 'A comparison between Mean Frequency Estimators for Multigated Doppler Systems with Serial Signal Processing', submitted for publication in IEEE Trans. Biomed. Eng.

[12] K. Kristoffersen, F. Nyhavn, B. Angelsen: 'DAISY - Doppler analysis and imaging system', Report STF48 F82021, SINTEF Trondheim, July 1982.

[13] L. Hatle, B. Angelsen: 'Doppler ultrasound in cardiology - physical principles and clinical applications', New York, USA: Lea and Fabiger 1982.

[14] M. Walby: 'A time base compressor for low frequency Chirp Z Transforms', Application note No. 115, Reticon, Sunnyvale, California, 1978.

[15] A.P.G. Hoeks: 'On the development of a Multi-gate pulsed Doppler system with serial data-processing', University of Maastricht, Ph.D. dissertation, Maastricht, the Netherlands, 1982.

[16] R.W. Brodersen, C.R. Hewes, D.D. Buss: 'A 500-stage CCD transversal filter for spectral analysis', IEEE Trans. Electron. Dev., Vol. ED-23, No. 2., pp. 143-152, 1976.

[17] L.I. Bluestein: 'A linear filtering approach to computation of Discrete Fourier Transform', IEEE Trans. Audio and Electroac., Vol. AW-18, No. 4., pp. 451-456, 1970.

[18] 'Data Sheet R5601 quad chirped transversal filter', Reticon, Sunnyvale, California, 1978.

[19] 'Data Sheet R5602 transversal filter family', Reticon, Sunnyvale, California, 1979.

[20] D.S. Tunstall Pedoe, P.C. Macpherson, S.J. Meldrum: 'Absolute intracardiac blood velocities measured with continuous wave Doppler and a new real-time spectral display', in C.T. Lancee (ed.): 'Echocardiology', proc. 3rd symp. echocard., pp. 77-80, Amsterdam: Martinus Nijhoff, June 1979.

[21] P. Zuech, R.S.C. Cobbold, M. Kassam, K.W. Johnston: 'The application of CCD transversal filters for real time spectral analysis of Doppler ultrasound arterial signals', Ultrasound in Med. and Biol., Vol. 8, No. 1, pp. 57-69, 1982.

[22] C. Atzeni: 'SAW signal transform techniques', Wave electronics, Vol. 2, No. 1,2,3, pp. 238-265, July 1976.

[23] B.A.J. Angelsen: 'Transcutaneous Measurement of Blood Velocity and Flow in the Thorax by Ultrasound and the Doppler Effect'. Report 75-78-W, Inst. of. eng. cyb., Norwegian Institute of Technology, Trondheim, 1974.

[24] P. Atkinson, J.P. Woodcock: 'Doppler Ultrasound and its use in clinical measurements', London: Academic press 1982.

[25] S.P. Creekmore, M.M. Graham, G.E. Jahn, R.C. Targett, M.B. McIlroy: 'Comparison of methods of recording and analysis of Doppler blood velocity in normal subjects', Ultrasound in Med. and Biol., Vol. 8, No. 5, pp. 525-535, 1982.

[26] D.J. Phillips, J.E. Powers, M.K. Eyer, W.M. Blackshear jr., K.C. Boidly, D.E. Strandness jr, D.W. Baker: 'Detection of peripheral vascular desease using the Duplex Scanner III', Ultrasound in med. and. biol., Vol. 6, No. 3, pp. 205-218, 1980.

[27] R.B. Blackman, J.W. Tukey: 'The measurement of Power Spectra From the Point of View of Communications Engineering', New York: Dover 1959.

[28] B.A.J. Angelsen, K. Kristoffersen: 'Zerocrossing density for ultrasonic Doppler signals obtained from computer simulations', Ultrasound in Med. and Biol., Vol. 9, No. 6, pp. 661-665, 1983.

[29] B.A.J. Angelsen: 'Spectral estimation of a narrow-band Gaussian process from the distribution of the distance between adjacent zeros', IEEE Trans. Biom. Eng., Vol. BME-27, No. 2, pp. 108-110, 1980.

[30] K. Steiglitz: 'Computer-Aided Design of recursive digital filters', IEEE Trans. Audio. Electroac., Vol AU-18, No. 2, pp. 451-455, June 1970.

[31] R. Fletcher, M.J.D. Powell: 'A rapidly convergent descent method for minimization', Computer Journal, Vol. 6, No. 2, pp 163-168, 1963.

[32] 'System 360 Scientific Subroutine Package (360-CM-03X), Version 3, programmer's manual', IBM Data Processing Division, White Plains N.Y., Document H20-0205-3, 1968.

[33] S.E. Rittgers, W.W. Putney, R.W. Barnes: 'Real-time spectrum analysis and display of directional Doppler Ultrasound blood velocity signals', IEEE Trans. Biom. Eng., Vol. BME-27, No. 12, pp. 723-728, Dec. 1980.

[34] K. Kristoffersen, B.A.J. Angelsen: 'On timeshared operation of Doppler Ultrasound Blood Velocity Meters for real time combination with 2D Echo Imaging Systems', in preparation.

[35] B.A.J. Angelsen, K. Kristoffersen: 'Discrete time estimation of the mean Doppler frequency in ultrasonic blood velocity measurements', IEEE Trans. on Biom. Eng., Vol. BME-30, No. 4, pp. 207-214, 1983.

[36] C.J. Hartley: 'Resolution of frequency aliases in ultrasonic pulsed Doppler velocimeters', IEEE Trans. Sonics Ultrasonics, Vol. SU-28, No. 2, pp. 69-75, March 1981.

[37] 'MF10 Universal monolithic dual switched capacitor filter', National Semiconductor Corp., Santa Clara, Cal., Dec. 1981.

[38] H. Torp, private communication.

[39] M.G.J. Arts, J.M.J.G. Roevros: 'On the instantaneous measurements of blood flow by ultrasonic means', Med. Biol. Eng., Vol. 10, pp. 23-24, 1972.

[40] B.A.J. Angelsen: 'Analog estimation of the maximum frequency of Doppler spectra in ultrasonic blood velocity measurements', rep. no. 76-21-W, SINTEF div. of autom. control, Trondheim, Jan. 1976.

[41] S.W. Flax, J.G. Webster, S.J. Updike: 'Statistical evaluation of the Doppler ultrasonic blood flowmeter', ISA Transactions, Vol. 10, No. 1, pp. 1-20, 1971.

[42] J. Holen, R. Aaslid., K. Landmark, S. Simonsen: 'Determination of pressure gradient in mitral stenosis with a non-invasive ultrasound Doppler technique'. Acta Med. Scand., vol 199, pp. 455-460, 1976

[43] L. Hatle, A. Brubakk, A. Tromsdal, B.A.J. Angelsen: 'Noninvasive assessment of pressure drop in mitral stenosis by Doppler ultrasound', Br. Heart J. 40, pp. 131-140, 1978.

[44] R.G. Gosling, M.G. Beasly, R.R. Lewis: 'Non-invasive demonstration of disease at the carotid bifurcation by ultrasound', in R.S. Reneman and A.P.G. Hoeks (eds.): 'Doppler ultrasound in the diagnosis of cerebrovascular disease', Letchworth, England: Research Studies Press, 1982.

[45] W.R. Brody: 'Theoretical analysis of the Ultrasonic Blood Flowmeter', Ph.D. thesis and technical report, Stanford Electronics

Laboratories, Stanford University, California (1971). Report no. 4958-1.

[46] S.M. Kay, S.L Marple jr.: 'Spectrum analysis - a modern perspective', Proc. IEEE, Vol. 69, No. 11, pp. 1380-1419, Nov. 1981.

[47] L.H. Light: 'A recording spectrograph for analysing Doppler signals in real time', Journ. Physiol. 207, 42-44, 1970.

[48] 'Kay Sona-Graph', Kay Elemetrics Corp., 12 Maple Av., Pine Brook, N.J. 07058, USA.

[49] B.A. Coughlan, M.G. Taylor, D.H. King: 'On-line display of Doppler-shift spectra by a new time-compression analyser', in R.S. Reneman (ed.): 'Cardiovascular applications of Ultrasound', pp. 55-65, Amsterdam: North-Holland 1973.

[50] R. Fehr: 'Pulsed-Doppler with real-time Fourier transform', in H. Rijsterborgh (ed.): 'Echocardiology', proc. 4th symp. echocard., Amsterdam: Martinus Nijhoff, June 1981.

[51] C.K. Yuen: 'A comparison of five methods for computing the power spectrum of a random process using data segmentation', Proc. IEEE, Vol. 65, pp. 984-986, June 1977.

[52] C.K. Yuen: 'Comments on modern methods for spectral estimation', IEEE Trans. Acoust., Speech, Signal Proc., Vol. ASSP-27, pp. 298-299, June 1979.

[53] A.H. Nuttall, G.C. Carter: 'Spectral estimation using combined time and lag weighting', Proc. IEEE, Vol. 70, No. 9, pp. 1115-1125, Sept. 1982.

[54] NEC Electronics (Europe) GmbH: 'NEC µPd7720: Digital Signal Processor', Western Germany 1981.

[55] Texas Instruments: 'TMS 32010 and TMS 32M10 High-performance 16/32-bit microcomputer', England Texas Instr. ltd., 1982.

[56] A.H. Nuttall: 'Spectral estimation by means of overlapped FFT processing of windowed data', New London, CT, Naval Underwater Research Center Report 4169, Oct. 13, 1971.

[57] A.H. Nuttall: 'Probability distribution of spectral estimaties obtained via overlapped FFT processing of windowed data', New London, CT, NUSC Rep. 5529, Dec. 3, 1976.

[58] S. Magar, R. Hester, R. Simpson: 'Signal-processing µC builds FFT-based spectrum analyzer', Electronic Design, Aug. 19, 1982.

A Time Shared Ultrasound Doppler Measurement and 2D Imaging System

K. Kristoffersen, M.Sc.[1]
B.A.J. Angelsen, dr. techn., senior member IEEE.

Division of Engineering Cybernetics
The Norwegian Institute of Technology
N 7034 Trondheim-NTH
Norway

[1]Mailing address: VINGMED SOUND a/s, p.o. box 141, 3191 Horten, NORWAY.

ABSTRACT

A brief review of different methods for obtaining image guided Doppler blood velocity measurements is given. It is argued for the use of a timesharing scheme where the Doppler measurement is turned off during the data acquisition period for a 2D image frame (typ. 20 ms). The signal dropout that occurs during the image updating period is removed from the Doppler audio by insertion of a synthetic signal segment. The synthetic signal is generated by passing white noise through a discrete-time FIR filter, where the filter coefficients are a windowed version of the Doppler signal measured immediately prior to the imaging interrupt. It is shown that the artificial signal has spectral properties (and, thus, audible sound) similar to those of the real Doppler signal segment that it is based upon. The timesharing method is analyzed and evaluated experimentally, using dedicated hardware.

The proposed algorithm allows for the design of timeshared Doppler/imaging systems where pulsed or continuous Doppler measurements can be done with essentially real time imaging guidance.

1. INTRODUCTION

The combination of ultrasound echo amplitude imaging systems and Doppler blood velocity meters offers in most cases significant clinical advantages compared to stand alone Doppler equipment. The location of the sample volume can then be related to an echo image of some form (A-, B- or M- scan), which is particularly important within the complex geometry of the heart. Due to mutual interference, independent echo/Doppler systems cannot run simultaneously. Several solutions to the combination problem have been presented:

a) **Frequency multiplexed 2D imaging and Doppler measurement [16].** Imaging and Doppler is done using different ultrasound frequencies, and the different echos are separated by electronic filtering.

b) **M/Q-mode [1],[2].** The same transducer is used for both M-mode and pulsed wave (PW) Doppler. M-mode and Doppler information is acquired from the echo of the same ultrasound burst.

c) **Duplex combination [3]-[5].** Every other ultrasound burst is used for 2D image scanning or PW Doppler measurement. The principle can be used with electronically steered scanners, or with separate Doppler and mechanical imaging transducers.

d) **Pulsed Doppler with simultaneous, low frame rate imaging [6].** In this concept, every Nth Doppler burst (N on the order of 10) is replaced with a short imaging pulse. An estimate is inserted for the missing signal sample, providing continuity in the range gated signal.

e) **Frozen B-scan image [3][5].** This consists of the sequential use of a mechanically interlinked echo and Doppler equipment. The location of the sample volume is shown on a frozen B-scan image, recorded immediately prior to the Doppler investigation. A variation of this technique is to update the image using an ECG-trigger, i.e. once per heartbeat. The Doppler signal is lost during the image updating period.

f) **Fast, sequential timesharing between B-scan and Doppler mode of operation[1] [7].** The image scanning and the velocity measurement are made on disjointed time intervals of 10 ms duration or more. The Doppler signal is lost during the image scans, but estimates of the missing signal segments are provided in the audio channel to minimize the disturbance from the timesharing.

All of the above solutions have shortcomings which are inherent

[1]Pats. pending.

in their principles. Because of the large bandwidths and dynamic ranges involved, it seems to be very difficult to make method **a)** work at all. To get acceptable M-mode resolution, method **b)** requires that the Doppler measurement be performed with a short burst of ultrasound. This limits the signal-to-noise ratio that can be attained in the Doppler measurement [8]. The combination of Doppler and M-mode employing a common transducer is in itself of limited value; good quality M-mode is rarely obtained in the same beam direction as optimum velocity recordings [9].

The Duplex principle eliminates some of the drawbacks of the M/Q mode, but introduces a new one: The PRF of the pulsed Doppler measurement drops by at least a factor of two, and consequently, so does also the maximum velocity that can be measured without frequency aliasing. The Nyquist limit is a major problem in PW measurements in heart lesions, and any reduction of the Doppler PRF is highly undesirable. The Duplex mode also tends to give noisy, unclean Doppler signals; this occurs when reverberant echos from the sweeping imaging beam arrive at the same time as the desired direct echo from the Doppler burst [5].

Approach **d)** is not associated with a drop in the Doppler PRF. It has, however, other deficiencies: The relatively high frequency Doppler shifts from blood are obscured in the received signal by strong, low frequency Doppler signals from tissue. The power ratio between these may become extremely unfavourable (-60 dB to -80 dB), but the low frequencies can still be removed efficiently by high-pass filtering of the range gated signal. The missing sample in type **d)** of timeshare consists of components from both tissue and blood, and even a slight fractional error in the estimate becomes large when it is compared to the amplitude of the signal from blood. As a result, the filtered Doppler signal tends to appear noisy and unclean. Further problems with the method are its low image update rate, and the fact that each image is formed with a scan rate of the beam that is only 10 percent of that of an ordinary B-scan system. This may cause geometric distortion when a beating heart is imaged. Moreover, neither of the methods **b)** - **d)** allows for the use of continuous wave (CW) Doppler to overcome the limitations of pulsed Doppler when aliasing occurs.

A frozen image or very low framerate imaging is acceptable for measurements on vessels whose movement is small, e.g., the carotid artery. It is normally incorporated as a mode of operation in Duplex instruments, to allow for full-PRF pulsed measurements with imaging [5]. It can also be used with CW Doppler. However, the absence of a real time image makes the method less suited for cardiology.

The last scheme, method **f)**, is characterized by fast alternation (> 15 Hz) between the 2D scanning and the Doppler measurement. Hence, it provides Doppler with apparently simultaneous real time 2D imaging. There will be no mutual interference, as the two systems operate in different time intervals. They can therefore be optimized separately with regards to frequency, bandwidth, etc. The two systems may share a common transducer, e.g., that of a phased array scanner. An image quality similar to that of Duplex systems can be obtained, without a reduction of the velocity limit in the case of PW Doppler. The method works even with CW Doppler.

In its basic form, the method has two apparent drawbacks: Because of the gated operation, rapid changes in the velocity may be difficult to reproduce faithfully. Secondly, a rapid on-off gating of the Doppler signal is perceived as a strong degradation of the quality of instrument's audio output. In cardiac applications this cannot be accepted, as the audio signal provides invaluable operator feedback; its pitch information is important in the minimization of the angle between high-velocity blood jets and the soundbeam [9]. Even if aiming problems in general are reduced when the location of the sample volume can be related to a real time image, this angle can rarely be assessed from the image in the case of jet flow. The need for a high quality Doppler audio output is, therefore, essential.

The audio disturbances are greatly reduced if the missing portions of the measured Doppler signals are 'filled' with signal segments having similar spectral properties to the ones gated out [7]. If these substitute segments are of sufficient quality, spectrum analysis of the 'filled' Doppler signal may give a better looking spectral display than that of the interrupted measured signal; the reason is that interpolated spectral information is then obtained during the interrupt periods. A simple way of performing such a signal filling is to repeat the most recent measured segment of the Doppler signal during the interrupt period [7]. However, this algorithm may give artifacts in the spectral display in phases of the cardiac cycle where the blood velocity is changing rapidly. The repetition method also has the limitation that it requires the interrupt to be shorter than the Doppler-on time.

This paper describes a new algorithm for the synthesis of artificial Doppler signal segments to be used for signal filling in type f) of timeshare operation. Knowledge of both the properties of the Doppler signal and spectrum analysis techniques is needed in the derivation and analysis of the algorithm, so a brief review of these subjects is given in the next section. The basic synthesis method is then derived and analyzed in Section 3, followed by an experimental evaluation in Section 4.

2. BASICS OF THE DOPPLER BLOOD VELOCITY METER.

2.1 Signal Characteristics.

For a Doppler instrument with ultrasound carrier frequency f_o, blood cells with velocity v give a Doppler shift

$$f_d = 2f_o \frac{v \cos \alpha}{c} \tag{1}$$

where c is the speed of sound in blood (1560 m/s), and α is the angle between the beam direction and the velocity vector.

In blood velocity measurements, the backscattered Doppler signal $\hat{x}(t)$ is a zero mean, complex Gaussian process [10]. In a pulsed Doppler system, samples $\{\hat{x}(k)\}$ are obtained for the time instants $\{kT_s\}$, k integer, where the sampling frequency $f_s = 1/T_s$ is the system PRF. The **complex Doppler signal** can be decomposed into its real quadrature components x and y by

$$\hat{x}(k) = x(k) + j\, y(k) \qquad (2)$$

A zero-mean Gaussian process is entirely characterized in terms of its second order moments. All information about the velocity field available in the signal is therefore contained in the **auto-correlation function**,

$$R_{\hat{x}\hat{x}}(k,n) \triangleq \langle \hat{x}^*(k)\hat{x}(n)\rangle \qquad (3)$$

where $*$ denotes the complex conjugate, and < > denotes an ensemble expectation value. The Doppler signal from a time invariant velocity field is stationary [10], which means that $R_{\hat{x}\hat{x}}(n,k)$ only depends on the lag n-k. All information is then contained also in the **power spectrum**,

$$G_{\hat{x}\hat{x}}(\omega) \triangleq \sum_{n=-\infty}^{\infty} R_{\hat{x}\hat{x}}(k,k+n)e^{-jn\omega T_s} \qquad (4)$$

Under idealized conditions, the power spectrum becomes a mapping of the velocity distribution within the sample volume, such that the power in a small frequency interval is proportional to the blood volume giving rise to the Doppler shifts in that range. In practice, the mapping from velocity distribution to power spectrum is blurred by the **transit time effect**, which occurs because each scatterer that travels through the sample volume contributes to the signal with a finite duration Doppler burst of random amplitude and phase. This causes the Doppler signal to become incoherent; its autocorrelation function decays with increasing lag even in the case of plug flow. It can be shown that when the axial transit length L_t of the blood cells along the sample volume is bounded, then

$$R_{\hat{x}\hat{x}}(k,k+n) \equiv 0 \qquad \text{for} \qquad |n| > M_v \qquad (5)$$

where

$$M_v = \frac{L_t}{T_s\, v \cos\alpha} = 2\Lambda \frac{f_s}{f_d} \qquad (6)$$

Eq. (1) was used to eliminate the axial velocity component $v \cos\alpha$. The parameter $\Lambda = L_t/\lambda_o$ is the normalized transit length, measured in ultrasound wavelengths λ_o of the carrier frequency. Eqs. (5) and (6) follow directly from an expression for the autocorrelation function derived by Angelsen [10, (29) with $z_1 = z_2$]. They imply that **in the plug flow case, the Doppler signal can be modeled as a Moving Average (MA) process of order M_v.**

In the general case, there will be velocity gradients in the sample volume. The signal can then, by linearity, be modeled as a sum of a large number of independent MA processes of different orders. It then becomes a MA process of order

$$M_v = 2\Lambda \frac{f_s}{f_{min}} \tag{7}$$

where f_{min} is the smallest Doppler shift originating from the sample volume.

The length of the sample volume is determined by the number of oscillations in the Doppler burst received from a point scatterer that travels along the beam axis, which in turn is determined by both the duration of the transmitted burst and the overall system bandwidth. Typical values for 2Λ may range from 4 - 20, depending on the system resolution. For a Doppler shift of magnitude PRF/4, the order of the signal MA process then varies between 16 and 80.

Alternately, the transit time effect may be described in the frequency domain. In the plug flow case, the **transit time bandwidth** of the Doppler signal is on the order of [11]

$$B_t \simeq \frac{1}{M_v T_s} = \frac{1}{2\Lambda} f_d \tag{8}$$

With velocity gradients in the sample volume, B_t becomes a rough measure of the width of the finest details that can be resolved in the Doppler spectrum in the vicinity of the frequency f_d.

Note that (6) was derived using the far-field approximation to the sound field. In the near field, M_v will be even smaller than indicated by (6), since spectral broadening caused by rapid fluctuations in the sound field then dominates over the transit-time broadening [17].

2.2 Analysis techniques.

The power spectrum is defined for an infinite observation interval, and gives no information about temporal variations of the velocity field. However, under laminar conditions, the time variations of the blood velocity are rather smooth; frequency components above 10 - 15 Hz contribute little to the flow waveform in the adult arterial system [12]. This justifies the use of a quasistationary approach, in which the backscattered signal is assumed to be stationary when observed for a sufficiently short period of time. This period is on the order of 10 ms for measurements in the central circulatory system. Spectrum analysis of a K sample signal segment with $KT_s \approx 10$ ms then gives information about the instantaneous velocity distribution in the sample volume.

The **modified periodogram** is a commonly used spectrum estimator for analysising Doppler signals from blood. At the time kT_s, it is defined as

$$\tilde{G}_{\hat{x}\hat{x}}(k,\omega;K) \triangleq |\sum_{n=1}^{K} w_a(n;K)\hat{x}(k+n-K/2)e^{-jn\omega T_s}|^2 \tag{9}$$

The K sample sequence $\{w_a(n;K)\}$ is a smoothly tapered time window that reduces sidelobes in the spectrum estimate. It is normalized such that its energy (sum of squared coefficients) is unity. When the Doppler signal is stationary, the expectation value of the periodogram is [15]

$$\langle\tilde{G}_{\hat{x}\hat{x}}(\omega;K)\rangle = W_a(\omega;K) \ast G_{\hat{x}\hat{x}}(\omega) \tag{10}$$

where $\ast$ denotes convolution and

$$W_a(\omega;K) = \frac{1}{\omega_s} |\sum_{n=1}^{K} w_a(n;K)e^{-j\omega T_s}|^2 \tag{11}$$

is a spectral window associated with the time window $\{w_a(n;K)\}$. A good spectral window has a narrow mainlobe at $\omega = 0$, and small sidelobes. The modified periodogram thus is a biased estimator; the nonzero width of its resolution window may cause blurring of spectrum details. This **analysis broadening effect** becomes negligible at a given Doppler frequency if the mainlobe width is much smaller than the transit time bandwidth at that frequency.

The window's **statistical bandwidth** may be used as a measure of its mainlobe width. It is defined as [13]

$$B_a \triangleq \frac{1}{2\pi} \frac{|\int_{-\omega_s/2}^{\omega_s/2} d\omega\, W_a(\omega;K)|^2}{\int_{-\omega_s/2}^{\omega_s/2} d\omega\, W_a^2(\omega;K)} = \frac{k_a}{KT_s} \tag{12}$$

where the shape factor $k_a \geq 1$ is on the order of unity[1]. Combining (8) and (12) now gives the equivalent requirements

[1]Hanning window gives $k_a = 2.1$, rectangular window $k_a = 1.5$.

$$B_a \ll B_t \qquad \Leftrightarrow \qquad K \gg M_v = 2\Lambda \frac{f_s}{f_d} \tag{13}$$

Note that k_a was set to unity in the derivation of this formula, since no corresponding shape factor was included in (8). The number of samples required is inversely related to the fractional Doppler shift f_d/f_s. For a unidirectional velocity field, aliasing errors occur when the fractional Doppler shift exceeds unity.

Short time spectral analysis inevitably leaves uncertainty in the estimate. The **fractional variance**, defined as

$$\mathrm{Fracvar}\{\tilde{G}_{\hat{X}\hat{X}}(\omega)\} \triangleq \mathrm{Var}\{\tilde{G}_{\hat{X}\hat{X}}(\omega)\}/\langle\tilde{G}_{\hat{X}\hat{X}}(\omega)\rangle^2 \tag{14}$$

where $\mathrm{Var}\{(\cdot)\}$ is the variance operator, is well suited as a performance measure in this respect. The following relation holds for the periodogram of a complex Gaussian signal [14],

$$\mathrm{Fracvar}\{\tilde{G}_{\hat{X}\hat{X}}(\omega;K)\} = 1 \tag{15}$$

The uncertainty of the periodogram is, therefore, very large; on a logarithmic scale the standard deviation of the estimate is equal to 5.6 dB [14].

There are two common methods for reducing the variance of the modified periodogram when the length of the data record to be analyzed is fixed; both of which cause a decreased frequency resolution. One is to smooth the modified periodogram by convolving it with a suitable spectral window $W_c(\omega)$ of bandwidth $B_c > B_a$. The variance of the smoothed spectrum is then reduced to (see Appendix for proof)

$$\mathrm{Fracvar}(\tilde{G}_{\hat{X}\hat{X}}(\omega;K) * W_c(\omega)\} \simeq \frac{\sum_{k=1}^{K} w_a(k;K)^4}{B_c T_s \left[\sum_{k=1}^{K} w_a(k;K)^2\right]^2} = \frac{k_a'}{B_c K T_s} \tag{16}$$

which holds when $B_c \gg B_a$. The constant k_a' is approximately the same as k_a for smoothly tapered windows. Under the same conditions, the resolution of the smoothed periodogram reduces to B_c, approximately.

A different approach to variance reduction is to split the data record into M subsegments of lengths $K' < K$, with an overlap between adjacent segments on the order of 50 percent [15]. The final spectrum estimate is then formed as the average of the modified periodograms of the subsegments. In this case, the variance becomes

$$\mathrm{Fracvar}\{\frac{1}{M}\sum_{n=1}^{M} \tilde{G}_{\hat{x}\hat{x}}(k+nq,\omega;K')\} = \frac{1}{M}\, k_M \qquad q \geq 1 \tag{17}$$

where the overlap fraction is $(K'-q)/K'$. The constant k_M is a function of the overlap, being unity for nonoverlapping segments ($q > K'$). For typical tapered windows (Hanning, e.g.) it increases only slightly above unity when the overlap is increased from zero to approx. 50 percent [14]. Apparently, the resolution of the averaged periodogram is the same as for a K' sample modified periodogram.

The use of periodogram techniques in Doppler signal analysis can be justified by the fact that a K sample periodogram models the Doppler signal as a MA process of order K. Intuitively, selecting $K = M_v$ should then be a sufficient requirement to avoid analysis broadening. The stronger requirement (13) occurs because the finite K modified periodogram is a biased estimator of any nonwhite spectrum, including that of a MA process of order K.

3. THE MISSING SIGNAL ESTIMATOR.

3.1 Basic approach

An algorithm for the filling in of the missing Doppler signal segments during the imaging interrupt periods, a 'Missing Signal Estimator' (MSE), is derived in this section. It is assumed that the interrupts are so short that the Doppler signal can be modeled as a stationary process during N samples prior to, and throughout the interrupt. The problem can then be stated as; given N samples $\{\hat{x}(k)\}_1^N$ of a stationary, complex Gaussian MA process; how should the process be extrapolated for $k > N$?

At first glance it may seem natural to do the signal filling by least squares linear prediction methods. However, the correlation time of the Doppler signal is much shorter than the interrupt. Any MMSE estimate of a zero mean random process will rapidly decay to zero during this timeframe, implying that standard extrapolation algorithms will not perform well.

A more fruitful approach is to identify a model for the Doppler signal on the basis of the samples given, and let this model generate a synthetic Doppler signal during the interrupt. If the power spectrum of the Doppler signal is known, such a signal can be generated by passing Gaussian white noise through a linear filter with transfer function $H(\omega)$, satisfying $|H(\omega)|^2 = G_{\hat{x}\hat{x}}(\omega)$. The output of the filter and the real Doppler signal then would be sample functions from the same ensemble, with equivalent information contents.

Based on the above, the following approach seems viable: A spectrum estimate $\hat{G}_{\hat{x}\hat{x}}(\omega)$ is computed from the known signal samples. The estimate is used to design a filter which satisfies $|H(\omega)|^2 = \hat{G}_{\hat{x}\hat{x}}(\omega)$. When Gaussian white noise is passed through this filter, a stationary Gaussian process is synthesized. A segment of this process can be used as a replacement for the missing signal during the interrupt period. The filter design part of this problem is developed in the next section. A method for adjoining the measured and the synthesized segments in a smooth way is derived in Section 3.5.

3.2 Synthesis of a Gaussian signal with a specified spectrum.

In Section 2 it was argued for the use of standard Fourier transform techniques in the estimation of power spectra of Doppler signals from blood. The **N** sample modified periodogram, therefore, forms a suitable basis for the determination of the transfer function of the synthesizer filter. Initially, assume that the filter is of an all-zero form, i.e.,

$$H(\omega) = \sum_{m=-\infty}^{\infty} h(m) e^{-jm\omega T_s} \tag{18}$$

where $\{h(m)\}$ is a set of complex coefficients that must be chosen to satisfy

$$\sum_{m=-\infty}^{\infty} h(m) e^{-jm\omega T_s} = \sqrt{\tilde{G}_{\hat{x}\hat{x}}(N/2,\omega;N)\, e^{j\tau(\omega)}} \tag{19}$$

where $\tau(\omega)$ is an arbitrary phase function. Multiplying both sides of this equation with $\exp(jn\omega)$ and integrating from $-\omega_s/2$ to $\omega_s/2$ on both sides then yields

$$h(n) = \frac{1}{\omega_s} \int_{-\omega_s/2}^{\omega_s/2} d\omega \sqrt{\tilde{G}_{\hat{x}\hat{x}}(N/2,\omega;N)\, e^{j\tau(\omega)}}\, e^{jn\omega T_s} \tag{20}$$

It turns out that the following phase function is advantageous;

$$\tau(\omega) = \arg\{ \sum_{k=1}^{N} w_s(k;N)\hat{x}(k) e^{-jk\omega T_s} \} \tag{21}$$

where $\{w_s(k;N)\}$ is the N point window associated with the periodogram $\tilde{G}_{\hat{x}\hat{x}}(\omega;N)$. Substitution of (9) and (21) in (20) now yields

$$h(n) = \frac{1}{\omega_s} \int_{-\omega_s/2}^{\omega_s/2} d\omega \sum_{k=1}^{N} w_s(k;N)\hat{x}(k) e^{-jk\omega T_s}\, e^{jn\omega T_s}$$

$$= \begin{cases} w_s(n;N)\hat{x}(n) & n = 1, \ldots, N \\ 0 & \text{elsewhere} \end{cases} \tag{22}$$

The synthesizer filter thus becomes a FIR filter of order N, with coefficients that are simply windowed signal samples. Note that, because of the phase function chosen, no spectrum estimation needs to be carried out in the computation of the coefficients. The synthesis equation for a stationary, artificial Doppler signal thus becomes

$$\tilde{x}(k) = \sum_{n=1}^{N} h(n)\hat{v}(k-n) \tag{23}$$

where $\{\hat{v}(n)\}$ is a Gaussian complex white noise process with the properties

$$\langle\hat{v}(k)\rangle = 0 \tag{24}$$

$$\langle\hat{v}^{*}(k)\hat{v}(n))\rangle = \delta_{kn} \tag{25}$$

and δ_{kn} is the Kronecker delta symbol. The synthesized signal is a MA process of order N. By linearity, when the noise excitation is Gaussian, the synthesized signal is Gaussian also.

The auto- and cross-correlation functions of the quadrature components x,y of a complex Gaussian process satisfy the symmetry relations $R_{xx}(k) = R_{yy}(k)$ and $R_{xy}(k) = R_{yx}(k)$ [10]. It can be shown that the quadrature components of the synthesized signal will not satisfy these relations unless the excitation $\{\hat{v}(k)\}$ is complex, with identically distributed, jointly uncorrelated quadrature components (stated without proof). For optimum quality synthesis it is necessary that these criteria be satisfied, even if the spectrum of the synthesized signal is the same for any type of white noise excitation (see Section 5).

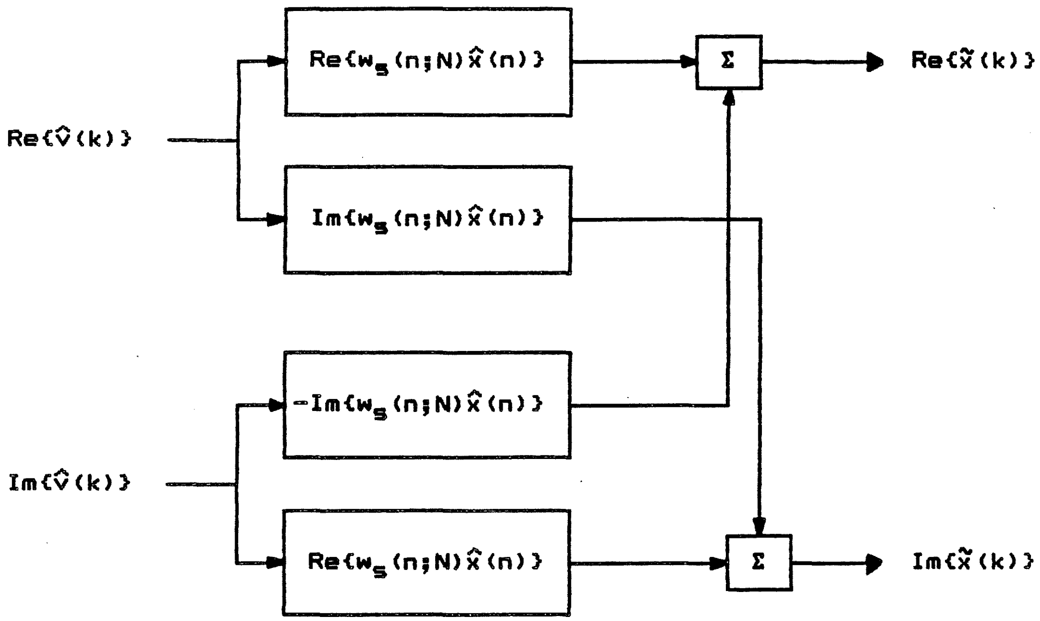

Fig. 1 Structure of the synthesis filter. The individual filters are designated with their impulse responses.

The structure of the synthesis filter is shown in Fig. 1. The complex excitation requires the use of four FIR filters, each of order N, in a structure similar to the well known FFT butterfly. Note that only two filters are required if a real valued excitation is used.

The computational complexity of the synthesis operation can be reduced by using a noise excitation with quadrature components that are binary distributed {-1,1}, instead of being Gaussian. The operations in (23) then reduce to a set of additions and subtractions, depending on the sign of the noise samples. With a reasonably large N, the synthesized signal still approximates a Gaussian process, according to the Central Limit Theorem.

3.3 Spectral properties of the synthesized signal.

It is of interest to quantify how well the properties of the synthesized signal approximate those of the original Doppler signal. The synthesized signal is formed as a combination of sample functions from the two independent stochastic processes {$\hat{x}$(k)} and {$\hat{V}$(n)}, and a deterministic time window of length N (see Fig. 2). Its spectrum therefore becomes a random variable; different sample functions of the ensemble of the measured

Doppler signal yield, in general, synthesized signals with different power spectra. It follows from (10) and the preceding derivation that the expected spectrum is

$$\langle G_{\tilde{x}\tilde{x}}(\omega)\rangle = \langle\langle G_{\tilde{x}\tilde{x}}(\omega) \mid \{\hat{x}(k)\}\rangle_{\hat{v}}\rangle_{\hat{x}} = \langle \tilde{G}_{\hat{x}\hat{x}}(N/2,\omega;N)\rangle_{\hat{x}}$$

$$= W_s(\omega;N) \circledast G_{\hat{x}\hat{x}}(\omega) \qquad (26)$$

where the subscripts $\hat{v}, \hat{x}$ indicate averaging over the ensembles of the noise excitation and the Doppler signal, respectively. The convolution with the coefficient spectral window $W_s(\omega)$ may cause the spectrum of the synthesized signal to become broader than the original. This effect occurs for the same reason as the analysis broadening effect previously discussed; its implications are therefore the same. By analogy with (13), its influence on the spectrum at the frequency f_d can be neglected if

$$N \gg 2\Lambda \frac{f_s}{f_d} \qquad (27)$$

Similarly, the fractional variance of the power spectrum becomes

$$\mathrm{Fracvar}\{G_{\tilde{x}\tilde{x}}(\omega)\} = 1 \qquad (28)$$

The large variance implies that the power spectrum of an arbitrary sample function of the synthesized signal may deviate strongly from its expected value. This type of bias differs from the broadening effects previously discussed; it results from the use of the high-variance modified periodogram to form the coefficients of the synthesizer filter. If (19) were solved for the coefficients using a lower variance spectrum estimator, the variance of the spectrum of the synthesized signal would also become lower. However, this variance reduction would have taken place at the expense of a decreased frequency resolution. Moreover, the simple relation between the signal samples and the filter coefficients would be lost.

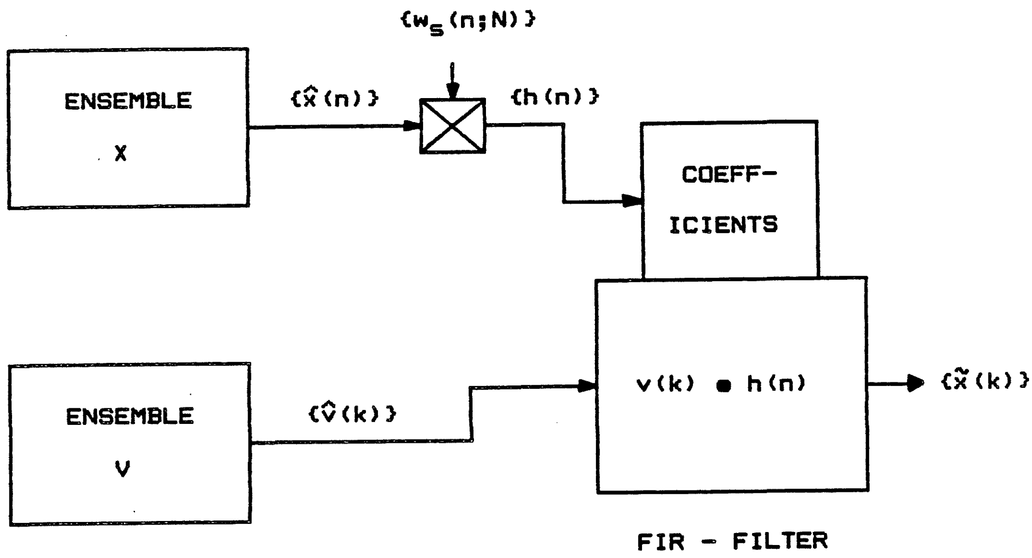

Fig. 2. The synthesized signal as a combination of the stochastic processes X, V and the deterministic time window $\{w_s(n;N)\}$.

3.4 Spectrum analysis of the synthesized signal.

Suppose that the synthesis method is employed in a Doppler instrument where the output of the synthesis filter is monitored by a K sample modified periodogram spectrum analyzer. The expected value of the periodogram becomes

$$\langle \tilde{G}_{\tilde{x}\tilde{x}}(\omega;K) \rangle = W_a(\omega;K) \bullet W_s(\omega;N) \bullet G_{\hat{x}\hat{x}}(\omega) \tag{29}$$

Thus, the net spectral window of the combined synthesis/analysis operation is the convolution between the analyzer and the synthesizer spectral windows. The one with the larger bandwidth becomes the limiting factor in terms of resolution.

The variance of the estimate is somewhat more difficult to compute. Initially, assume that K >> N. The modified periodogram then becomes essentially unbiased, and it follows that

$$\begin{aligned}
\mathrm{Var}\{\tilde{G}_{\check{x}\check{x}}(\omega;K)\} &= \langle\langle \mathrm{Var}\{\tilde{G}_{\check{x}\check{x}}(\omega;K) \mid \{\hat{x}(k)\}_1^N\}\rangle_{\check{v}}\rangle_{\hat{x}} \\
&= \langle\langle \tilde{G}_{\check{x}\check{x}}(\omega;K) \mid \{x(k)\}_1^N\rangle_{\check{v}}{}^2\rangle_{\hat{x}} \\
&\simeq \langle \tilde{G}^2_{\hat{x}\hat{x}}(N/2,\omega;N)\rangle_{\hat{x}} \\
&\triangleq \mathrm{Var}\{\tilde{G}_{\hat{x}\hat{x}}(N/2,\omega;N)\} + \langle \tilde{G}_{\hat{x}\hat{x}}(N/2,\omega;N)\rangle^2 \\
&= 2\ \langle \tilde{G}_{\hat{x}\hat{x}}(N/2,\omega;N)\rangle^2 \\
&\simeq 2\ \langle \tilde{G}_{\check{x}\check{x}}(\omega;K)\rangle^2 \qquad\qquad K \gg N \qquad\qquad (30)
\end{aligned}$$

i.e., its fractional variance is two. On a logarithmic scale, this corresponds to a standard deviation of the estimate equal to 9.8 dB [14]. The poor performance occurs as a result of using high-variance spectrum estimators as the basis for both synthesis and analysis.

Assume instead that a low-variance spectrum estimator is employed in the analysis, e.g., the method that averages a number of K sample modified periodograms of signal segments with approx. 50 percent overlap. If $K \ll N$, the finite resolution of the spectrum estimator causes considerable smoothing of the power spectrum (see (29)). This is equivalent to the frequency domain smoothing discussed in (16); the effective analysis bandwidth now becomes $B_a = k_a/KT_s$. If a sufficiently large number of periodograms is averaged, the variance of the analysis operation becomes negligible compared to the variance of the expected value over the ensemble of $\hat{x}$, and the attainable variance according to (16) becomes

$$\begin{aligned}
&\mathrm{Fracvar}\{\sum_{n=1}^{M} \tilde{G}_{\check{x}\check{x}}(k+nK/2,\omega;K)\} \\
&\qquad \simeq \mathrm{Fracvar}\{\langle\sum_{n=1}^{M} \tilde{G}_{\check{x}\check{x}}(k+nK/2,\omega;K)\rangle_{\check{v}}\}_{\hat{x}} \\
&\qquad \simeq \mathrm{Fracvar}\{W_a(\omega;K) \bullet \tilde{G}_{\hat{x}\hat{x}}(N/2,\omega;N)\} \\
&\qquad \simeq \frac{k_s' KT_s}{k_a NT_s} \simeq \frac{K}{N} \qquad K \ll N, \qquad M \gg \frac{N}{K} \qquad\qquad (31)
\end{aligned}$$

where $k_s' \approx k_a$ is the shape factor of the coefficient window $\{w_s(k;N)\}$. Therefore, if the ratio $Q = N/K$ can be made large, a low-variance spectrum estimate is obtained from a synthesized signal based on the simple method employing windowed signal samples. This ratio becomes in a sense a quality measure on the combined synthesis/analysis operation. The duration of the data segment that forms the basis for the synthesis is $T_m = NT_s$. If K is adjusted such that (13) is satisfied with equality, the quality factor becomes

$$Q = \frac{N}{K} = \frac{T_m}{2\Lambda} f_d \qquad (32)$$

In Doppler/imaging timeshared operation at a fixed frame rate, T_m will also be fixed. The attainable quality of the combined synthesis/ analysis operation then improves in proportion with the Doppler shift.

3.5. Signal filling using the synthesized signal.

In timeshared imaging/ Doppler operation, the measured Doppler signal is interrupted on the interval $N < k \leq N_i$, and the filling in of the missing samples must be performed on the basis of $\{\hat{x}(k)\}_1^N$. Even if a synthesis algorithm for a stationary signal was derived in Section 3.2, it is not evident how the measured and the synthesized signals should be adjoined. The synthesis method yields a signal of infinite time duration, which needs to be truncated to a segment of duration on the order of $N_i - N$ samples, without changing its spectrum significantly. A study of how the synthesized signal is generated gives insight into the truncation problem. To do so, (23) is rewritten as

$$\tilde{x}_s(k) = \sum_{m=k-N}^{k-1} \hat{V}(m)h(k-m) \qquad \forall\, k \qquad (33)$$

showing that each complex noise sample $\hat{V}(m)$ excites a corresponding signal burst $\hat{V}(m)\{h(k-m)\}$, $k = m+1,..,m+N$, with random complex amplitude. Thus, the synthesized signal is formed by incoherent addition of proportional bursts with different times of arrival. Its power spectrum is then proportional to the magnitude squared Fourier Transform of each burst. Note the strong similarity with the way the original Doppler signal is generated; independent scatterers with different time of arrival then each contribute to the signal with finite duration bursts of proportional shapes. Apparently, the shape of the expected spectrum will not change if the synthesized signal is truncated simply by employing a finite number of bursts. This is obtained by using a finite length noise excitation.

For this situation, it is appropriate to turn on the noise excitation on the interval $1 \leq k \leq N_i$. This yields a synthesized signal with a smoothly tapered envelope that is nonzero for $1 \leq k < N_i + N$. By inspection of (23), this **substitute segment** can be written as

$$\tilde{x}_s(k) = \begin{cases} \sum\limits_{n=\max\{1,k-N_i+1\}}^{\min\{k,N\}} w_s(n;N)\hat{x}(n)\hat{v}(k-n) & k = 1,..,N_i+N-1 \\ 0 & \text{elsewhere} \end{cases} \tag{34}$$

where the properties of the excitation have been defined previously ((24) and (25)). Even if this signal is of a finite duration, its expected power spectrum is the same, within a constant factor, as for the infinite sequence generated by (26).

The normalized envelope of the substitute signal is defined as

$$e(k) \triangleq \sqrt{\langle|\tilde{x}_s(k)|^2\rangle / R_{\hat{x}\hat{x}}(0)}$$

$$= \begin{cases} \sqrt{\sum\limits_{\max\{1,k-N_i+1\}}^{\min\{k,n\}} w_s^2(n;N)} & k = 1,..,N_i+N-1 \\ 0 & \text{elsewhere} \end{cases} \tag{35}$$

It increases smoothly from zero to unity during samples 1 to N (the square sum of the window coefficients is unity), and decreases to zero again from sample N_i+1 to N_i+N-1 (see Fig. 3).

The substitute segment must be adjoined with the measured signal in a way that gives a low disturbance of the output. A viable method is to add the substitute segment and a windowed version of the measured signal, i.e.,

$$\hat{x}_f(k) \triangleq w_f(k;N,N_i)\hat{x}(k) + \tilde{x}_s(k) \tag{36}$$

where $\{\hat{x}_f(k)\}$ designates the 'filled' Doppler signal that is presented to the operator. The window $\{w_f(k)\}$ can be determined uniquely by requiring the envelope of the filled signal to be time invariant,

$$\langle|\hat{x}_f(k)|^2\rangle = R_{\hat{x}\hat{x}}(0) \quad \forall\ k \tag{37}$$

Assuming $\langle\hat{v}(k)\hat{x}^*(l)\rangle = 0 \quad \forall\ k,l$ then yields

$$w_f(k;N,N_i) = \sqrt{1 - e^2(k)} \tag{38}$$

which is illustrated in Fig. 3. The approach chosen leads to a fade out/ fade in type of use of the measured signal, with two N sample transition periods where the measured and the substitute segments both contribute to the output.

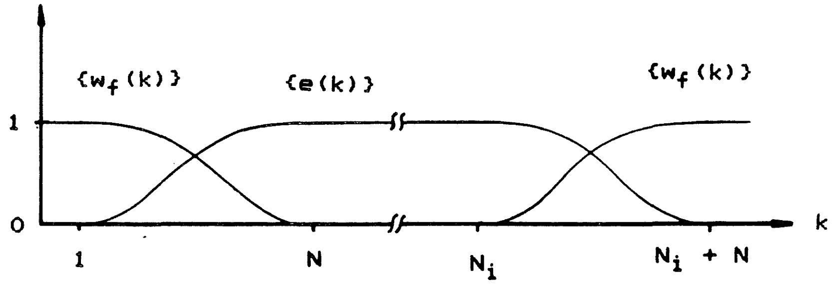

Fig. 3. Envelopes of the synthesized and the measured signals during an interrupt (Hanning windowed filter coefficients assumed).

4. EXPERIMENTAL EVALUATION.

A hardwired 8 bit digital MSE was designed and built on 320 cm^2 of printed circuit board area. The number of samples N used in the synthesis filters could be chosen from the set {16,32,48,64,96,128,192,256}, with maximum sampling frequency limited to 41 kHz. A high speed/complexity ratio was made possible by the use of a degenerated noise excitation; adjacent samples of the white noise excitation defined by (24) and (25) were interleaved with zeros such that only 16 complex noise samples contributed to the output at any time instant. The degenerated noise sequence can be written as

$$\tilde{V}(k) = \begin{cases} \hat{V}(16k/N) & (16k \bmod N) = 0 \\ 0 & \text{elsewhere} \end{cases} \tag{39}$$

where (16k mod N) is the remainder of the integer division 16k/N (N is an integral multiple of 16). The power spectrum of the degenerated noise is flat, but it has, apparently, fewer degrees of freedom than a full-bandwidth white noise sequence. This is reflected by the fact that its modified periodogram is periodic, i.e.

$$\tilde{G}_{\tilde{V}\tilde{V}}(k,\omega;K) \equiv \tilde{G}_{\tilde{V}\tilde{V}}(k,\omega + 16n\omega_s/N;K) \qquad \begin{matrix} n = 0,1,..,N/16 \\ K = mN, \; m = 1,2,... \end{matrix} \tag{40}$$

The Doppler instrument was set for operation with 23 ms interrupts at 15 Hz repetition rate. This corresponds to 15 Hz imaging with 16 ms image data acquisition per frame; the additional 7 ms were needed for settling of the Doppler highpass filters (f_c = 400 Hz) after an interrupt. The signal filling scheme outlined in the previous section was employed during each interrupt, using Hanning windowed filter coefficients. The 8 bit A/D convertion was preceded by a fast AGC to reduce saturation effects during the synthesis data acquisition periods.

The data collecting time to the synthesis filter $T_m = N/f_s$ must be chosen subject to conflicting requirements. It should be long to avoid broadening effects and give a reliable spectrum estimate (see (27),(31)). On the other hand, the quasistationarity assumption is violated if T_m is much larger than 10 ms. Also, the lengths of the transition periods in Fig. 3 increase with T_m, so that an increased acquisition time leads to a reduction in the amount of real data in the filled signal. It was found from experiments that a nominal value of 10 ms was a reasonable compromize. With f_s as the independent variable, N was chosen from the available set such that $T_m \approx 10$ ms. This gives a maximum spectral resolution equal to 210 Hz in the synthesized signal (follows from (26) and (12)).

The output of the MSE was evaluated by both listening to the quadrature components of $\{\hat{x}_f(k)\}$ and by spectrum analysis. The spectrum analysis was done on a $K = 64$ Hanning windowed DFT computer with 1 ms computation time[2]. Modified periodograms of eight consecutive signal segments were averaged to reduce variance; the length of the non-overlapping part of two adjacent segments was fixed at 1 ms, and the average was updated every millisecond for display and hardcopy on a stripchart recorder. A typical spectral display is shown in Fig. 4, together with the outputs of the synthesis MSE and a correspondingly parametrized repetition-type MSE as mentioned to in the introduction (see [7] for further information). Some distortion due to undersampling can be noticed in both, especially during the upstroke of the velocity waveform. For the repetition-type MSE this shows up as breakups or dual upstrokes; for the synthesis type the spectrum either breaks up, or is 'held' during the interrupt. The basic features of the waveform, however, are retained in both

[2]PCD-4, VINGMED a/s, Horten, Norway

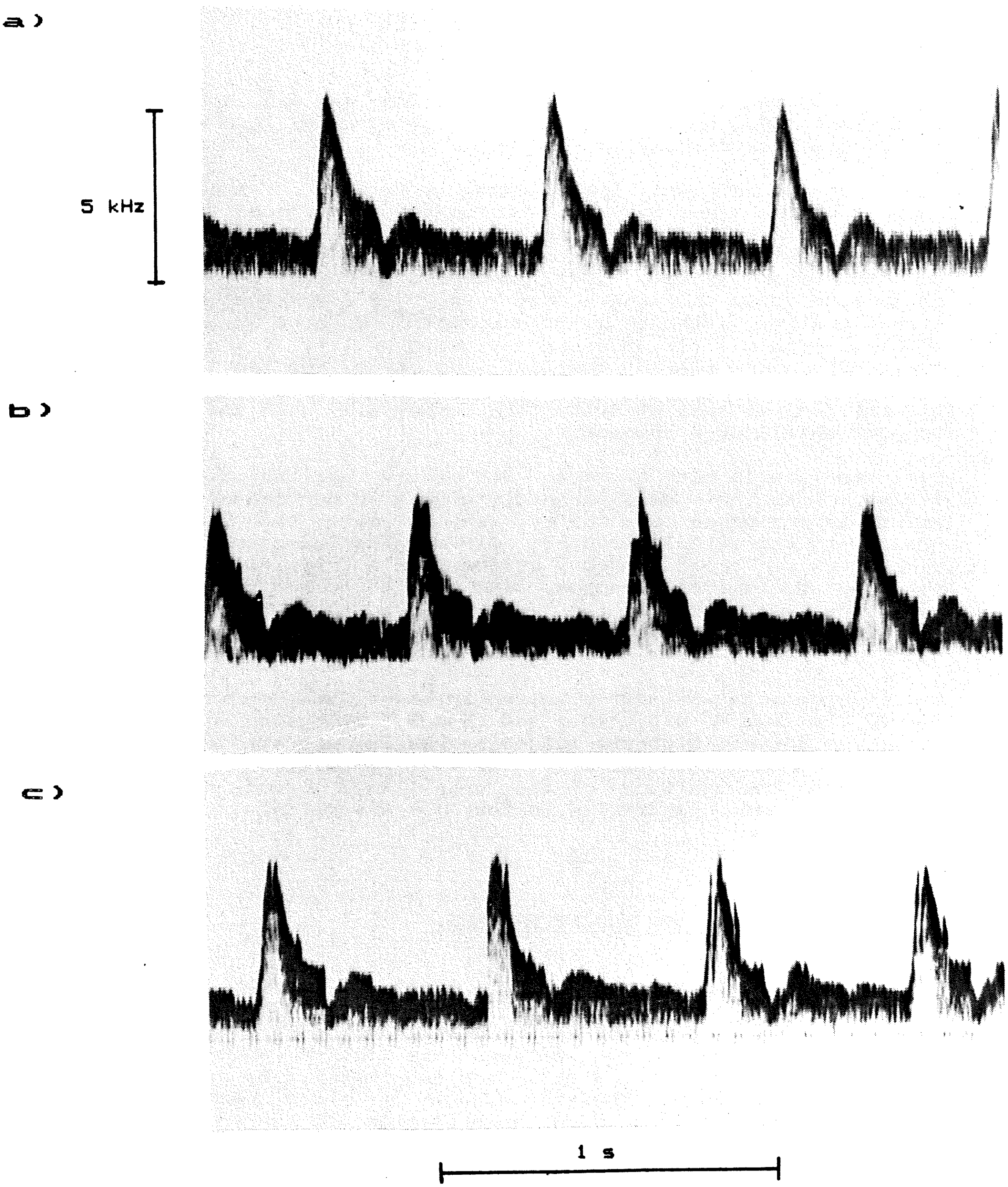

Fig. 4. Spectral displays of signals from the common carotid artery, measured with 5 MHz pulsed Doppler, sample volume length 11 mm, and 12.5 kHz PRF. The three panels show different heartbeats of a healthy person in steady state physiological conditions.
a) Original signal.
b) Timeshared operation with synthesis type MSE, N = 128.
c) Timeshared operation with repetition type MSE.

cases. For the case shown, the ratio K/N was 0.5, so in agreement with (31), no severe increase of variance can be noticed in the spectral display in Fig. 4(b).

The synthesis MSE was tested using a variety of signals. The quality of the audio output was in general very good. For narrow-to-medium bandwidth signals (relative to f_s) it was hard to discriminate between the output of the MSE and the original noninterrupted signal. Very wideband signals, such as white background noise or signals from veins, had a somewhat more artificial quality, although no deterioration could be noticed in the spectral display. In general, the audio quality of the synthesis type MSE approximated that of the true Doppler signal more closely than the repetition type MSE; the latter suffered from a modulation-like type of distortion, especially when low frequency Doppler shifts were present.

Experiments with both Gaussian and binary excitations were performed, with no perceivable difference in performance. Binary noise was preferred eventually, as it gave less quantization noise with the actual hardware. It was also found that a complex excitation performed markedly better than a real excitation with the same degrees of freedom. The latter tended to give reverberation-like effects in the synthesized audio signal, especially when low frequency signals from tissue (wall thumps) vere present.

One problem area was moving valves in heart measurements. These tended to sound distorted and become elongated in time; the transient nature of these signals clearly violated the stationarity assumption. Moreover, their amplitudes were normally much larger than the amplitude of the signal from blood, so that it was hard to avoid saturation in the A/D conversion.

5. DISCUSSION AND CONCLUDING REMARKS.

The new MSE algorithm yields a filled signal with a spectral display that is essentially a 'track and hold' approximation to the true one: The spectrum is 'held' during the interrupt periods, and the transitions between the 'hold' and the 'live' segments of the spectral display are smoothed by the simultaneous use of measured and synthesized signals in these periods. Whether or not this is a good approximation to the true velocity waveform depends on the duration of the interrupt compared to the rate of change of the velocity. For an interrupt on the order of 25 ms, the stationarity assumption is violated during the upstroke of the velocity in an artery. Signal filling by means of a stationary process then inevitably leads to a spectral display with a poor representation of rapid velocity changes. In the audio signal, however, this effect is much less noticeable. The representation of rapid velocity changes may be improved by reducing the interrupt time, e.g., by using a small number of scan lines in the 2D image.

Eq. (40) indicates that the simplified excitation (39) introduces deterministic components in synthesized signals of bandwidths greater than $16f_s/N$ (corresponding to 1600 Hz bandwidth for a data collection time $T_m = 10$ ms). This is probably the reason why the audio quality of synthesized wideband signals was poorer than that of the more narrowband signals. This effect would have been avoided by the use of a full-bandwidth white noise excitation.

The benefit of using a complex valued excitation was surprising at first. The explanation is that for low frequencies (on the order of $1/T_m$), the amount of data acquired to the synthesis is sparse, and due to random variations, the energy of the coefficient set $\{w(k;N)\hat{x}(k)\}$ may become unevenly distributed between $\{w(k;N)\mathrm{Re}\{\hat{x}(k)\}\}$ and $\{w(k;N)\mathrm{Im}\{\hat{x}(k)\}$. Because of the cross-coupling between the quadrature components illustrated in Fig. 1, this unbalance is not transferred to the synthesized signal when the excitation is complex. With a real excitation, however, the powers of the real and the imaginary parts of the synthesized signal remain unbalanced for the entire interrupt period. This problem is encountered in the audio only; the spectrum calculated on the basis of the complex signal does not depend on how the power is distributed between the quadrature components.

The synthesis method derived in this paper resembles that used in speech processing, where white noise excitation of a programmable IIR filter is used to synthesize unvoiced sounds, whereas a deterministic impulse train excitation is used to generate voiced sounds. The simplified excitation (39) is in essence a hybrid of the two. It is interesting to note that if the single-impulse excitation $\{\hat{v}(k)\} = \delta_{Nk}$ is chosen in (34), and the data collecting time T_m is chosen equal to the net interrupt time, the synthesis MSE degenerates to a repetition-type MSE.

In conclusion, the new MSE scheme gives better results than the repetition scheme described previously. Most of the limitations encountered in the experiments were caused by the hardware implementation, rather than being fundamental. Although this paper has dealt exclusively with pulsed Doppler systems, the scheme applies equally well to CW systems. The algorithm allows for the design of timeshared Doppler/real time imaging systems where high frame rate imaging introduces only minor disturbances or limitations to the Doppler measurement.

ACKNOWLEDGEMENT

This work has been supported by grants from the Norwegian Institute of Technology, Trondheim.

6. REFERENCES.

[1] D.W. Baker, S. Rabenstein, G.S. Lorch: "Pulsed Doppler Echocardiography: Principles and applications," **Am. J. of Med.**, Vol. 63, pp. 69-80, July 1977.

[2] M.A. Brandestini, M.K. Eyer, J.G. Stephenson: "M/Q-mode Echocardiography - the synthesis of conventional echo with digital multigate Doppler". In: **Proceedings 3rd Symposium on Echocardiology.** Amsterdam, The Netherlands: Martinus Nijhoff, 1979, pp. 441-446.

[3] D.J. Phillips, J.E. Powers, M.K. Eyer, W.M. Blackshear jr., K.C. Boidly, D.E. Strandness jr., D.W. Baker: "Detection of peripheral vascular desease using the Duplex Scanner III". **Ultrasound in Med. and Biol.**, Vol. 6, No. 3, pp. 205-218, 1980.

[4] A. Kitabatake et. al.: "Non-invasive visualization of intracardiac flow by multigate Doppler technique". In: W. Bleifeldt, D. Harder, H.-K. Leetz, N. Schaldac (eds): **Proceedings World Congress on Medical Physics and Biomedical Engineering**, Hamburg, sept. 1982. Published by NPBE-1982 e.W, Hamburg 1982.

[5] Kazuhiro Iinuma, Kinya Takamizawa: "Ultrasonic Doppler Apparatus". US patent # 4,318,413, Mar. 9, 1982.

[6] J.F. Suarez jr., H.L. Schwarz, A.J. Rosetti, P.D. Corb: "Ultrasonic imaging apparatus for providing simultaneous B-scan and Doppler data". US patent # 4,407,293, Oct. 1983.

[7] B.A.J. Angelsen, K. Kristoffersen: "Combination of 2D-Echo Amplitude Imaging and Doppler Measurements. In: M.P. Spencer (ed.): **Cardiac Doppler Diagnosis.** Boston: Martinus Nijhoff 1984.

[8] K. Kristoffersen: "Optimal Receiver Filtering in Pulsed Doppler Ultrasound Blood Velocity Measurements". **IEEE Trans. Ultras. Ferr. Freq. Cont.**, vol. UFFC-33, pp. 51-58, Jan. 1986.

[9] L. Hatle, B.A.J. Angelsen: **"Doppler Ultrasound in Cardiology - Physical Principles and Clinical Applications".** New York: Lea and Fabiger 1982.

[10] B.A.J. Angelsen: "A Theoretical Study on the Scattering of Ultrasound from Blood". **IEEE Trans. Biomed. Eng.**, vol. BME-27, pp. 61-67, Feb. 1980.

[11] A.P.G. Hoeks: "On the development of a Multi-gate pulsed Doppler system with serial data-processing". University of Maastricht, Ph.D. dissertation, Maastricht, The Netherlands 1982.

[12] D.A. Mc.Donald: **"Blood Flow in Arteries"**. London: Edward Arnold 1974.

[13] A.H. Nuttall: "Spectral estimation by means of overlapped Fast Fourier Transform processing of windowed data". NUSC tech. rep. # 4169, New London, CT, Oct. 13., 1971.

[14] K. Kristoffersen: "Real Time Spectrum Analysis in Doppler Ultrasound Blood Velocity Measurements". SINTEF rep. #STF48 F84030, SINTEF - the Foundation of Industrial and Technical Research at the Norwegian Institute of Technology, 7034 Trondheim-NTH, Norway, Nov. 1984.

[15] P.D. Welch: "The use of fast Fourier transform for the estimation of power spectra: A method based on time averaging over short, modified periodograms". **IEEE Trans. Audio and Electroacoustics**, vol. AU-15, pp. 70-73, June 1967.

[16] P. S. Green, L. F. Schafer, J. C. Taenzer, J. F. Holzemer, S. D. Ramsey Jr., J. R. Suarez, "Real-time Ultrasonic Imaging and Doppler Profile Display System and Method," U.S. pat. no. 4141 347, Feb. 1979.

[17] V. L. Newhouse, E. S. Furgason, G. F. Johnson, D. A. Wolf, "The dependence of Ultrasound Doppler Bandwidth on Beam Geometry." IEEE Trans. Sonics Ultras., vol SU-27, pp. 50-59, March 1980.

APPENDIX

Variance of the Smoothed Modified Periodogram

Assume a sampling frequency of unity ($T_s = 1$). The smoothed modified periodogram is then defined by

$$S(\omega) = \int_{-\pi}^{\pi} d\Omega\, \tilde{G}_{\hat{X}\hat{X}}(\Omega) W_c(\Omega-\omega) \tag{A1}$$

where $W_c(\omega)$ is a real valued smoothing window with statistical bandwidth $B_c \gg k_a/K$. For simplicity, it has been assumed that $W_c(\omega)$ is periodical with period 2π. The variance of $S(\omega)$ is given by

$$\mathrm{Var}\{S(\omega)\} = \int_{-\pi}^{\pi} d\Omega_1 \int_{-\pi}^{\pi} d\Omega_2\, W_c^*(\omega-\Omega_1)\mathrm{Cov}\{\tilde{G}_{\hat{X}\hat{X}}(\Omega_1), \tilde{G}_{\hat{X}\hat{X}}(\Omega_1+\Omega_2)\} W_c(\omega-\Omega_1-\Omega_2) \tag{A2}$$

When the signal is a complex Gaussian process, the covariance of the modified periodogram is given by [14]

$$\mathrm{Cov}\{\tilde{G}_{\hat{X}\hat{X}}(\omega), \tilde{G}_{\hat{X}\hat{X}}(\omega+\Delta)\}$$

$$= \frac{1}{(2\pi)^2} \left| \int_{-\pi}^{\pi} d\lambda\, W(\lambda) W(\Delta-\lambda) G_{\hat{X}\hat{X}}(\omega-\lambda-\Delta) \right|^2 \tag{A3}$$

where

$$W(\omega) = \sum_{k=1}^{K} w_a(k;K) e^{-k\omega} \tag{A4}$$

is the frequency response of the modified periodogram time window. Eq. (A3) shows that periodogram spectral estimates spaced more than one mainlobe width apart ($\Delta > k_a/K$) are essentially uncorrelated. Because of the larger bandwidth of the smoothing window, the term $\mathrm{Cov}\{\tilde{G}_{\hat{X}\hat{X}}(\Omega_1), \tilde{G}_{\hat{X}\hat{X}}(\Omega_1+\Omega_2)\}$ therefore behaves as a delta function in the integrand of (A2). This gives the approximation

$$\mathrm{Var}\{S(\omega)\} \approx \int_{-\pi}^{\pi} d\Omega_1\, |W_c(\omega-\Omega_1)|^2 \int_{-\pi}^{\pi} d\Omega_2\, \mathrm{Cov}\{\tilde{G}_{\hat{X}\hat{X}}(\Omega_1), \tilde{G}_{\hat{X}\hat{X}}(\Omega_1+\Omega_2)\}$$

$$= \frac{1}{(2\pi)^2} \int_{-\pi}^{\pi} d\Omega_1\, |W_c(\omega-\Omega_1)|^2 \int_{-\pi}^{\pi} d\Omega_2 \left| \int_{-\pi}^{\pi} d\lambda\, W(\lambda) W(\Omega_2-\lambda) G_{\hat{X}\hat{X}}(\Omega_1-\lambda-\Omega_2) \right|^2 \tag{A5}$$

where (A3) has been inserted. Now assume that the bandwidth of the spectrum is much larger than k_a/K. The frequency responses

$W(\lambda)$, $W(\Omega_2-\lambda)$ then behave as delta functions in the two rightmost integrals in (A5), which gives the approximation

$$\mathrm{Var}\{S(\omega)\} \approx$$

$$\frac{1}{(2\pi)^2}\int_{-\pi}^{\pi} d\Omega_1\ |W_c(\omega-\Omega_1)|^2\ G^2_{\hat{X}\hat{X}}(\Omega_1)\int_{-\pi}^{\pi} d\Omega_2\ \left|\int_{-\pi}^{\pi} d\lambda\ W(\lambda)W(\Omega_2-\lambda)\right|^2 \tag{A6}$$

Finally, assume that the bandwidth of the spectrum is much larger than that of the smoothing window $W_c(\omega)$. Arguing along the same lines as previously then gives the following expression for the variance;

$$\mathrm{Var}\{S(\omega)\} \approx$$

$$\frac{1}{(2\pi)^2}\ G^2_{\hat{X}\hat{X}}(\omega)\int_{-\pi}^{\pi} d\Omega_1\ |W_c(\Omega_1)|^2\ \int_{-\pi}^{\pi} d\Omega_2\ \left|\int_{-\pi}^{\pi} d\lambda\ W(\lambda)W(\Omega_2-\lambda)\right|^2 \tag{A7}$$

Under the same assumptions as previously, the expected value of the smoothed modified periodogram becomes

$$\langle S(\omega)\rangle \approx \frac{1}{2\pi}\ G_{\hat{X}\hat{X}}(\omega)\int_{-\pi}^{\pi} d\Omega_1\ W_c(\Omega_1)\int_{-\pi}^{\pi} d\Omega_2\ |W(\Omega_2)|^2 \tag{A8}$$

which yields the fractional variance

$$\mathrm{Fracvar}(S(\omega)) = \frac{B'_a}{B_c} \tag{A9}$$

where B_c is the statistical bandwidth of the smoothing window (compare with the definition (12)), and B'_a is given as

$$B'_a = \frac{1}{2\pi}\ \frac{\int_{-\pi}^{\pi} d\omega\ \left|\int_{-\pi}^{\pi} d\Omega\ W(\Omega)W(\omega-\Omega)\right|^2}{\left[\int_{-\pi}^{\pi} d\omega\ |W(\omega)|^2\right]^2} = \frac{\sum_{k=1}^{K} w_a(k;K)^4}{\left[\sum_{k=1}^{K} w_a(k;K)^2\right]^2} = \frac{k'_a}{K} \tag{A10}$$

The time domain version of the equation was obtained by substituting (A4) into both the numerator and denominator of the frequency domain expression, and then interchanging the order of summation and integration. The bandwidth B'_a is the inverse of what may be called the 'statistical time duration' of the time window $\{w_a(k;K)\}$ (compare with (A4)). The constant k'_a is a function of the window shape. It is unity for the rectangular window and 1.94 for the Hanning window. For smooth, tapered windows k'_a and k_a become nearly equal, which implies that $B'_a \approx B_a$.

For sampling frequencies different from unity, the denominators of (A10) must be multiplied by T_s.